Analytical Modeling of Tube Bending with Hydroforming

by

Franco V. Normani

A thesis
presented to the University of Waterloo
in fulfillment of the
thesis requirement for the degree of
Master of Applied Science
in
Mechanical Engineering

Waterloo, Ontario, Canada, 2004

I hereby declare that I am the sole author of this thesis.

I authorize the University of Waterloo to lend this thesis to other institutions or individuals for the purpose of scholarly research.

Signature

I further authorize the University of Waterloo to reproduce this thesis by photocopying or by other means, in total or in part, at the request of other institutions or individuals for the purpose of scholarly research.

Signature

Borrower's Page

The University of Waterloo requires the signatures of all persons using or photocopying this thesis. Please sign below, and give address and date.

Abstract

A rotary-draw tube bending process is modeled analytically. The model is based on total deformation theory for the plastic bending calculations, and elastic theory of curved beams for the springback calculations. The model is applied to simulate bending of 76.2 mm outside diameter DQAK steel tubes of 1.57 mm wall thickness. Bends with R_c/d ratios (ratio of bend centerline-radius to tube outside diameter) of 2.5, 2.0 and 1.5 are considered. Supporting experiments are presented, considering the $R_c/d = 2.5$ and 2.0 bends, as well as numerical finite element (FE) simulations. In general, agreement between the analytical model with the experimental and FE bend results is shown to be good.

The analytical bend results are then used as input to secondary hydroforming FE simulations and compared with experiment. In addition, FE bend results are also used as input into the same hydroforming simulations. The agreement between the two different hydroforming simulations and experiment is also shown to be good.

Acknowledgements

The results of this thesis would not be possible without the guidance and instruction of Professor Michael Worswick. His dedication and encouragement made this experience fulfilling and satisfying.

I would like to thank all others who contributed to this work. In particular, I would like to thank Josh Dyment for being an invaluable team member, Dino Oliveira for his guidance and insights, and all other members of the Worswick research group who have had a hand in offering support and advice along the way.

I would like to give sincere thanks to Andrew Barber and Richard Gordon for their very helpful technical assistance, their expertise and experience in equipment setup and practical considerations. I would also like to thank John Boldt and all the machinist team in the machine shop.

Finally, I gratefully acknowledge the financial support for this research provided by AUTO21, Dofasco, Stelco, Eagle Precision Tools, IRDI, Nova Tube, D.A. Stuart, and CANMET.

Three years and 50 code revisions later and I am finally finished! A big salute to all the people who gave me support along the way: friends, co-workers, and especially family (Mom, Dad and big brother) who always had the big picture in mind and helped me keep my sights on the eventual outcome. I also want to thank the kind people at Club Abstract for their inspiration regarding the "elephant" theory, and all the other theories stemming from it.

"You have to like me, I'm an Engineer!" – Frank (Buddha) Normani

Table of Contents

List of Figures

List of Tables

Nomenclature

A = distance of neutral axis below tube centerline, for pure bending

A_{cs} = cross-sectional area

d = tube outside diameter

E = Young's elastic modulus

E_{ct} = centroid distance below centerline

E_s = modulus of plasticity

E_s^a = modulus of plasticity for element a

E_s^b = modulus of plasticity for element b

$e(\alpha)$ = membrane component of axial strain due to boost force

F_{boost} = axial boost force

K = strength coefficient

L_a = circumferential arc length of compressive region of tube

L_b = circumferential arc length of tensile region of tube

L_{SB} = arc length of strip B in curved region of bend

L_{stock} = original stock length of tube

l^b = boost distance

l_i = straight region length of section i of bent tube

l_o = initial fibre length before bending

l_1 = arbitrary fibre length at bend radius R

M = bending moment about centroid

m = displacement at neutral axis interface between elements a and b

n = strain hardening exponent

R = arbitrary bend radius

R_c = centerline bend radius

R_{NA}^e = distance measured from the bend axis to the elastic neutral axis

r = circumferential radius

r_c^e = distance measured from the bend axis to the centroid of area

r_o = radius at mid-thickness surface

r_b^e = distance measured from the bend axis to the point where the elastic stress is to be determined

S = travel of the back of tube for general bending case

S^* = travel of the back of tube for pure bending

s = linear distance along straight region, measured from end of bend

t = original tube wall thickness

t^* = arbitrary distance above or below mid-thickness surface on original un-deformed geometry

t_A, t_B, t_C = individual thickness values

t_b = thickness for pure bending

t_{new} = wall thickness after bending

u_r = radial displacement

u_α = circumferential (hoop) displacement

V = volume of strip A

V_1 = volume of strip B for pure bending

V_2 = volume of strip B for the general bending case

v = circumferential displacement of tube material due to hoop straining

w = infinitesimal strip width

w_1 = displacement field in axial direction

w_r = radial displacement

y = vertical distance above or below the tube centerline

θ = final bend angle

θ^* = particular bend angle within the bend region

α = circumferential angle

φ = change in tangential angle due to the deformation of mid-thickness surface after bending

ν = Poisson's ratio

ϕ_d = decay angle

α_{NA} = circumferential angle where the axial and hoop strain change sign

ε_1 = strain in axial direction

ε_2 = strain in hoop direction

ε_3 = strain in thickness direction

ε_1^{true} = axial true strain in bend (θ) direction

ε_1^a = average axial true strain over the compressive region of tube

ε_1^b = average axial true strain over the tensile region of tube

ε_2^a = average true hoop strain over the compressive region of tube

ε_2^b = average true hoop strain over the tensile region of tube

ε_3^a = average true thickness strain over the compressive region of tube

ε_3^b = average true thickness strain over the tensile region of tube

$\varepsilon_2^{a,eng}$ = average engineering hoop strain over the compressive region of tube

$\varepsilon_2^{b,eng}$ = average engineering hoop strain over the tensile region of tube

ε_{eff}^a = effective plastic true strain for element a

ε_{eff}^b = effective plastic true strain for element b

ε_{hoop} = average through-thickness engineering hoop strain, for general bending case

ε_{hoop}^o = average through-thickness engineering hoop strain, for pure bending

ε_{yp} = strain at yield point

σ_1 = stress in axial direction

σ_2 = stress in hoop direction

σ_3 = stress in thickness direction

σ_1^a = average axial stress over the compressive region of tube

σ_1^b = average axial stress over the tensile region of tube

σ_{eff}^a = effective von-Mises stress for element a

σ_{eff}^{b} = effective von-Mises stress for element b

σ_{y} = yield stress of material

Chapter 1 - Introduction

1.1 Overview

Pre-bending of tubes is often the first stage in the production of hydroformed structural members. Although much research has been done on the hydroforming process itself, there has been considerably less effort dedicated to studying the effect of pre-bending operations on the subsequent hydroformability of tubular parts.

Hydroforming is a process in which a hollow workpiece is expanded into a die under high internal water pressure. Upon application of the internal pressure, the workpiece "balloons" out until it reaches a desired final shape. Figure 1.1 shows an example of a hydroforming die, with a tubular sample in the as-bent and as-hydroformed conditions [1]. Figure 1.2 illustrates how the tube is hydroformed inside a die until it contacts the inside surface, thereby taking on the desired shape. The ability of a workpiece, or material, to reach this desired final shape without failure is often referred to as its "hydroformability".

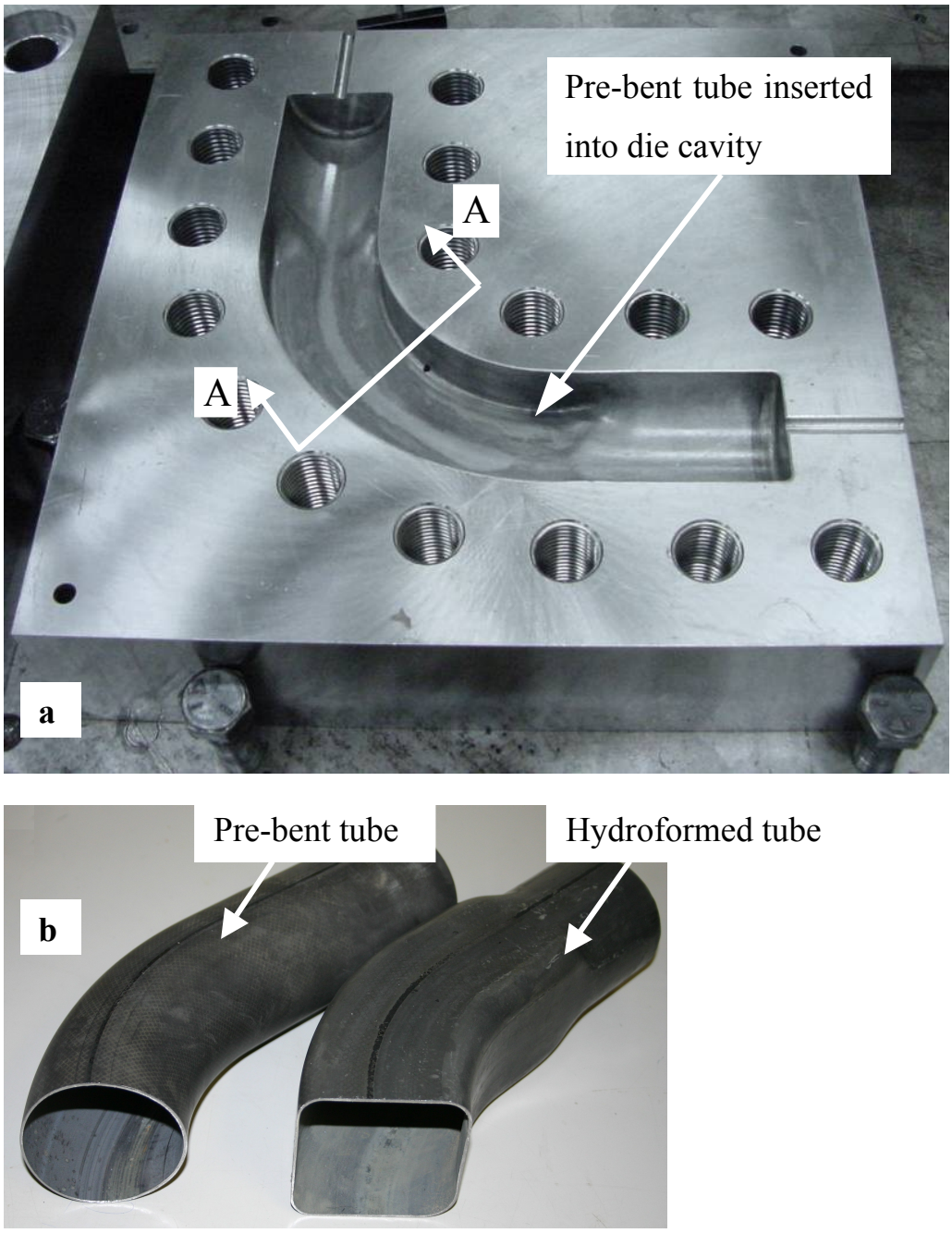

Figure 1.1: (a) Half of hydroform die, and (b) tube cross-sections shown, before and after hydroforming

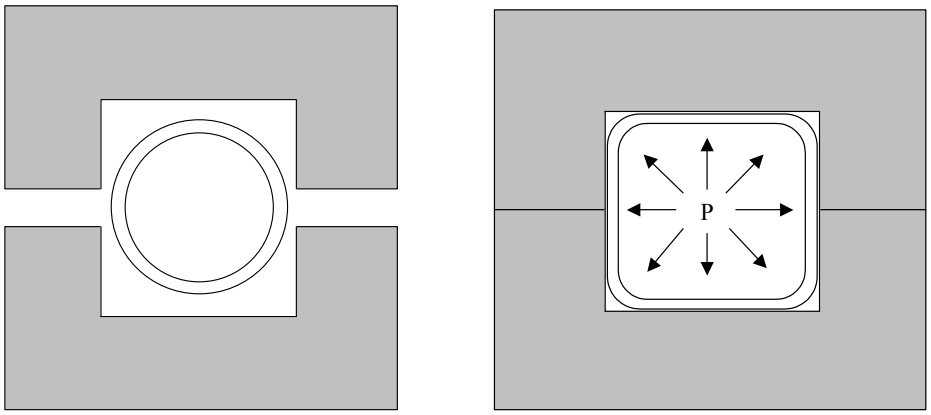

Figure 1.2: Section A-A showing full view of hydroforming-die cross-section, before and after hydroforming

Typical applications of hydroformed parts in automotive structures are illustrated in Figure 1.3. This figure shows a range of parts, all of which are pre-bent and then hydroformed in order to create their irregular shape.

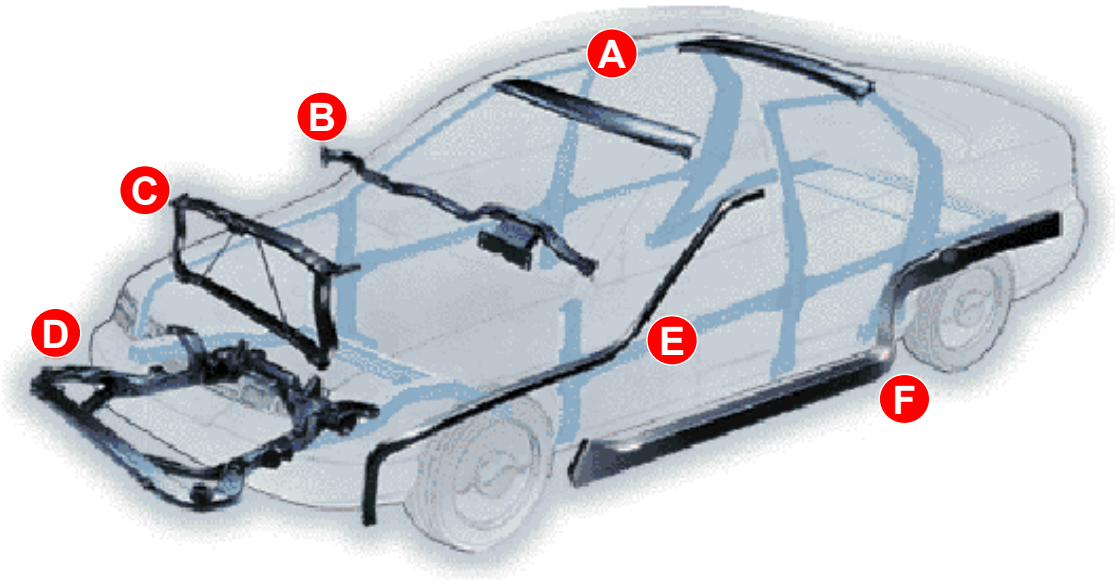

Figure 1.3: Hydroformed parts in an automobile frame: A – Roof Header, B – Instrument Panel Support, C – Radiator Support, D – Engine Cradle, E – Roof Rail, F – Frame Rail

In order for a tube to fit inside a hydroforming die, it must often be bent at multiple locations (pre-bending). The hydroforming then expands the diameter of the tube outward into the desired cross-sectional shape, which can be quite irregular, as shown in Figure 1.3.

A major focus of this thesis is to examine the effect that pre-bending has on the hydroforming of a part. By adjusting certain bending process variables (discussed in Section 1.2), one can observe the effect these have on the subsequent hydroforming behaviour. In particular, pre-bending operations partially consume the ductility of the workpiece, which can limit its subsequent hydroformability and lead to premature bursting failure before the desired final expansion is reached. Ideally, one would set the pre-bend forming conditions such that pre-form "damage" is minimized.

By creating computational models it is possible to simulate the pre-bend and hydroforming processes and predict strains and thickness in parts. This activity is important because such simulations can serve as a predictive means to evaluate the hydroformability of parts without resorting to expensive (trial and error) die fabrication and tryout time. By adjusting process variables in the simulations one can, through iteration, reach an optimum combination of process variables that are best suited to form a particular part.

The most common approach to simulating pre-bending and hydroforming is based on the finite element method (FEM). Unfortunately, FEM models of pre-bending tend to be complex and expensive computationally. The main focus of this thesis is the development of an analytical bend model that is much simpler than a detailed FEM bend model, but still retains good accuracy. The motivation for creating such a bend model is that it runs much faster, computationally, than an equivalent FEM simulation and is much simpler to set up.

In this thesis, the validation of the bend model is performed in two ways, the first being comparison of strain and thickness predictions, after bending, to FEM and experimental results. In the second validation, the strain and thickness predictions from the analytical model are used to initialize a FEM model of a hydroforming operation. The predicted strains and thickness after hydroforming are compared to experimental results to evaluate the accuracy of the modeling. As well, the predictions from the analytical model are compared to hydroforming FE simulations using strain and thickness predictions from FE models of bending.

Prior to presenting the models and results from this research, previous work on the analytical modeling of elastic-plastic tube bending will be discussed in detail. As well, an overview of hydroforming will be presented to give a summary of this process and its breadth of application, including discussion of hydroforming of pre-bent tubes.

1.2 Plastic Bending of Straight Tubes

The bending of metal is one of the most common metalworking processes in industry. In the past, the bending of tube was viewed as a skilled craft based on long experience. However, with the implementation of numerically-controlled bending equipment, such as rotary-draw tube bending machines (illustrated in Figure 1.4), it has become important to study the basic mechanics involved in the bending process. The stress and strain distributions developed in a tube during bending are important to predict the springback and structural properties of the tube in the as-bent condition.

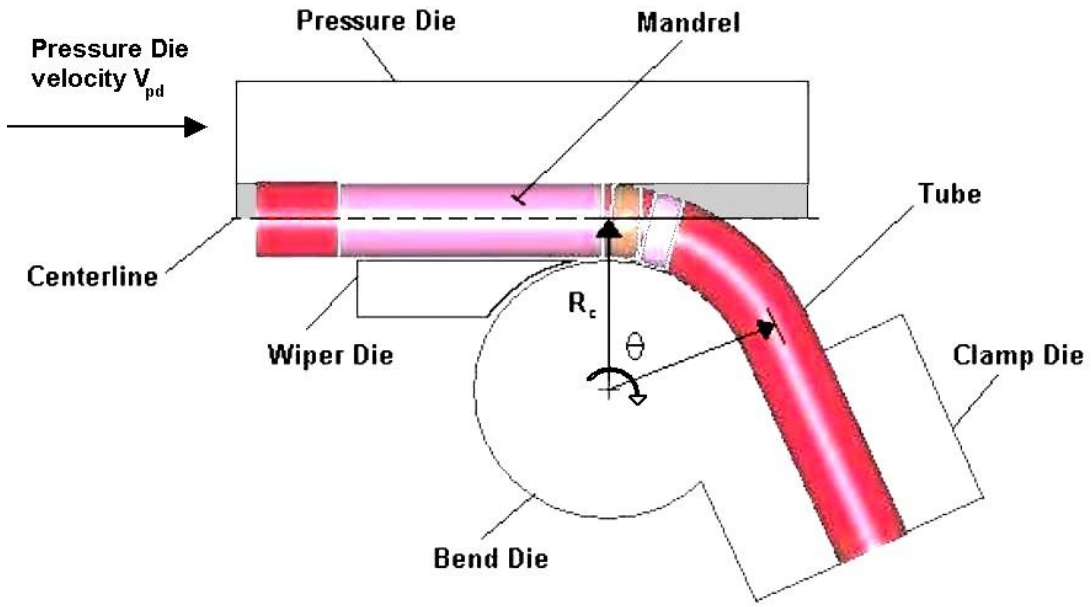

Figure 1.4: Half-symmetry view of rotary-draw tube bender

It is evident that the principles of tube bending are similar to bending of a solid bar, except that internal support is normally needed. In practice, this is provided by a mandrel positioned inside the tube during bending. The mandrel can be rigid, or flexible (Figure 1.5).

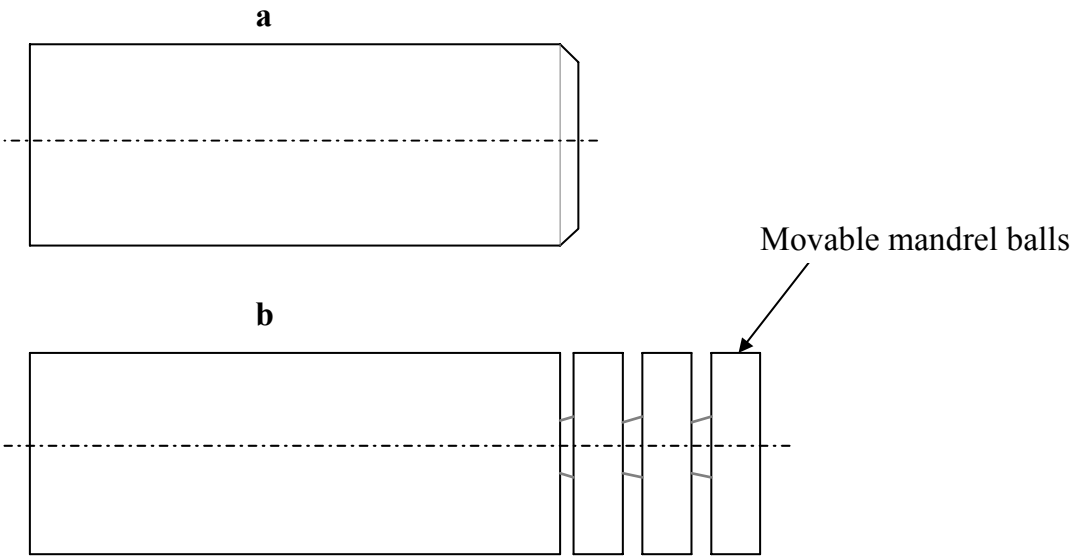

Figure 1.5: a) Rigid mandrel, b) Flexible mandrel

Deciding on whether to use a rigid or flexible mandrel depends on factors such as the ratios of tube wall thickness to tube outside diameter (OD), and tube OD relative to centerline radius R_c of bend (shown in Figure 1.4). Also, the number of mandrel balls to use on a flexible mandrel, as well as their spacing or pitch, depends on these factors as well. For example, a thicker wall tube would require fewer mandrel balls than a thinner wall tube, since a thicker wall tube requires less internal support since it is less likely to collapse, or buckle, during bending.

To bend a tube in a rotary-draw bender, it is first positioned inside the bender. It is then locked in place by closing of the clamp die onto the bend die. The role of the pressure die is two-fold. First, it must exert sufficient pressure by pushing the tube against the wiper die to prevent wrinkling on the inside of the tube, and secondly it must control the axial movement of the back of the tube feeding into the bend. The bend die and clamp die then rotate around as one piece, bending the tube around the bend die, with the pressure die maintaining pressure against the wiper, and moving along at a prescribed percent boost (or boost force). This is continued until a desired bend angle θ is reached. This process will be explained in greater detail in Chapter 2.

The percentage boost is the ratio of the linear velocity of the pressure die (V_{pd} in Figure 1.4), to the instantaneous tangential velocity of the rotating bend die, at centerline radius R_c. The tangential velocity of the bend die, at radius R_c, is equal to $R_c \cdot d\theta/dt$, at any time during the bend. This ratio is then converted to a percentage. The level of pressure die boost controls the movement of the back of the tube feeding into the bend, which affects the thickness and strains generated in the tube during bending.

1.2.1 Historical Work on Plastic Bending of Tubes

One of the earliest works on plastic bending of tubes was in 1968, by Afendik [2], who investigated tube bending with small bend radii, where the change in cross-sectional shape is considerable. He considered a rectilinear (straight) thin-walled tube, as being bent with a pure moment M applied to its ends. The assumptions he makes are: the ratio of wall thickness *t* to the tube radius d/2 is such that $2t/d \leq 0.2$, and the ratio of tube radius *d/2* to centerline bend radius R_c is such that $0.005 \leq d/(2R_c) \leq 0.1$. In solving the problem, it was also assumed that the cross-sections remain plane in bending (while the tube material strain-hardens as plastic strains grow), and that the tube is allowed to ovalize meaning there is no internal mandrel support.

The mathematical development of Afendik [2] is based on the cross-section shown in Figure 1.6. The y coordinate for the position of a point on the centerline of the deformed cross-section, with respect to the neutral axis is given by

$$y = A + r(\alpha)\sin\alpha \tag{1.1}$$

where A is the neutral axis shift below the centerline and $r(\alpha)$ is the radius as a function of the meridional coordinate α on the deformed cross-section.

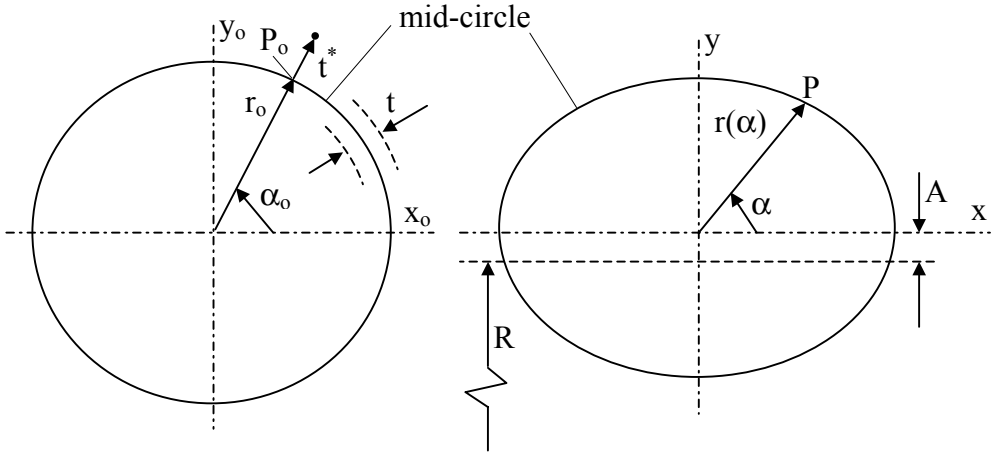

Figure 1.6: Mid-surface geometry before and after deformation (ovalization) [2]

On the basis of the original undeformed geometry this can be written as

$$y = A + (r_o + u_r + t^*)\sin\alpha_o + u_\alpha \cos\alpha_o \tag{1.2}$$

from which the axial bending (engineering) strain becomes

$$\varepsilon_1 = \frac{y}{R} = \frac{A + (r + u_r + t^*)\sin\alpha_o + u_\alpha \cos\alpha_o}{R} \tag{1.3}$$

where $u_r = u_r(\alpha_o)$ is the radial displacement on the original un-deformed geometry, $u_\alpha = u_\alpha(\alpha_o)$ is the meridional (circumferential) displacement. t^* is the distance, measured from the mid-thickness circle along r_o, in the un-deformed cross-section; $t^* > 0$ above this mid-circle and $t^* < 0$ below it, $t^* = t/2$ on the OD and $t^* = -t/2$ on the ID. t is the original wall thickness, and α_o is the angle on the original un-deformed cross-section.

The meridional engineering strain can be expressed as

$$\varepsilon_2 = -\frac{t^*}{r_o^2}\left(u_r + \frac{d^2 u_r}{d\alpha_o^{\,2}}\right) - \mu\varepsilon_1 \tag{1.4}$$

As the plastic strain increases, the parameter $\mu = 0.5$, and for true strain

$$\varepsilon_1 + \varepsilon_2 + \varepsilon_3 = 0 \tag{1.5}$$

Note that the subscript 1 denotes the axial (θ) direction, 2 denotes the circumferential/hoop (α) direction, and 3 denotes the radial (r) direction.

For true strain, the effective strain is expressed as

$$\varepsilon_{eff} = \frac{2}{\sqrt{3}}\sqrt{\varepsilon_1^2 + \varepsilon_1\varepsilon_2 + \varepsilon_2^2} \tag{1.6}$$

With the thin shell assumption ($\sigma_3 = 0$), one can write

$$\begin{aligned} \sigma_1 &= \frac{2}{3}\frac{\sigma_{eff}}{\varepsilon_{eff}}(2\varepsilon_1 + \varepsilon_2) \\ \sigma_2 &= \frac{2}{3}\frac{\sigma_{eff}}{\varepsilon_{eff}}(2\varepsilon_2 + \varepsilon_1) \end{aligned} \tag{1.7}$$

The effective stress can be expressed as

$$\sigma_{eff} = \sqrt{\sigma_1^2 - \sigma_1\sigma_2 + \sigma_2^2} \tag{1.8}$$

in which σ_1 and σ_2 are stresses in the axial and circumferential directions, respectively.

For large plastic strains the strain hardening behaviour was assumed to follow a power law rule,

$$\sigma_{eff} = K\varepsilon_{eff}^n \tag{1.9}$$

This formulation proves to be a simple, but useful, representation of the underlying physics of tube bending.

Zhang and Yu [3], and Pan and Stelson [4] produced similar formulations to analytically describe the plastic deformation of a tube during bending, with Pan and Stelson [4] going into greater detail. Their main assumptions were: tube cross-sections remain plane during bending, and the tube material is incompressible and elastic strains can be neglected during bending.

Consider now, Figure 1.7 and 1.8, and the following mathematical development. Note that the angle term φ is the change in tangential angle due to the deformation of the middle surface after bending. For no deformation, φ = 0, by definition.

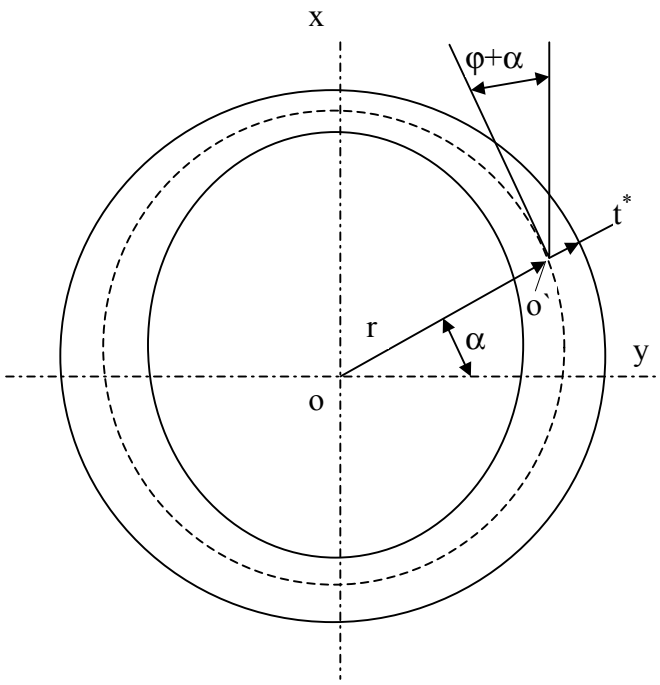

Figure 1.7: Geometry of deformed cross-section [4]

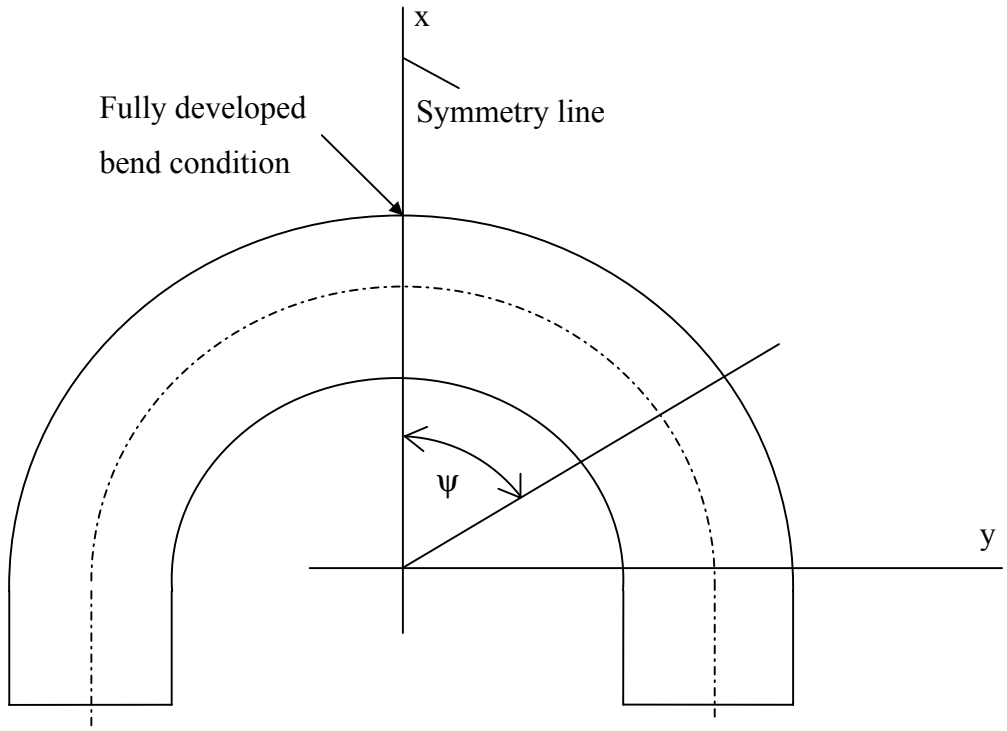

Figure 1.8: Bent tube showing coordinate system [4]

Based on experimental observations, when using a mandrel, the displacement field (upon deformation) in the axial direction is approximated by [4]

$$w_1(\alpha,\psi,t^*) = r_o\xi\cos^n(\pi\psi/2\psi_b)\cos 2\alpha + r_o\zeta\cos^n(\pi\psi/2\psi_b)\sin 3\alpha - t^*\eta\cos^n(\pi\psi/2\psi_b)\sin\alpha \tag{1.10}$$

where r_o is the meridional radius of the tube mid-circle before deformation. ξ, ς, η are constant coefficients determined by the principle of minimum potential work.

t is the tube wall thickness, before deformation, where

$-t/2 < t^* < t/2$, $0 < \psi < \psi_b$, $0 \le \alpha \le 2\pi$

At the two edges of the bending area where $\psi = \pm\psi_b$, one obtains (see Figure 1.8)

$$\cos^n(\pi\psi/2\psi_b) = 0 \tag{1.11}$$

and at the middle of the bending area, $\psi = 0°$, one obtains

$$\cos^n(\pi\psi / 2\psi_b) = 1 \tag{1.12}$$

which agrees with experiment.

From these equations, the distance from the center of un-deformed cross-section (see Figure 1.7), o and a point at deformed middle surface o′ is [4]:

$$r(\alpha,\psi) = r_o[1 + \xi\cos^n(\pi\psi / 2\psi_b)\cos 2\alpha + \zeta\cos^n(\pi\psi / 2\psi_b)\sin 3\alpha] \tag{1.13}$$

This distance is r_o before the tube is bent.

Referring to Figure 1.7, the axial strain field, for an arbitrary position x, can be determined as [4]

$$\varepsilon_1 = [x + t^*\sin(\alpha+\varphi)] / R_c = \varepsilon_{S1}^o + t^*\sin(\alpha+\varphi) / R_c \tag{1.14}$$

where ε_{S1}^o is the axial strain on the middle surface (mid-circle), and R_c is the bend radius of curvature of the centerline.

Now,

$$\sin(\alpha+\varphi) = \frac{r\sin\alpha + r_\alpha^{'}\cos\alpha}{(r^2 + r_\alpha^{'2})^{1/2}} \tag{1.15}$$

The circumferential strain can be written as [4]

$$\varepsilon_2(\alpha, t^*) = \frac{t^*}{r_o + t^*}\left(\varepsilon_{S1}^o + t^*\frac{d\varphi}{ds}\right) \tag{1.16}$$

where

$$\frac{d\varphi}{ds} = \left|(1+\varepsilon_{S2}^o)\left[r^2 + 2\left(\frac{dr}{d\alpha}\right)^2 - r\frac{d^2r}{d\alpha^2}\right]\right| \tag{1.17}$$

where ε_{S2}^o is the circumferential (hoop) strain on the middle surface.

By deformation theory the axial stress can be written as [3]

$$\sigma_1 = \frac{2}{9} K \varepsilon_{eff}^{n-1} (2\varepsilon_1 - \varepsilon_2) + \frac{E}{3(1-2\nu)} (\varepsilon_1 + \varepsilon_2) \tag{1.18}$$

and the hoop (circumferential) stress can be written as [3]

$$\sigma_2 = \frac{2}{9} K \varepsilon_{eff}^{n-1} (2\varepsilon_2 - \varepsilon_1) + \frac{E}{3(1-2\nu)} (\varepsilon_1 + \varepsilon_2) \tag{1.19}$$

where the material behavior, relating σ_{eff} and ε_{eff}, can be written as

$\sigma_{eff} = \sigma_y + \sigma_1 \varepsilon_{eff}$ [4] (1.20)

$\sigma_{eff} = K \varepsilon_{eff}^n$ [3]

where σ_y is the yield stress of the material, σ_1 is a strain hardening coefficient, and K is a strength coefficient.

Furthermore, the rightmost term in the equations (1.18) and (1.19) can be neglected since the elastic part of the strain is negligible (for plastic deformation involving zero volume change, where $\varepsilon_1 + \varepsilon_2 + \varepsilon_3 \cong 0$) [4].

The results of this work are not quite adequate (within 25 % error for strains). However, considerable improvement in accuracy can be realized if axial boost force is taken into account as well as improved modeling of boundary condition effects between the tooling and the tube [4].

Zhang and Duncan [5] presented simplified models of the strain distribution in tube bending. They make the following assumptions: the cross-section remains plane and circular during bending, the radius of the tube does not change, and the neutral axis is midway through the tube diameter, at the centerline location.

To illustrate the mathematical development consider Figure 1.9.

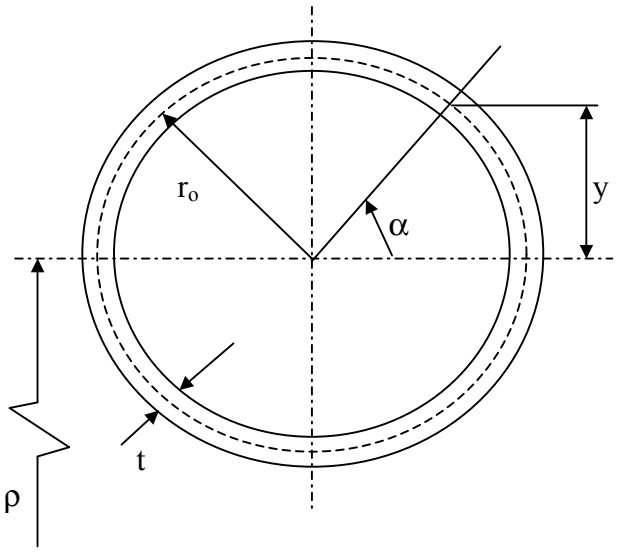

Figure 1.9: Tube cross-section [5]

The true axial strain in the mid-surface of the tube can be written as

$$\varepsilon_1 = \ln(1 + \frac{r_o \sin\alpha}{R_c}) \tag{1.21}$$

With the assumption of zero circumferential strain

$$\varepsilon_3 = -\varepsilon_1 \tag{1.22}$$

Using a more accurate model

$$\varepsilon_1 = \ln(1 + \frac{cy}{R_c}) + \varepsilon_o \tag{1.23}$$

where c is the flattening coefficient and ε_o is the stretching strain at the centerline of the tube diameter. This assumes the neutral axis is at the tube centerline and the shift towards the compressive side is due to a tensile (axial) membrane component ε_o.

If the ratio of the circumferential strain to the thickness strain is expressed as r_a, similar to the anisotropy coefficient in sheet metals, the thickness and circumferential strain is calculated by

$$\varepsilon_3 = -\frac{1}{1+r_a}\varepsilon_1$$
$$\varepsilon_2 = -\frac{r_a}{1+r_a}\varepsilon_1 \qquad (1.24)$$

The effective strain is

$$\varepsilon_{eff} = \sqrt{\frac{2}{3}(\varepsilon_1^2 + \varepsilon_2^2 + \varepsilon_3^2)} \qquad (1.25)$$

Since the circumferential strain is not neglected, the latter equations give a good approximation of the axial strain, as compared to experiment (Figure 1.10).

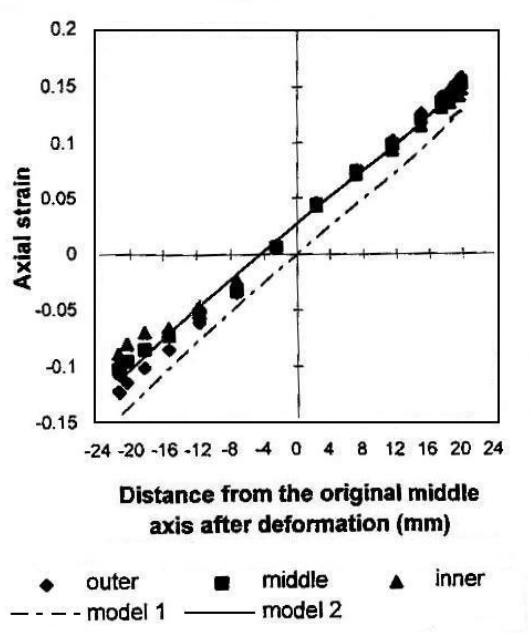

Figure 1.10: Axial strain distribution as a function of position y [5]

This figure also reinforces the assumption that axial strain distribution varies linearly with linear distance from the neutral axis, over the cross-section.

In 2000, Tang used deformation plasticity theory to investigate the plastic deformation in pipe and tube bending [6]. Now consider Figure 1.11,

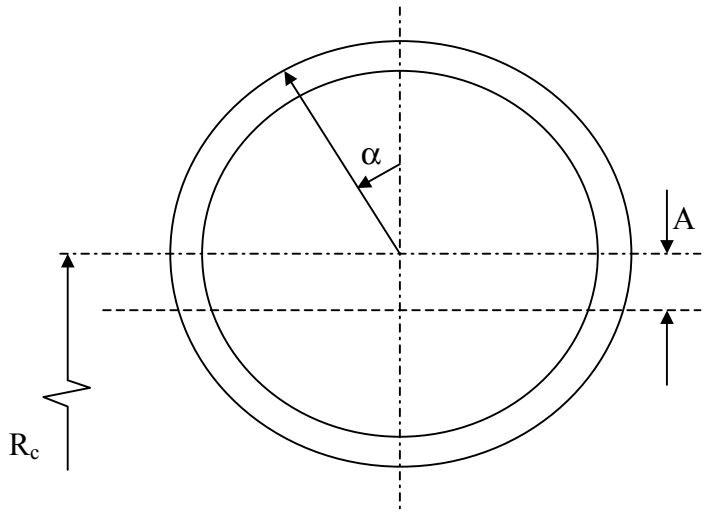

Figure 1.11: Geometry of cross-section [6]

The relationship between longitudinal and circumferential stress is expressed as

$$\sigma_2 = -\sigma_1 \frac{1-\cos\alpha}{2k+1} \tag{1.26}$$

where $k = R_c/d$.

For the stress in the outer semi-circle, the longitudinal stress σ_1 is tensile, and the circumferential stress σ_2 is compressive. For a thin wall, the radial stress σ_3 can be neglected.

By the maximum-shear-stress theory, the relation between the two stresses is given by

$$|\sigma_1| + |\sigma_2| = \sigma_y \tag{1.27}$$

where σ_y is the yield strength of the tube material, assuming perfectly plastic flow.

Substituting this expression for the longitudinal stress one obtains

$$\sigma_1 = \sigma_y \frac{2k+1}{2k+2-\cos\alpha} \tag{1.28}$$

and the circumferential stress becomes

$$\sigma_2 = -\sigma_y \frac{1-\cos\alpha}{2k+2-\cos\alpha} \tag{1.29}$$

Similarly, for the inner semi-circle, both σ_2 and σ_1 are compressive. By the maximum-shear-stress theory, the relation between them is given by

$$|\sigma_1| - |\sigma_2| = \sigma_y \tag{1.30}$$

Substituting this expression for the longitudinal stress one obtains

$$\sigma_1 = -\sigma_y \frac{2k+1}{2k+\cos\alpha} \tag{1.31}$$

and the circumferential stress becomes

$$\sigma_2 = -\sigma_y \frac{1-\cos\alpha}{2k+\cos\alpha} \tag{1.32}$$

The axial engineering strain can be written as

$$\varepsilon_1 = \frac{y}{R_c} = \frac{r\cos\alpha}{R_c} = \frac{\cos\alpha}{2k} \tag{1.33}$$

where r is an arbitrary radius. The radial strain can be written as

$$\varepsilon_3 = \frac{-\sigma_1 - \sigma_2}{2\sigma_1 - \sigma_2} \cdot \frac{\cos\alpha}{2k} \tag{1.34}$$

Also, the circumferential strain can be written as

$$\varepsilon_2 = \varepsilon_1 \frac{2\sigma_2 - \sigma_1}{2\sigma_1 - \sigma_2} \tag{1.35}$$

A crude approximation of the neutral axis deviation A is

$$A = \frac{0.42r}{k} \tag{1.36}$$

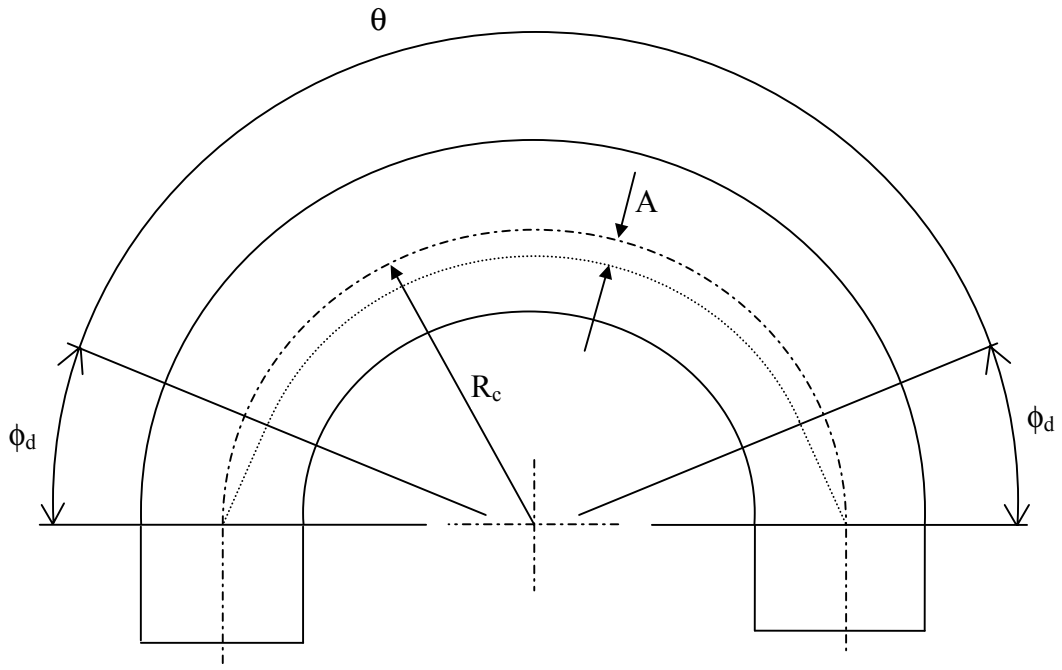

Figure 1.12: Bent tube showing developed region and decay sections [6]

For pure bending the feed preparation length (tube stock length of original straight tube) for a bend is shorter than the geometric centroid axis arc length (see Figure 1.12).

The length of the constant deviation sector is

$$l_c = (R_c - A)(\theta - 2\phi_d) \tag{1.37}$$

The length of the transitional sector is

$$l_t = \left(R_c - \frac{A}{2} \right) 2\phi_d \tag{1.38}$$

Then the feed preparation length (tube stock length) of the whole bend is

$$l = l_c + l_t \tag{1.39}$$

where ϕ_d is the angle of the transitional section and θ is the total bend angle, $\phi_d \approx$ 30-35°.

Al-Qureshi and Russo [7, 8] presented an elastic-plastic analysis of tube bending, as well as a formulation for residual stress distribution. Their assumptions are: the cross-section has an axis of symmetry perpendicular to the plane of external forces, buckling and tearing are absent, the material has an elastic perfectly-plastic behaviour, and conditions are of plane strain.

To start the development, consider the bending moment for an elastic-plastic regime

$$M = 2kEI_e + 2EkY_eS_p \tag{1.40}$$

where

$$I_e = \int_0^{y_e} y^2 B(y)dy \tag{1.41}$$

$$S_p = \int_{y_e}^{d/2} yB(y)dy \tag{1.42}$$

$k \equiv 1/R`_c$, and y_e are the change in curvature (of the geometric centerline), and the distance to the elastic-plastic boundary from the neutral axis. E is Young's Modulus. Consider Figure 1.13, which illustrates key parameters used in the analysis.

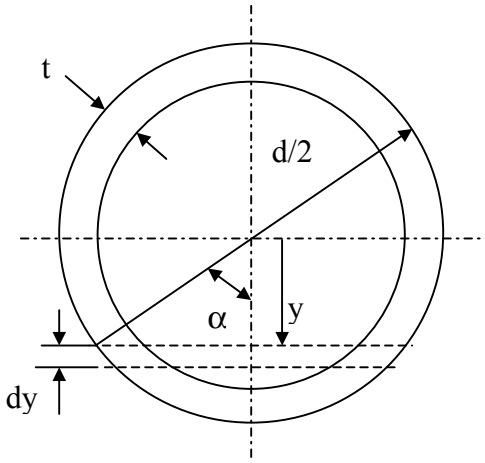

Figure 1.13: Geometry of tube [7]

$$B(\alpha) = d\sin\alpha - 2\sqrt{(d/2-t)^2 - (d/2)^2\cos^2\alpha}, \quad for\ 0 \le y \le d/2 - t \tag{1.43}$$

$$B(\alpha) = d\sin\theta, \quad for\ d/2 - t \le y \le d/2$$

where

$$\begin{aligned} y &= (d/2)\cos\alpha \\ dY &= -(d/2)\sin\alpha \cdot d\alpha \end{aligned} \tag{1.44}$$

The elastic bending moment is

$$\sigma = \frac{My}{I_o} \tag{1.45}$$

and

$$M = \frac{\sigma I_o}{y} = \frac{E\varepsilon_1 I_o}{y} = \frac{EI_o\left(y \middle/ R_c^{'}\right)}{y} = \frac{EI_o}{R_c^{'}} \tag{1.46}$$

Now,

$$\frac{1}{R_c^{'}} = \frac{1}{R_{co}} - \frac{1}{R_{cf}} \tag{1.47}$$

Note that when the material recovers elastically, the strain changes by a small amount

$$\varepsilon = \frac{y}{R_c^{'}} = \frac{y}{R_{co}} - \frac{y}{R_{cf}} \tag{1.48}$$

where R_{co} and R_{cf} are the initial and final centerline radius of the tube.

The moment of inertia of the hollow circular section is given by

$$I_o = \frac{\pi}{4}[(d/2)^4 - (d/2 - t)^4] \tag{1.49}$$

The net residual stress distribution can be expressed as

$$\sigma_1^{res} = \sigma_1 \pm yE\left(\frac{1}{R_{co}} - \frac{1}{R_{cf}}\right) \tag{1.50}$$

where σ_1 is the stress before springback. To give the correct distribution one must use the correct sign for σ_1 and y. Overall, good agreement is found between theoretical and experimental results, for residual stress distribution and stress-strain behaviour, over a range of tube materials tested [7].

1.2.2 Summary

Previous analytical work on analytical modeling of tube bending is somewhat limited, in the sense that:

- There is little work accounting for the membrane strain contribution due to axial boost forces, in say, rotary-draw bending. This is an important consideration if one wishes to accurately capture the stress and strain distribution owing to the addition of axial force.

- The formulation of circumferential strain is very approximate and more analytical work can be done to better represent the circumferential strain development during the bending process.

- Static equilibrium is not rigorously accounted for. In reality, satisfying equilibrium would involve considering the shear stress acting on the tube, particularly the in-plane shear. However, the shear stresses are quite small as compared to the hoop and axial stress. Thus the stress formulations in the literature are satisfactory.

Despite these limitations, the mathematical development in the literature does prove useful for giving a good physical understanding of the tube-bending problem, and how one can approach its solution from a mathematical point of view.

1.3 Hydroforming Overview

Hydroforming of tubes has major advantages over conventional stamping, and joining of multiple parts. The advantages are: cost and weight reduction, improved repeatability in dimensions after forming, better structural integrity, and increased strength and stiffness since the resulting cross-sections are closed.

The forming principle involves the tube stock being placed within the internal cavity of a die, and then deformed by internal pressurization and, often, mechanical loading on tube ends, referred to as end feed. Such end feed can be a useful means to minimize thinning of the workpiece during hydroforming by "feeding" extra material into the part. If the two load types (pressure and end feed) are used together, then a successful hydroforming operation requires optimization of the internal pressure and axial compression force at the tube ends. Potential failure modes include bursting, wrinkling, and buckling.

A variety of differently shaped parts can be hydroformed, some complex and others quite simple. The following summarizes hydroforming research done on the most basic of shapes, such as tee-shaped and straight tubes. These simplified parts are analyzed in depth, in the literature, to give a good understanding of the physics underlying the basic hydroforming process. Such analysis includes material friction, and load scheduling (pressurization and end feed considerations).

As relevant to this thesis, previous work done on pre-bending of tubes, prior to hydroforming, is also discussed, as a first stage of hydroforming. The effect of bending on the subsequent hydroformability of tubes is described [9-14].

Finally, a technological review of the hydroforming process, from early years to most recent dates, as well as an overview of the fundamental principles, is discussed [15-17].

1.3.1 Bulge Forming of Straight Tubes

Considerable experimental, analytical and numerical work has been done on the bulge forming (free-expansion) of straight tubes, and their hydroformability (Figure 1.14). In particular, different steel grades have been studied, by means of experiments, and compared to simple analytical and detailed FEM models [18, 19]. It has been shown that the anisotropic r-value and strain hardening n-value, have significant impact on the shape of the free-expanded tube [18].

Dedicated analytical models [18, 20] also prove useful since they are able to predict trends observed in both experiment and FEM simulation with regard to variations in material parameters. These models also help to explain shape transitions during free-expansion hydroforming of tubes.

Chow and Yang [21] found formability during free expansion to be proportional to the strain hardening n-value and anisotropy parameter r, under axial plane stress loading. If the ends of the tubes were fixed, however, the formability is observed to be independent of r. Also, burst pressure increases with increasing anisotropy parameter r, for both free and fixed ends, but decreases with decreasing exponent n. Furthermore, the formability of the tube is strongly dependent on the load path, demonstrating that the end feeding condition has a significant effect on the onset of bursting.

Nefussi and Combescure [22] discuss the hydroforming limit of isotropic tubes subjected to internal pressure and independent axial (end feed) load. By incorporating buckling

into the plastic instability analysis, a hydroforming-Swift criterion is developed which is a very good tool to study necking instability of tubes.

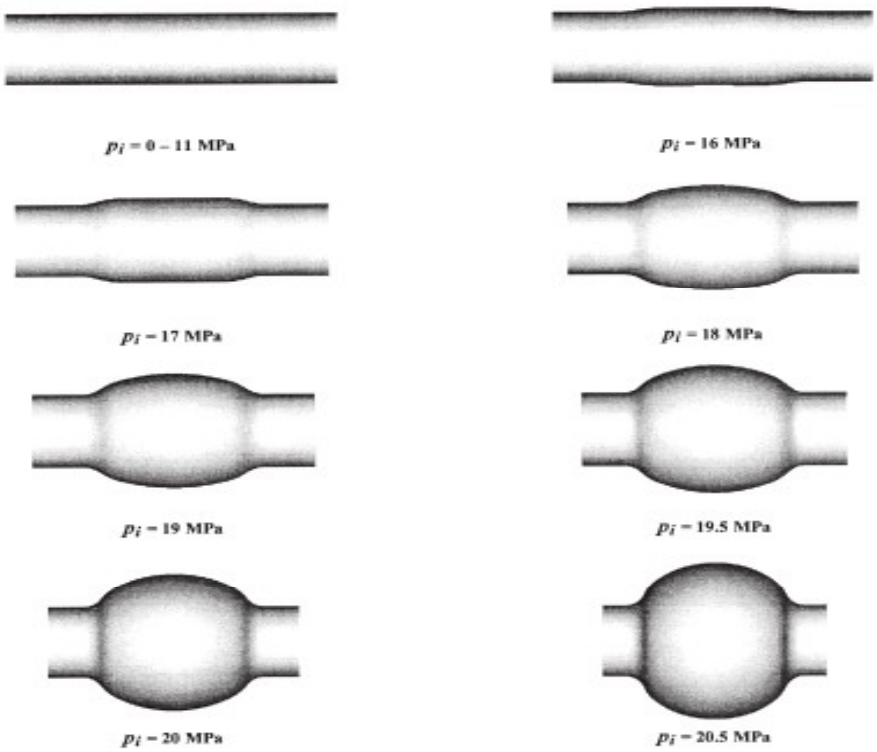

Figure 1.14: Degree of expansion in bulge forming for different pressures [20]

Also, of concern in bulge forming is the investigation of loading paths for axial end feed as a function of pressurization, over time. There is an operating "window" in which one can form an ideal part, avoiding wrinkling due to excess end feed and avoiding excess thinning (leading to bursting) due to too little end feed. Therefore an optimal range exists as shown in Figure 1.15 [25]. Such failure predictions and optimal operating "windows" are useful to

engineers and designers, even if based on simple models, as it allows one to make early process changing decisions.

Xing and Makinouchi [23] investigated differences in forming limits based on plastic instability, for bulge forming, using analytical and numerical models. They also focus on how to obtain optimum processing parameters through numerical analysis to meet the practical requirements. Similar work has been carried out by Rimkus et al. [24], Xia [25], Tirosh et al. [26] and Koc and Altan [27]. Xia [25] shows that material anisotropy plays an important role in the failure development. Tirosh et al. demonstrated that thicker tubes have less likelihood of buckling prematurely than a thinner tube.

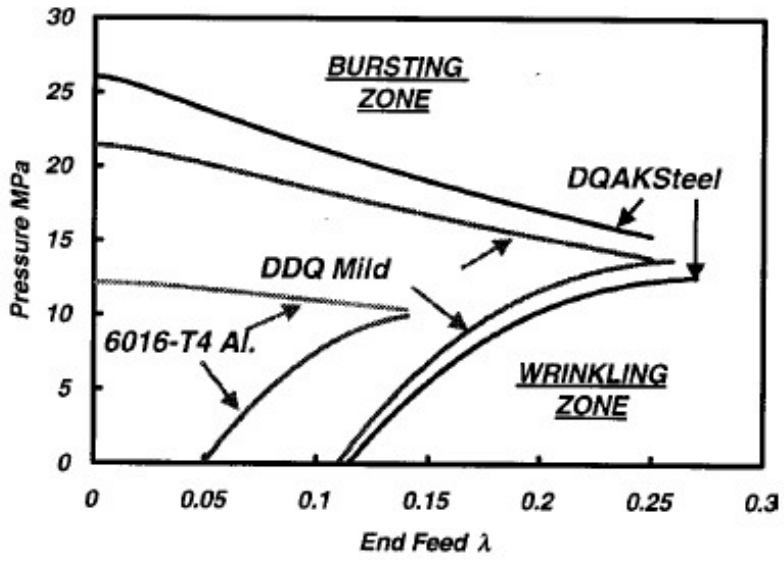

Figure 1.15: Chart showing operating window to avoid failure [25]

Using both experimental and numerical methods, Koc [28] found that loading path and variation in material properties has a significant effect on the robustness of the tube hydroforming process, and final part specifications.

Asnafi and Skogsgardh [29] conduct experiments to show the error that may occur when theoretically obtained loading paths are used as input in the hydroforming equipment. They find that the precision of the hydroforming equipment plays a significant role. Even if precision is as good as ±0.5% in internal pressure, there will be a discrepancy between experimental and predicted strains.

Low pressurization and excess axial feeding can cause wrinkling failure (Figure 1.15). To assess numerical predictions of wrinkling behaviour, Kim et al. [30] apply static implicit and dynamic explicit FEM to predict wrinkling in straight tube bulge forming. They report superior predictions using the explicit method, compared to implicit calculations.

1.3.2 Tee-shape Forming

Another useful hydroform experiment considers a "tee-shaped" part, as in plumbing fixtures (Figure 1.16). The main objective in forming such a part is to get the desired protrusion height while avoiding excessive thinning.

Koc et al. [31] present models to predict the limiting protrusion height of tee-shaped hydroformed parts, for various geometry, material properties, axial force, and friction conditions.

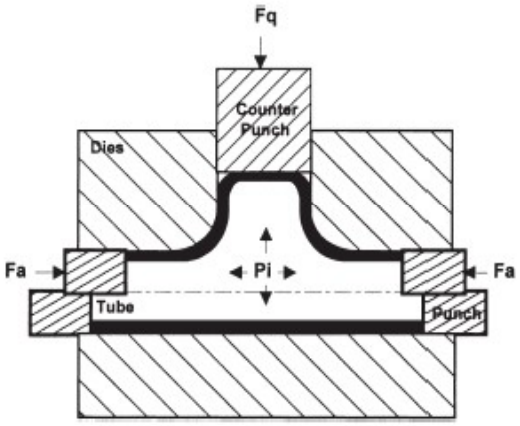

Hydroforming of a typical Tee-shaped part. (P_i) is pressure, (F_a) is axial, and (F_q) is counter force.

Figure 1.16: The hydroforming of a tee-shaped part [31]

The effect of loading path and variation in material properties on the final configuration of the tee-shape has been studied numerically and experimentally [28]. Gelin and Labergere [32] use optimization strategies and sensitivity analysis to find the optimal process control in hydroforming of a tee-shape; the optimal process being that which minimizes thickness variations and gives the desired final part shape. MacDonald and Hashmi [33] discuss the application of bulge forming to the manufacture of near-net-shape components and discusses machine and tool design, and illustrate how FEM is playing a growing role in the design of bulge-forming processes, for tee-shapes.

A unique alternative to the use of pressurized fluid for hydroforming is examined by MacDonald and Hashmi [34]. They present a three-dimensional simulation of the manufacture of a tee-shape using a solid bulging medium (Figure 1.17).

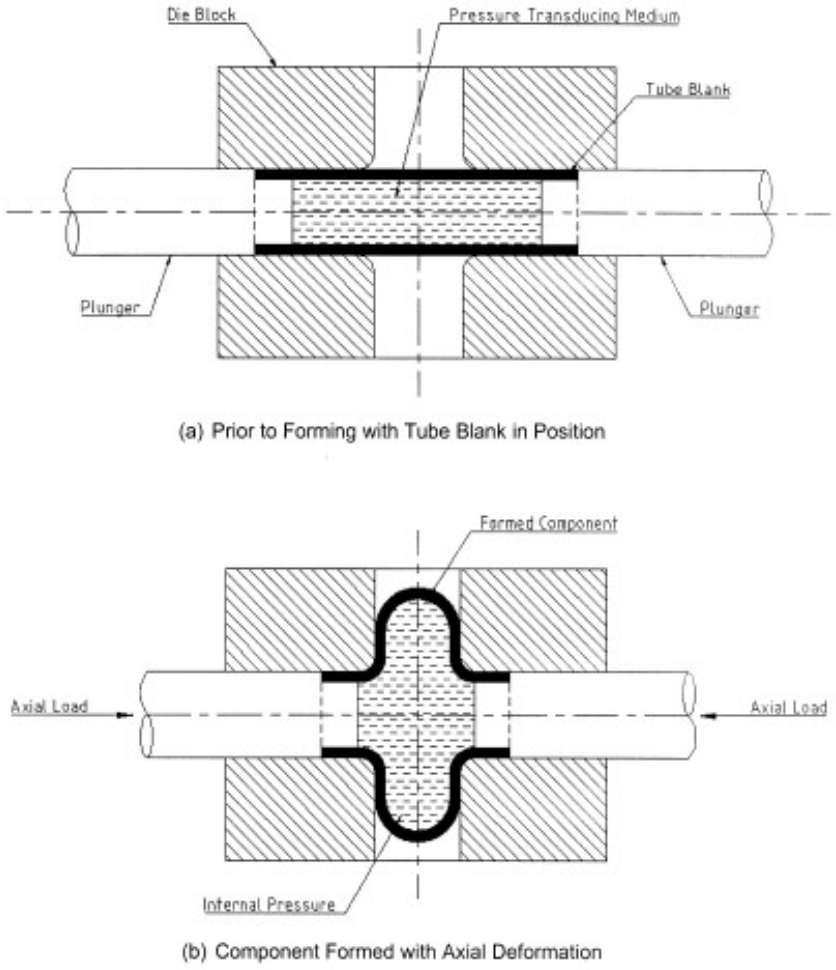

Fig. 1. Bulge forming of cross branch components.

Figure 1.17: Bulge forming using solid bulging medium [34]

They concluded that the solid bulging medium allows for greater protrusion height, less thinning in the protrusion section, and lowers stresses overall.

1.3.3 Straight Tube Hydroforming into Rectangular Die

There are two primary methods to form a tube in a die. The first is to pre-crush the tube to allow an oversized tube to fit in the die, followed by hydroforming (Figure 1.18) [35] and 1.19. The other method requires an undersized tube that fits into the die and then that is expanded during hydroforming (Figure 1.20) [35]. Both methods will be discussed.

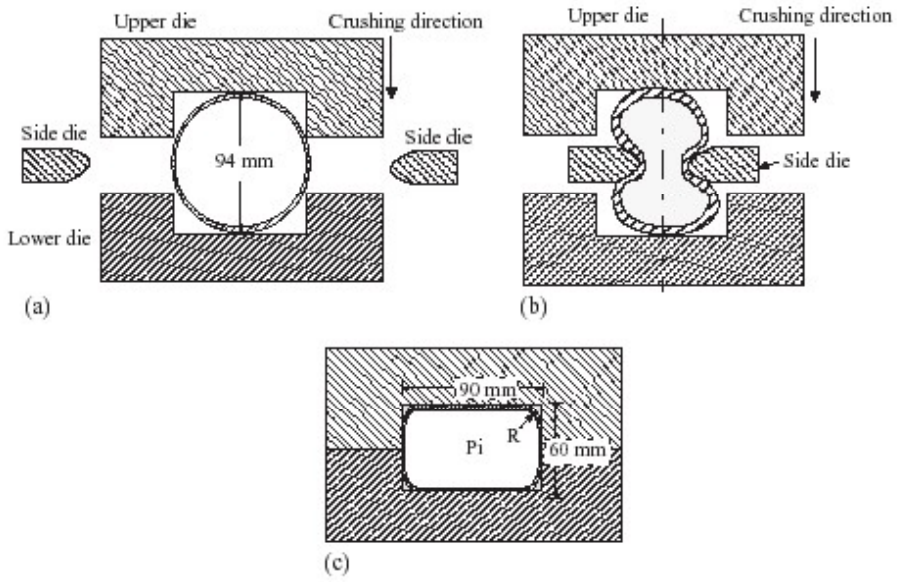

Figure 1.18: Tube configuration in die: a) before crushing and pre-forming, b) after pre-forming and before crushing, and c) after crushing [35]

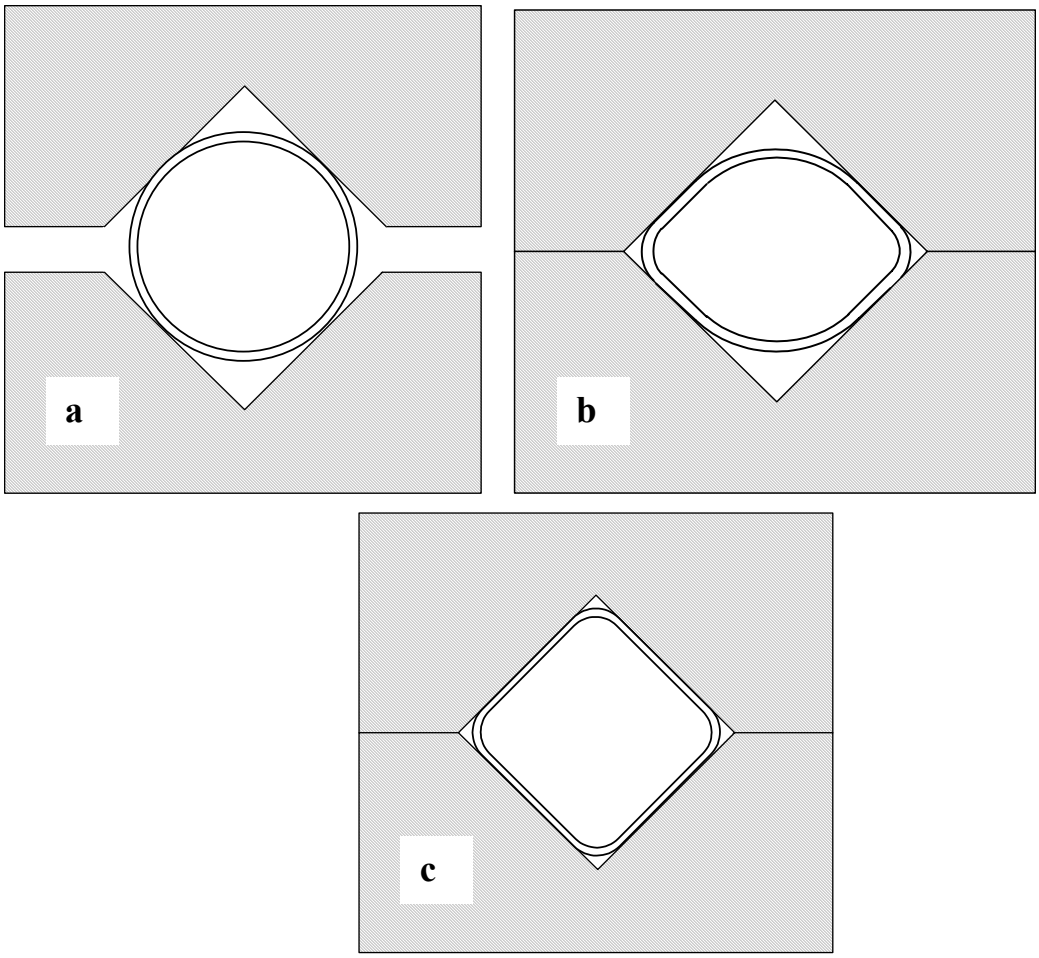

Figure 1.19: Tube configuration in die: a) before crushing, b) after crushing, and c) after hydroforming

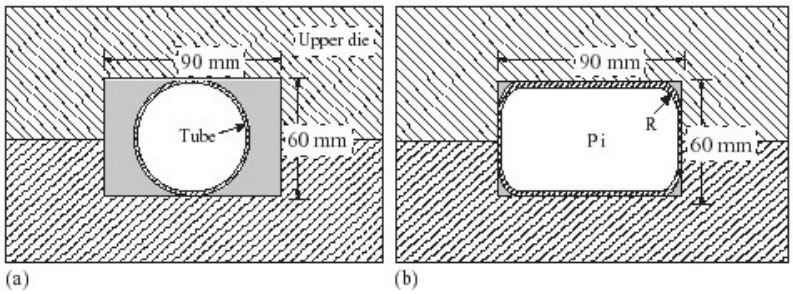

Figure 1.20: Tube configuration in die: a) before expansion, b) after expansion [35]

Hwang and Altan [62] use the FEA method to explore the plastic flow pattern of a circular tube that is hydraulically expanded, or crushed into a rectangular cross-section and then expanded. The loading path and the forming procedures during the crushing process are discussed [35]. Simulation results for thickness distributions, clamping forces, and forming pressures are compared between hydraulic expansion and crushing processes [35]. They found:

- The maximum forming pressure needed by the crushing processes is only 5% of that required by hydraulic expansion processes;

- The maximum crushing force needed in the crushing process is only about 7% of the clamping force (keeping two halves of die together) in the hydraulic expansion process;

- The thickness distribution of the formed product obtained by the crushing processes is much more uniform than that by hydraulic expansion processes.

Kridli et al. [36] used plane strain finite element analysis to study the effects of the strain-hardening exponent, initial tube wall thickness, and die corner radii on corner filling and thickness distribution of a straight hydroformed tube, inside a square die cavity. It was concluded that the thickness distribution is a function of the die corner radius and strain-hardening behaviour of the material. A greater amount of variation is observed for lower n-values. Also, the variation in thickness distribution can be reduced if a larger die corner radius is used. A tube material with a high strain-hardening exponent can be formed to a smaller die corner radius than a material with a low strain-hardening exponent, since it can achieve a higher amount of strain at a given stress (pressure) level.

Chow and Yang [21] and Manabe and Amino [37] also used FEM to study straight tube hydroforming under a wide range of process conditions involving an enclosed square die with axial end feeding. The failure analysis focuses on the onset of critical bursting conditions.

1.3.4 Lubricant and Friction Studies

Lubrication is an important consideration in hydroforming and also one of the least understood from a modeling point of view. Good lubrication conditions allow a tube to reach its final desired expansion and shape in the die, whereas poor lubrication often results in premature failure, due to excessive local thinning. Therefore, it is important not only to accurately model friction effects in simulation, but also to accurately measure the coefficient of friction, under lubrication conditions that are representative of the actual operating conditions.

Khodayari et al. [38] tested four different lubricants, and water, in straight tube corner fill hydroforming trials, expanded to burst. They found that high burst pressure and axial displacement values are achieved with a low coefficient of friction.

An alternative technique for measurement of friction; suitable for hydroforming and tube bending is the so-called twist compression test (TCT) [39]. This test considers large interface pressures and sliding distances. Vollertsen and Plancak [40] discuss an alternative approach for determining the coefficient of friction (COF) between die and workpiece. This method is based on the upsetting of a tube and measuring the sliding friction.

Oliveira et al [41] examined the effect of different lubricants on steel and aluminum tubes, bent on a rotary-draw tube bender. The influence of the lubrication in terms of its effect on process variables, thickness and surface finish was studied. They found that tool forces were most affected by the type of lubricant used while thickness was minimally affected. Aluminum tubes proved to be quite sensitive to the choice of lubricant to avoid scratches on the inside surface, during bending.

1.3.5 Hydroforming of Pre-bent Tubes

In hydroforming of complex-shaped parts, a workpiece must often be pre-formed to fit in a shaped die. One such pre-form is the pre-bending of tubes, the focus of this thesis. Clearly, the effect of the pre-forming operation on ductility can be significant in determining the formability of the final hydroformed part. Therefore it can be quite important to adjust forming parameters in such pre-form operations to reduce any negative impact on hydroforming. Simulations can be very useful in studying this effect.

Trana [9] focused on the development of a practical simulation procedure for the entire hydroforming process, and how a tube bending (pre-forming) operation influences the hydroforming result. The simulation results were compared to the experimental results, for thickness, and the comparison proved to be good. They found that use of a mandrel without balls results in necking upon hydroforming, whereas with mandrel balls no necking develops (Figure 1.21). They also found significant mesh sensitivity in their models.

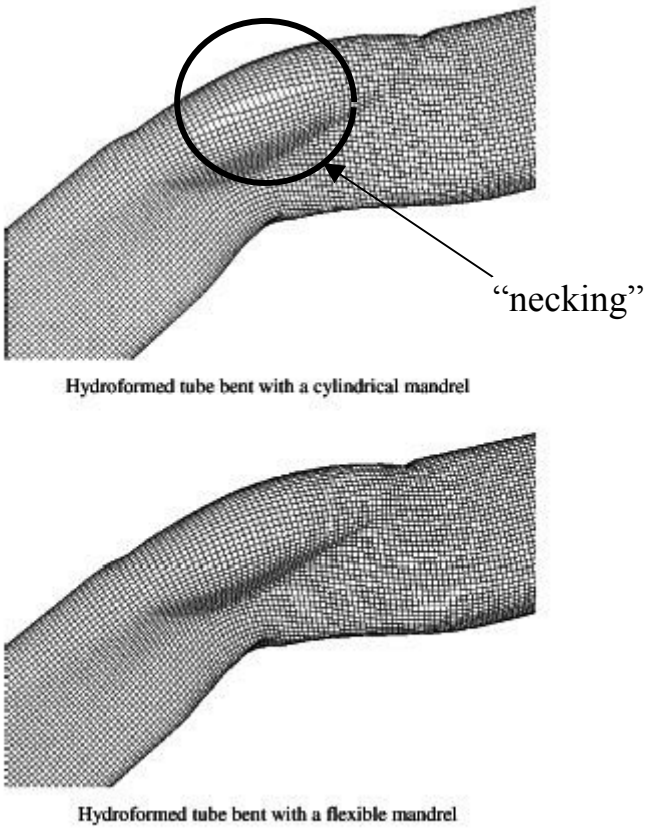

Fig. 17. Necking tendencies during the hydroforming simulation of tubes bent with different mandrel geometries.

Figure 1.21: Necking tendencies during the hydroforming simulation of tubes bent with different mandrel geometries [9]

Dwyer et al. [10] examined the variation of bending parameters, for aluminum tube, in such a way to reduce or minimize the loss in ductility, hence preserving formability for the subsequent hydroforming operations (Figure 1.22). The figure shows a comparison in axial, hoop, and thickness strains between a numerical FEM model, for hydroforming, and experiment. The strain shift indicated is the change in hoop strain at 180º, after hydroforming, from the previous pre-bend value (before hydroforming).

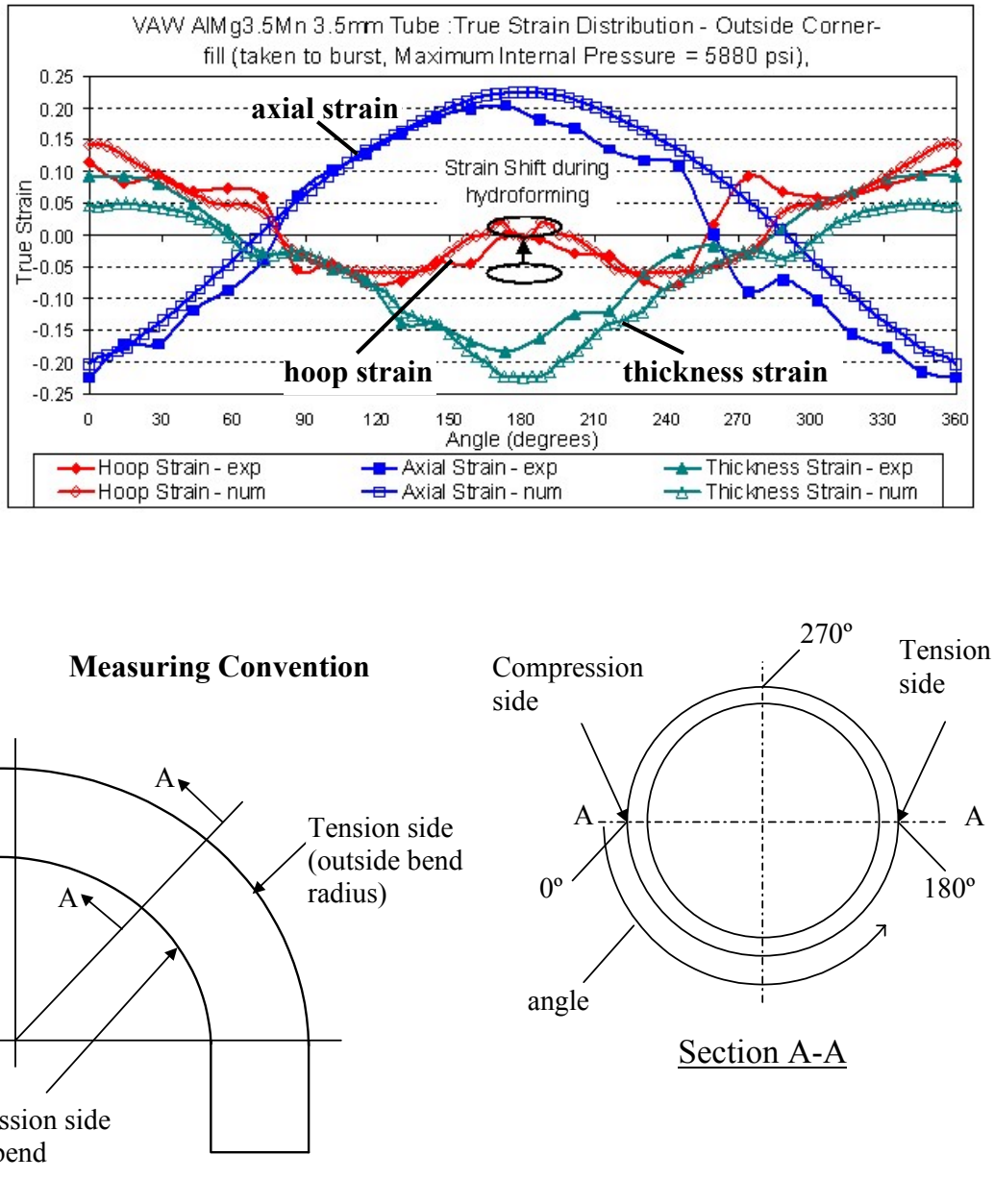

Figure 1.22: Strain after hydroforming around tube circumference – comparison of experimental and numerical results [10]

Dyment et al. [12] examine the effect of percent boost on pre-bending and hydroforming strains and thickness values, for steel tubes. They also discuss causes of premature failure during hydroforming, due to excessive localized thinning during the bending

process, as well as the potential adverse effect of strain path change. Their numerical bend models adequately capture experimental trends in strain and thickness distribution.

Gholipour et al. [13] discuss the application of an in-house Gurson-based damage model in tube bending and hydroforming of aluminum tubes, using void nucleation and growth parameters determined for the aluminum material tested. In general, good agreement was found between predicted results for strains and burst pressure, and experimental data.

Pavlovskaia and Xia [14] developed a simplified analytical solution for the deformation of a tube cross-section when bending without a mandrel, to be used in place of a more computationally expensive FEM model. Although an analytical investigation is conducted in their study, comparisons with numerical and experimental results have not been performed.

Yang et al. [11] presented the simulation results on pre-bending and hydroforming processes that are used to form a tie bar, an automotive part. The pre-bending is performed with an upper-lower bend die, and with a rotary-draw bending machine. The tests are performed on 48 mm OD tube with three different centerline bend radii of 55, 65, and 76 mm. As it turns out the upper-lower bend die is a better pre-bend method then the rotary-draw tube bending machine, since the thickness reduction is smaller, resulting in a more uniform thickness distribution.

1.3.6 Overview of Hydroforming

A technological review of the hydroforming process, from its early years to recent dates is given by Koc and Altan [15], on various topics such as material, tribology, equipment, tooling, etc. Dohmann and Hartl [16] provide an overview of the fundamental principles of hydroforming processes and their variants. The more significant conclusions they make are that

hydroforming has moved into many different applications over the past decades [16]. The technology available to produce more complex shaped parts, with favorable strength, has developed to a great extent.

Ahmetoglu and Altan [17] review the fundamentals of tube hydroforming technology and discuss how various parameters, such as tube material properties, pre-form geometry, lubrication and process control, affect product design and quality. For example, the selection of a proper lubricant can be critical for a tube hydroforming process.

Hydroforming can cost-effectively reduce the number of production steps, such as in the manufacture of frame components. Computer modeling helps engineers develop reliable control strategies for hydroforming process parameters.

1.4 Present Research

As outlined in the previous discussion of the bending and hydroforming literature, pre-bending of tubes is an important stage in the manufacture of hydroformed parts. It is necessary to understand the influence of pre-bending on the secondary hydroforming operation in order to optimize formability and part quality. Computational models are an effective means to study this forming process, as well as being very useful predictive tools that can save cost by removing a large degree of the trial and error in die-fabrication and try-out time.

The work in this thesis focuses mainly on the development of an analytical model of rotary-draw tube bending, which serves to replace a much more time consuming FEM simulation, while still retaining a good degree of accuracy in its predictive capability. By accounting for the effect of the pre-bend analytically one can then model the subsequent

hydroforming process, with FEM, using the analytically-generated bending strains, thickness and residual stresses. A software program, coded in C, has been created to predict the post-bending strains, thickness and residual stresses without having to run a much more time-consuming FEM simulation. The predictive capability of the analytical model is assessed against bending experiments and equivalent FEM models, for validation.

This remainder of this thesis is organized as follows. Chapter 2 describes the experimental procedure and the equipment used for the bending experiments performed in this study. Chapter 3 provides a mathematical description of the analytical bend model, the derivations and equations used, as well as the physical explanations supporting the mathematical assumptions. Chapter 4 discusses the numerical FEM models, both of the bending and hydroforming processes, and their implementation. Chapter 5 compares the analytical results to the detailed FEM models of bending along with experimental and numerical results for both bending and hydroforming. Chapter 6 provides a general discussion of the analytical, numerical (FEM), and experimental results. The conclusions and recommendations stemming from this research are given in Chapter 7. Appendix A gives details of the more involved aspects of the mathematics of the bend model, while Appendix B gives a practical description of the bend model, outlining its basic functionality.

Chapter 2 - Experiments

2.1 Material Selection

The tubes used in this study were fabricated from 1.57 mm thick, Drawing Quality Aluminum Killed (DQAK) steel. The tubes were 76.2 mm in outside diameter and were seam welded using an induction electrical resistance welding (ERW) process. The sheet material was galvanneal (GA) coated. The bending experiments were performed at the University of Waterloo, and the hydroforming was done at the Industrial Research and Development Institute (IRDI), as part of the AUTO21 project on tube and sheet forming.

2.2 Material Characterization

Tensile tests were performed on the DQAK tubes, from samples cut at different locations around the circumference (Figure 2.1), at the 3, 6, and 9 o'clock positions (with the weld seam located at 12 o'clock). The samples were tested with the tensile axis aligned with the tube axis. Curved grips were used to avoid flattening of the samples.

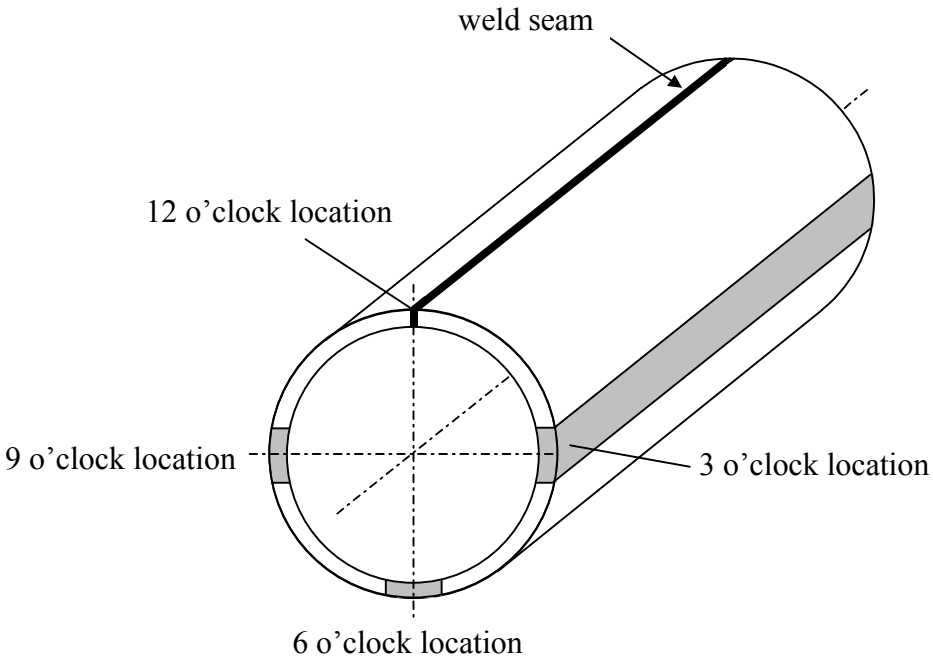

Figure 2.1: Schematic of cut tensile samples around tube circumference

Figure 2.2 is a plot of the resulting true stress-true strain curves for the 3, 6, and 9 o'clock tensile specimens. There was a small variation in strength of roughly 20 MPa between the various orientations, with the 6 o'clock sample having the highest yield strength. A power law curve,

$$\sigma = K\varepsilon^n \tag{2.1}$$

was fit to the average tensile data from all the three orientations, resulting in K = 531.6 MPa and n = 0.119 (Table 2.1). This value for the hardening exponent, n, was surprisingly low. Normally DQ sheet samples have n-values in the range 0.2.

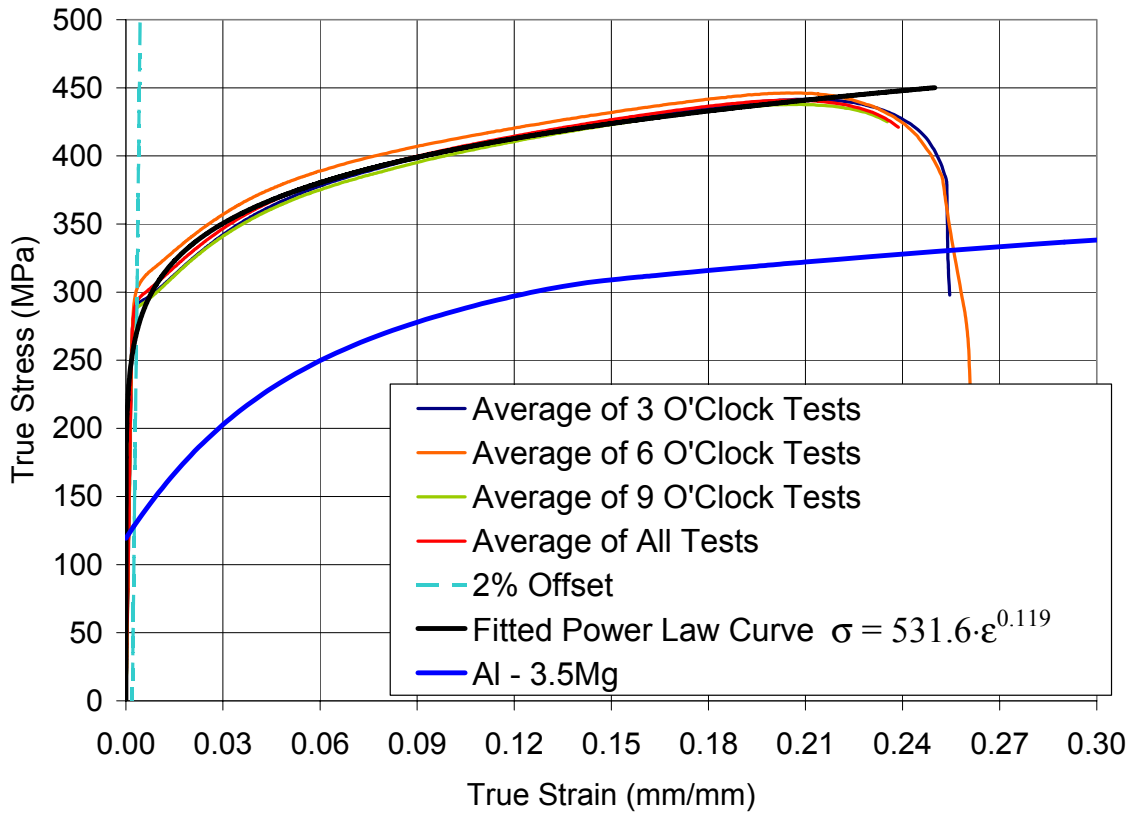

Figure 2.2: Tensile data for DQAK steel and Al-3.5Mg aluminum alloy

Table 2.1 shows the mechanical properties of DQAK steel. Also given is data for Al-3.5Mg aluminum alloy tubes that were also considered in the bending studies for comparison purposes. The K and n values are not given for the aluminum tubes. Instead, flow curve data was taken from tube samples for 2mm tube, from a US/CAR hydroforming study [42], and is also plotted in Figure 2.2.

Material	Yield Strength σ_y (MPa)	Young's Modulus E (MPa)	Poisson's Ratio ν	Strength Coefficient K (MPa)	Strain Hardening Exponent n
DQAK steel	294.0	207000	0.29	531.58	0.119
VAW AlMg3.5Mn (Aluminum)	119.32	67900	0.34	Not given	Not given

Table 2.1: Mechanical properties of DQAK steel and Al-3.5Mg tubes

2.3 Rotary-Draw Tube Bender

Bending of the tubes was carried out using an instrumented rotary-draw tube bender, provided by Eagle Precision Technologies, and located at the University of Waterloo. The bender is hydraulically actuated and is controlled with MTS 406 servo-controllers (Figure 2.3). Through the use of actuators, load cells and displacement transducers, the tooling can be independently controlled. Program signals are generated using a custom in-house Labview program developed by Dyment [43].

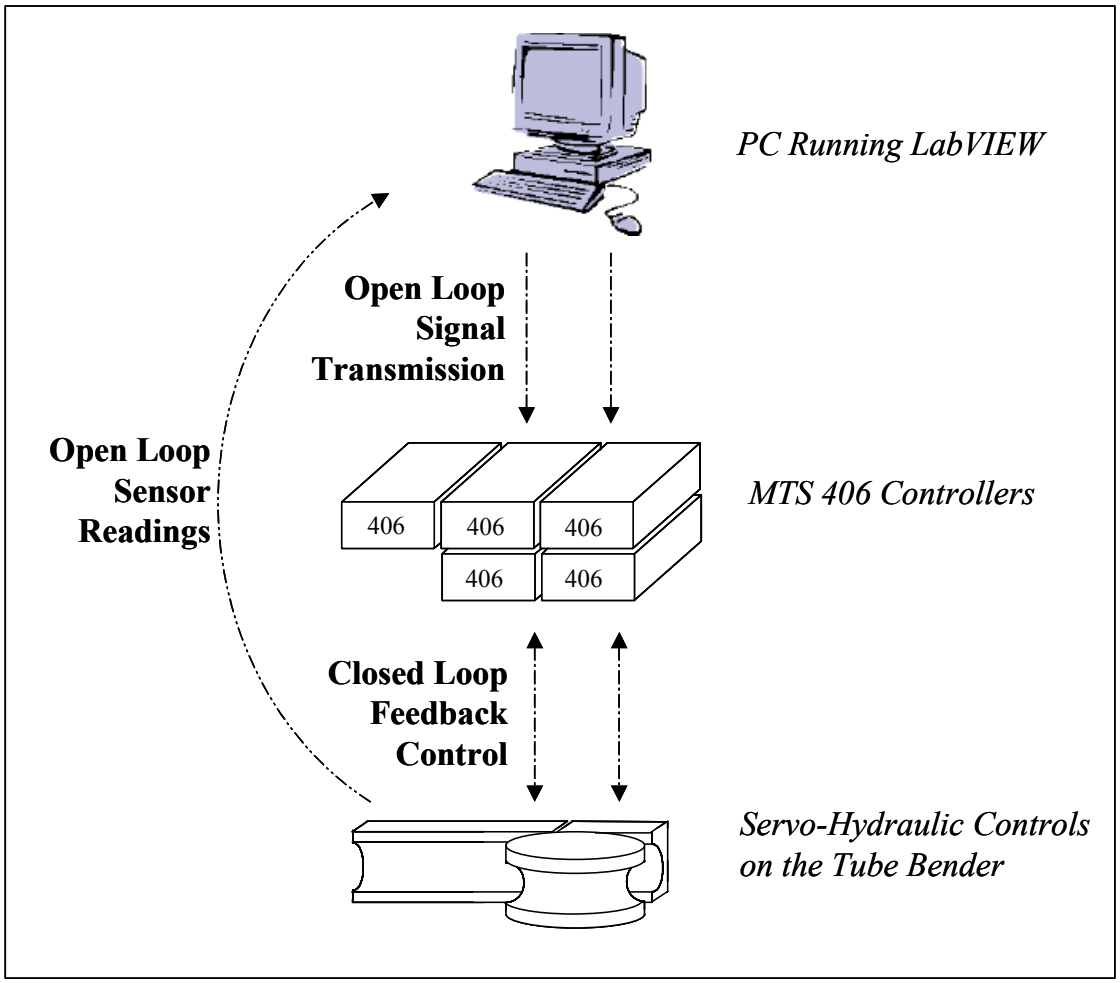

Figure 2.3: Schematic showing in-house setup of tube-bender control system

A mandrel rotary-draw tube bender operates by bending a tube around a rotating bend die (Figure 2.4 and 2.5). A mandrel is positioned inside the hollow tube to prevent collapse, and minimize flattening (ovalization) of the cross-section. The pressure die serves to push the tube against the wiper die to prevent wrinkling on the inside (compressive) region of the bend, while at the same time feeding the tube into the bend. Figure 2.4 and 2.5 show different illustrations of a bender. Figure 2.7 is a photograph of the rotary-draw tube bender used in this research.

The axial motion of the pressure die is prescribed as a "percentage boost" level. The percent boost is a displacement-based boundary condition imposed on the pressure die during bending. Boost is described as the ratio of the pressure die velocity (V_{pd} in Figure 2.5) to the instantaneous tangential velocity measured at the centerline bend radius of the bend die (R_c). For example, a 105% boost level means that the prescribed linear velocity V_{pd} of the pressure die, in the Z-direction, is $1.05 \cdot R_c \cdot d\theta/dt$. Alternatively, a boost force boundary condition can be prescribed (also in the Z-direction) and the resulting movement of the pressure die is dependent on the magnitude and direction of this force.

To control the tube motion, the pressure die applies force to the tube either through friction or through an optional boost block, which sits at the back of the tube (Figure 2.7) and pushes against the back during bending.

A typical sequence of operations to bend a tube, once loaded into the tube bender, is as follows:

- The clamp die closes to grip the tube between the clamp and bend die
- The mandrel advances to the prescribed forward position beyond tangency (see Figure 2.6). This magnitude of this forward position can be an important factor in determining a wrinkle-free bend
- The pressure die closes on the tube applying the prescribed clamping force
- The clamp and bend die rotate together and draw the tube around the bend, while the pressure die advances according to the prescribed boost level
- The mandrel is retracted at the end of the bend
- The clamp die opens and the pressure die releases, allowing the tube to be removed

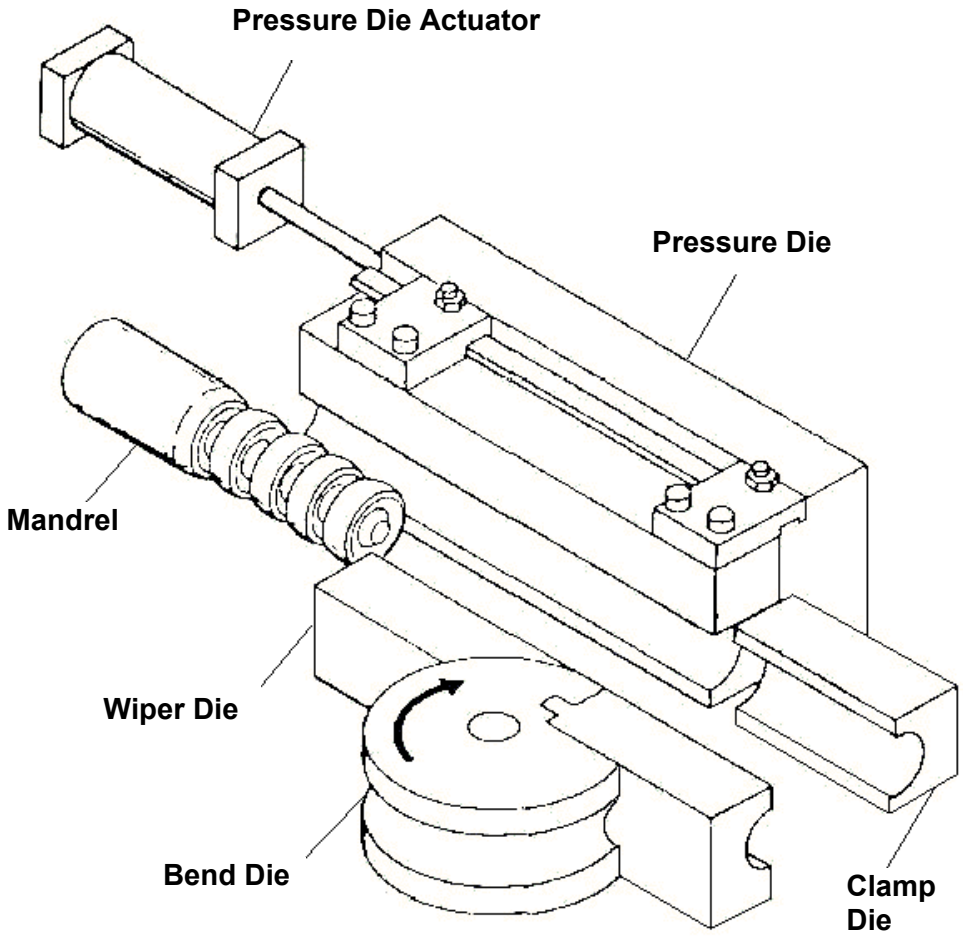

Figure 2.4: Perspective view of tube-bender tooling

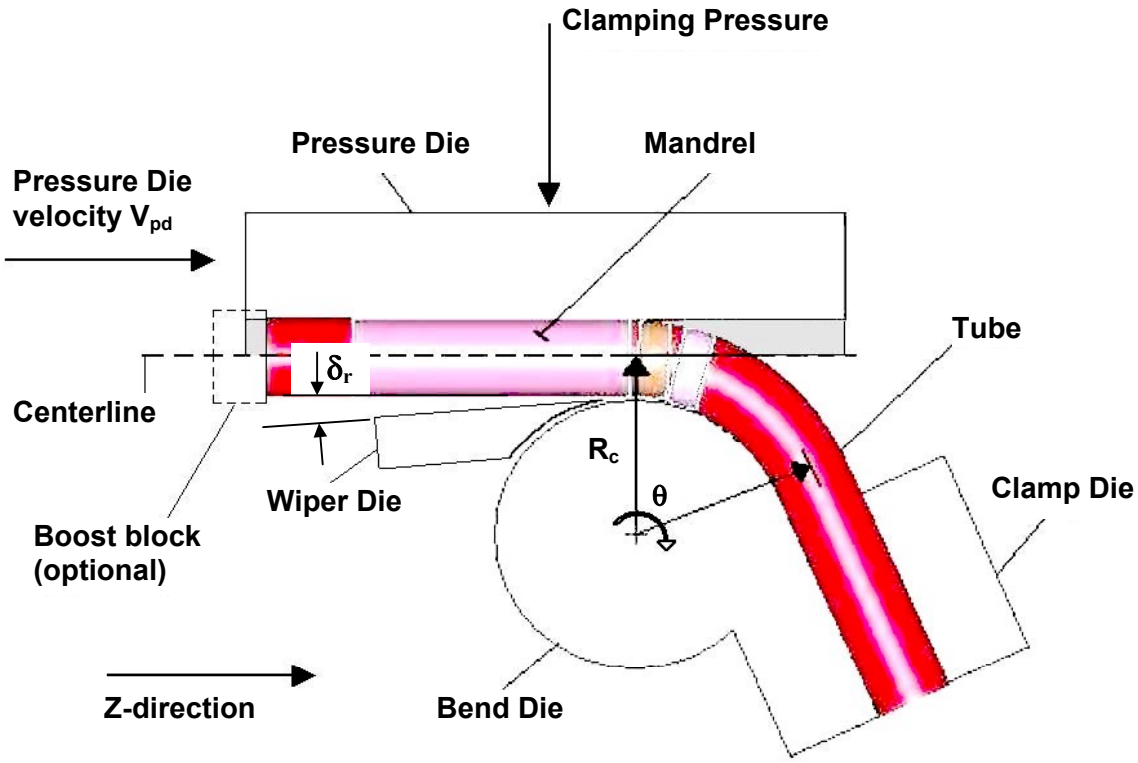

Figure 2.5: Top view of tube-bender (half-symmetry)

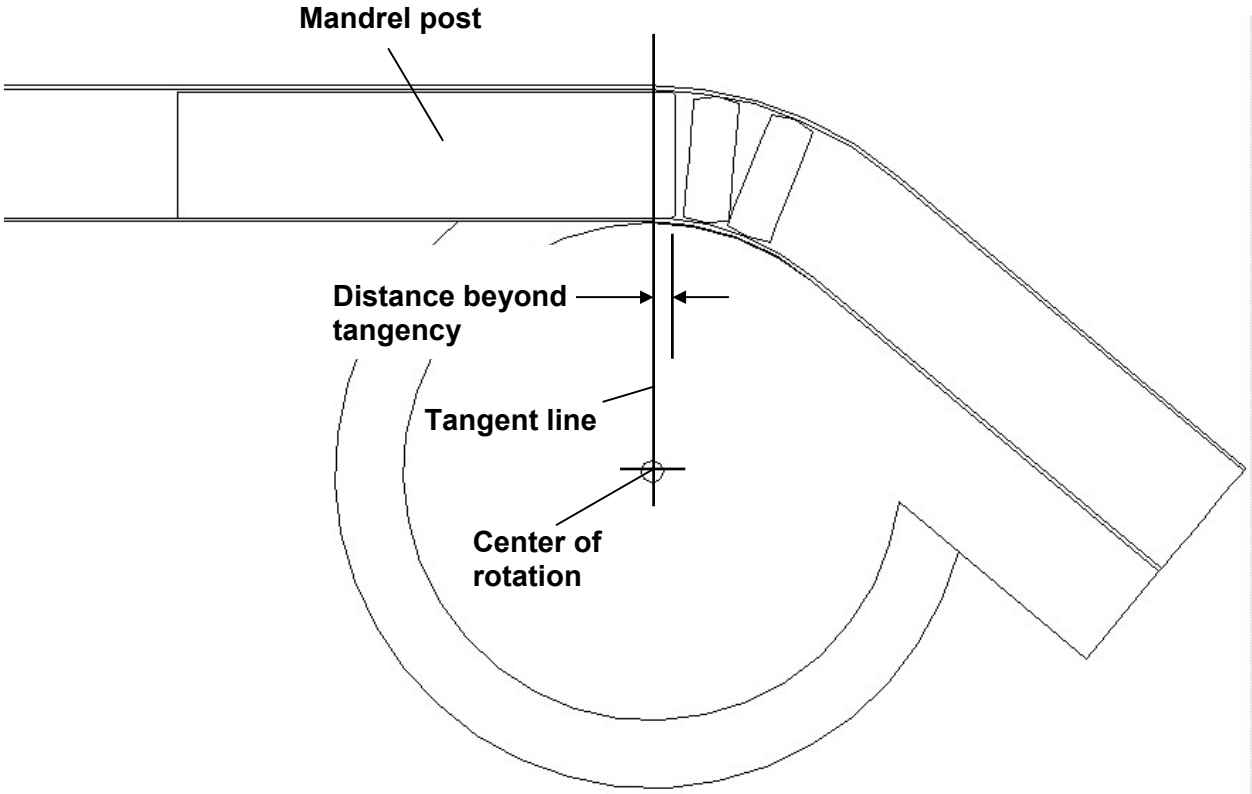

Figure 2.6: Distance of mandrel post beyond tangency

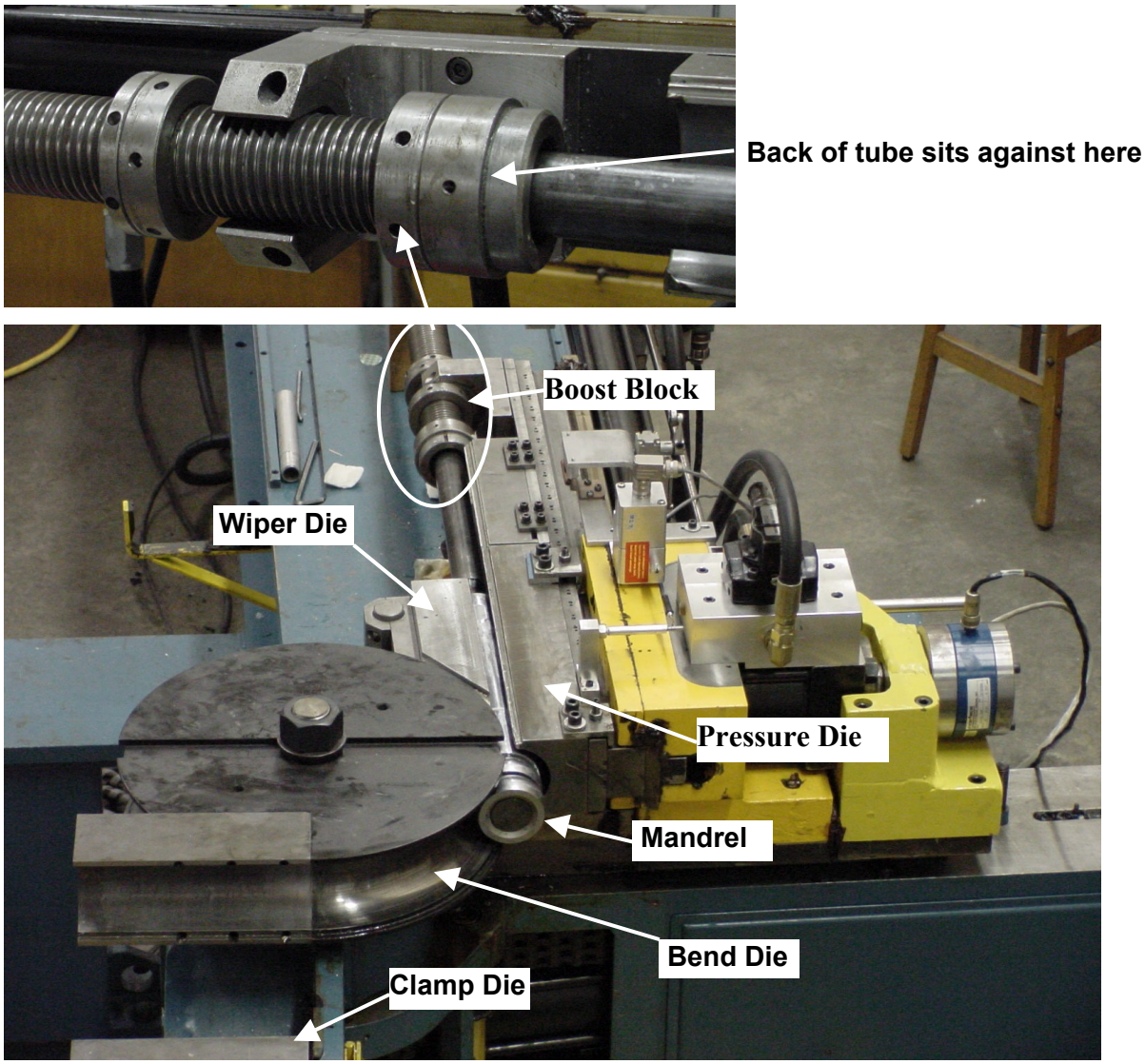

Figure 2.7: View of tube-bender located at the University of Waterloo

As discussed briefly in Section 1.3, the number of mandrel balls to use, their spacing apart, as well as the size of the mandrel, depends on factors such as tube wall thickness relative to tube outside diameter (OD), and tube OD relative to centerline radius of bend, R_c. For example, a thicker wall tube would require less mandrel balls than a thinner wall tube, since a thicker wall tube requires less internal support as it is less likely to collapse during bending.

Furthermore, an important consideration is the "rake angle" of the wiper die (δ_r), as shown at an inclination in Figure 2.5. The wiper die is oriented at an optimal angle from the axis of the tube, typically in the 0.25º range, to minimize frictional drag between tube and wiper during bending, and also to prevent wrinkling on the inside of the bend.

2.3.1 Tool Description

The bend tooling consists of: the bend die, pressure die, clamp die, wiper die, and mandrel (Figure 2.8). The bend die, clamp die and pressure die were manufactured from 4130 tool steel and then nitrided to 60-62 Rc. The wiper die used in this work was made from 4130 tool steel and was not hardened. The mandrel was fabricated from 8620 tool steel, hardened to 58-62 Rc, and then given a chrome surface-finish. The mandrel has two mandrel balls. The mandrel size was chosen such that the diametral clearance between the tube ID and mandrel OD is in the range 0.5-0.7 mm. A low clearance is ideal to maintain the circular cross-section (minimize ovalization) and to reduce risk of wrinkling during bending.

Bend tooling corresponding to an R_c/d ratio of 2.5 was used for the majority of the DQAK tube studied in this thesis. There is also a brief discussion, in Chapter 5, of results for an R_c/d of 2.0. Pictures and major dimensions of the $R_c/d = 2.5$ bend tooling are shown in Figure 2.8. Note that the actual bend centerline radius (CLR) of the bend die was 188.6 mm, rather than 190.5 mm, corresponding to $R_c/d = 2.5$, for a 76.2 mm OD. The actual bend radius compensates for springback after bending to obtain a final R_c/d ratio close to 2.5.

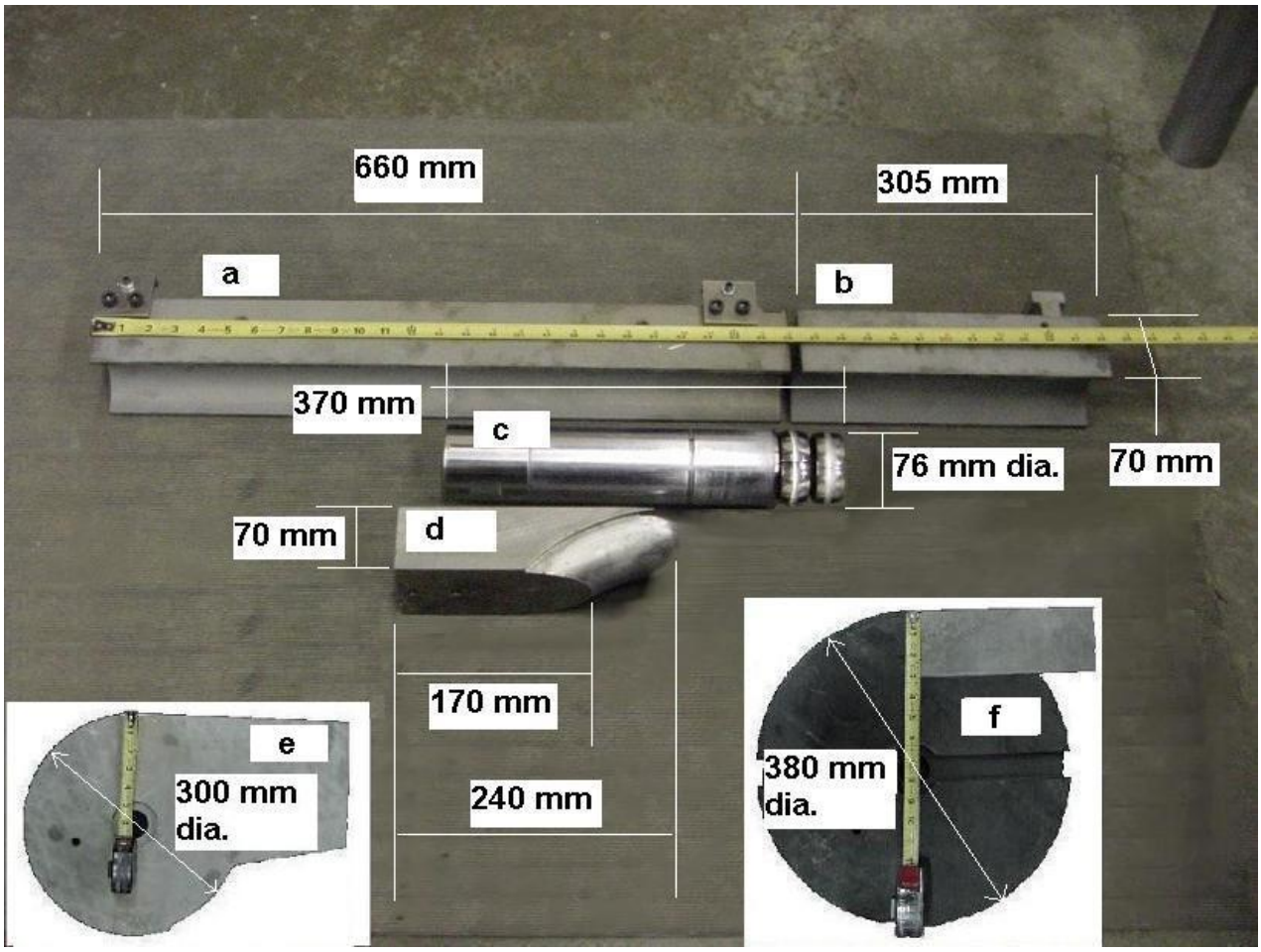

Figure 2.8: Pictures of bend tooling showing: a) Pressure Die, b) Clamp Die, c) Mandrel, d) Wiper Die, e) $R_c/d = 2.0$ Bend Die, f) $R_c/d = 2.5$ Bend Die

2.4 Bend procedure

Prior to testing, the tube is lubricated with Hydrodraw 615, on the outside surface of the tube coming into contact with the wiper die during bending. Hydrodraw 615 is a thick, highly viscous fluid lubricant, which has excellent corrosion resisting properties when used on ferrous alloys such as steel [9]. The tube was aligned so that the weld seam of the tube was positioned upwards, lying approximately along the neutral axis, such that the material properties in the vicinity of the weld seam have a limited effect on the strain and thickness evolution on the inside

and outside of the bend. A brass plug was inserted into the clamped region of the tube to help support high clamping loads needed to reduce slip during the bend.

In this study, a tube would be placed inside the bender, and the bend would be initiated by first raising the clamp die to secure the position of the tube. Then Hydrodraw 615 lubricant was pumped through the mandrel to lubricate the inside of the tube. The mandrel was then advanced forward to the test position, beyond tangency. This forward motion serves to spread out the lubricant along the mandrel surface and the inside surface of the tube. The pressure die was then closed to the appropriate clamping load. Lastly, the bend die and pressure die are moved in a synchronized fashion to bend the tube to the required angle. The bend angle was such that, after springback, the tube would fit snugly inside the 90º hydroforming die for the second forming operation. To remove the tube, the clamp die was opened, followed by release of the pressure die clamping force. The tube could then be taken out and cleaned prior to strain grid measurement (discussed in Section 2.6).

2.5 Hydroforming

The pre-bent tubes were hydroformed at the Industrial Research and Development Institute (IRDI). A teardrop-shaped outside corner-fill die, as shown in Figure 2.9, was used in the hydroforming operation [44]. The material of the die and end-plugs is P20 tool steel, and non-hardened.

This die forces the tube to expand in the region of largest bending strains and thinning (outside of the bend). Tapered end plugs were used to seal the ends of the tube during hydroforming. The lubricant used was Hydrodraw 625, a very effective solid film lubricant, which was applied to the surface of the tube in liquid form, and then upon drying leaves a solid film behind.

The tubes were expanded with a slowly increasing internal water pressure, ramped up linearly with time, and the expansion of the tube on the outside of the bend, at a bend angle location of 45°, was recorded in real time. Several tubes were expanded to burst, while others were expanded to 70% and 90% of the expansion at burst (at the 45º location), as well as to the onset of necking. The strains and thickness on selected hydroformed tubes were then measured at the University of Waterloo.

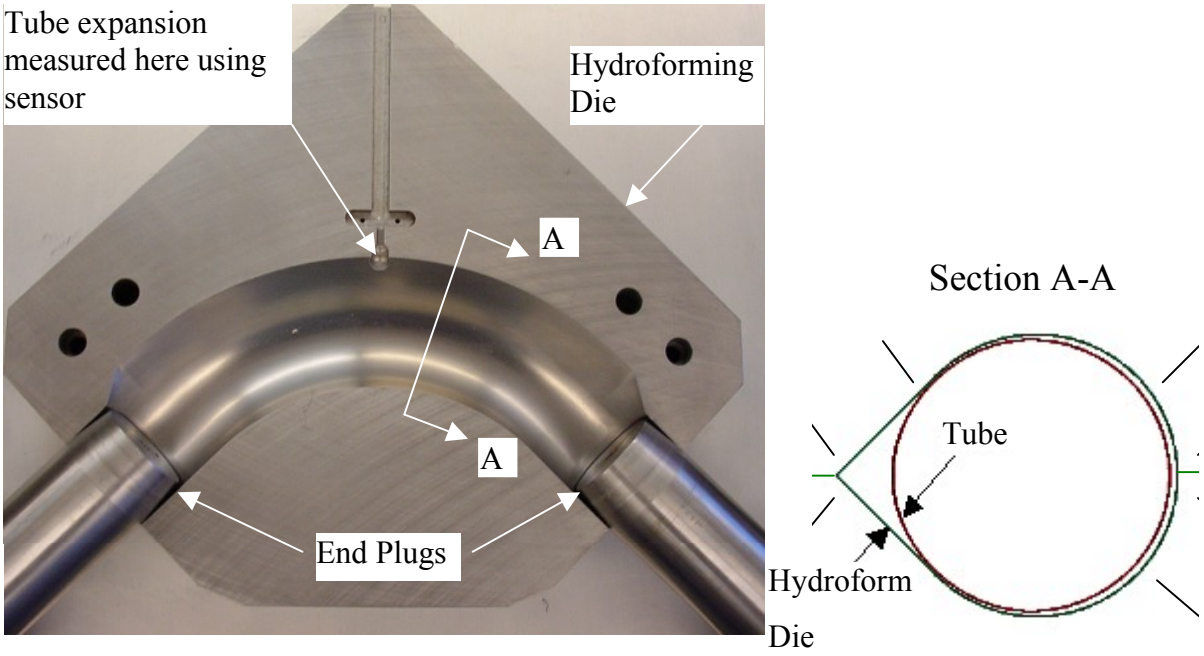

Figure 2.9: Half of outside corner-fill hydroforming die with closed section A-A shown [44]

2.6 Specimen Preparation

Depending on the test condition, the DQAK steel tubes were cut to either 750 mm or 1000 mm in length. The 750 mm length tubes were used for bend cases, where the boost block was not required since it was intended that friction between pressure die and tube be the means to push the tube forward. For the boost cases which used the boost block, the tubes were cut to 1000 mm, long enough to allow the back of the tube to sit against the boost block on the pressure

die. After cutting, the tubes were deburred and cleaned thoroughly using the Lectroetch Co.'s Formula 1 – All Purpose Cleaner. Next, an in-house apparatus was used to electrochemically etch circle grids onto the outside surface of the tubes using the Lectrotech Co.'s Formula 112A etchant. The circle grid stencil was covered with a felt pad soaked with the electrolyte. A 20-30 V DC current was used and a conducting plug was inserted into one end of the tube. The tube was rolled on a copper plate, which acts as an electrical conducting base underneath the felt-pad and stencil. The electrical circuit is completed once the tube is rolled, with downward pressure, over the stencil. As the tube slowly rolls over the stencil the imprint of the circle grids is electrochemically etched onto its outer surface. Following the etching procedure, the outside of the tubes were cleaned again using the cleaner, to remove any excess electrolyte. The tubes were gridded using a nylon sheet stencil, with a 0.1" circle size.

In order to accurately determine the change in dimensions of the grids after deformation, it was necessary to measure their initial dimensions (before deformation) and use these measurements as a means of calibration. To calibrate, four tubes were randomly selected from a batch of 60 straight (undeformed) gridded tubes. Three circle grids were measured on each tube, chosen at random locations. Each of these circle grids had four separate measurements taken on them, for a total of 48 calibration measurements. This large calibration sample, taken as an overall average of the initial grid sizes, allowed for good accuracy in measuring grid strains after deformation, both in bending and hydroforming. The variability in grid size was roughly 2 – 3%.

The strain measurement equipment consisted of a micro-CCD video probe, attached to a PC, which was used to capture an image of the grids. Using manually selected points, a custom image analysis system was used to fit an ellipse to the grids in the image. The program then calculates the strains the circle grid experienced, relative to the calibration measurements. The percentage changes in the major and minor diameters represent the percentage principal

engineering strains at the grid. Further details regarding the grid strain measurement system, are given by Lee [45] and Cinotti [46]

After bending, strains were measured on the inside and outside of the bend (the two extremes), as well as around the circumference at the 45º bend location, where the strain and thickness is fully developed. After hydroforming, the strains and thickness values were measured on the outside of the tube and at the 45º bend location. See Figure 2.10 for the measurement convention used in this study.

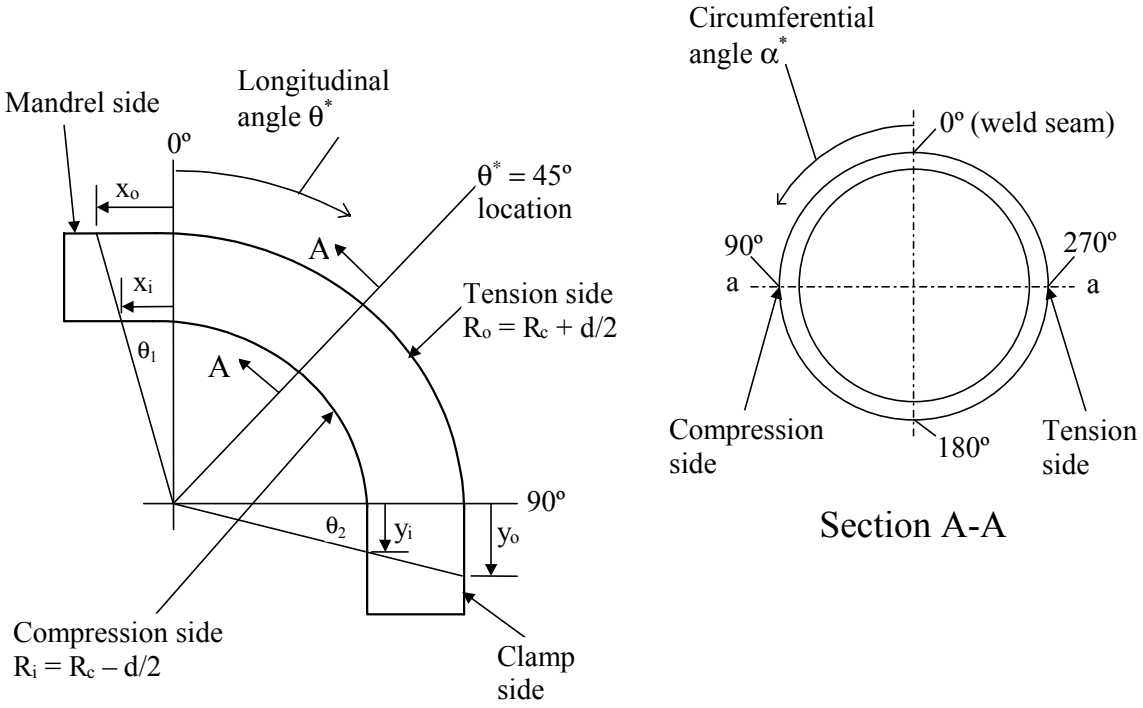

Figure 2.10: Measuring convention for bent and hydroformed tubes

In the curved region of the tube the measured longitudinal angle is simply θ^*. The right hand figure shows the measuring convention around the circumference, for angle α^*. Note that the left hand illustration, in Figure 2.10, shows the inside and outside longitudinal angles θ_1 and θ_2, in both straight regions. In the mandrel region, the longitudinal angle in the straight region is

measured as $\theta^* = -\theta_1 = -\text{atan}(x_i/R_i)$ on the inside of the bend, and $\theta^* = -\theta_1 = -\text{atan}(x_o/R_o)$ on the outside. In the clamp region, the longitudinal angle in the straight region is measured as $\theta^* = 90^o + \theta_2 = 90^o + \text{atan}(y_i/R_i)$ on the inside and $\theta^* = 90^o + \theta_2 = 90^o + \text{atan}(y_o/R_o)$ on the outside. Note that x_i, x_o, y_i, y_o denote the distance of a circle grid from the *start* of the straight region, on the clamp and mandrel side.

2.7 Test Matrix

For each boost condition in the $R_c/d = 2.5$ study, 19 tubes were bent, for a total of 57 tubes. The boost conditions tested were:

- LE95 (low, 95% boost with boost block)
- ME100 (medium, 100% boost with boost block)
- NB100 (medium, 100 % boost with no boost block - friction feed)

It was intended to study a fourth boost case at a high boost of 105%, but the medium boost case was the highest that could be achieved reliably given the existing pressure die assembly and actuator.

As mentioned, the majority of the experiments in this study considered a bend condition corresponding to a centerline bend radius R_c to tube diameter ratio of 2.5. Table 2.2 summarizes the three different boost conditions for bending, corresponding to $R_c/d = 2.5$.

Boost Condition	Bend Angle	Pressure Die Clamp Force	Mandrel Position (beyond tangency)	Wiper Orientation	Lubrication Conditions
100% Boost (ME100)	91°	66.7 kN	1.5 mm	~0.25°	Hydrodraw 615: mandrel and wiper
95% Boost (LE95)	91°	57.8 kN	5.0 mm	~0.25°	Hydrodraw 615: mandrel and wiper
100% No Boost Block (NB100)	91°	66.7 kN	1.5 mm	~0.25°	Hydrodraw 615: mandrel and wiper

Table 2.2: Process Conditions for Bending for $R_c/d = 2.5$

From Table 2.2, one can see that the pressure die clamping force and the mandrel position were not held constant throughout all the tests. It was necessary to find a set of conditions that would produce good wrinkle-free bends at each level of boost, even if this meant altering the test conditions, somewhat, for each case.

Table 2.3 shows the test conditions for *each* of the three boost cases, for hydroforming of the $R_c/d = 2.5$ tubes. While the majority of the tubes were hydroformed after bending, only selected cases are examined in this thesis, which focuses primarily on the analytical bend model. More in-depth treatment of the hydroforming results is provided by Dyment [43].

Hydroforming Condition	Samples Needed	Extra Samples	Total Samples
Burst	3	1	4
90% of Expansion at Burst	2	1	3
70% of Expansion at Burst	2	1	3
Necking	5	4	9
Totals	12	7	19

Table 2.3: Hydroforming Test Matrix

Chapter 3– Mathematical Model Development

The purpose of this chapter is to give an in-depth overview of the solid mechanics incorporated into the analytical bend software program. Derivations from first principles are presented for the more fundamental equations, and also their implementation in the code is discussed. Equations are developed on the basis of the final bent-tube geometry.

As it turns out, the specific mathematical formulae in the literature surveyed proved to be overly-simplified for direct use in the analytical model. However, basic tube bending equations found in the published literature did serve to aid in understanding the tube-bending problem. One major shortcoming in the published literature is the lack of consideration of the contribution of axial forces on strains and thickness. In reality, large axial "boost" forces are present in rotary-draw tube bending, and one must take into account the membrane component of axial strain. In the current analytical model, "axial boost" is taken into account, as will be discussed in detail in this chapter.

It was also found in the literature surveyed that the prediction of hoop strain is not given rigorous treatment, and in some cases neglected altogether. Adequate prediction of hoop strain is necessary for better overall strain prediction, resulting in improved thickness predictions. In this

chapter, an approximate means of formulating and predicting hoop strain in tube bending, using a mandrel, is presented.

Also of significance, an empirical formulation for the decay of stress, strain, and thickness change at each end of the bend is presented, as implemented in the current bend model. Analytical formulation of decay near the ends of the bend proved to be too complex, instead; exponential decay functions were developed with constants adjusted to best match experimental and numerical data.

The simplifying physical assumptions in the model are:

- The mandrel keeps tube ovalization to a minimum during bending; hence, the tube is assumed to remain circular
- The tubes are thin-walled
- Planar cross-section surfaces remain plane before and after bending
- Frictional effects between the tooling and tube are not considered
- No normal stress exists in the through-thickness direction
- In-plane shear stresses and shear strains are neglected

3.1 Strain Distribution

Figure 3.1 shows the deformed tube cross-section and highlights key parameters that are referred to in the model description. In this analysis, subscript '1' denotes the axial direction (θ), '2' denotes the hoop direction (α), and '3' denotes the thickness direction (t).

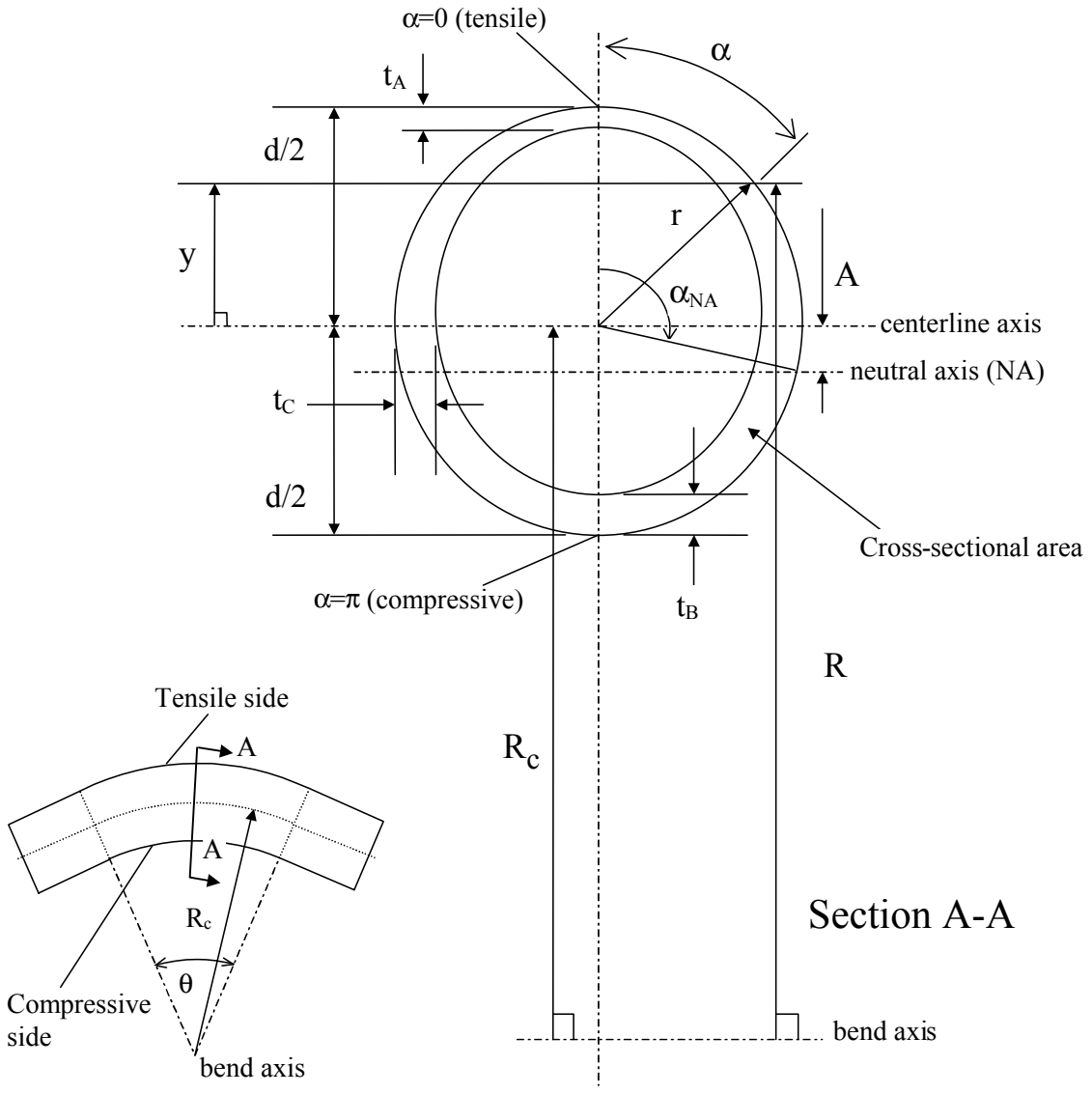

Figure 3.1: Geometry of cross-section

A general strain distribution formulation is presented below, first taking into account pure bending and the corresponding neutral axis shift, a distance A, below the tube centerline.

In the pure bending case, consider the distribution of axial true strain as

$$\varepsilon_1^{\text{true}} = \ln\left(1 + \frac{y + A}{R_c - A}\right) \tag{3.1}$$

where $y = r \cdot \cos\alpha$. To derive this expression, consider first a tube bent to an arbitrary angle θ (see Figure 3.1). There is a neutral fibre (arc) located at a distance A below the centerline (at bend radius R = R_c –A), which experiences no axial strain. Consequently, this neutral fibre has an arc length equal to its length before bending. Since the tube was straight before bending, this length can be used as the *initial* length of *all* fibres before bending. Call this length

$$l_o = (R_c - A) \cdot \theta \tag{3.2}$$

At any arbitrary bend radius *R* of the tube one can write

$$l_1 = (R_c + y) \cdot \theta \tag{3.3}$$

where y is measured from the centerline, as shown in Figure 3.1. The engineering strain is given by

$$\varepsilon_1^{eng} = \frac{l_1 - l_o}{l_o} = \frac{(R_c + y) \cdot \theta - (R_c - A) \cdot \theta}{(R_c - A) \cdot \theta} = \frac{y + A}{R_c - A} \tag{3.4}$$

and the true strain becomes $\ln\left(1 + \varepsilon_1^{\text{eng}}\right)$ as in (3.1).

3.1.1 Hoop Strain Calculation for Pure Bending Case

Consider the calculations for average hoop strain (average through the thickness for each α). This average is approximately at the mid-surface radius, $r = r_o$, so that $r_o = \frac{d}{2} - \frac{t}{2}$, with t as the original wall thickness. See Figure 3.2 for an illustration of the hoop strain calculation.

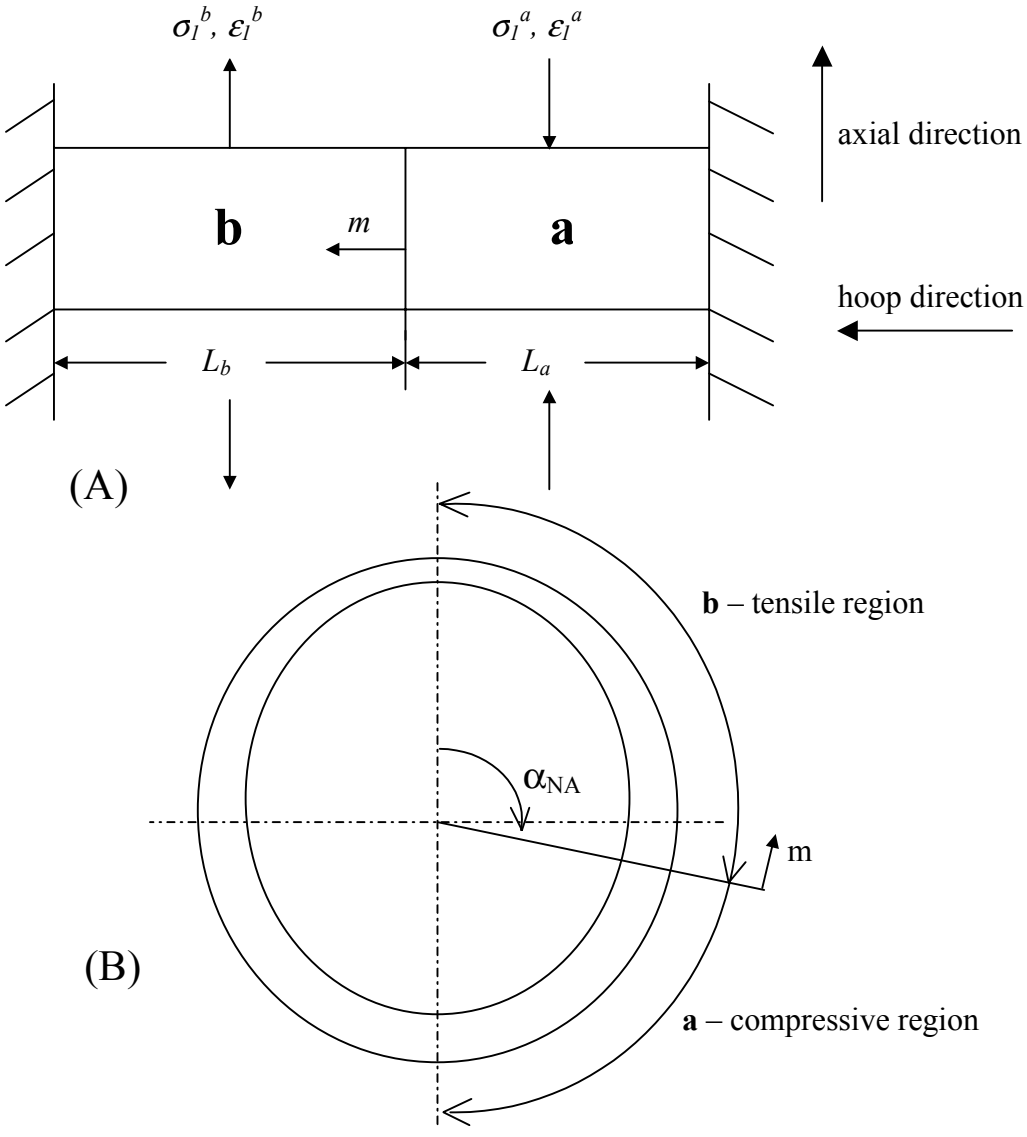

Figure 3.2: Physical representation for calculating hoop strain

The very useful simplification for the hoop strain calculation is shown in Figure 3.2. Note that the hoop direction is the α direction, and the axial direction is the θ direction. The tube cross-section in Figure 3.2 (B) can be divided into two distinct regions of axial stress and strain, one compressive and the other tensile. It is assumed the hoop strain is constant in each region. Furthermore, if the tube diameter is constant due to the presence of the mandrel, then the total change in circumference due to the hoop strains must be zero. If one imagines "unwrapping the tube", then the flat plate shown in Figure 3.2 (A), with rigidly constrained edges, is analogous to the hoop strain analysis of the tube.

ε_1^b is the average, or "effective", (positive) axial true strain over the range $0 \le \alpha \le \alpha_{NA}$, where α_{NA} is the particular angle α where the axial, and hoop strain, change sign. ε_1^a is the average, or "effective", (negative) axial true strain over the range of $\alpha_{NA} \le \alpha \le \pi$. Half-symmetry is assumed in the modeling, corresponding to a range $0 \le \alpha \le \pi$.

Mathematically, this can be expressed as

$$\varepsilon_1^b = \frac{1}{r_o \cdot \alpha_{NA}} \int_0^{\alpha_{NA}} \varepsilon_1^{true}(\alpha) \cdot r_o \cdot d\alpha \tag{3.5}$$

and

$$\varepsilon_1^a = \frac{1}{r_o \cdot (\pi - \alpha_{NA})} \int_{\alpha_{NA}}^{\pi} \varepsilon_1^{true}(\alpha) \cdot r_o \cdot d\alpha \tag{3.6}$$

Now set

$$L_b = r_o \cdot \alpha_{NA} \tag{3.7}$$

and

$$L_a = r_o \cdot (\pi - \alpha_{NA}) \tag{3.8}$$

The compatibility condition is illustrated in Figure 3.2 (A), and is such that, at the interface, the two elements (**a** and **b**) move the same distance *m*. The average, or effective, values of stress and strain (for elements **a** and **b**) are used *only* for the purpose of approximating the interface displacement *m*. With this displacement *m* known, the approximate average hoop strains are calculated. The assumption here is that the hoop strain is roughly constant over the compressive and tensile regions, justifying the use of average values. This assumption is justified by the numerical FEM and experimental results, presented in Chapter 5. Also, accounting for the hoop strain gradient, in the α direction, would require a much more complex mathematical treatment, solving partial differential equations of stress equilibrium, coupled with constitutive equations. This would greatly increase the model complexity and computation time without an appreciable increase in accuracy.

Both elements experience the same hoop stress σ_2 at the interface, and using Hencky's plastic stress-strain relations [47]:

$$\varepsilon_1^a = \frac{1}{E_s^a} \cdot (\sigma_1^a - \frac{1}{2}\sigma_2) \tag{3.9}$$

$$\varepsilon_2^a = \ln(1 + \frac{m}{L_a}) = \frac{1}{E_s^a} \cdot (\sigma_2 - \frac{1}{2}\sigma_1^a) \tag{3.10}$$

$$\varepsilon_1^b = \frac{1}{E_s^b} \cdot (\sigma_1^b - \frac{1}{2}\sigma_2) \tag{3.11}$$

$$\varepsilon_2^b = \ln(1 - \frac{m}{L_b}) = \frac{1}{E_s^b} \cdot (\sigma_2 - \frac{1}{2}\sigma_1^b) \tag{3.12}$$

Now,

$$E_s^a = \frac{\sigma_{eff}^a}{\varepsilon_{eff}^a},\ \varepsilon_{eff}^a = \sqrt{\frac{2}{3}[(\varepsilon_1^a)^2 + (\varepsilon_2^a)^2 + (\varepsilon_3^a)^2]} \tag{3.13}$$

where $\sigma_{eff}^a = \sigma_{eff}^a(\varepsilon_{eff}^a)$, and this functional relationship is defined by the power law expression $\sigma_{eff} = K \cdot (\varepsilon_{yp} + \varepsilon_{eff})^n$, or flow curve data. Note that ε_{eff} is the effective plastic strain, and ε_{yp} is the yield point, which is calculated by solving for the intersection of $\sigma = E \cdot \varepsilon$ and $\sigma = K \cdot \varepsilon^n$, for the power law formulation. Solving, $\varepsilon_{yp} = \left(\frac{E}{K}\right)^{1/(n-1)}$.

Similarly,

$$E_s^b = \frac{\sigma_{eff}^b}{\varepsilon_{eff}^b},\ \varepsilon_{eff}^b = \sqrt{\frac{2}{3}[(\varepsilon_1^b)^2 + (\varepsilon_2^b)^2 + (\varepsilon_3^b)^2]}, \text{ and } \sigma_{eff}^b = \sigma_{eff}^b(\varepsilon_{eff}^b) \tag{3.14}$$

Equations (3.9) - (3.12) are solved numerically (for *m*) using the bisection method (discussed in Appendix A.1 and A.2). With *m* calculated one can directly calculate the engineering hoop strains:

$$\varepsilon_2^{a,eng} = \frac{m}{L_a}, \text{ constant over } \alpha_{NA} \le \alpha \le \pi \tag{3.15}$$

$$\varepsilon_2^{b,eng} = -\frac{m}{L_b}, \text{ constant over } 0 \le \alpha \le \alpha_{NA} \tag{3.16}$$

Then, for pure bending

$$\varepsilon^{o}_{hoop} = \begin{Bmatrix} f \cdot \varepsilon_2^{b,eng},\ for\ 0 \le \alpha \le \alpha_{NA} \\ f \cdot \varepsilon_2^{a,eng},\ for\ \alpha_{NA} \le \alpha \le \pi \end{Bmatrix} \tag{3.17}$$

where $f = 1 - \exp\{-3.0 \cdot (\alpha - \alpha_{NA})^2\}$ which "forces" a smooth transition between $\varepsilon_2^{b,eng}$ and $\varepsilon_2^{a,eng}$ at $\alpha = \alpha_{NA}$ (Figure 3.3). This forced transition is mathematically necessary to avoid unrealistic discontinuity affects (such as a thickness "spike") near the transition angle $\alpha = \alpha_{NA}$. Note that ε^{o}_{hoop} is, effectively, a through-thickness average.

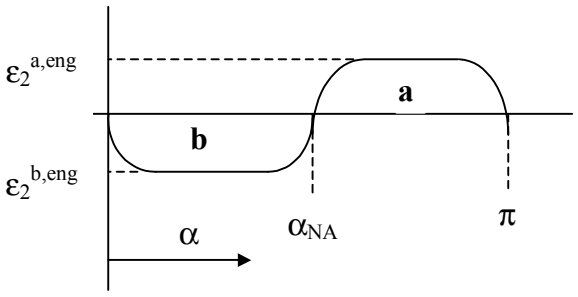

Figure 3.3: Hoop strain distribution

This approach essentially amounts to adopting two nearly constant average hoop strains, one over the region of the tube where axial strain is positive, and the second where axial strain is negative. Physically speaking, for positive axial strain the hoop strain is negative, by volume conservation, and similarly, for negative axial strain the hoop strain is positive.

Mathematically, the pure bending requirement (zero axial boost force) can be expressed as an integral of the stresses over the cross-sectional area

$$\int_{Area} \sigma_1(\varepsilon_1^{true})\, dArea = 0 \tag{3.18}$$

(3.18) is calculated numerically using a double integral, over the (final) deformed cross-sectional area. The distance A is such that this expression is satisfied. Furthermore, the cross-sectional area is such that Area = Area(ε_1 , ε_{hoop}^{o}), justifying the use of iteration to solve for A.

In Figure 3.1, t_A, t_B, and t_C are thickness values used as input for fitting an ellipse of best fit on the inside diameter of the deformed tube. This allows the cross-sectional area to be calculated with very good accuracy.

To illustrate how the program solves for A (neutral axis offset from centerline, for pure bending), consider Figure 3.4.

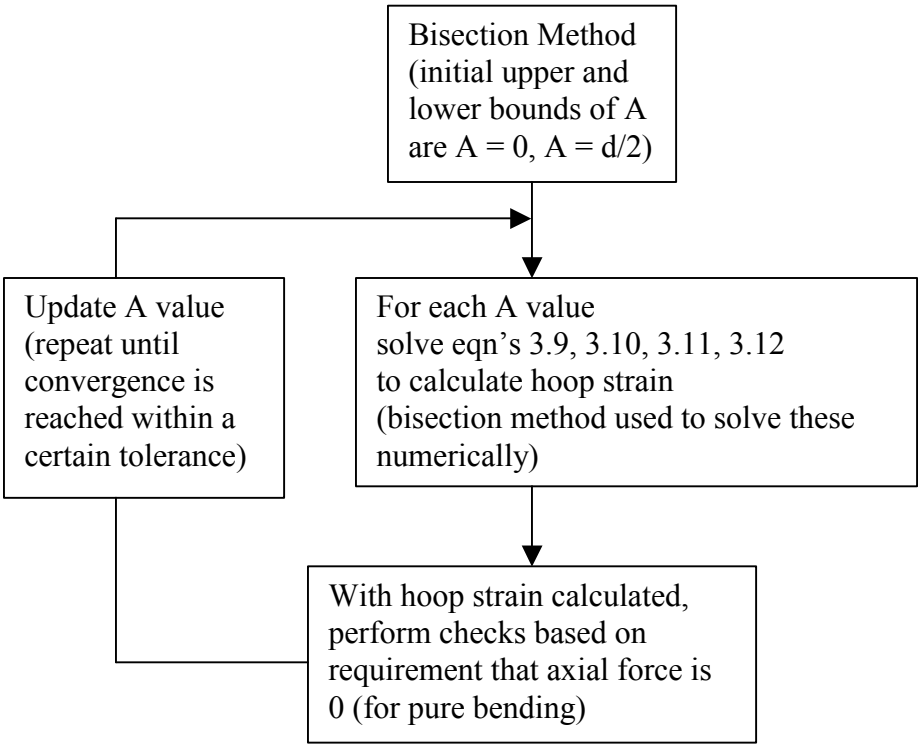

Figure 3.4: Schematic of neutral axis offset calculation for pure bending

3.1.2 Pure Bending with addition of Membrane Strain

For the general case consider the distribution of axial strain as

$$\varepsilon_1^{\text{true}} = \ln\left(1 + \frac{y + A}{R_c - A}\right) + e(\alpha) \tag{3.19}$$

where $e(\alpha) \neq 0$ is the membrane component of axial strain due to the addition of axial push/pull boost force on the tube during bending (as shown by Zhang and Duncan [5]). For pure bending with zero axial force, $e(\alpha) = 0$. Thus, with the addition of axial force, there will be an additional membrane axial strain superimposed on the pure bending strains. Here, the (net) axial force is the force due to deformation and does not include friction.

Mathematically,

$$F_{\text{deformation}} = F_{\text{applied}} - F_{\text{friction}} \tag{3.20}$$

To illustrate the methodology used to calculate $e(\alpha)$, consider Figure 3.5 for a 90° bend.

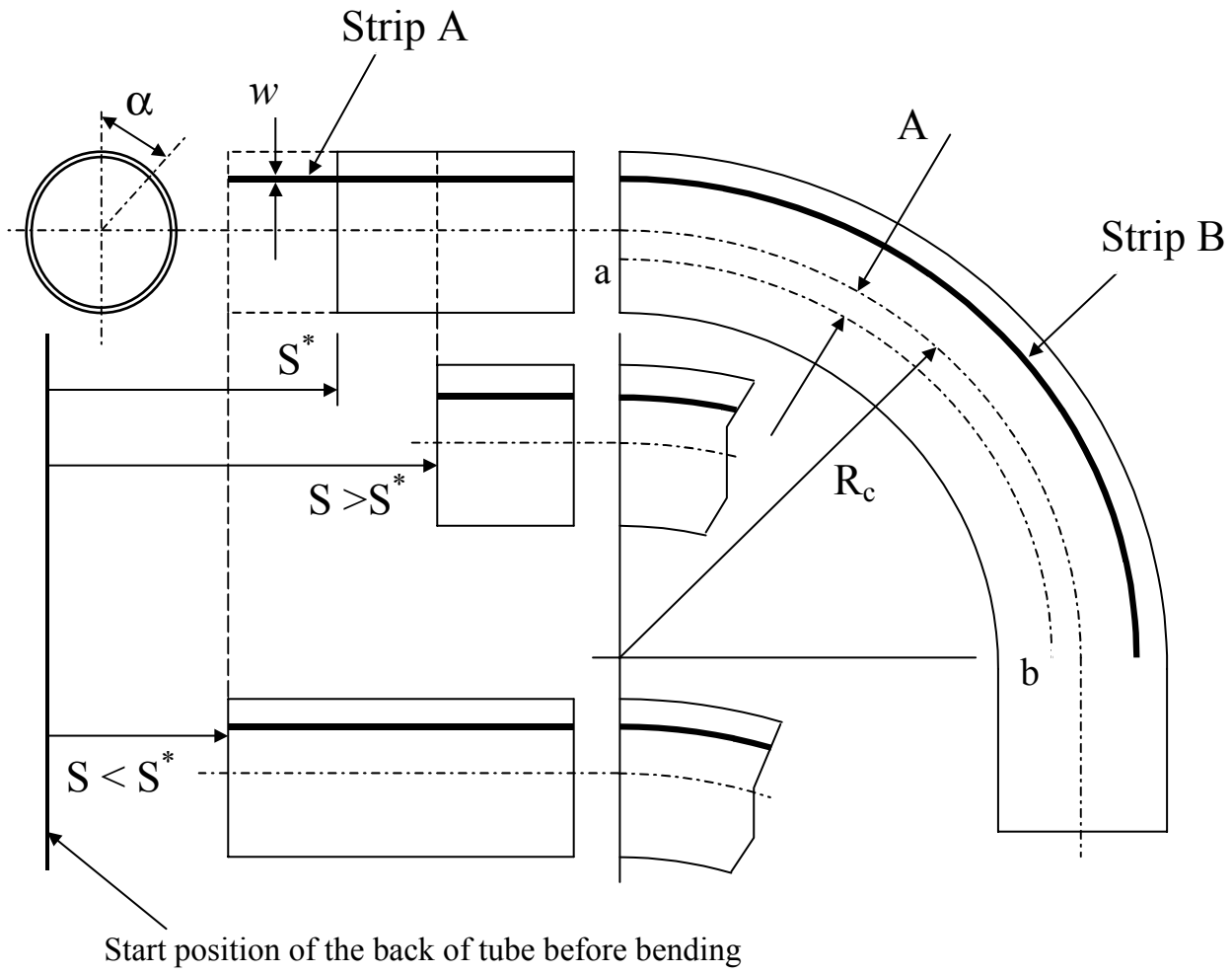

Figure 3.5: Diagram illustrating different boost conditions

From the figure, S^* denotes the travel of the back of the tube during the bend, for pure bending. S is defined as the travel of the back of the tube for the general bending case, which may include boost. Set $S-S^* = l^b$, in which $l^b>0$ for "pushing" boost and $l^b<0$ for "pulling" boost.

$S = S^*$ for pure bending and S^* may be viewed as a reference value. For pure bending, $S = S^*$ is the arc length ab (at bend radius $R = R_c$-A), shown on Figure 3.5.

Strip A and B are thin strips of tube material taken through the tube thickness, at angle α.

The boost distance can be written as,

$$l^b = R_c \cdot \theta \cdot \frac{percent\,boost}{100} - (R_c - A) \cdot \theta \tag{3.21}$$

where θ corresponds to any arbitrary bend angle.

Since the volume of strip A, of length $|S\text{-}S^*|$, must equal the volume added on to or taken away from the volume of strip B, for pure bending, one can form an expression to solve for $e(\alpha)$ in terms of l^b.

To show how the expression relating $e(\alpha)$ and l^b is derived, first set the volume of strip A as

$$V = t \cdot l^b \cdot w \tag{3.22}$$

For $l^b > 0$, $V > 0$; and for $l^b < 0$, $V < 0$. For pure bending, $l^b = 0$, $e(\alpha)=0$.

The width of strip A is *constant* for *all* boost cases and is set equal to w. However, the width of strip B, in the curved region, changes with different boost cases and is set equal to w for the pure bending case, in eq. (3.23).

One can write directly the width of strip B as

$$w_{new} = w + w\frac{\varepsilon_{hoop} - \varepsilon^{o}_{hoop}}{1 + \varepsilon^{o}_{hoop}} \tag{3.23}$$

w is the width of the strip for pure bending, which is evident if one sets $\varepsilon_{hoop} = \varepsilon^{o}_{hoop}$ for the degenerate case where $e(\alpha)=0$. ε_{hoop} is the hoop strain for the general case where $e(\alpha)\neq 0$.

For pure bending, the volume of the strip B in the curved bend, of angle θ, is

$$V_1 = t_{new}\{e(\alpha) = 0\} \cdot w \cdot L_{SB} \tag{3.24}$$

where L_{SB} is the arc length of strip B and is approximately

$$L_{SB} = [(\frac{d}{2} - t_b) \cdot \cos(\alpha) + R_c] \cdot \theta \tag{3.25}$$

t_b corresponds to the wall thickness for pure bending ($e(\alpha) = 0$).

Now consider the volume of strip B for the general case when there is axial force present, $e(\alpha)\neq 0$. Call this volume V_2.

Using the same approximate arc length L_{SB} as for pure bending, one can write the volume of strip B as

$$V_2 = t_{new}\{e(\alpha)\} \cdot [w + w\frac{\varepsilon_{hoop} - \varepsilon^{o}_{hoop}}{1 + \varepsilon^{o}_{hoop}}] \cdot [(\frac{d}{2} - t_b) \cdot \cos(\alpha) + R_c] \cdot \theta \tag{3.26}$$

t_{new} is the tube wall thickness after bending. An expression for t_{new} will be derived later on.

Using the fact that volume is conserved in plastic deformation, one can write $V_2 - V_1 = V$. As a result, one can write the final expression relating $e(\alpha)$ and l^b, with w canceling out:

$$\left(t_{new}\{e(\alpha)\} \cdot (1 + \frac{\varepsilon_{hoop} - \varepsilon^{o}_{hoop}}{1 + \varepsilon^{o}_{hoop}}) - t_{new}\{e(\alpha) = 0\} \right) \cdot \left((\frac{d}{2} - t_b) \cdot \cos(\alpha) + R_c \right) \cdot \theta = t \cdot l^b \tag{3.27}$$

(3.21) is substituted for l^b, on the right side. Note that θ cancels out meaning that the above expression is independent of bend angle.

3.1.2.1 Hoop Strain Calculation for non-zero Boost Force

For the general case where $e(\alpha) \neq 0$, consider again the hoop strain calculation where an average hoop strain (through the thickness) is used, at the mid-surface radius, $r_o = \frac{d}{2} - \frac{t}{2}$.

As before, set ε_1^b as the average positive axial strain over the range $0 \leq \alpha \leq \alpha_{NA}$, where α_{NA} is the particular angle α where the axial and hoop strain change sign. Note that $0 < \alpha_{NA} < \pi$, since the membrane strain component can shift this neutral axis to any arbitrary angle α, within this range.

Set ε_1^a as the average negative axial strain over the range of $\alpha_{NA} \leq \alpha \leq \pi$. Mathematically, this can be expressed as

$$\varepsilon_1^b = \frac{1}{r_o \cdot \alpha_{NA}} \int_0^{\alpha_{NA}} \varepsilon_1^{true}(\alpha) \cdot r_o \cdot d\alpha \tag{3.28}$$

and

$$\varepsilon_1^a = \frac{1}{r_o \cdot (\pi - \alpha_{NA})} \int_{\alpha_{NA}}^{\pi} \varepsilon_1^{true}(\alpha) \cdot r_o \cdot d\alpha \tag{3.29}$$

Note that $\alpha_{NA} \neq \alpha_{NAo}$ necessarily, where α_{NAo} is the neutral axis angle for pure bending. Equality is *only* for $e(\alpha) = 0$.

As before, set

$$L_b = r_o \cdot \alpha_{NA} \tag{3.30}$$

and

$$L_a = r_o \cdot (\pi - \alpha_{NA}) \tag{3.31}$$

Solving the same set of equations as before, (3.9) - (3.12), one obtains

$$\varepsilon_2^{a,eng} = \frac{m}{L_a}, \text{ for } \alpha_{NA} \le \alpha \le \pi \tag{3.32}$$

and

$$\varepsilon_2^{b,eng} = -\frac{m}{L_b}, \text{ for } 0 \le \alpha \le \alpha_{NA} \tag{3.33}$$

Then, for the general bending case

$$\varepsilon_{hoop} = \begin{Bmatrix} f \cdot \varepsilon_2^{b,eng}, \; for \; 0 \le \alpha \le \alpha_{NA} \\ f \cdot \varepsilon_2^{a,eng}, \; for \; \alpha_{NA} \le \alpha \le \pi \end{Bmatrix} \tag{3.34}$$

using the same expression *f* from before. Note that ε_{hoop} is, effectively, a through-thickness average.

For axial loading, $\varepsilon_1^{\text{true}} = \ln\left(1 + \frac{y + A}{R_c - A}\right) + e(\alpha)$, and *e(α)* depends on hoop strain, from eq. (3.27). This means that for axial loading, $\varepsilon_1^{\text{true}}$ depends on hoop strain, so that $\varepsilon_1^{true} = \varepsilon_1^{true}(\varepsilon_{hoop})$. This means that ε_{hoop} must be such that $\varepsilon_1^{\text{a}} = \varepsilon_1^{\text{a}}\{\varepsilon_1^{\text{true}}(\varepsilon_{hoop})\}$ and $\varepsilon_1^{\text{b}} = \varepsilon_1^{\text{b}}\{\varepsilon_1^{\text{true}}(\varepsilon_{hoop})\}$ give the same ε_{hoop} back out again when solving (3.9) - (3.12). Mathematically, an iterative method is used to solve for ε_{hoop}, which can mathematically be expressed as

$$\varepsilon_{hoop}[i+1] = g(\varepsilon_1^a\{\varepsilon_1^{true}(\varepsilon_{hoop}[i])\}, \varepsilon_1^b\{\varepsilon_1^{true}(\varepsilon_{hoop}[i])\}) \tag{3.35}$$

This iteration is performed a sufficient number of times to get convergence within a desired tolerance so that $\varepsilon_{hoop}[i+1] \cong \varepsilon_{hoop}[i]$, with $\varepsilon_{hoop}[1] = \varepsilon^{o}_{hoop}$ to start the iteration. The calculation of ε^{o}_{hoop} does *not* require iteration to solve for, because $e(\alpha) = 0$. Furthermore, since α_{NA} is coupled with ε_{hoop}, then α_{NA} is solved for along with ε_{hoop}.

There are two distinct cases to consider when dealing with the addition of axial force. The first case is when the program user specifies a percent boost, from which l^b can be calculated directly. With l^b known, one can immediately obtain $e(\alpha)$ which can be calculated directly after solving for ε_{hoop} using the recursive iteration method just described. In this case the net axial boost force can be determined directly by numerically calculating an integral of the stresses over the cross-sectional area. This integral can be expressed as

$$\int_{Area} \sigma_1(\varepsilon_1^{true}) dArea = F_{boost} \tag{3.36}$$

To illustrate how the program solves for F_{boost} consider the following schematic in Figure 3.6:

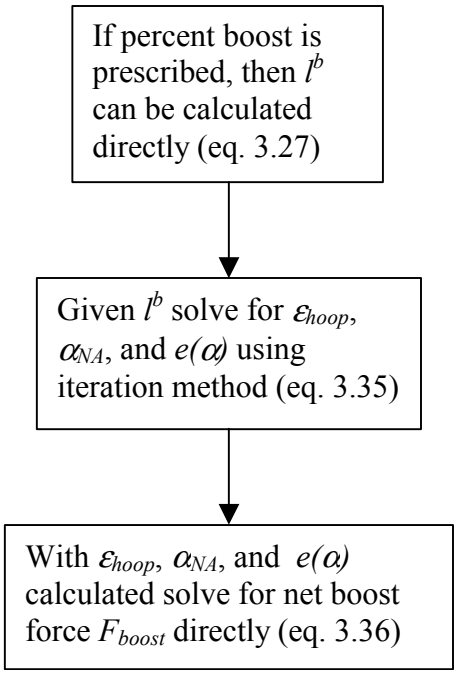

Figure 3.6: Schematic showing solution for F_{boost}

The second case is when F_{boost} is prescribed, meaning that one must use a numerical method to solve for the particular l^b such that $\int_{Area} \sigma_1(\varepsilon_1^{true})dA = F_{boost}$. In this case the bisection method is used once more. The only difference between this second case and the first case is that the program must march though a series of l^b values until the prescribed boost force is satisfied, within a certain tolerance. Consequently, the run time takes longer. Schematically this is illustrated in Figure 3.7:

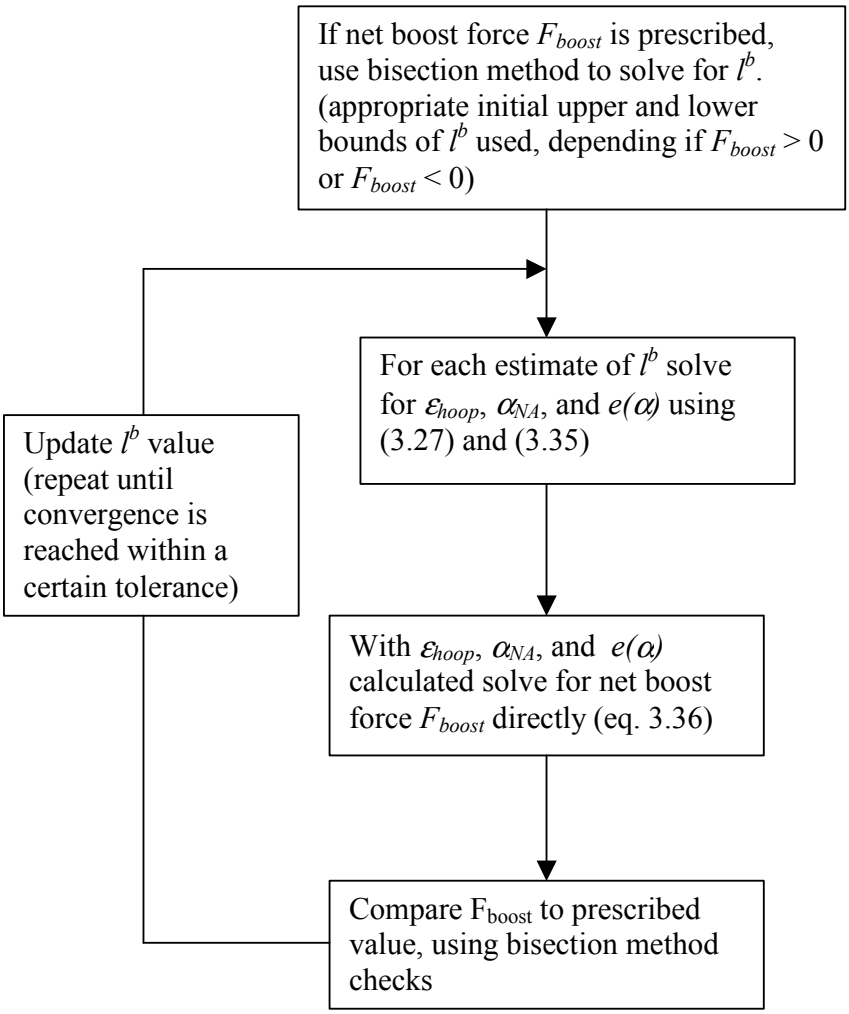

Figure 3.7: Schematic showing iterative F_{boost} calculation

3.2 Thickness Calculation

To solve for the wall thickness after bending, one must first consider volume conservation for plasticity.

By volume conservation for plastic deformation,

$$\ln\left(1+\frac{y+A}{R_c-A}\right)+e(\alpha)+\ln(1+\varepsilon_2^{eng})+\ln(1+\varepsilon_3^{eng})=0 \tag{3.37}$$

Therefore,

$$\varepsilon_3^{eng}=\frac{1}{\exp\{e(\alpha)\}}\cdot\frac{1}{\left(1+\frac{y+A}{R_c-A}\right)\cdot(1+\varepsilon_2^{eng})}-1 \tag{3.38}$$

Substituting y = r·cosα into (3.38), the new wall thickness after bending is calculated as $t_{new}=t+\int_{d/2-t}^{d/2}\varepsilon_3 dr$ (integrated from inside radius of tube to outside radius, on original un-deformed geometry). If one uses the average through-thickness engineering hoop strain ($\varepsilon_{2,avg}^{eng}$) to simplify calculations then

$$t_{new}(\alpha)=\frac{R_c-A}{\exp\{e(\alpha)\}\cdot\cos(\alpha)}\cdot\frac{1}{(1+\varepsilon_{2,avg}^{eng})}\cdot\ln\frac{R_c+(d/2)\cdot\cos(\alpha)}{R_c+(d/2-t)\cdot\cos(\alpha)} \tag{3.39}$$

From before, $\varepsilon_{2,avg}^{eng}\equiv\varepsilon_{hoop}$ for the general bending case, with non-zero axial boost force; and $\varepsilon_{2,avg}^{eng}\equiv\varepsilon_{hoop}^{o}$ for pure bending, with zero axial boost force.

3.3 Plasticity Equations – Stress Formulation

In the local coordinate frame $x_1x_2x_3$ of the bent tube (see Figure 3.8) the boundary condition is $\sigma_3 = 0$. Once more one can apply the Hencky equations for total plasticity [47].

These equations are valid for near proportional loading, as is the case in the tube bending process. One can write:

$$\varepsilon_1^{true} = \frac{1}{E_s} \cdot (\sigma_1 - \frac{1}{2}\sigma_2)$$
$$\varepsilon_2^{true} = \frac{1}{E_s} \cdot (\sigma_2 - \frac{1}{2}\sigma_1) \qquad (3.40)$$
$$\varepsilon_3^{true} = \frac{1}{E_s} \cdot (-\frac{1}{2}\sigma_1 - \frac{1}{2}\sigma_2)$$

From the first 2 equations of (3.40), one can obtain expressions for σ_1 and σ_2.

$$\sigma_1 = \frac{2A_{pl} + B_{pl}}{1.5}$$
$$\sigma_2 = \frac{2A_{pl} + 4B_{pl}}{3} \qquad (3.41)$$

where $A_{pl} = \varepsilon_1^{true} \cdot E_s$ and $B_{pl} = \varepsilon_2^{true} \cdot E_s$

For given material constants K and n, one can write

$$E_s = \frac{\sigma_{eff}}{\varepsilon_{eff}} = \frac{K(\varepsilon_{eff} + \varepsilon_{yp})^n}{\varepsilon_{eff}} \qquad (3.42)$$

using the same ε_{yp} from before. Alternatively, E_s can be calculated from flow curve data.

Now,

$$\varepsilon_{eff} = \sqrt{\frac{2}{3}[(\varepsilon_1^{true})^2 + (\varepsilon_2^{true})^2 + (\varepsilon_3^{true})^2]} \qquad (3.43)$$

By volume conservation

$$\varepsilon_1^{true} + \varepsilon_2^{true} + \varepsilon_3^{true} = 0 \tag{3.44}$$

From (3.41) one can solve for $\sigma_1 = \sigma_1(\varepsilon_1^{true}, \varepsilon_2^{true})$. This is substituted into (3.18) and (3.36).

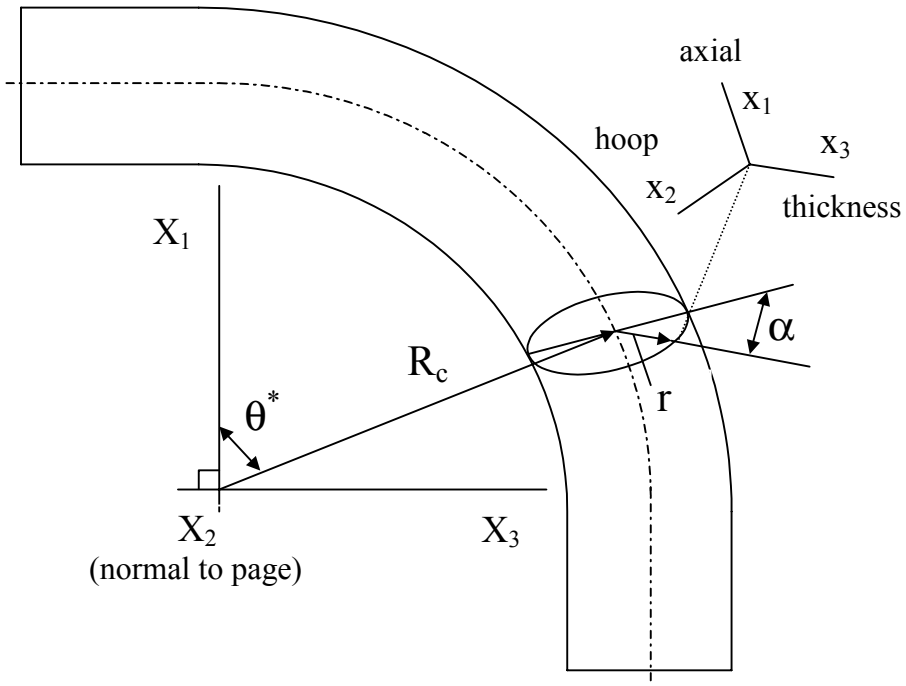

Figure 3.8: Local ($x_1x_2x_3$) and global ($X_1X_2X_3$) coordinate system of tube

The true strains ε_{ij}, and the residual stresses after springback, σ_{ij}^{res}, are calculated in the local system $x_1x_2x_3$. Using stress and strain transformation equations, ε_{ij} and σ_{ij}^{res} are then calculated in the global reference frame $X_1X_2X_3$ for each integration point, and output to files in a format suitable for FEM simulation of a subsequent hydroform process. This is discussed in greater detail in Appendix A.5.

3.4 Elastic Stress and Springback Calculations

To predict elastic springback, after unloading, a moment calculation must be performed over the cross-sectional area, about the centroid of area, for the elastic-plastic stresses due to bending.

$$M = \int_{Area} \sigma_1(\varepsilon_1^{true}) \cdot (y + E_{ct}) \cdot dArea \tag{3.45}$$

where E_{ct} is the centroid distance below the centerline (shown in Figure 3.1). In the program, M is calculated numerically with a double integral, and is calculated with ε_{hoop} and $e(\alpha)$ already calculated.

For springback calculations it is necessary to calculate the elastic stresses due to M and F_{boost} ($F_{boost} = 0$ for pure bending).

From elementary solid mechanics [48], the axial elastic stress during unloading (springback) is

$$\sigma_1^e = \frac{M(R_{NA}^e - r_b^e)}{A_{cs} \cdot r_b^e \cdot (r_c^e - R_{NA}^e)} + \frac{F_{boost}}{A_{cs}} \tag{3.46}$$

with the variables defined in the nomenclature section.

(3.46) is a general curved beam formula for elastic bending, and assumes that the cross-section of area remains plane during bending, and that the material is isotropic.

In the local $x_1x_2x_3$ system, the elastic hoop stress can be approximated using the same method as in Section 3.1.1. To start the calculation, two average (effective) axial stresses are

calculated instead of strains, since σ_1^e is already known by (3.46). Similar to before, one calculates two stress-averages for the tensile and compressive region, from (3.46). In particular, an average $\sigma_1^{e,b}$ and $\sigma_1^{e,a}$ is used instead of ε_1^b and ε_1^a, as in (3.5) and (3.6). In the same way as before, one solves for the elastic hoop strain ε_{hoop}^e using (3.9) - (3.12). Note that E is constant this time, and replaces E_s^b and E_s^a. Once the two average elastic hoop strains are calculated, the same transition function *f* is used as before at the transition angle for the elastic stresses, α_{NA}^e.

With elastic hoop strain calculated, and treating it as a through-thickness average, one can proceed to solve for σ_2^e at each point in the cross-section, using the three-dimensional Hooke's Law expression (3.47), with $\sigma_3 = 0$:

$$\sigma_2^e \cong \varepsilon_{hoop}^e \cdot E + \nu\sigma_1^e \tag{3.47}$$

and also from Hooke's Law, the axial elastic (engineering) strain is

$$\varepsilon_1^e \cong \frac{1}{E}(\sigma_1^e - \nu\sigma_2^e) \tag{3.48}$$

Thus, the residual stress is

$$\sigma_{ij}^{res} = \sigma_{ij} - \sigma_{ij}^{e} \tag{3.49}$$

in the local $x_1x_2x_3$ system.

After springback, the original centerline radius R_{co} becomes R'_c. The inside radius (at $\alpha = \pi$) becomes $R'_c - d/2$, and the outside radius (at $\alpha = 0$) becomes $R'_c + d/2$, after springback. Also, the tube springs back to a new bend angle θ', from original angle θ_o. Therefore, one can formulate the following expressions to solve for R_{co} and θ_o, based on the changes in arc length on the inside (compressive) side of tube and the outside (tensile) side of tube, respectively

$$(R_c^{'} - \frac{d}{2}) \cdot \theta^{'} = \{(R_{co} - \frac{d}{2}) - (R_{co} - \frac{d}{2}) \cdot \varepsilon_1^{e}(\alpha = \pi)\} \cdot \theta_o \tag{3.50}$$

$$(R_c^{'} + \frac{d}{2}) \cdot \theta^{'} = \{(R_{co} + \frac{d}{2}) - (R_{co} + \frac{d}{2}) \cdot \varepsilon_1^{e}(\alpha = 0)\} \cdot \theta_o \tag{3.51}$$

where $\varepsilon_1^e(\alpha = \pi)$ corresponds to the axial elastic strain at $R = R_{co}$-$d/2$, and $\varepsilon_1^e(\alpha = 0)$ corresponds to the axial elastic strain at $R = R_{co}$+$d/2$, after forming, and is determined from (3.48). In the program, one inputs the *desired* centerline radius R'_c and bend angle θ' *after* springback and use (3.50), (3.51) to calculate the *initial* centerline bend radius and bend angle, R_{co} and θ_o, such that after springback one obtains these desired dimensions.

Chapter 4- Finite Element Pre-bend and Hydroform Numerical Models

4.1 FE Bend Model

A numerical (FE) model of the bending operation was developed which utilizes an explicit dynamic finite element formulation. The LS-DYNA v970 code was used to perform the numerical pre-bend (and hydroforming) simulations.

Figure 4.1 shows an illustration of the mesh used in the bend model for $R_c/d = 2.5$. The model uses a half-symmetry shell-mesh, since the operation is symmetric about the bending plane. Thin shell elements, with 28 integration points (four in-plane and seven through-thickness), were used to model the tube geometry. Rigid shell elements were used to discretise the geometry of the tools. Beam elements and numerically formulated spherical joints were used to model the movement of the mandrel balls. After the bend simulation, a static implicit springback simulation is performed on the tube. An iterative approach was used to determine an angle to which the tube was bent such that the final included angle, after springback, was as

close as possible to 90º. This precision was required for a good fit in the hydroform die for the secondary forming simulation.

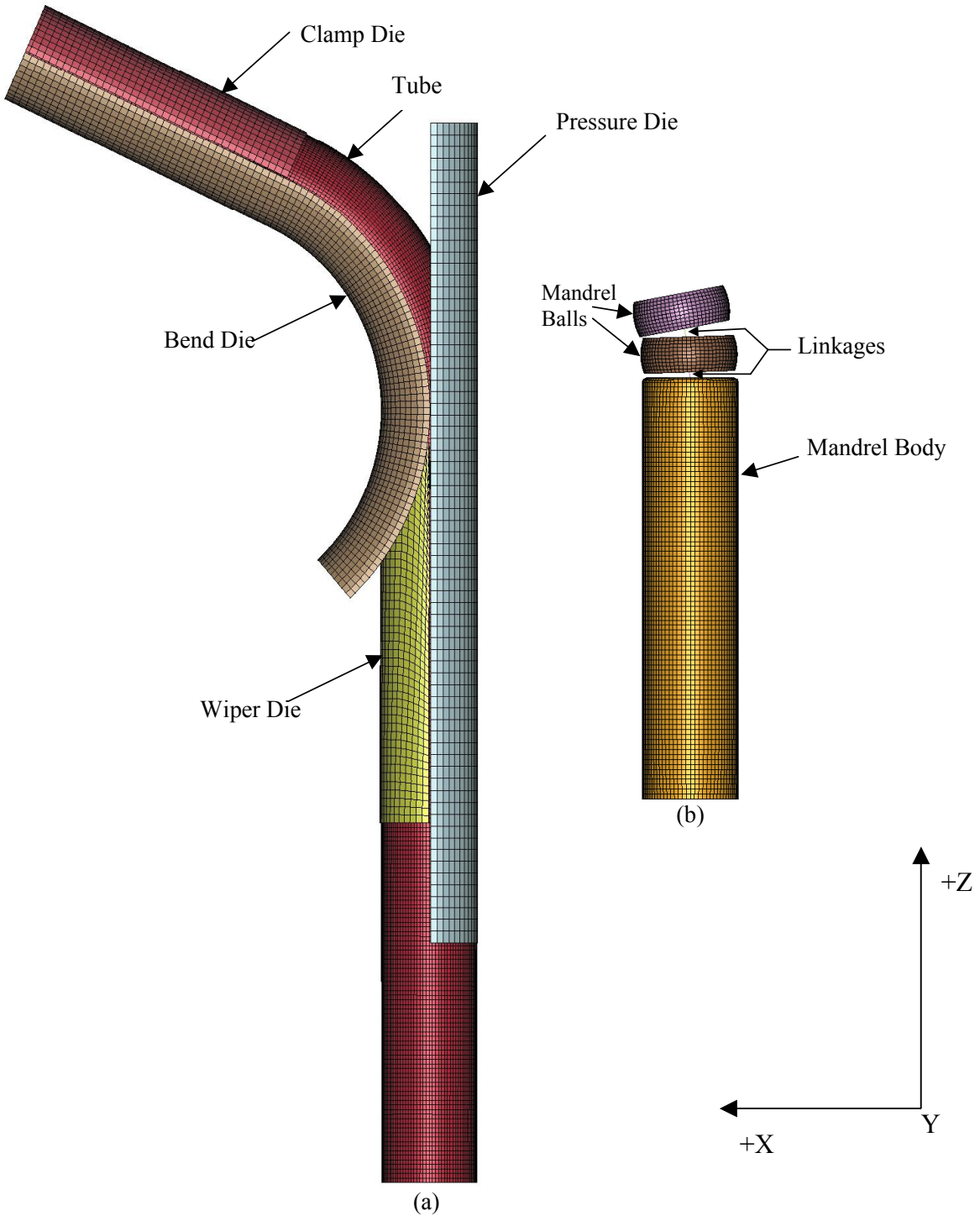

Figure 4.1: FE mesh of the bend tooling and tube, for half-symmetry (Dyment [43])

(a) External geometry (b) Internal geometry

The material-hardening characteristics of the tube were modeled with a power law equation. The K and n values given in Section 2.2 (Table 2.1) were adopted in the FE models.

In LS-DYNA, the contact between the tooling and the tube was modeled with the *CONTACT_FORMING_ONE_WAY_SURFACE_TO_SURFACE card. This enforces a penalty function-based contact stiffness to prevent penetration of the tooling by the tube nodes. Prescribed Coulomb friction was used to model the friction between tools and tube. The friction coefficients are summarized in Table 4.1. An improvement on the friction modeling can be realized once on-going twist compression tests are completed on the tube and tool materials [39].

Contacting Surfaces	Friction Coefficient
Tube - Bend Die	0.06
Tube - Pressure Die	0.25 (dry)
Tube - Clamp Die	0.60
Tube - Wiper Die	0.06
Tube - Mandrel Body	0.06
Tube - Mandrel Balls	0.06

Table 4.1: Friction Coefficients in the FEA model for $R_c/d = 2.5$

The tooling motion was modeled so as to be similar to the tool motion prescribed in the experiments. Time scaling was adopted in the simulations, in which the tooling velocity was increased to reduce run-time, such that the total simulation time was 10 ms. Care was taken to avoid inertial effects.

In the model, translational motion was prescribed for the mandrel assembly and the pressure die boost, using linear displacement control. Similarly, for the bend die and clamp die,

angular displacement (rotational) motion was prescribed during the course of the bend. For the pressure die clamping force, load control was prescribed in the +X-direction. For every boost case (except NB100), the nodes at the back of the tube were given the same Z-direction translation as the pressure die. This mimics the boost block and ensures no slip between the pressure die and tube. For the NB100 case, the nodes were not given the same displacement as the pressure die, and the tube was pushed by friction with the pressure die alone, as in the actual NB100 experiments. All the load curves shown below, for the FE bending, are for the ME100 case, with $R_c/d = 2.5$.

Between 0 and 2 ms, the pressure die closes on the tube, in the +X-direction, and maintains a clamping force of 66,700 N for the remainder of the bend (Figure 4.2). As well, between 0 and 2 ms, the clamp die moves in the +X-direction and closes over the tube with 0.1 mm over-close (Figure 4.3); this means that the clamp die closes 0.1 mm beyond the point where it just contacts the tube (the tube and clamp die are initially 1.0 mm apart). The clamp die maintains this over-close for the remainder of the bend

Figure 4.4 and 4.5 show displacement and velocity curves for the bend tooling motion. Starting at 2 ms, the clamp and bend die rotate together as one piece, counterclockwise, about the Y-axis, and the pressure die moves in the +Z-direction. At the intermediate bend angle $\theta = 75^{\circ}$ (at simulation time equal to 8.2 ms), the mandrel body starts to retract in the negative Z-direction reaching a final displacement of Z = -70 mm, at the end of the bend run-time of 10 ms (Figure 4.6). This mandrel retraction is used to help “iron” out wrinkling due to bending, as used in the experiments.

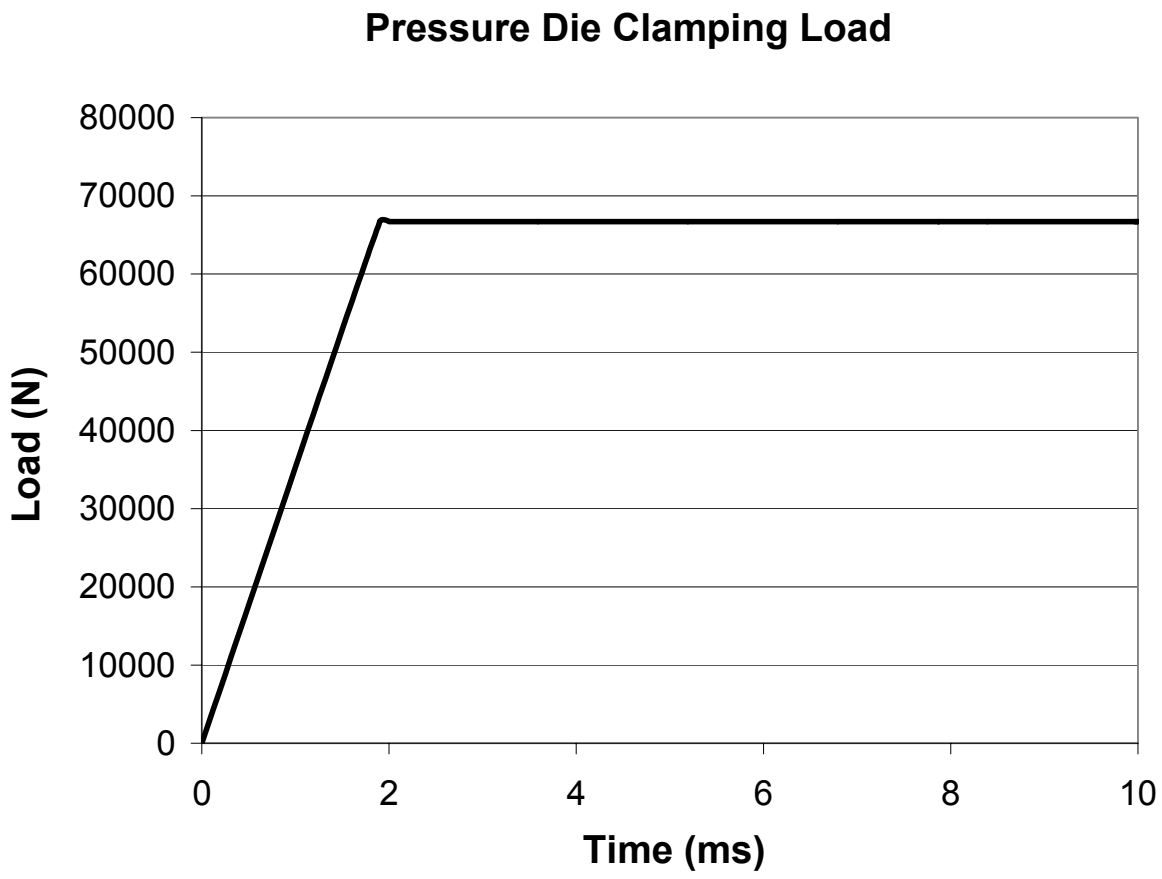

Figure 4.2: Pressure die clamping force

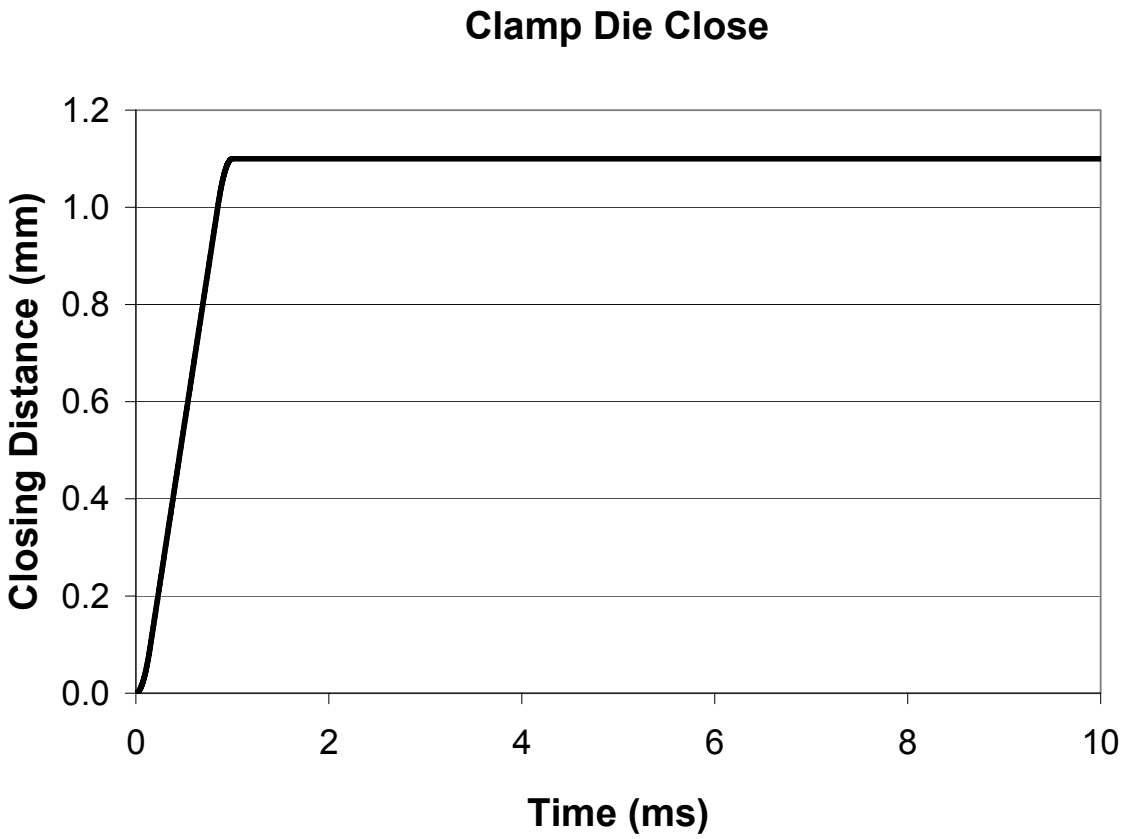

Figure 4.3: Clamp die closing

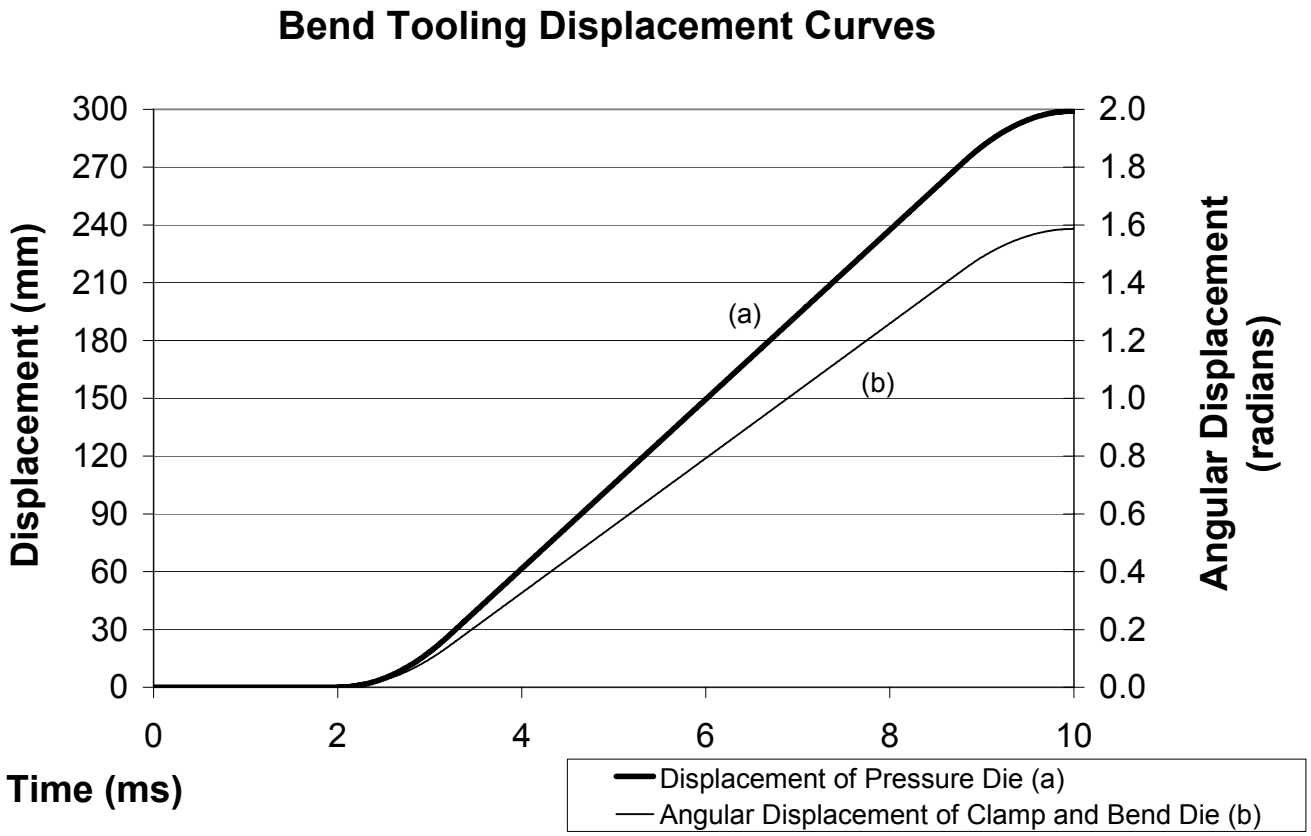

Figure 4.4: Displacement curves for Pressure Die, Bend Die and Clamp Die

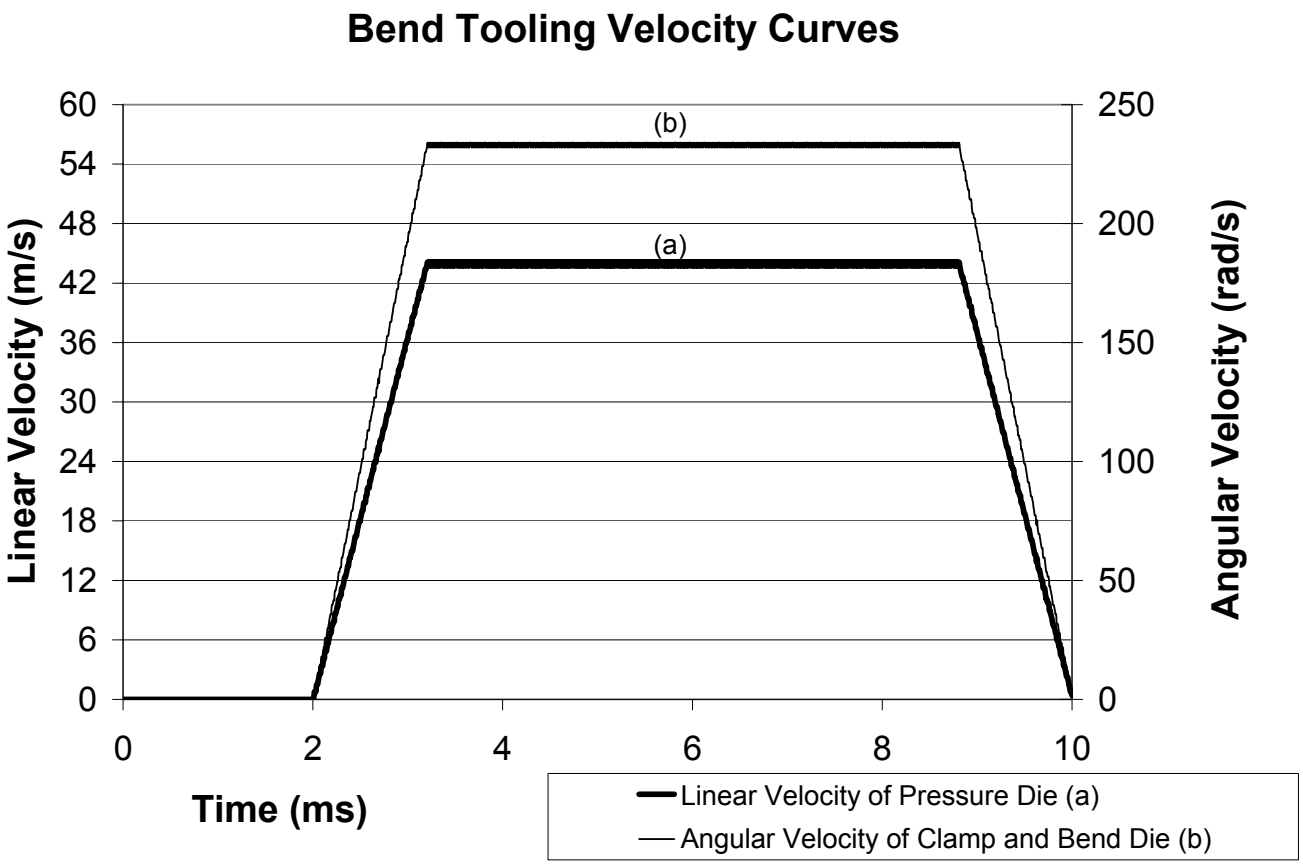

Figure 4.5: Velocity curves for Pressure Die, Bend Die and Clamp Die

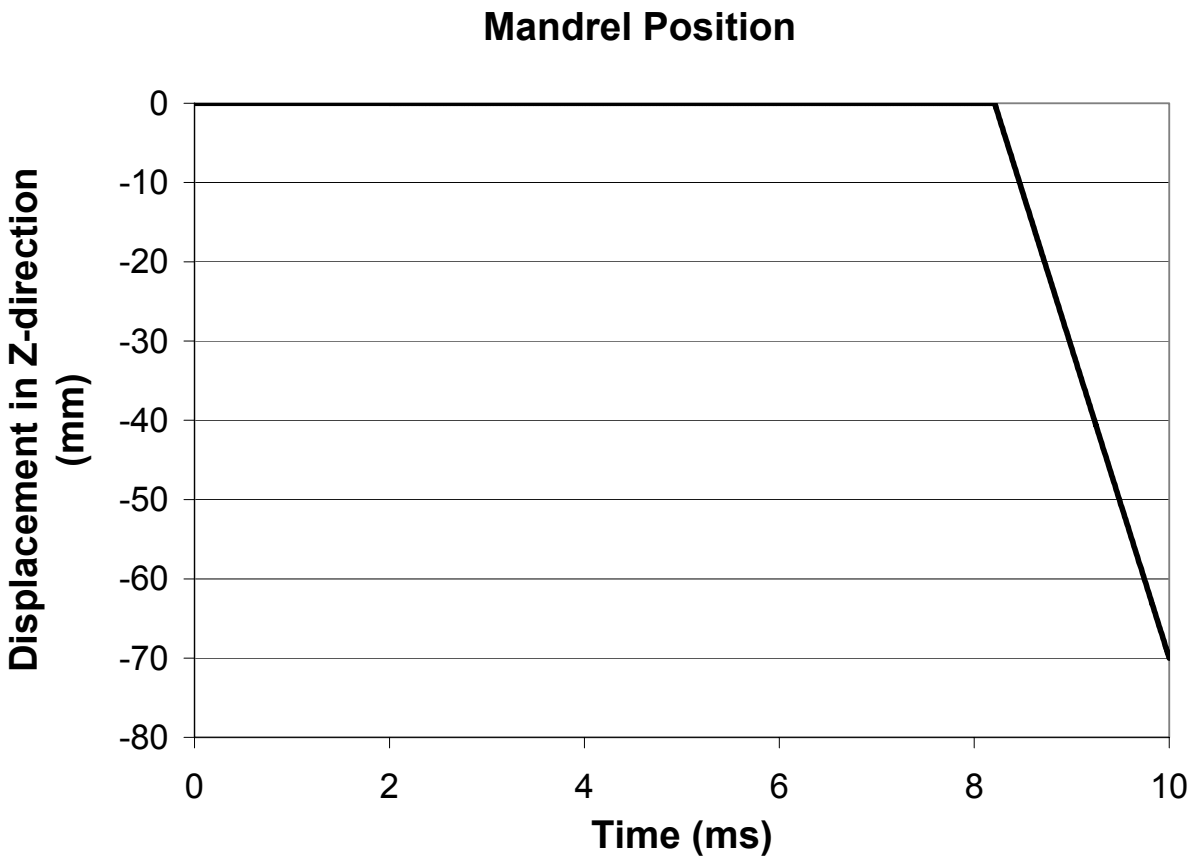

Figure 4.6: Mandrel position

Typically, in explicit dynamic models, a run time in the order of milliseconds (ms) is used. This effectively speeds up the runs and greatly reduces computation time. In so doing, artificial dynamic effects can be created, due to large workpiece and tooling velocities and accelerations, resulting in an overestimate of the tooling forces, predicted by the numerical models. These artificial dynamic effects must be accounted for and controlled, to avoid un-realistic vibration and "chattering" effects and an over-prediction of the tooling forces involved. The prescribed simulation time is 10 ms, roughly 1000 times faster than the real experimental time. Ongoing studies by Dyment [43] and Bardelcik [39] are addressing proper control of inertial effects. Further elaboration of the FE bend models, is presented by Dyment [43].

4.2 FE Hydroforming Model

A FE hydroforming model was developed that could accept pre-bend results from either the analytical or finite element pre-bend simulations. In other words, the analytically calculated residual stresses, strains, and thickness values, were used as initialization values, for the pre-bent tube, prior to the secondary forming operation (consisting of die closing and hydroforming). The FE-calculated residual stresses, strains, and thickness values, generated by the LS-DYNA bending and springback simulation, can also be used as initialization values prior to the same secondary forming operation. These simulations were developed to allow comparison between the hydroforming predictions obtained from both pre-bend simulation approaches.

In the numerical hydroforming operation, the die geometry consists of a teardrop shaped cross-section that is swept around the bend, as shown in Figure 4.7 and 4.8. This die configuration allows the outside of the tube, which is the thinnest region after bending, to undergo the greatest expansion. The same contact definition as in the numerical bend model is used in the hydroforming simulation, to enforce contact between the tube and hydroforming die. The Coulomb friction coefficient acting between the tube and die was prescribed as 0.08. All of the load curves shown below, for the FE hydroforming, are for the ME100 pre-bend case, with $R_c/d = 2.5$

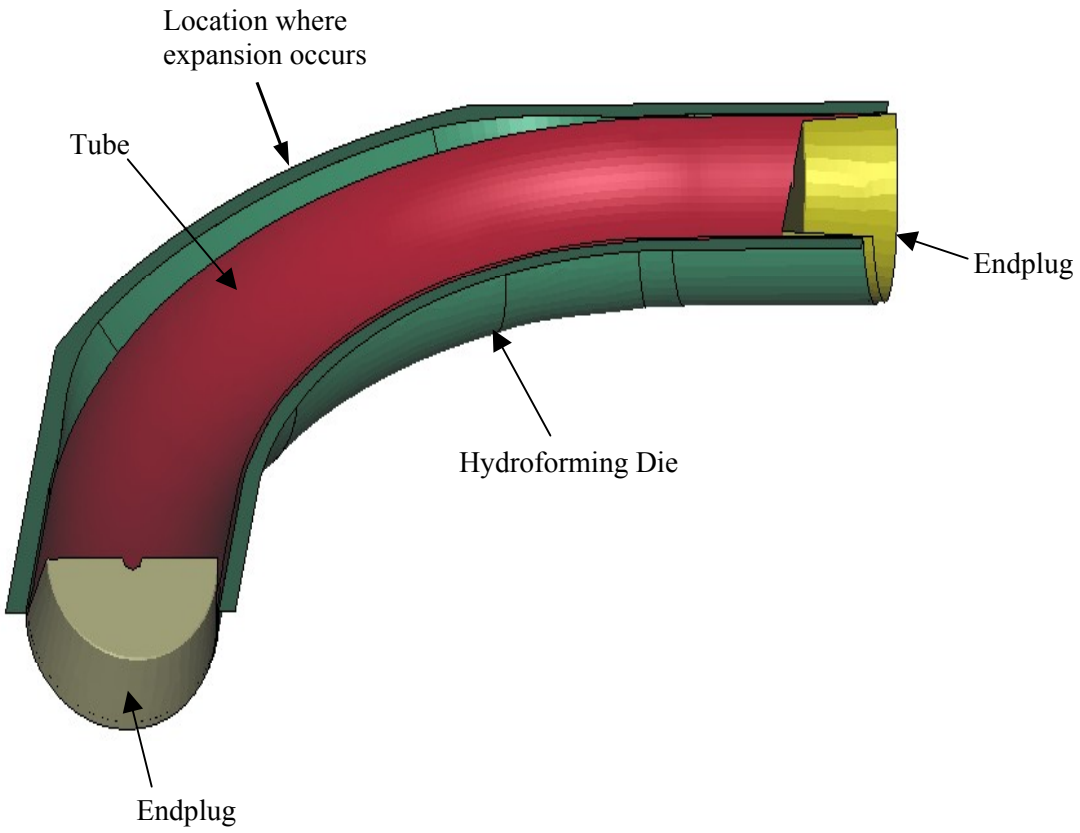

Figure 4.7: FE hydroforming half-symmetry geometry

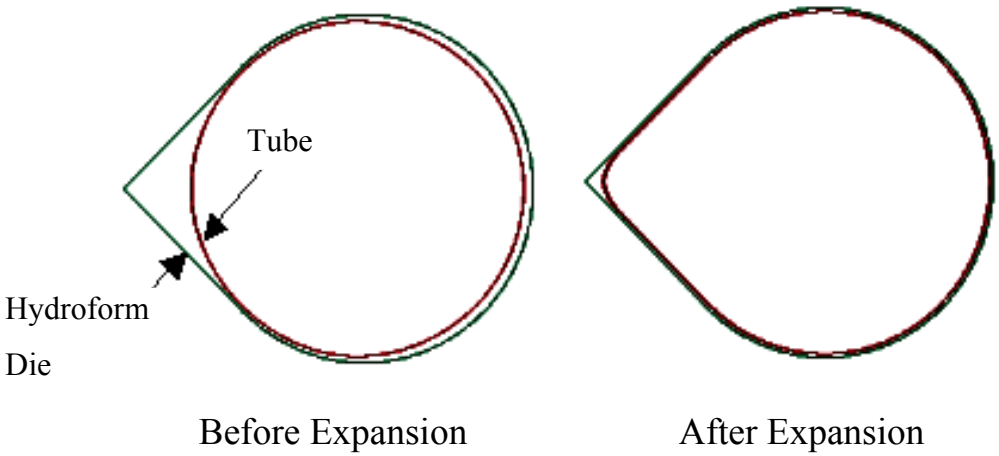

Figure 4.8: Cross-section of hydroforming die

The end plugs shown in Figure 4.7 are for illustration purposes only; in the actual simulation the end plugs were removed. The difficulty in using the end plugs in the simulation is that the nature of the edge contact between plug and shell elements is poorly captured numerically. To correct this, the end plugs were removed and replaced with a 60 kN nodal (sealing) force applied on the end nodes (matching the experimental sealing force applied to each end plug prior to hydroforming). In addition, an initial internal restraining pressure of 1 MPa was applied on the tube elements located in the vicinity of the end plugs, on the straight region of the tube (Figure 4.9). This sealing force plus 1 MPa pressure was applied simultaneously in the initial 1 ms of the hydroforming simulation. The combination of pressure and sealing force is a good artificial means of preventing buckling of elements nearest to the nodes for which the nodal sealing force is applied. Figure 4.10 shows the loading curves for the initial 1 ms.

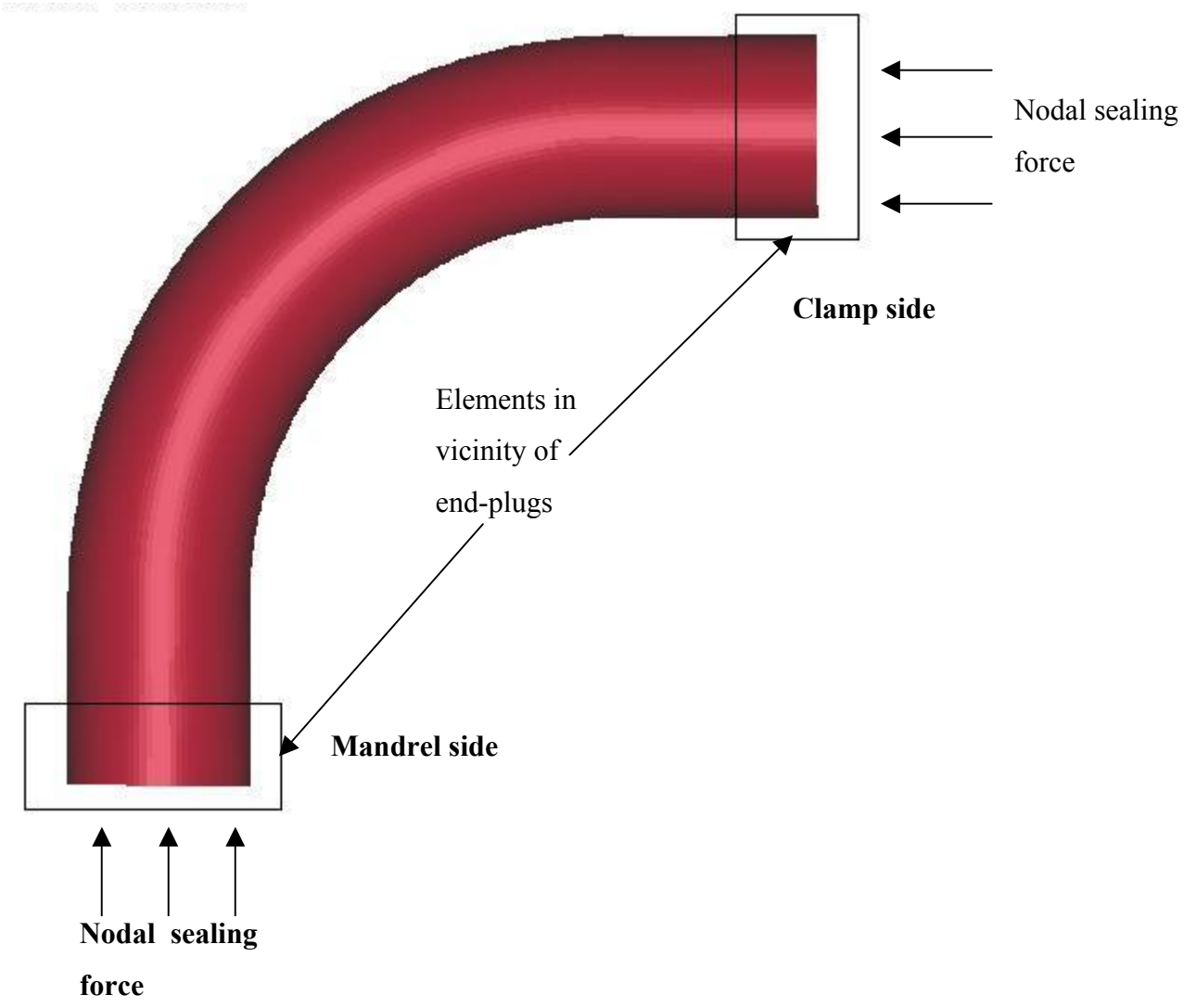

Figure 4.9: Schematic of sealing force and elements to which 1 MPa pressure is applied, in initial 1 ms

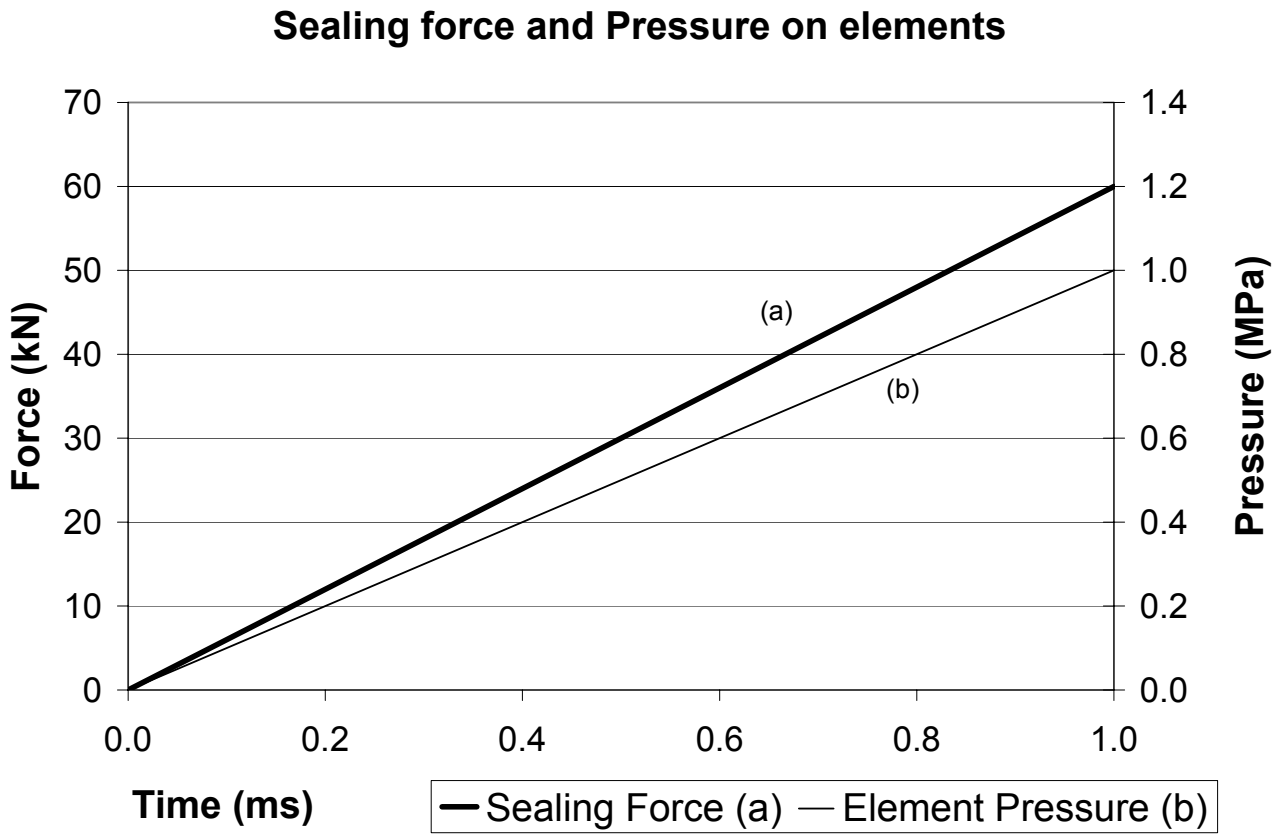

Figure 4.10: Initial sealing force and element-pressure curves

During the initial 1 ms, the sealing force forces the tube to settle into the die, as in the experiments. At the end of 1 ms, the 1 MPa pressure loading condition and the 60 kN nodal sealing force is replaced with internal pressure and displacement boundary conditions, as prescribed in the experiments. For $t \geq 1$ ms the nodes at the tube end are given a nodal displacement equal to the experimental end-feed displacements, for the plugs on the clamp and mandrel side. The experimental measurements are from a representative ME100 case (starting at the experimental time of $t = 0$). Additionally, for $t \geq 1$ ms the internal pressure is ramped up using the experimentally measured pressure curve for the same ME100 case (again, starting at the experimental time of $t = 0$). This allows for comparison between simulation and experiment. Figure 4.11 shows the experimental loading curves, used as model input, for $t \geq 1$ ms.

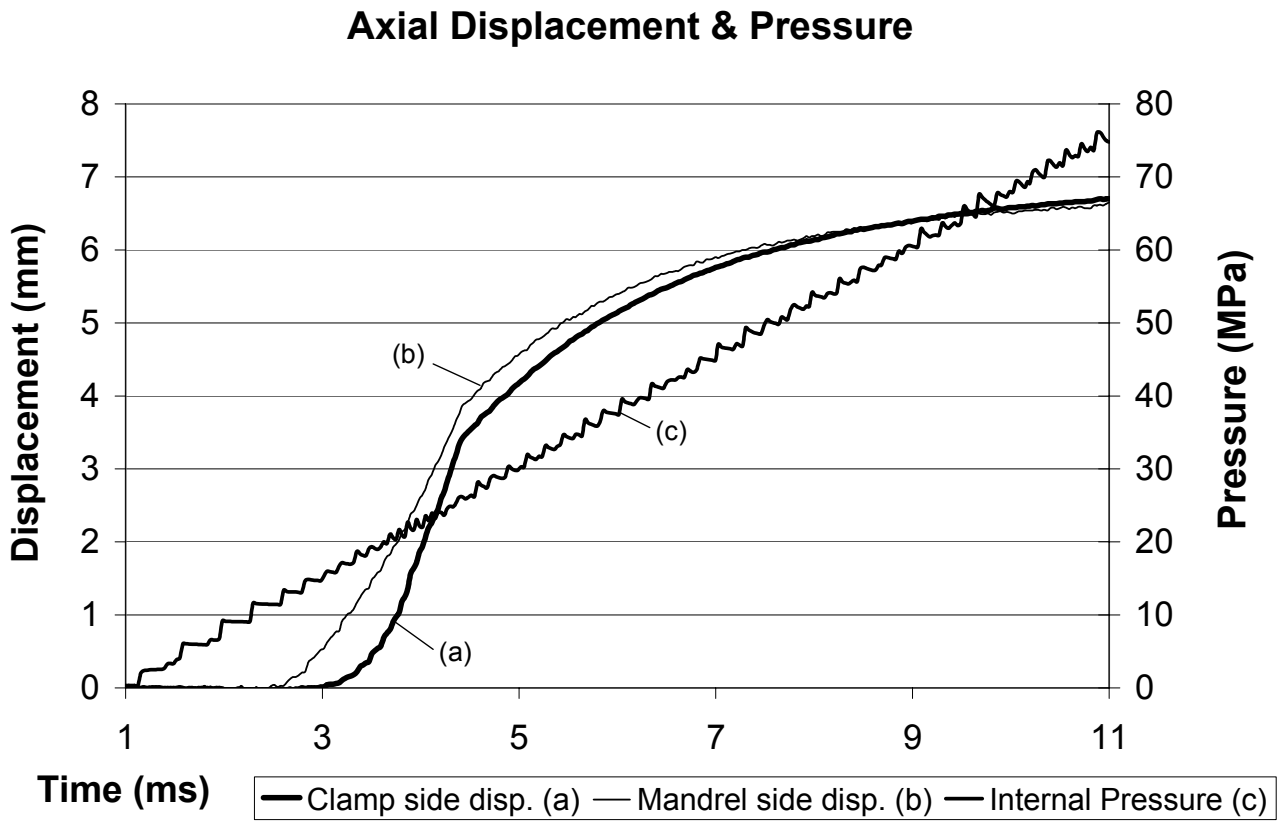

Figure 4.11: Axial end-feed and internal pressure curves

Chapter 5- Results

This chapter presents results from the bending experiments and models. Both analytical and numerical (FEM) simulations of bending are presented and compared with experiments and each other. Selected hydroforming experiments are also examined to demonstrate the effectiveness of combining analytical bend models with finite element (FE) models of hydroforming.

5.1 Bending Strains and Thickness

In the experiments, three boost cases were tested: LE95, ME100 and NB100 (for R_c/d = 2.5), as summarized in Table 2.2. A higher percent boost case could not be achieved in the experiments, but was modeled analytically and numerically. This case was designated HE105, with a boost level of 105%. The analytical predictions for the HE105 case can only be compared to the numerical (FE) results, since no experimental data is available for this higher boost case. Most of the bending comparisons in this chapter are for R_c/d = 2.5. There is a brief comparison between models and experiment for a sharper bend, R_c/d = 2.0 with 100% boost, presented in Section 5.1.6.

All strain and thickness data was measured along the same regions shown in Figure 2.10, after bending and hydroforming. Note that measurements along the inside of the bend correspond to $\alpha^* = 90^o$, and measurements on the outside correspond to $\alpha^* = 270^o$.

Table 5.1 summarizes the conditions during bending, including slip between tube and pressure die, and slip between tube and clamp die. In the experiments, the slip was recorded after each test, and the average values are shown. The transient slip over time was not recorded, only the final (total) slip at the end of the bend was recorded. Table 5.1 also shows the measured percent boost, which is the actual boost maintained by the pressure die during the bend.

	Average Experimental Results			Numerical Results		
Boost Condition	Clamp Die slip (mm)	Pressure Die slip (mm)	Measured Boost (%)	Clamp Die slip (mm)	Pressure Die slip (mm)	Measured Boost (%)
100% Boost (ME100)	0.6	0.0	99.6	0.1	0.0	100.0
95% Boost (LE95)	1.2	0.0	95.4	0.1	0.0	95.0
100% No Boost Block (NB100)	1.7	16.5	100.3	2.4	5.8	100.0

Table 5.1: Slip and boost for experimental and numerical results

If the pressure die slips relative to the tube, then its displacement in the Z-direction (Figure 2.5) is not representative of the actual travel of the tube, feeding into the bend. Therefore, in the presence of pressure die slip, one must calculate the "effective" boost based on the recorded (total) slip value. This is discussed in detail in Appendix A.11. As it turns out, only the NB100 test case experienced tube slip relative to the pressure die. There was 16.5 mm (average) relative slip between the tube and pressure die in the experiments; that is, the pressure die traveled 16.5 mm further than the back of the tube during bending. Using the calculation method in Appendix A.11, the effective boost of the tube turned out to be ~94.5%. Effectively, this boost level for the NB100 case is quite close to that for the LE95 case.

5.1.1 LE95 Boost Case

Figure 5.1 plots the measured and predicted strains and thickness around the tube circumference at the $\theta^* = 45^\circ$ section in the middle of the bend (Figure 2.10). The data shows the axial and hoop strains as well as the measured thickness. The analytical predictions correspond to axial and hoop strains, and thickness (which the model outputs directly). The experimental and numerical predictions, however, are of major and minor principal strains in the plane of the tube outer surface. Away from the neutral axis, in the tensile region of the bend (roughly 180 – 360º), the major strain will correspond to the axial strain while the minor strain corresponds to the hoop strain. In the compressive region (roughly 0 – 180º), this correspondence is reversed. The distinct regions of strain are labeled as "axial" and "hoop", as indicated in the figures.

The greatest degree of error between analytical and experiment is in the transition region where axial and hoop strain change sign, as shown in an enlarged view in Figure 5.2 for the LE95 case. In the experiments and numerically, the axial and hoop strain "jump" from one sign to the other. In the analytical model the axial and hoop strain are made to pass through zero with a smooth transition. Physically, the jump in strains is due to large shear strains present at the neutral axis, that are not accounted for in the analytical model. In the regions away from the neutral axis, however, the analytical model compares well to both experiment and FE predictions, especially in the fully developed part of the bend where "steady" values of strain are reached in the longitudinal (θ^*) direction.

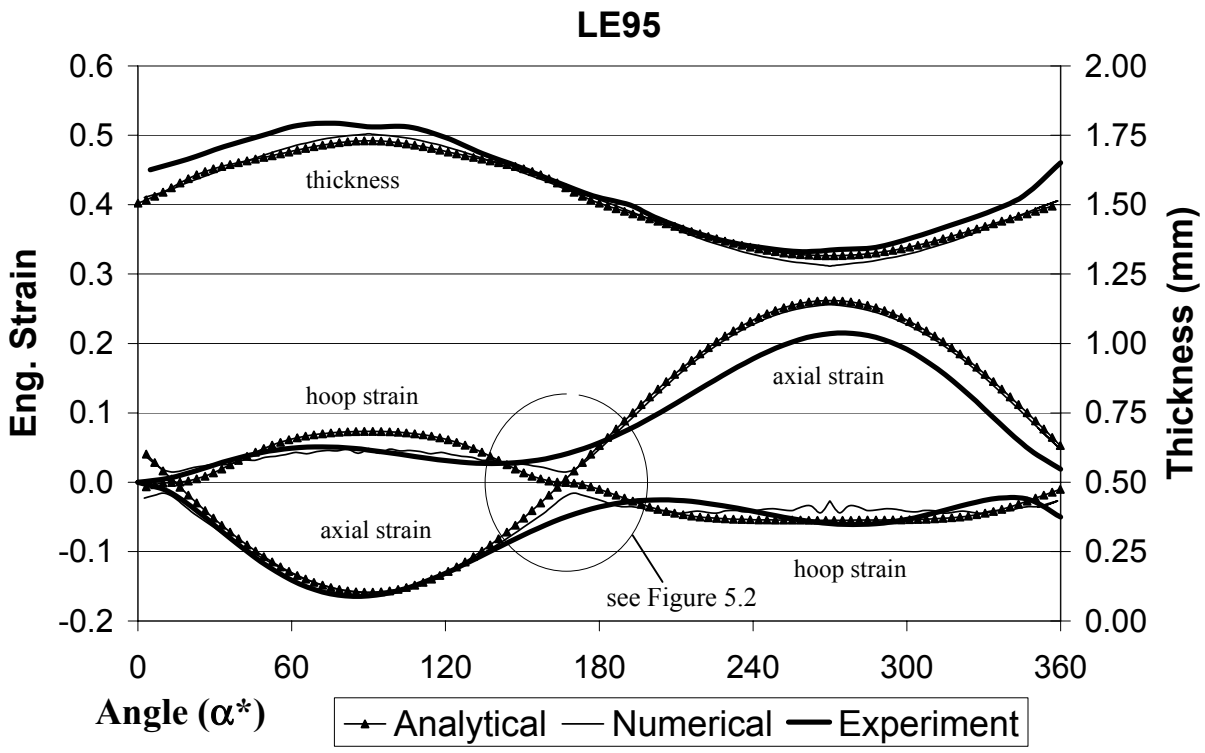

Figure 5.1: Strain and thickness comparison for LE95 at 45º location

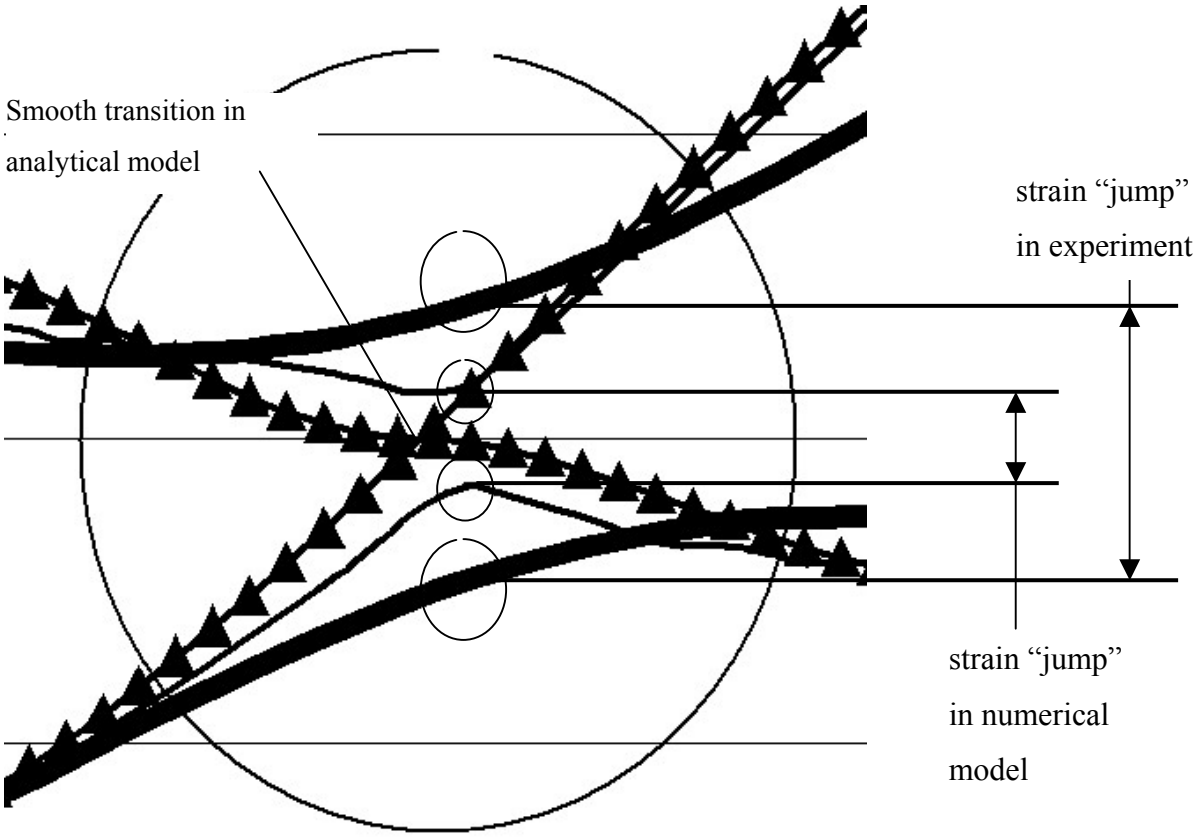

Figure 5.2: Enlarged view of transition region for LE95 case

Figure 5.3 and 5.4 show the strain distributions along the inside and outside of the bend region. On the outside of the bend (Figure 5.4) there is a thickness "spike" or region of thinning outside of the bend region at roughly $\theta^* = 92^\circ$. This spike was attributed to excess clamping force exerted by the clamp die and is not captured by either model. Strain measurements were only taken within the range $0 - 90^\circ$, and therefore do not exhibit a strain spike corresponding to the thickness spike.

Overall, there is good agreement between the experimental and numerical curves, especially in capturing the trends within the bend region (in the θ^* direction). The analytical

model does capture the level of bending strain and thickness-change relatively well in the fully developed part of bend. In the transition regions, where the thickness-change and strains decay to zero, the analytical model is empirically fit to match the decay seen in the numerical and experimental curves.

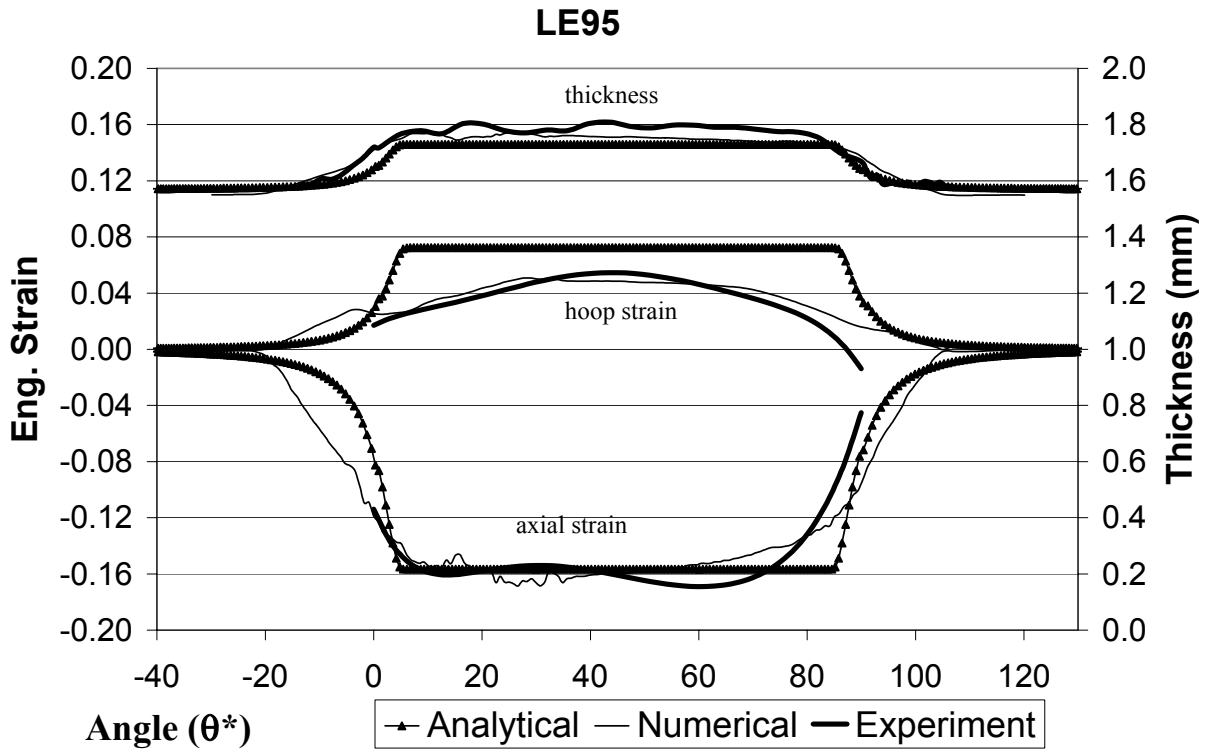

Figure 5.3: Strain and thickness comparison for LE95 on inside of bend

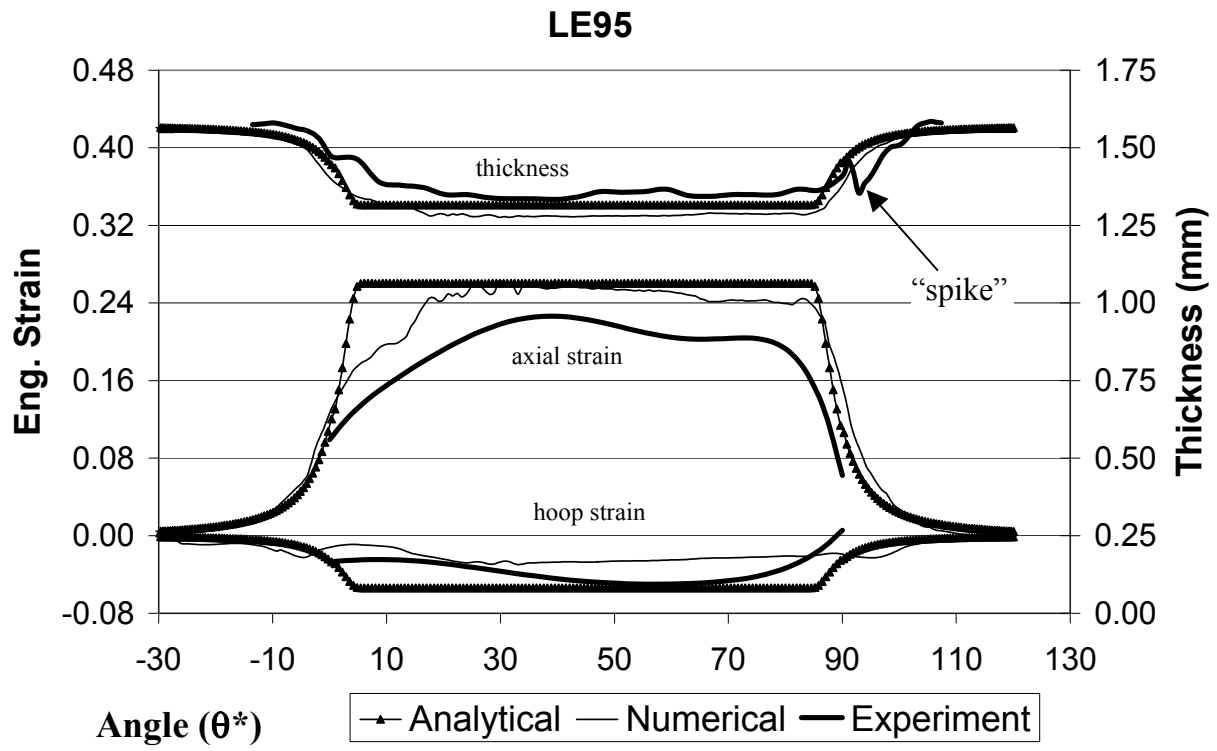

Figure 5.4: Strain and thickness comparison for LE95 on outside of bend

The data plotted in Figure 5.1 – 5.4 corresponds to "average" curves based on experimental measurements from three different tubes. The actual degree of scatter present in the data can be seen in Figure 5.5, which plots measurements from all three LE95 tubes. From the figure, it can be seen that the level of scatter is roughly 5% strain. The "average" curves are also plotted and are seen to capture the trends well. Only one tube for each boost case was measured for thickness, however, since the variation in thickness measurement between test-samples is typically much less than for strains.

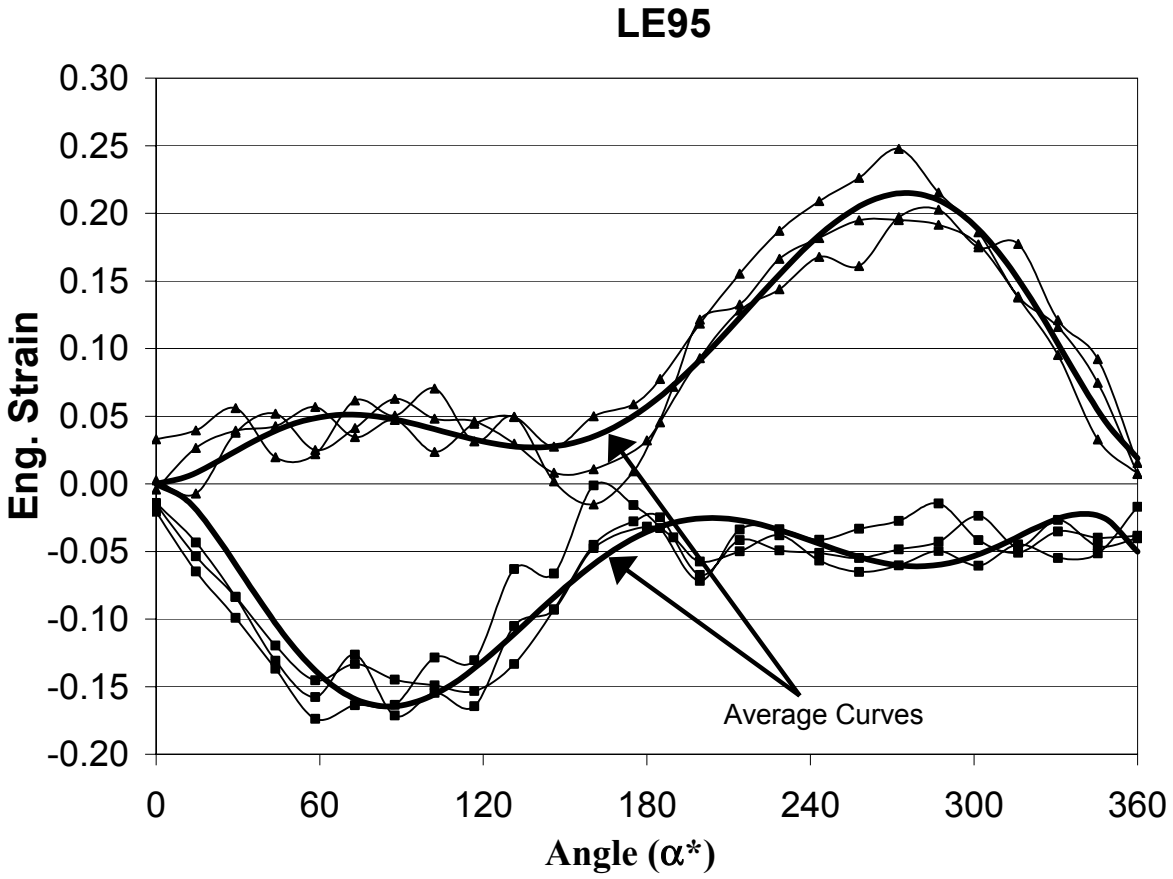

Figure 5.5: Variation in experimental measurements taken around circumference. LE95 tubes.

5.1.2 ME100 Boost Case

Figure 5.6 shows the strain and thickness distribution at the middle of the bend ($\theta^* = 45º$) for the ME100 boost case. The agreement between the predictions from the analytical and numerical models, and experiment is superior to that seen for the LE95 case, especially in the tensile (positive) axial strain region (180 – 360º). There is a downward "shift" in the axial strain relative to the LE95 case, and an upward shift in the thickness curve. This shift is due to the

greater compressive axial membrane strain component, as boost increases. The effect of boost level is discussed in greater detail in Section 5.1.5, below.

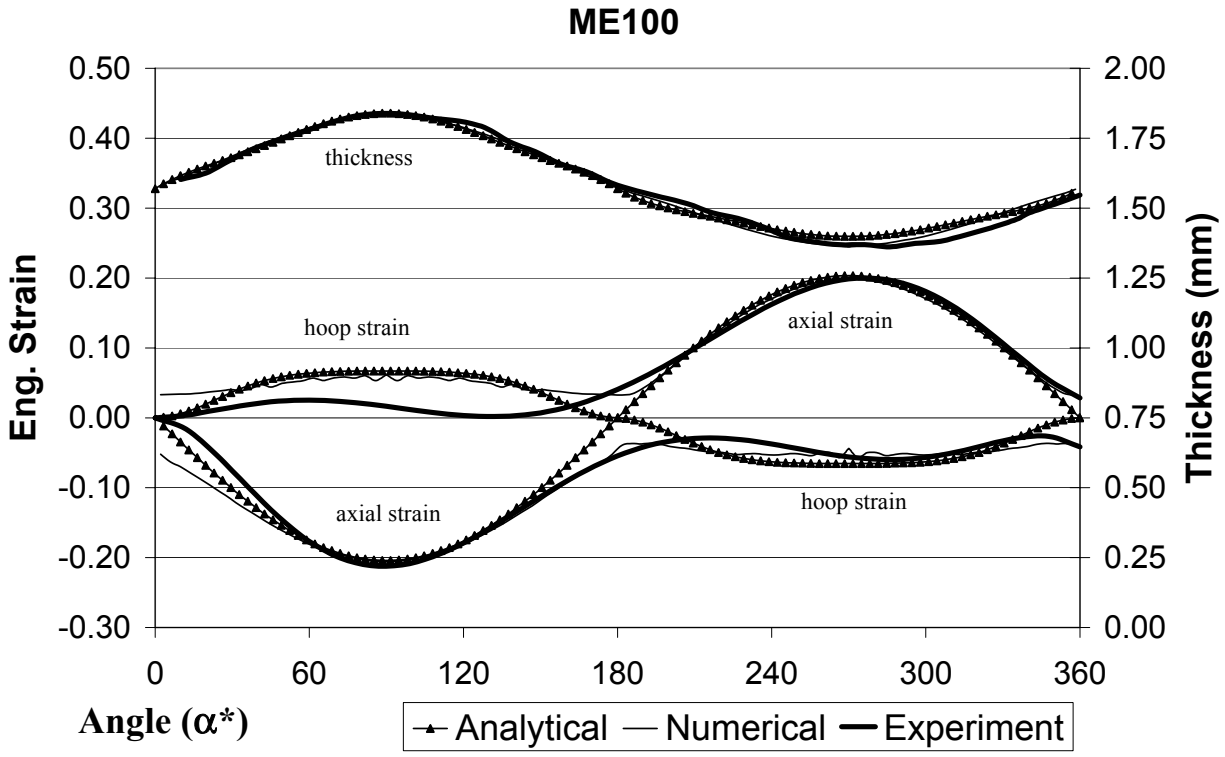

Figure 5.6: Strain and thickness comparison for ME100 at 45º location

Figure 5.7 and 5.8 show strain and thickness distribution along the bend direction. Good agreement between experiment and models is shown. A thickness spike does not appear in Figure 5.8 since the experimental measurements in this case was only taken from 0 – 90º. An independent study, measuring strains, was performed in the clamp region of the tubes for the LE95, ME100, and NB100 boost cases and it was discovered that a strain spike indeed exists for both the LE95 and ME100 cases. This spike is less profound for the NB100 case. This defect is discussed in greater detail in a related study by Dyment [43].

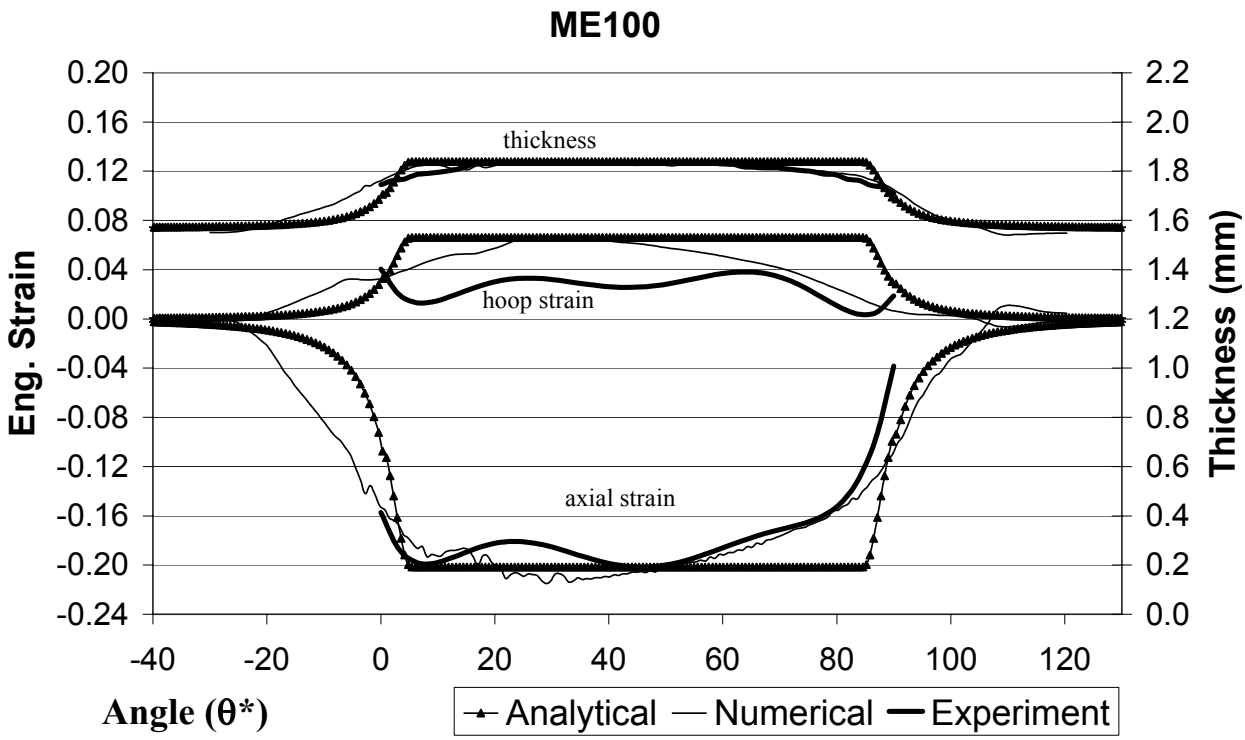

Figure 5.7: Strain and thickness comparison for ME100 on inside of bend

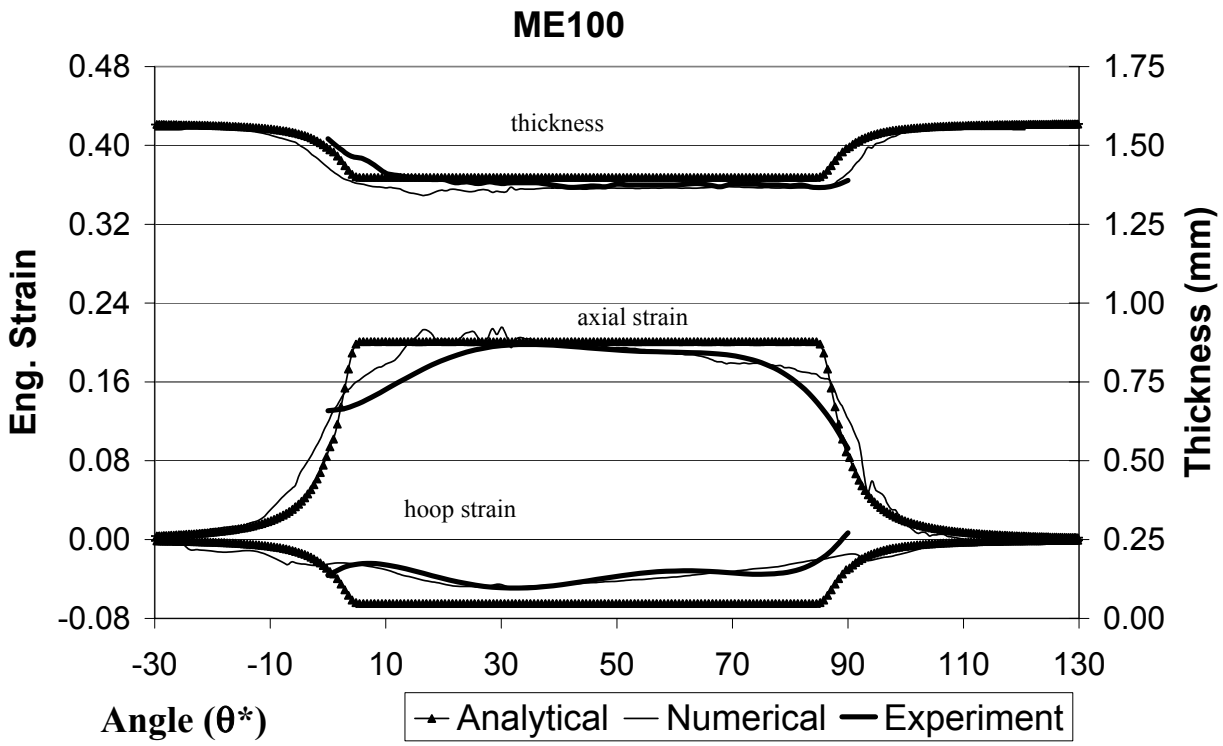

Figure 5.8: Strain and thickness comparison for ME100 on outside of bend

5.1.3 HE105 Boost Case

Figure 5.9, 5.10 and 5.11 show plots for the theoretical higher boost case of 105%, which could not be achieved experimentally. There is very good agreement between the analytical and numerical curves, except in the transition region. The compressive membrane strain component is highest for this case, meaning that graphically the axial strain curves are shifted downward from the ME100 and LE95 cases, and the resulting thickness curves shift upward.

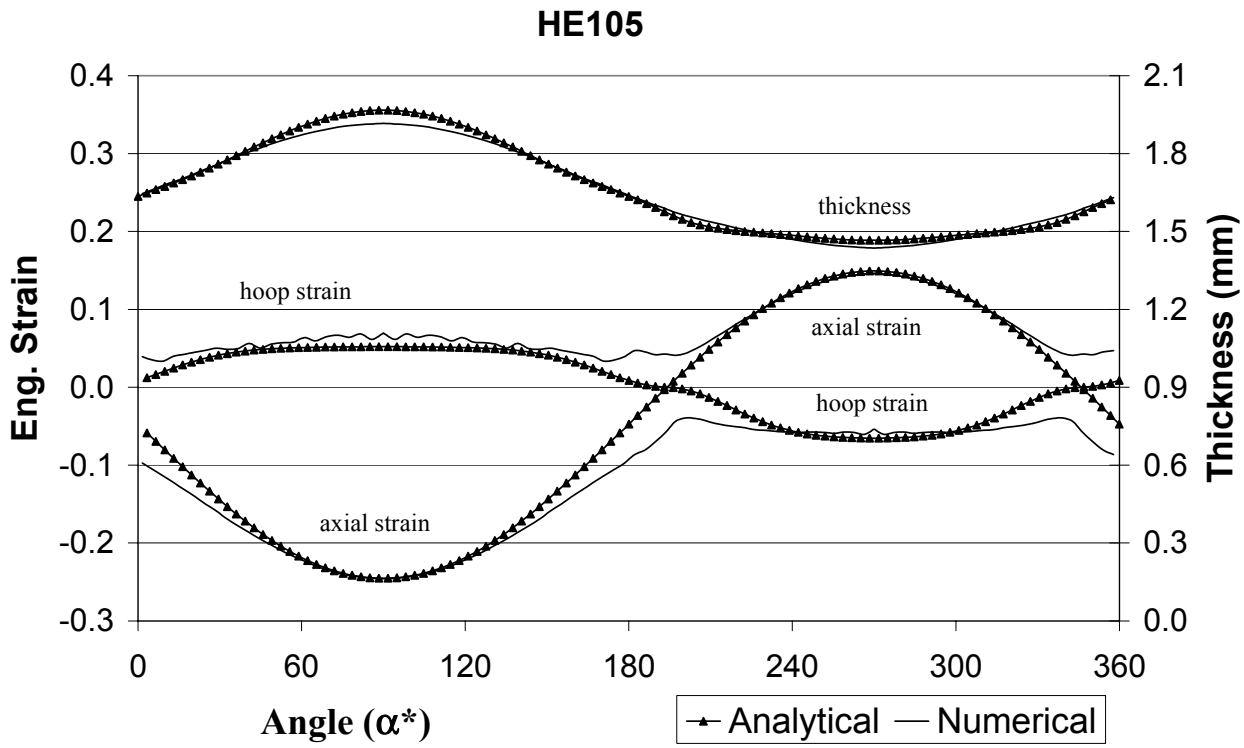

Figure 5.9: Strain and thickness comparison for HE105 at 45º location

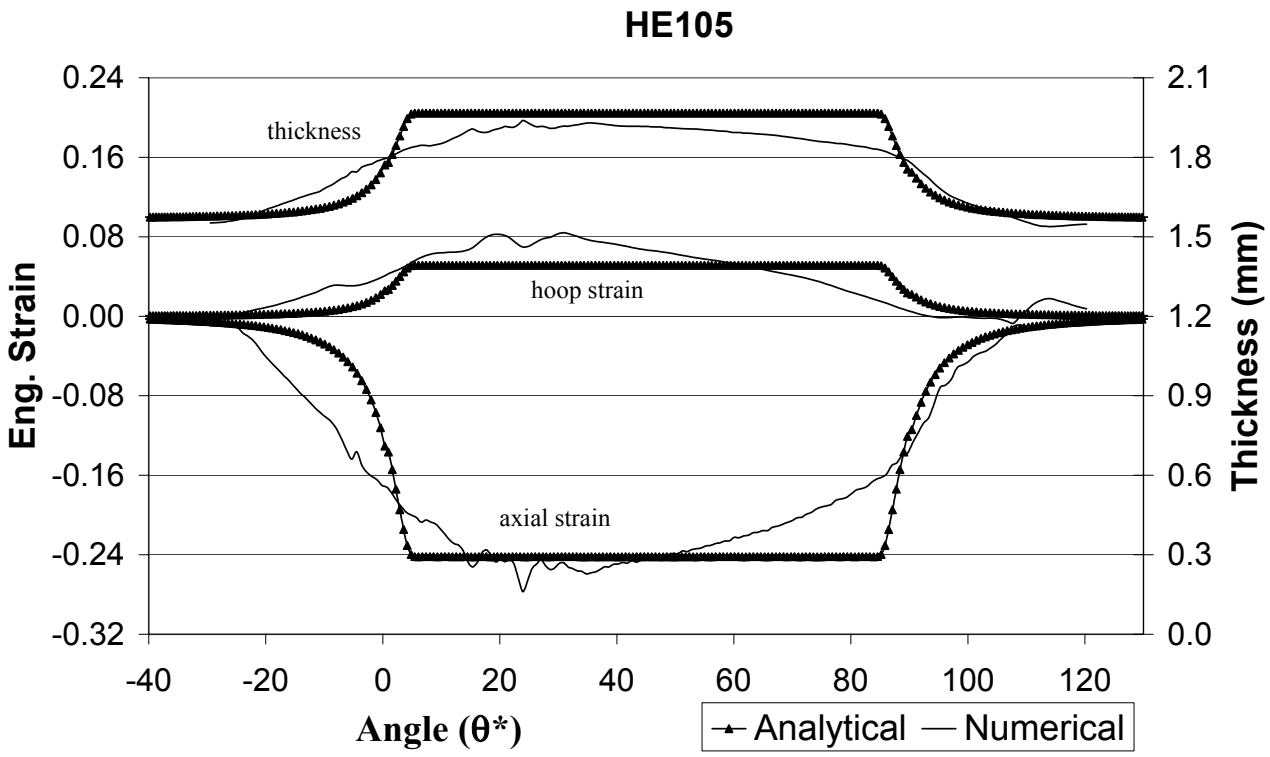

Figure 5.10: Strain and thickness comparison for HE105 on inside of bend

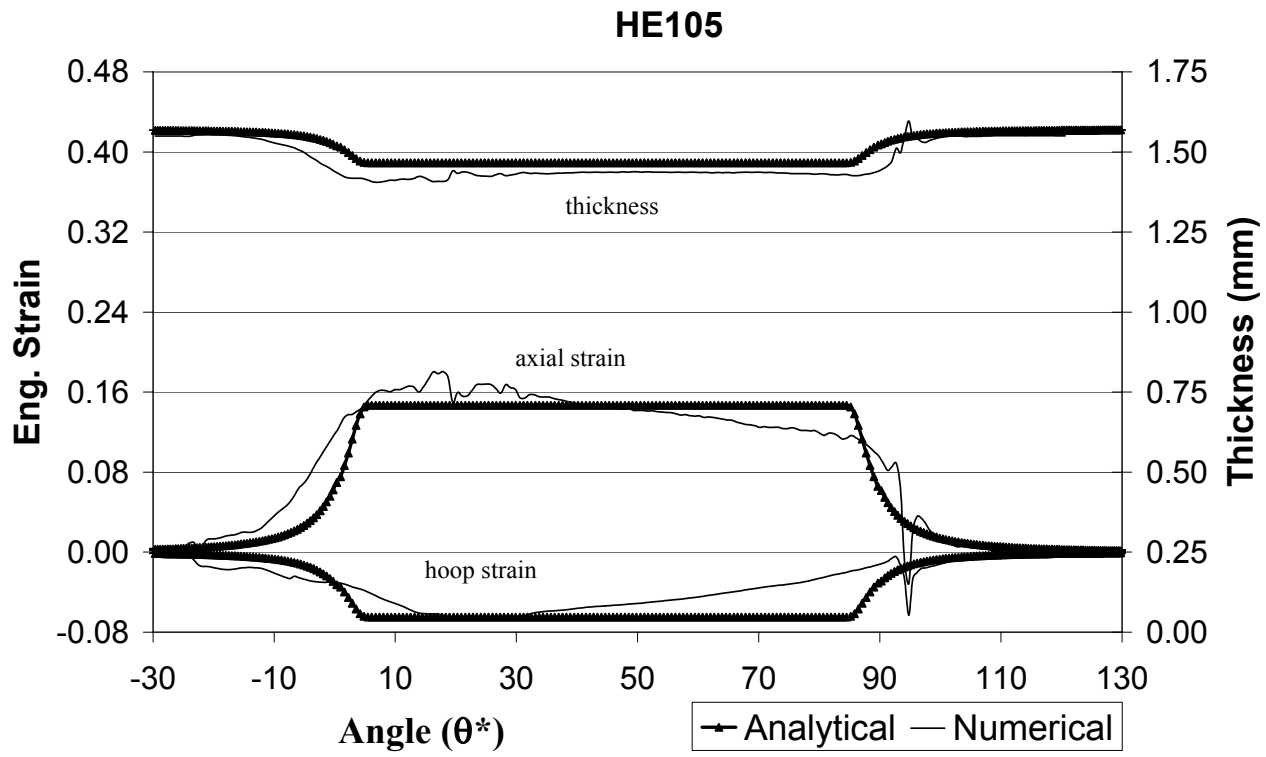

Figure 5.11: Strain and thickness comparison for HE105 on outside of bend

5.1.4 NB100 Boost Case

Figure 5.12, 5.13 and 5.14 show plots for the 100% boost case with no boost block. The resulting strain and thickness distribution is quite similar to the LE95 case, which is expected since the effective boost experienced by the tube is very similar. Note that in the analytical model, the boost used to simulate the NB100 case was the effective boost of 95%.

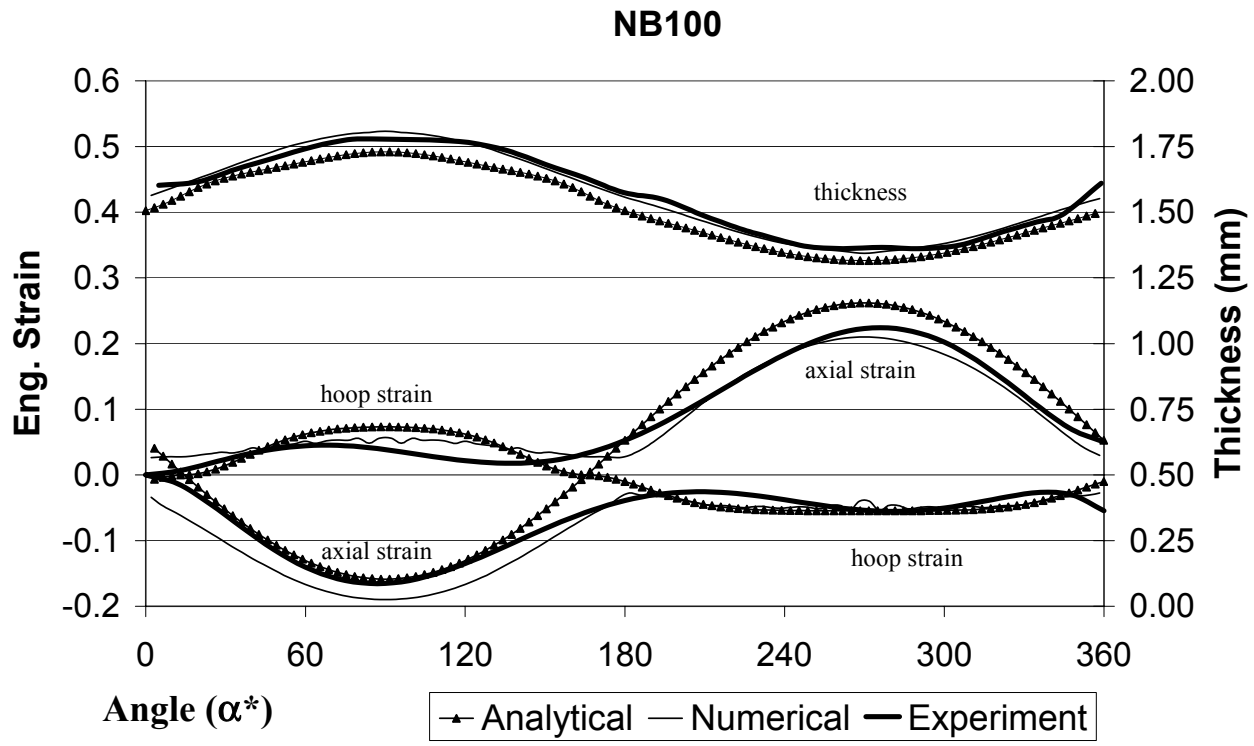

Figure 5.12: Strain and thickness comparison for NB100 at 45º location

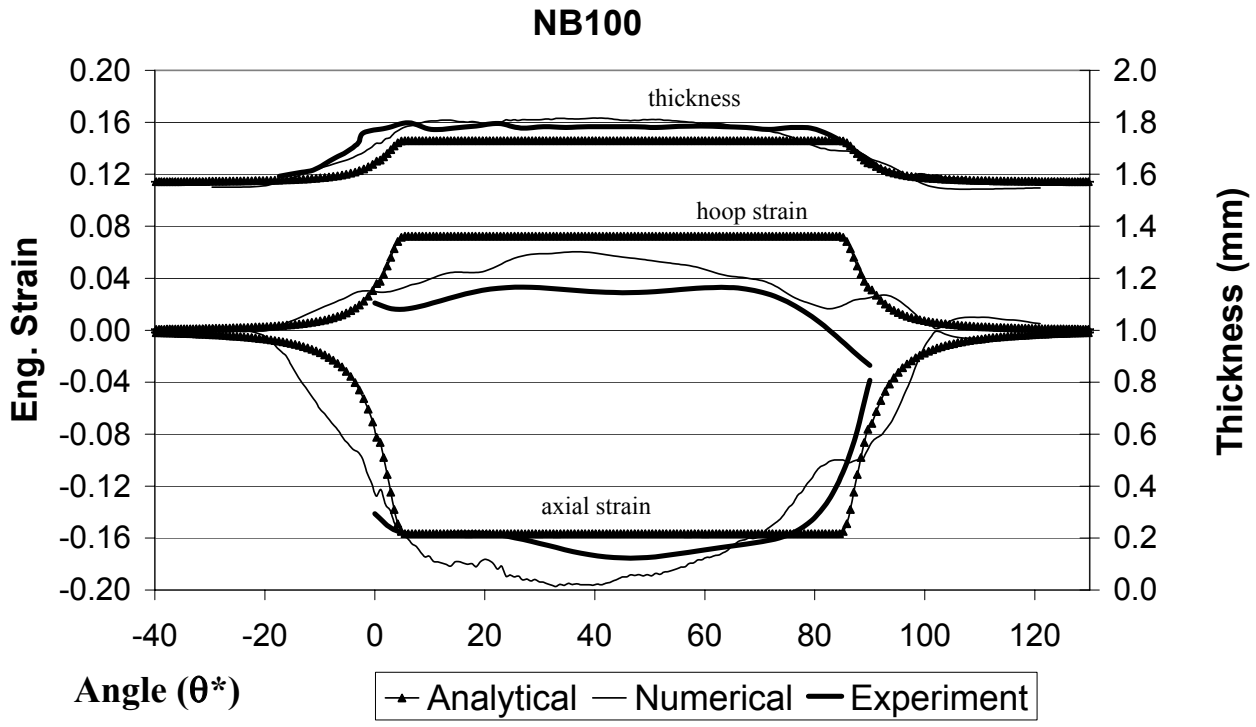

Figure 5.13: Strain and thickness comparison for NB100 on inside of bend

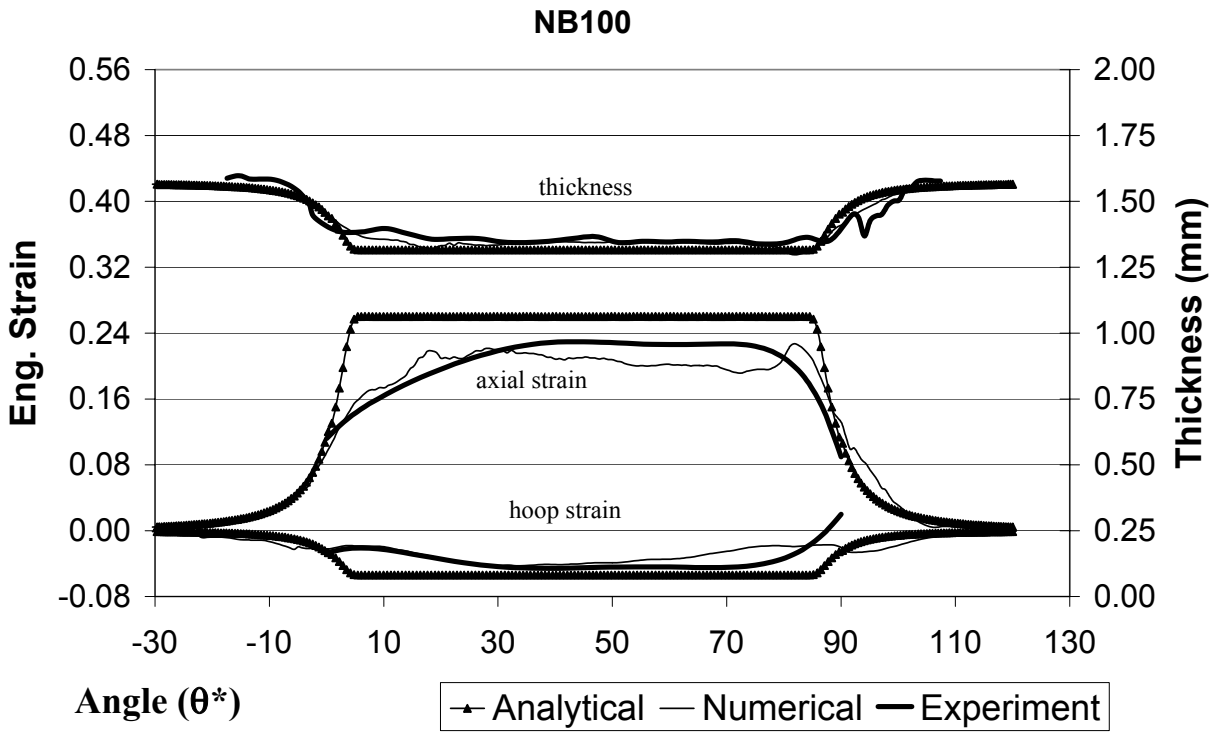

Figure 5.14: Strain and thickness comparison for NB100 on outside of bend

5.1.5 Effect of Boost Level on Strain and Thickness Distributions

Figure 5.15 and 5.16 show the strain and thickness distribution for different boost levels. Figure 5.15 plots the experimental data while the analytical results are shown in Figure 5.16. In the experiments there is a clear trend, as boost level increases from 95% to 100% (Figure 5.15), the tensile axial strain component decreases resulting in a vertical shift of the curves. Physically speaking, as boost level increases more material is "pushed" into the bend meaning greater compressive strain is induced resulting in reduced thinning on the outside of the bend. Since the LE95 case and the NB100 result in similar boost levels, their curves are nearly identical. The analytical curves (Figure 5.16), which include the 105% boost case as well, show

this shift in strain and thickness also. Hoop strains appear to be minimally affected by a change in boost level.

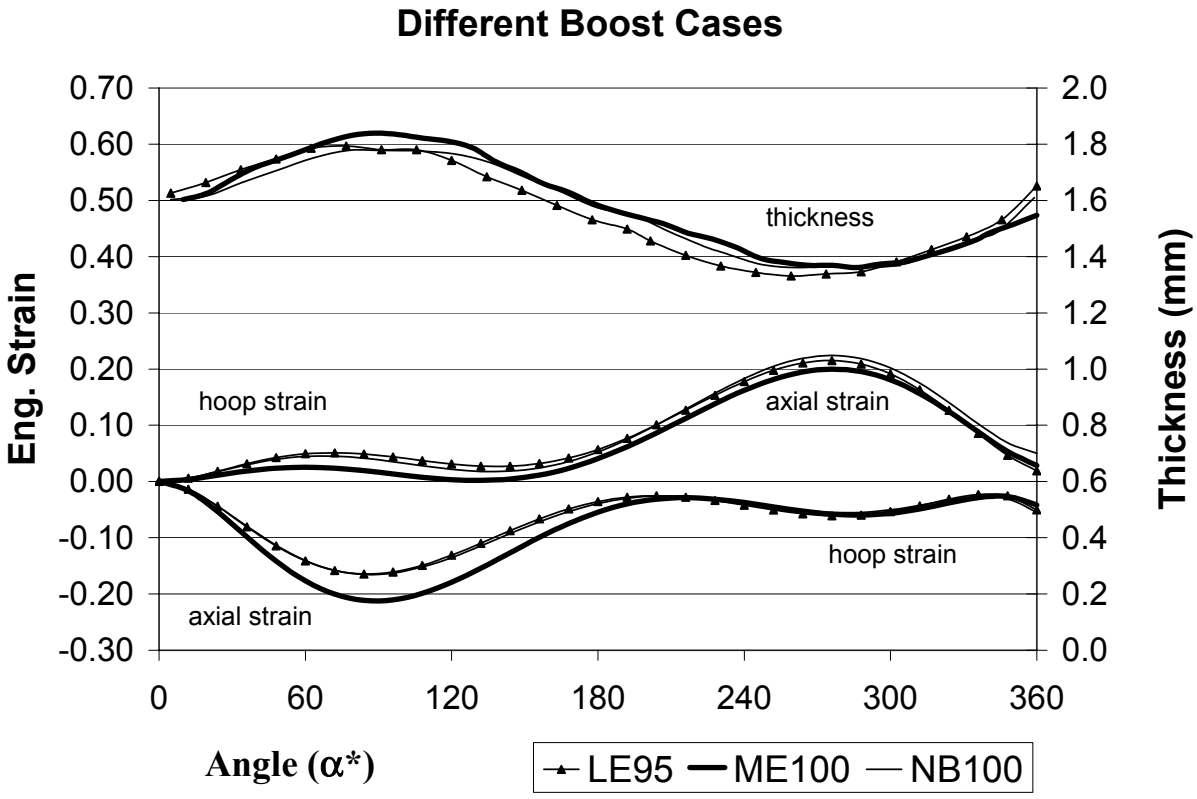

Figure 5.15: Experimental trends over different boost levels

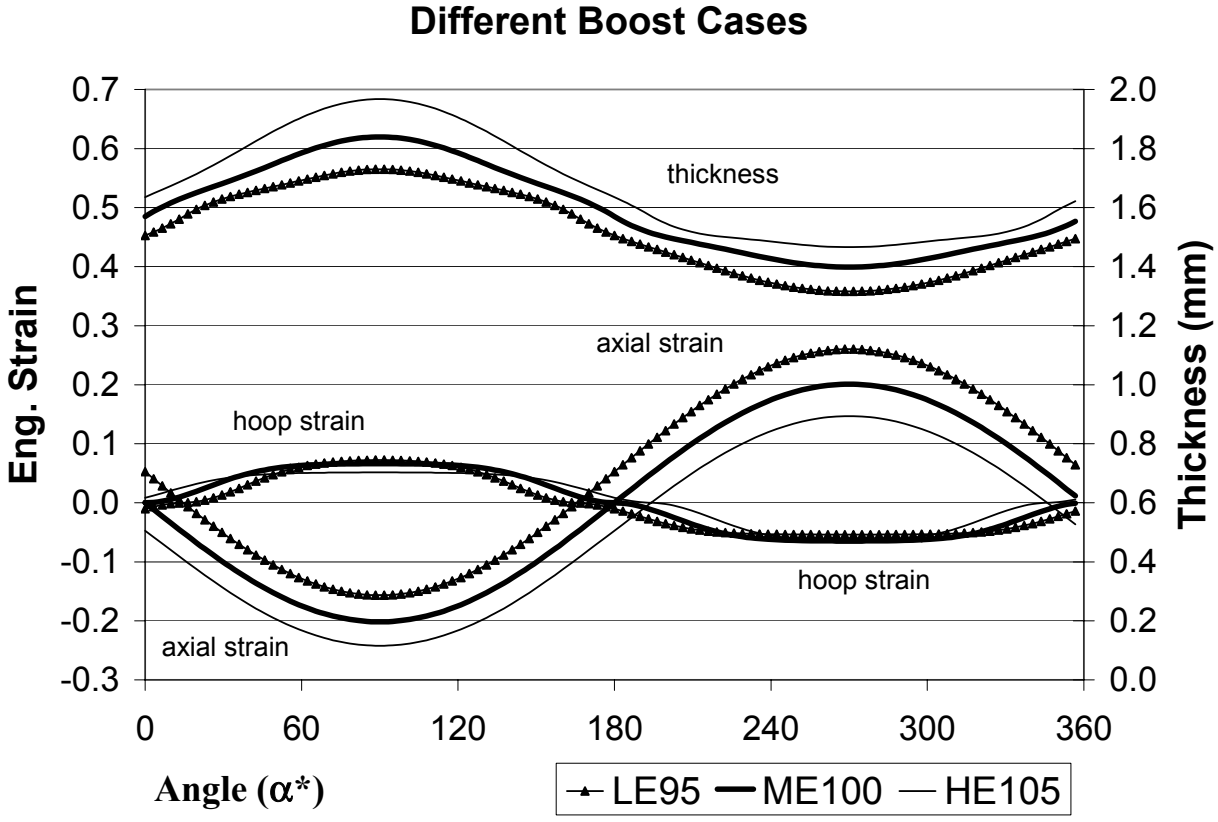

Figure 5.16: Analytical trends over different boost levels

5.1.6 Effect of R_c/d Ratio

A limited number of tests were performed with a smaller radius bend die, giving R_c/d = 2.0. Figure 5.17, 5.18, 5.19 show a plot of the strain and thickness values for the $\theta^* = 45^\circ$ location, and the inside and outside of the bend. The figures shown are for a 100% boost case. Observing the graphs, one sees very good agreement between analytical, numerical and experimental results. The largest errors in the analytical models occur in the transition zones at the ends of the bend region, suggesting that additional work is needed to model this transition more accurately.

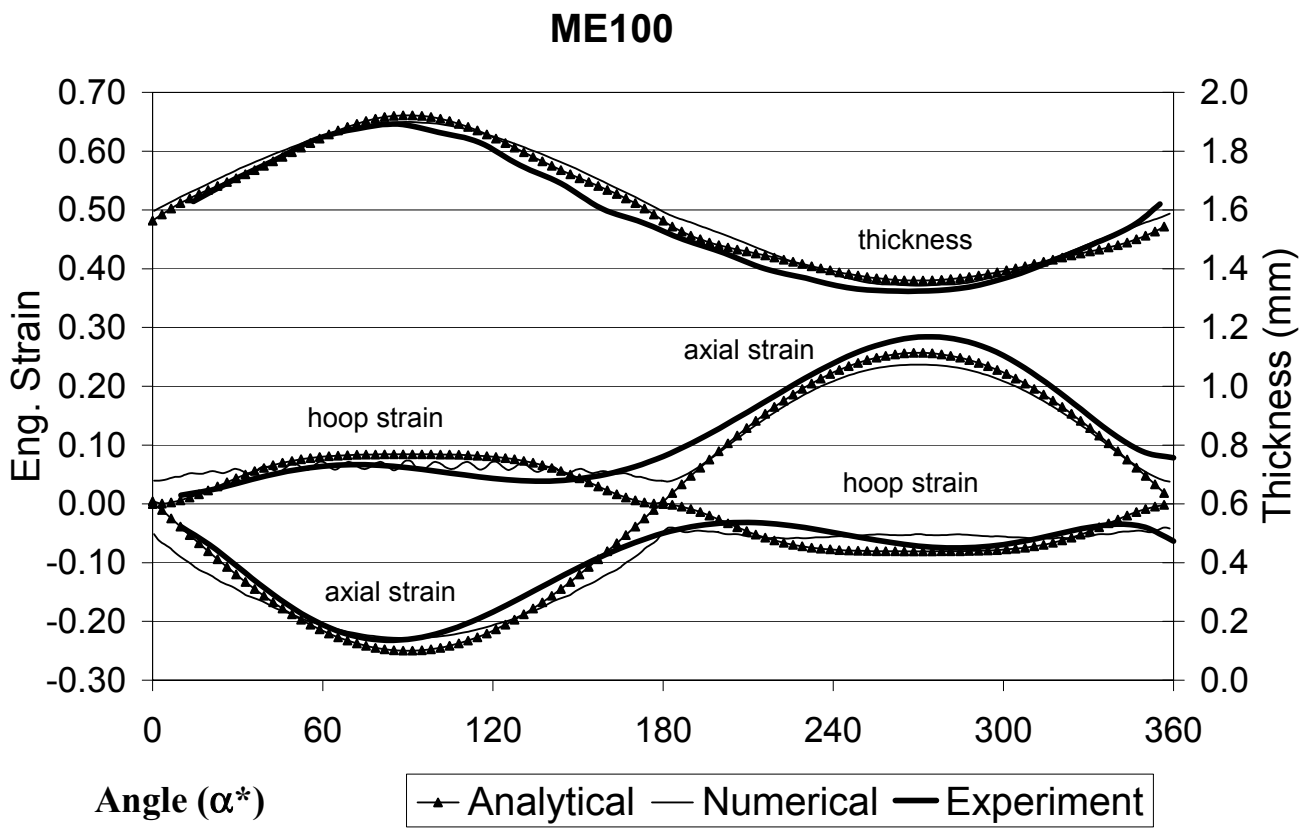

Figure 5.17: Strain and thickness comparison for ME100 at 45° location

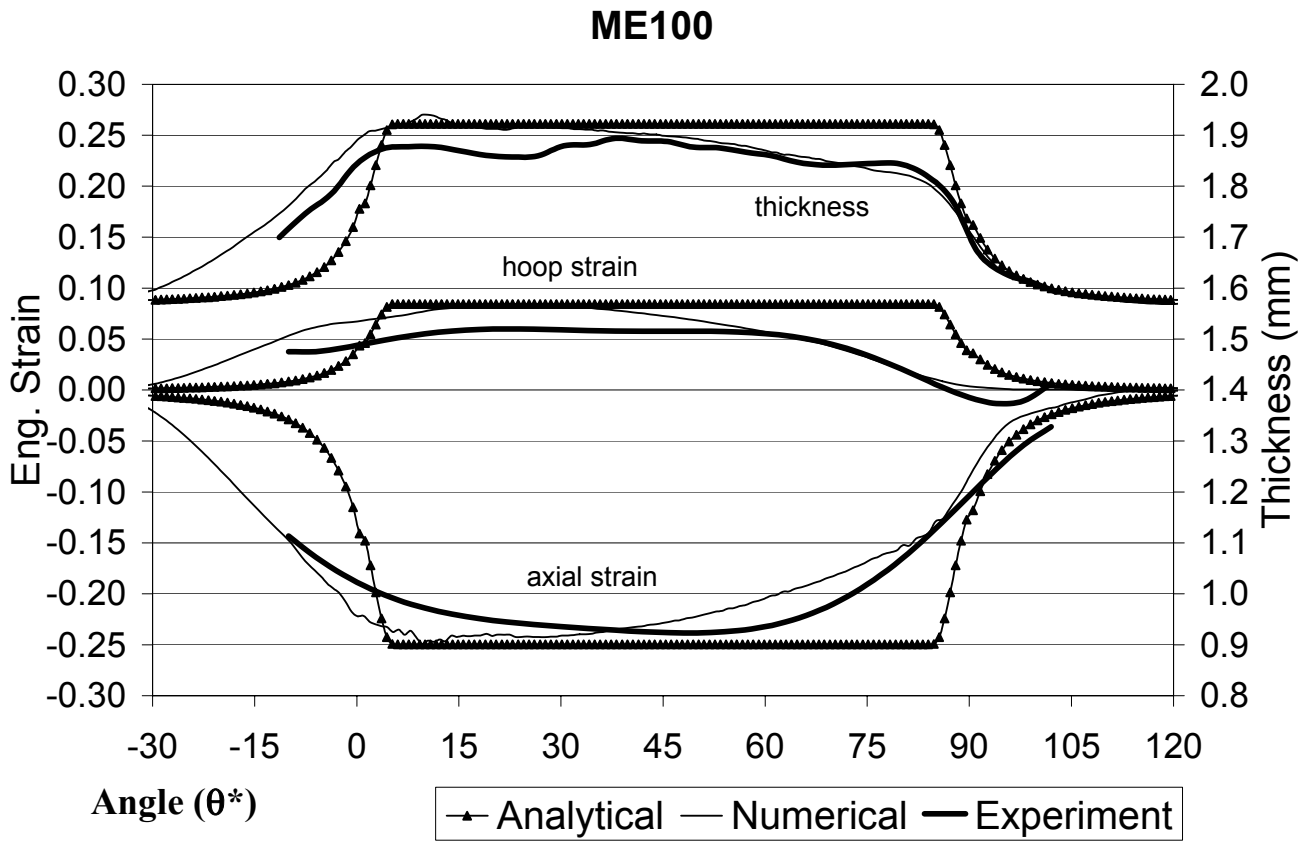

Figure 5.18: Strain and thickness comparison on inside of bend

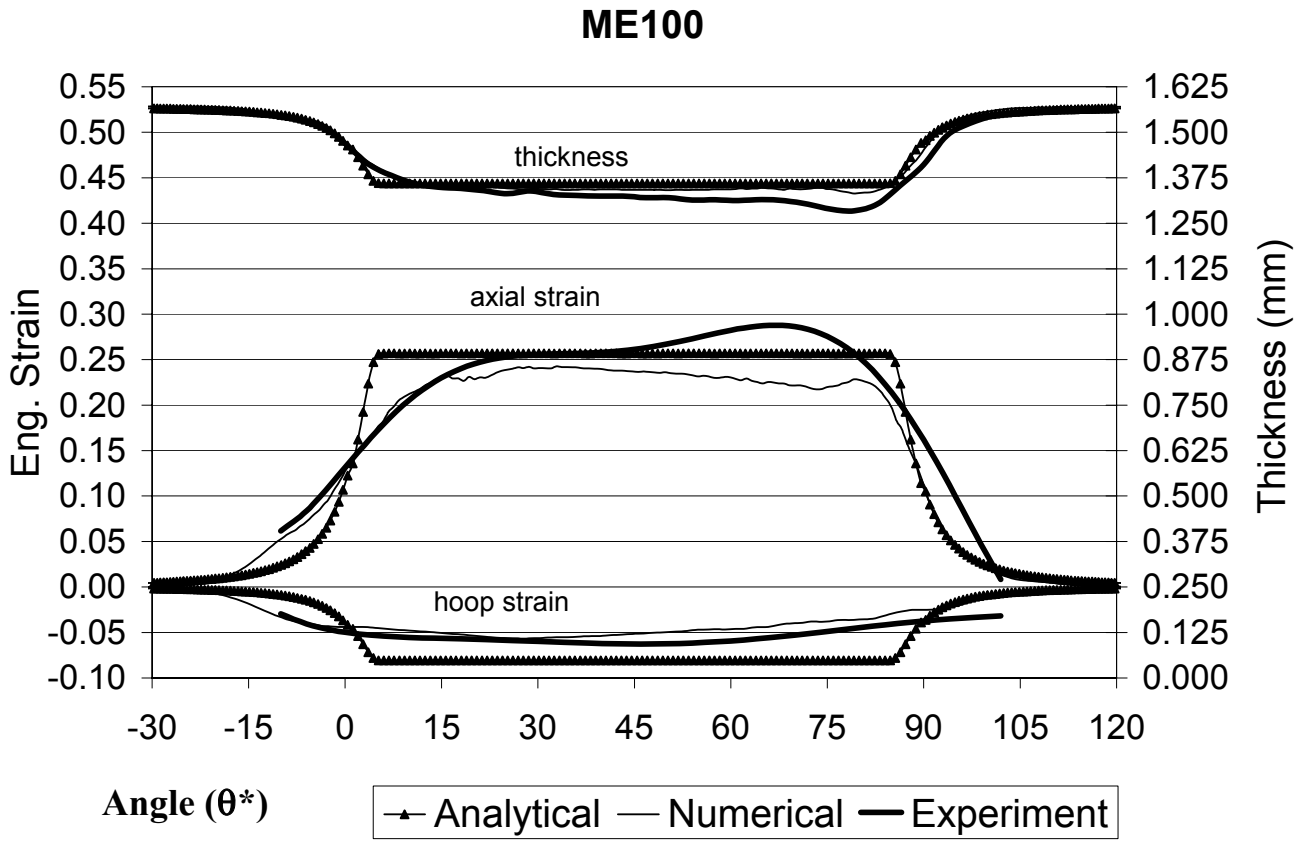

Figure 5.19: Strain and thickness comparison on outside of bend

Furthermore, it should be mentioned that the analytical assumption of constant hoop strain, in the tensile and compressive regions (from Chapter 3), is supported by the experimental and numerical curves, which exhibit relatively constant hoop strain on either side of the neutral axis.

The effect of bend severity can be further examined by considering Figure 5.20 which shows analytical predictions for $R_c/d = 2.5$, 2.0, and 1.5, using the steel properties for DQAK and 1.57 mm wall thickness. The curves are for constant 100% boost, in order to show the effect of

bend radius change alone. It is evident that as the bend radius decreases the magnitude of the axial strain, in the tensile and compressive regions, increases. This is due to the increase in pure bending component of total strain. The hoop strain shows only a small increase in magnitude with a decrease in bend radius.

It is interesting to see that the greatest thickness-change is in the compressive region of the tube, especially with $R_c/d = 1.5$. As it turns out, the 100% boost is high enough to introduce compressive membrane strain in all the different cases, but the smaller the bend radius, the greater the level of compressive membrane axial strain introduced.

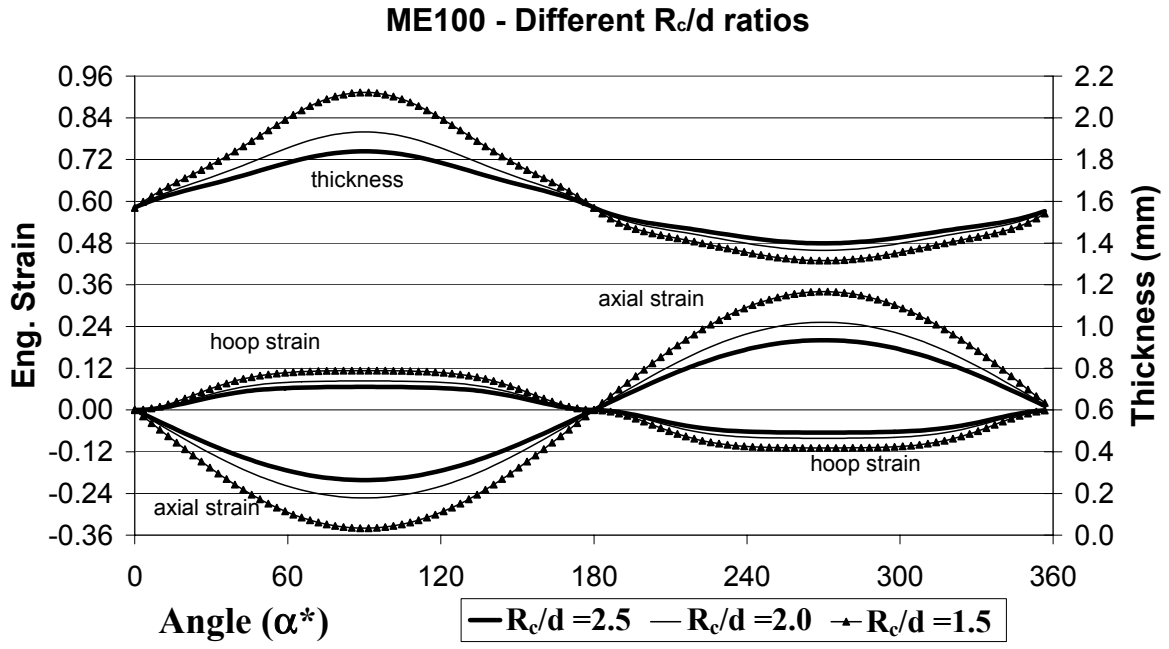

Figure 5.20: Strain and thickness distribution for different R_c/d ratios

Figure 5.21 shows the effect that changing R_c/d and percent boost has on the resulting strains and thickness on the outside of the bend, at $\alpha^* = 270^\circ$.

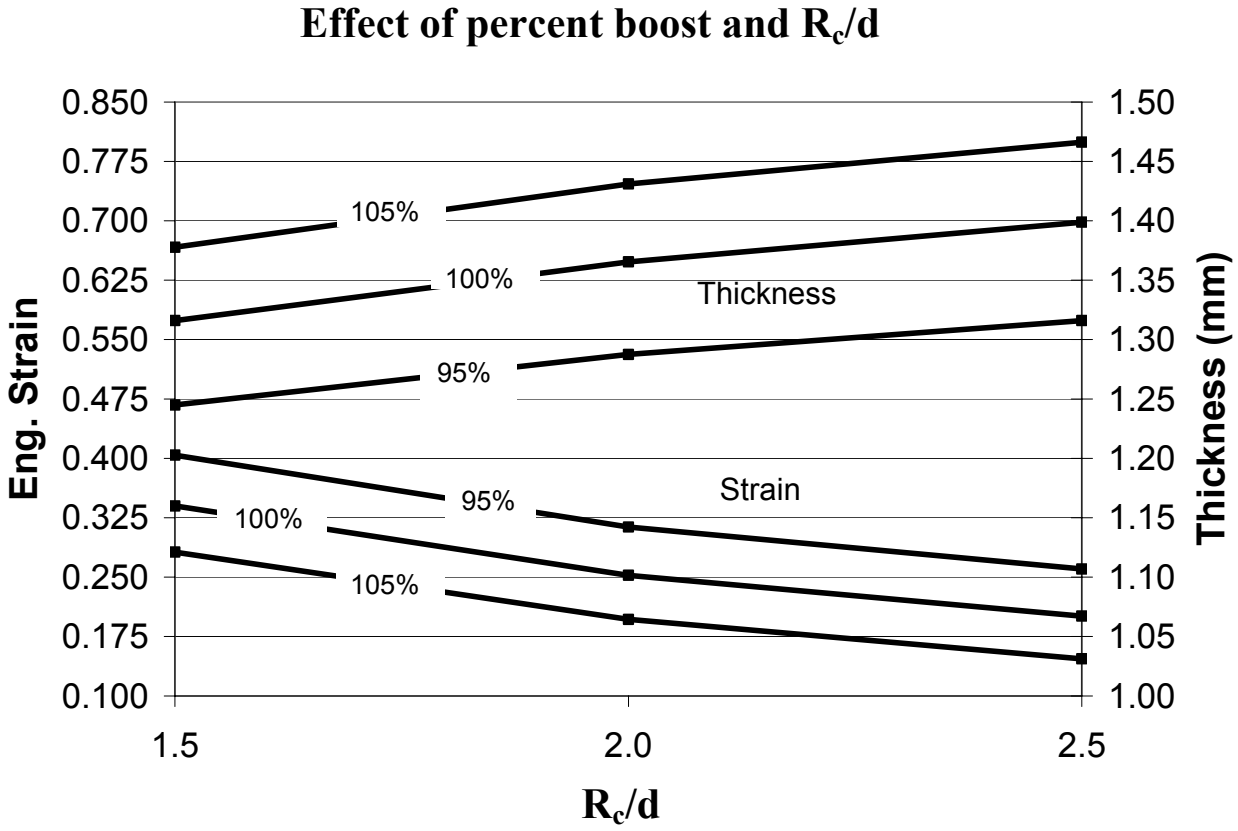

Figure 5.21: Effect of varying percent boost and R_c/d

Observing Figure 5.21 one can see that when changing R_c/d and percent boost, both have significant effect on the strain and thickness. Over the range $1.5 \leq R_c/d \leq 2.5$ the strains change roughly the same degree as when varying the percent boost from 95 to 105%. The thickness however, is less affected by change in R_c/d and affected more by change in percent boost. This is evident as one observes a relatively small increase in thickness from $R_c/d = 1.5$ to 2.5, as compared to a greater thickness-increase when increasing percent boost from 95 to 105%. Generally speaking, strains on the outside of the bend are equally affected by a change in percent boost and R_c/d, whereas thickness on the outside of bend is most affected by a change in percent boost.

5.2 Predicted and Measured Springback

Table 5.2 summarizes the analytical predictions for the bend R_c angle and centerline bend radius, such that, after springback, the final bend angle of the bent tube is 90º, and the centerline bend radius satisfies the desired R_c/d ratio of 2.5. For d = 76.2 mm, R_c = 190.5 mm.

The predicted bend angle required to produce a 90º final bend did not vary significantly with boost level. The predicted values (91.2-91.3º) agree reasonably well with the values used in the experiments.

Boost Case	Analytical Bend Angle (º)	Analytical Bend Radius (mm)	Experimental Bend Angle (º)
LE95	91.3	188.0	90.9
ME100	91.2	187.97	90.9
HE105	91.1	188.08	N/A
NB100*	91.3	188.0	90.9

*Since effective boost is roughly the same as for LE95 the same percent boost is input into the analytical model

Table 5.2: Analytical and experimental results for springback angle and centerline radius

The predicted change in radius required to obtain a final R_c/d ratio of 2.5 is also in accord with the experiments. For the R_c/d = 2.5 bend die, the actual centerline radius is roughly 188.6 mm, which is close to the required centerline radii predicted by the analytical bend model. However, obtaining the exact bend radius after springback is not quite as important, for die fitting purposes, as is obtaining the correct bend angle after springback. During the bending process, the tube ovalizes slightly, meaning that the radial clearance is 1 to 2 mm between the tube and the hydroforming die, on the inside and outside of the tube bend. This clearance aids in seating of the tube into the die.

5.2.1 Residual Stresses

Figure 5.22, 5.23 and 5.24 show the predicted stress distribution, before and after springback, as a function of distance from the tube centerline, for the three different boost cases (for $R_c/d = 2.5$). The stresses calculated are at the mid-thickness of the tube, $r = r_o = 37.315$ mm. The y-value lies in the range $-37.315 \leq y \leq 37.315$. Plotted are the hoop and axial stress, before and after springback. As mentioned in Chapter 3, the neutral axis corresponds to the line where strain (and stress) change sign from negative to positive.

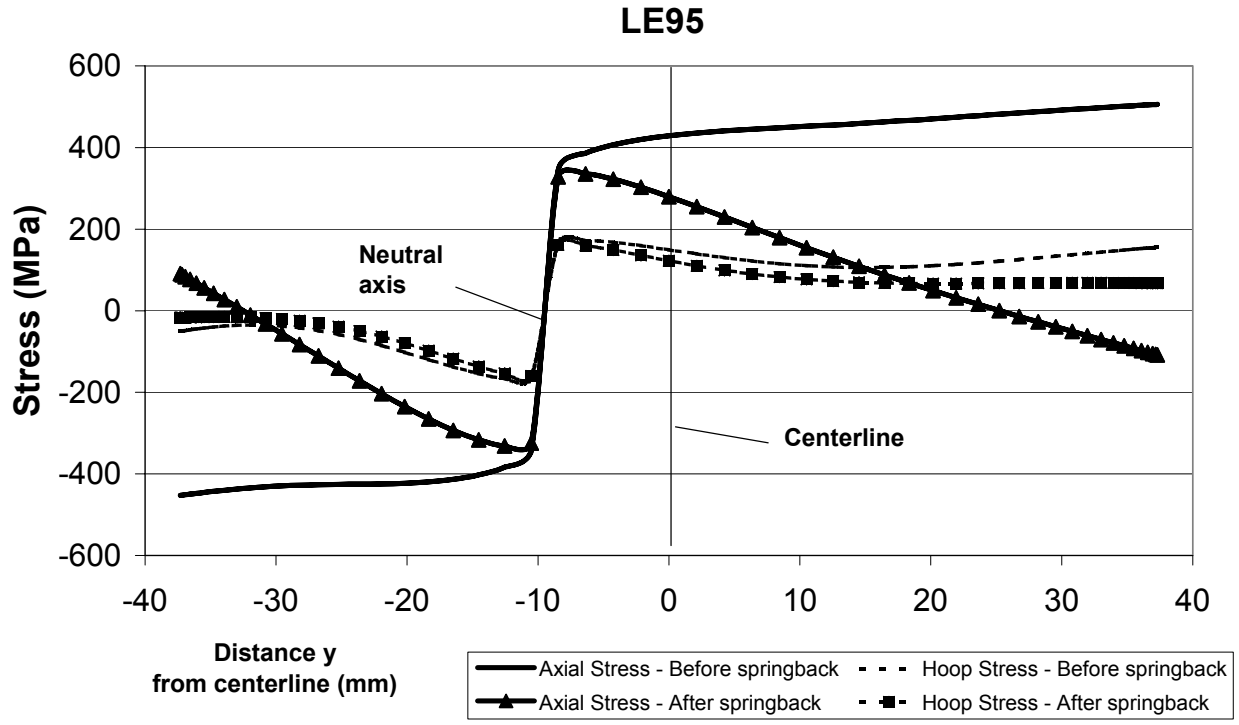

Figure 5.22: Stress distribution for LE95

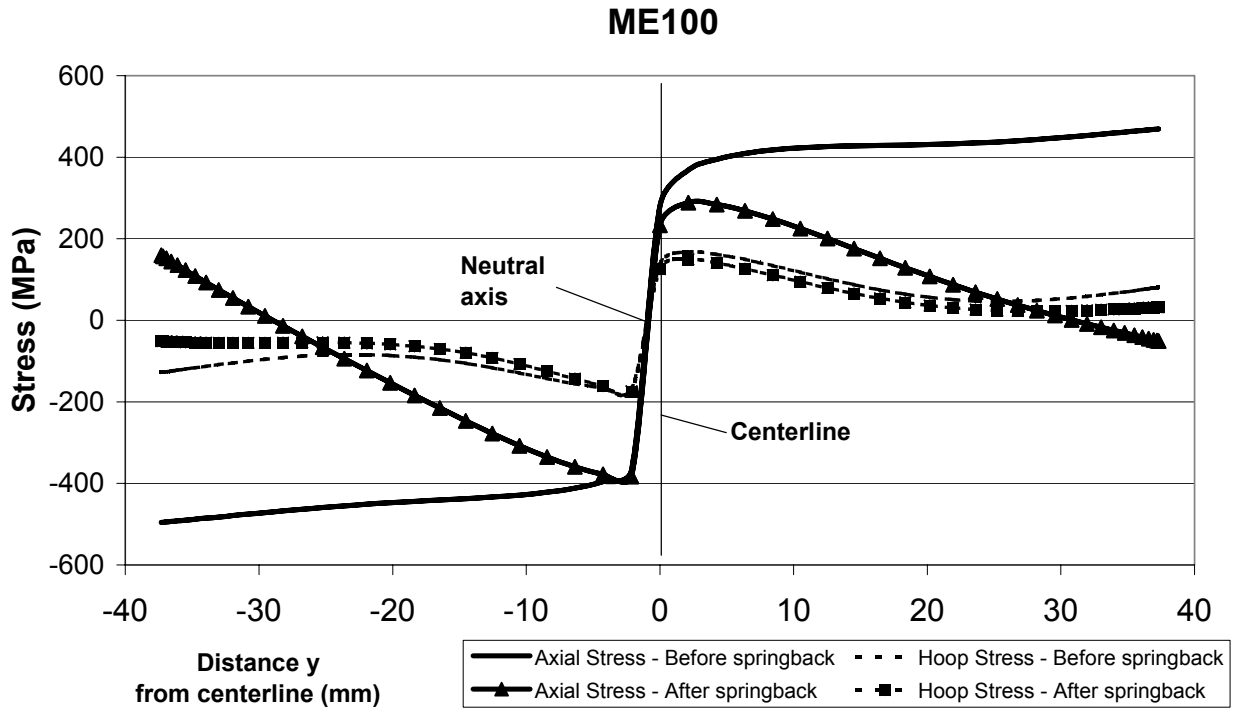

Figure 5.23: Stress distribution for ME100

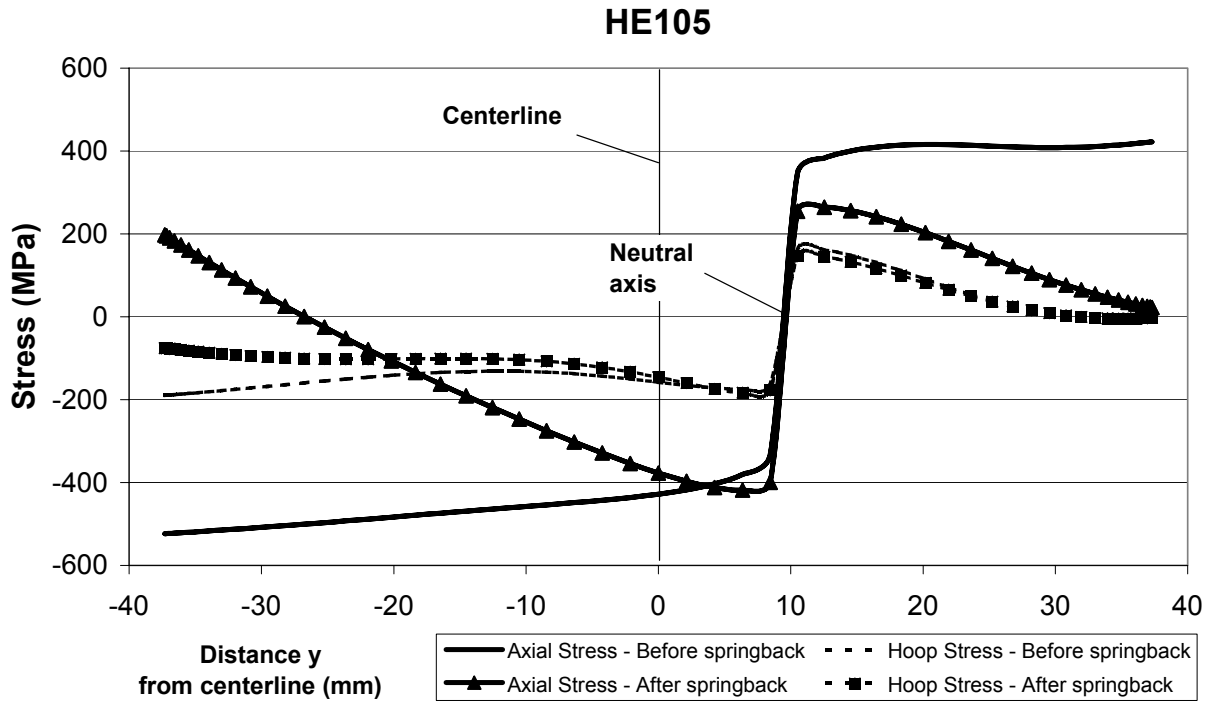

Figure 5.24: Stress distribution for HE105

Observing Figure 5.22, 5.23, and 5.24, as the level of boost increases, the stresses become more compressive, before and after springback. In addition, the neutral axis shifts in accordance with the different boost conditions, from $y \approx -10$, to $y \approx 0$, to $y \approx 10$ mm, roughly, for the LE95, ME100, and HE105 cases, respectively.

5.3 Predicted Effective Plastic Strain and Thinning

Effective plastic strain is often used as an indicator of the level of work-hardening and formability and a means to quantitatively analyze material behavior during a forming process. Effective plastic strain values above a critical value are also sometimes used as an indicator of

probable material failure. Therefore, an important means to compare the analytical model to the numerical model is by comparing contour plots of effective plastic strain.

Figure 5.25 shows the effective plastic strain for the R_c/d = 2.5, ME100 case, after bending. Also of interest is the comparison of predicted wall thickness, shown in Figure 5.26 for the same cases. Observing Figure 5.25 and 5.26 one sees very similar distributions, both in magnitude and uniformity. This good agreement was also found for the other boost cases, LE95, NB100, and HE105 (not shown).

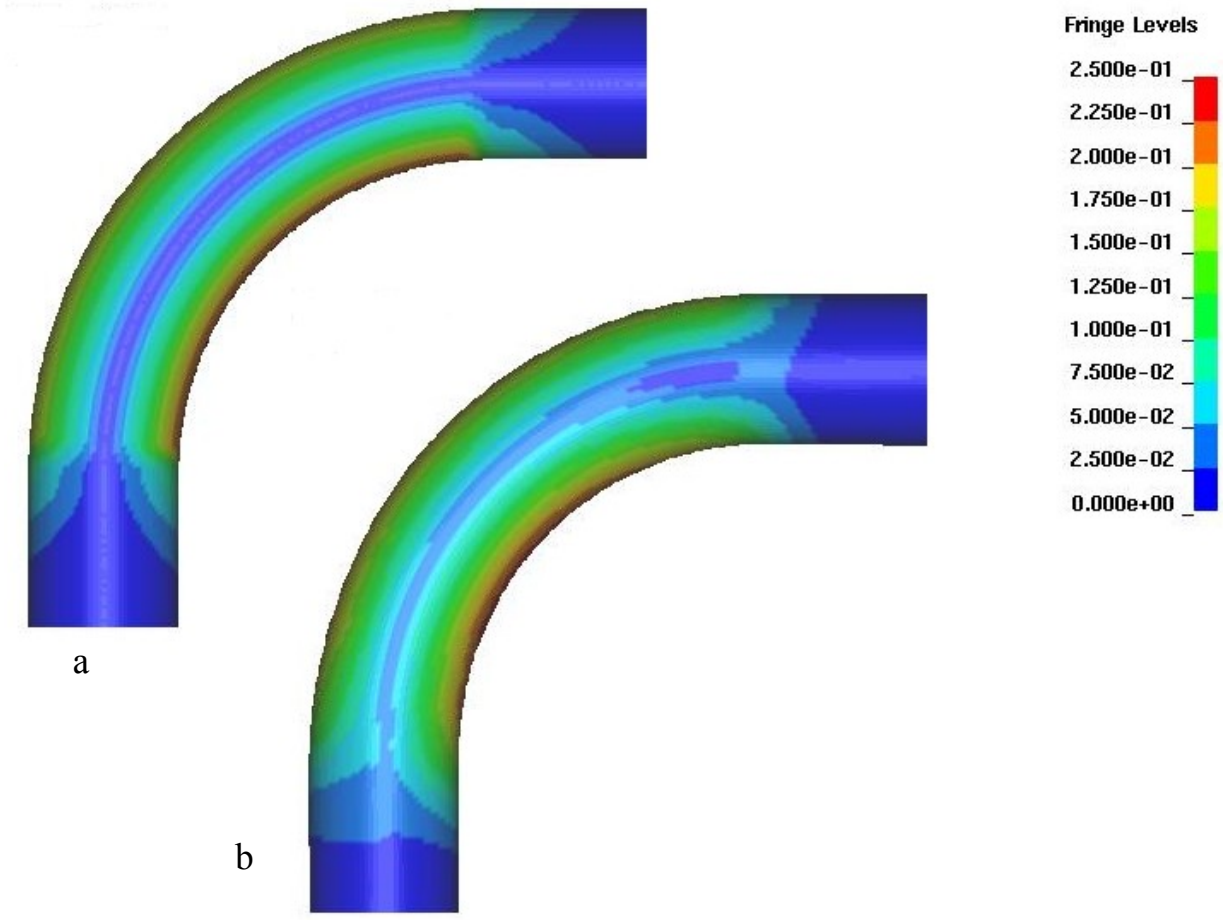

Figure 5.25: Contour plot showing predicted effective plastic strain for analytical (a) and numerical model (b)

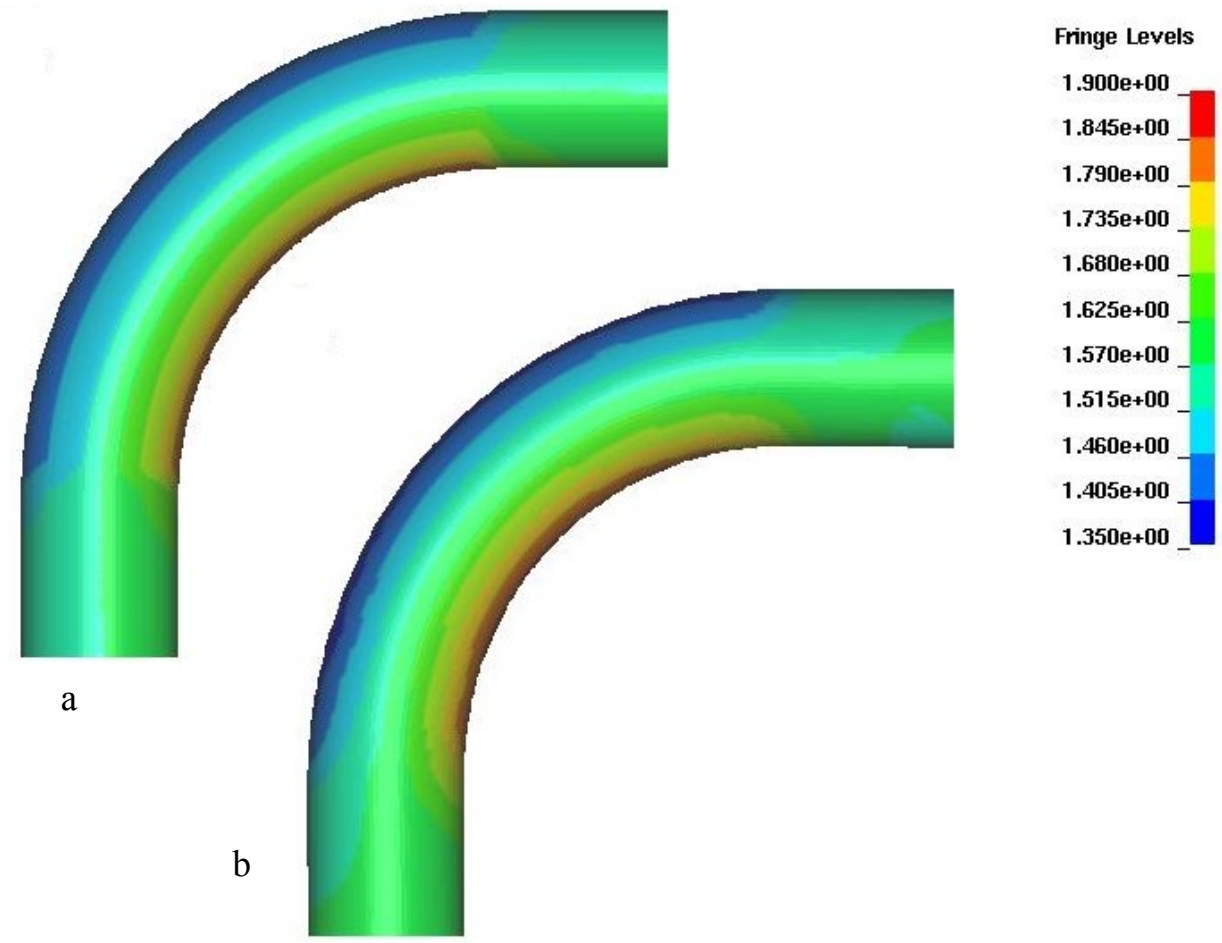

Figure 5.26: Contour plot showing predicted thickness for analytical (a) and numerical model (b)

5.4 Application to Aluminum Alloy Tubes

As a final validation of the analytical model, simulation of the bending of aluminum alloy tubes was considered. In this case, experimental data used in the validation was taken from a previous US/AMP (US Automotive Materials Partnership) study [10]. The comparison is along the circumference at the $\theta^* = 45^\circ$ location, as shown in Figure 5.27.

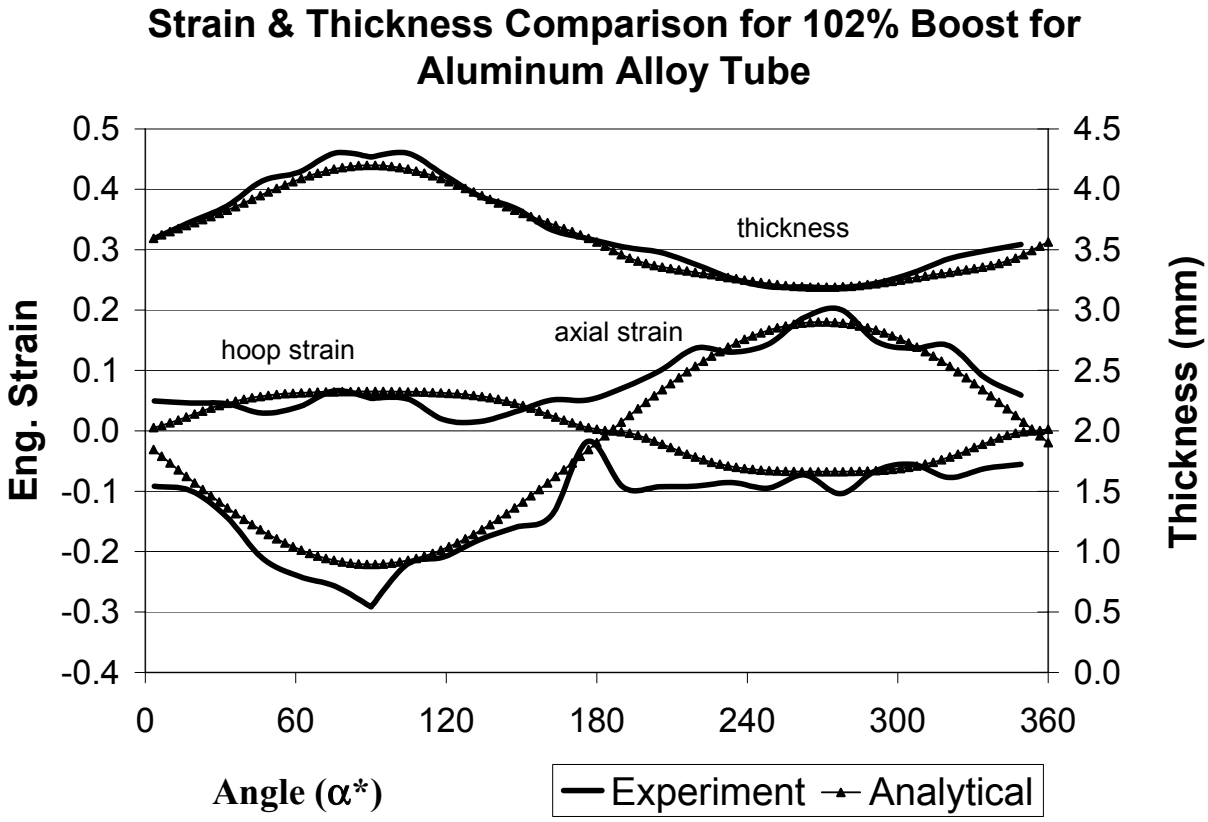

Figure 5.27: Strain and thickness comparison for aluminum tube at 45º location

This figure also shows good agreement between the experiment and model. The available experimental data is taken from the measurement of one tube. Note that the comparison is for a 3.5 mm thick Al-3.5%Mg tube. Further details of the tubes and experiments are given in [10].

The analytical model also did a reasonable job of predicting the necessary pre-springback bend angle, of 92.7º, to account for springback. In the experiments the necessary bend angle was determined to be 91.9º [10].

5.5 Run-time Comparison

For a single bend the analytical model takes 10-15 seconds to run on a 2.4 GHz Pentium IV processor, compared to roughly 2 hours for the FEM simulation on the same computer. This very fast run-time of 10-15 seconds corresponds to a given prescribed percent boost. If the model is given a prescribed boost force, the run time takes roughly 60-70 seconds for a single bend, since the calculations become more elaborate, as described in Chapter 3.

5.6 Application to Hydroforming

The previous sections of this chapter have served to provide an assessment of the analytical bend predictions. In this section, results are presented from the application of the analytical bending predictions in the simulation of a subsequent hydroforming operation. In this case, models of the ME100 case were developed, in which the as-bent tube was hydroformed using the outside corner-fill die, described in Section 2.5. For comparison purposes, hydroforming simulations were performed using bending predictions from both the analytical and the finite element (FE) models. The hydroforming predictions are then compared to one another, as well as to measured data for strain and thickness distribution, and corner expansion versus pressure.

The available measured strain and thickness data after hydroforming comes from a single representative tube sample. Due to time constraints, additional tubes could not be measured to obtain good average values, or ascertain the degree of scatter. It is expected, however, that the data lie within an error of 5% for strains, as for the bending measurements. Ongoing work by Dyment [43] will assess the hydroformability of these pre-bent tubes.

5.6.1 Predicted strains after hydroforming

Figure 5.28 shows predicted contours of effective plastic strain from the hydroforming FE models based on the analytical and numerical pre-bend, respectively. High levels of strain are seen on the outside of the bend, which is the region where the corner-fill deformation takes place. One can see very similar strain distributions for the two cases.

Contours of predicted percent thickness reduction are plotted in Figure 5.29. The good agreement seen again, suggests that the analytical predictions are in good accord with the FE models for bending.

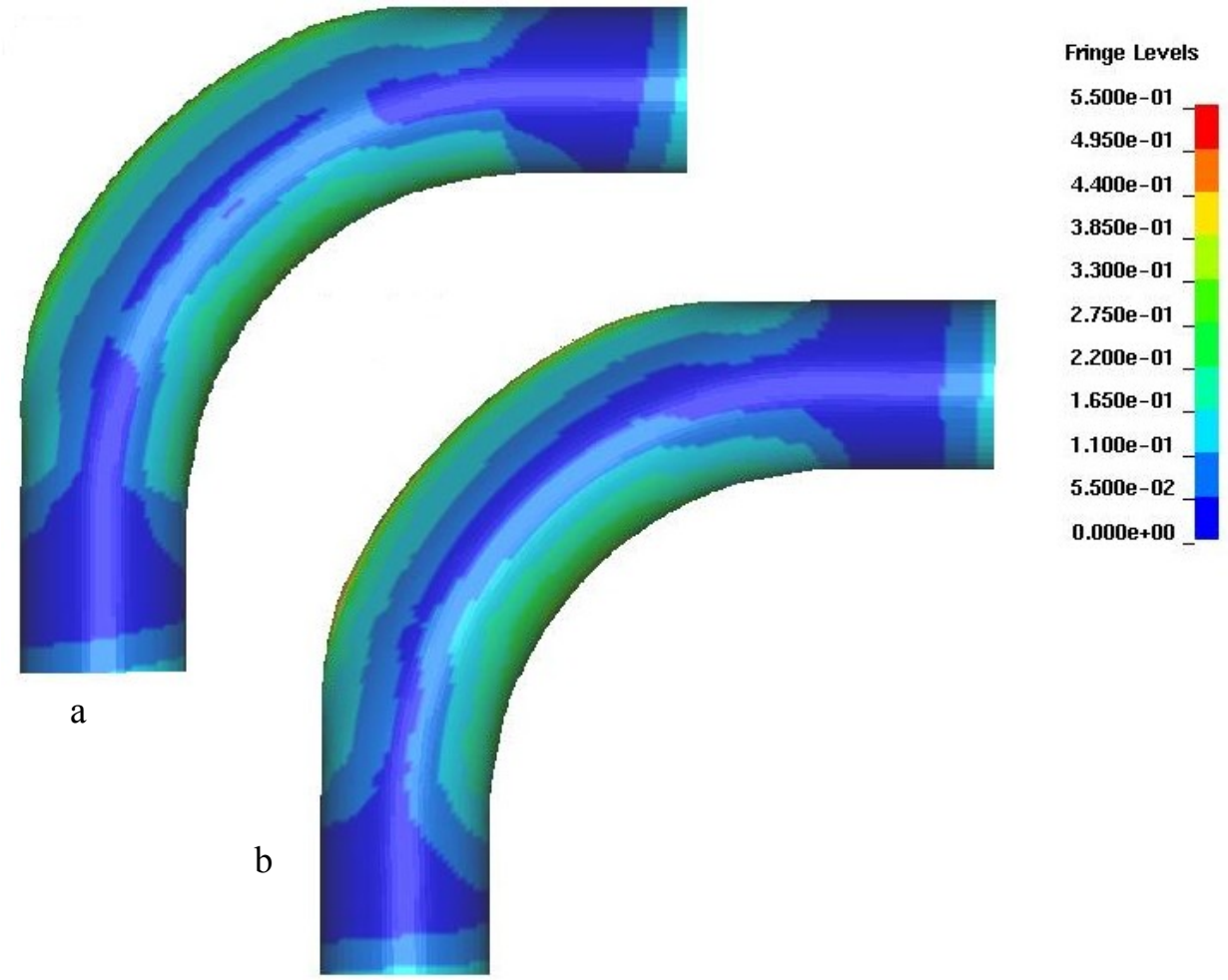

Figure 5.28: Contour plot showing predicted effective plastic strain in FE hydroforming for the analytical pre-bend (a) and numerical pre-bend (b)

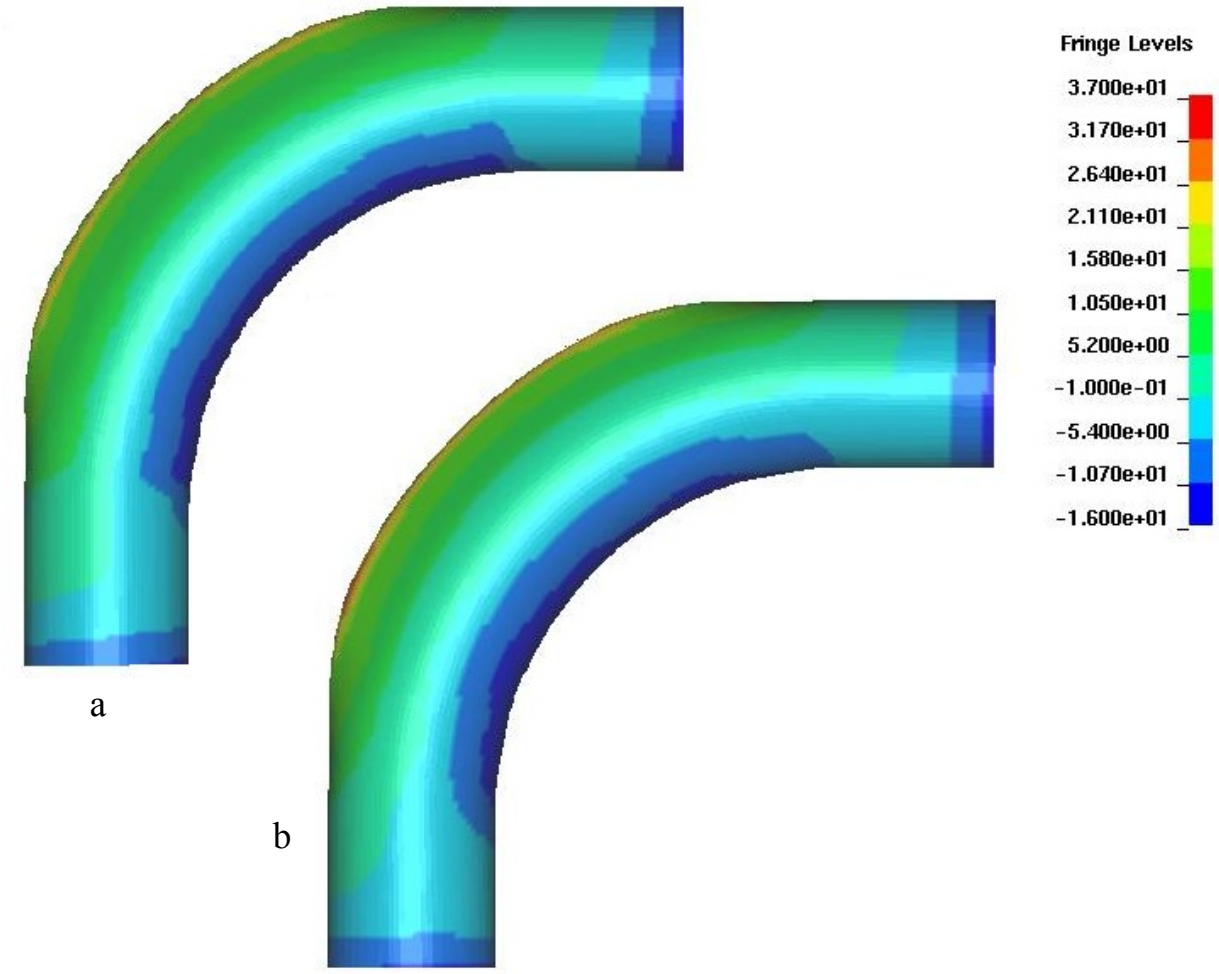

Figure 5.29: Contour plot showing predicted percent thickness reduction for analytical pre-bend (a) and numerical pre-bend (b)

Figure 5.30 shows the measured and predicted strain distributions in the hydroformed tubes, for the ME100 case. In general, the predicted distributions show two features that differ from the as-bent condition (Figure 5.6). First, in both FE predictions, there is a localization of strain in the hoop direction in the $\alpha^* = 240 - 300^\circ$ region of the tube (corresponding to the outside region of bend). The two strain peaks correspond to localization of strain at the points of tangency with the corner fill region of the die (see Figure 5.31). The tangency point is defined as the point of intersection of the tube wall, the open die space, and the die wall, as shown in Figure 5.32. There is also an increase in hoop strain on the inside of the bend ($60^\circ < \alpha^* < 120^\circ$). This

increase is due to lift-off of the tube from the die along the inside of the bend, as seen in the numerical prediction shown in Figure 5.33. The "lift-off" of the inside of the tube due to the force of the end seals. The end plungers have a conical profile that wedge against the tube wall (Figure 2.9), producing a metal-on-metal high-pressure seal. This wedging action also creates a high axial force on the tube ends, which pushes the tube into the outside of the die as illustrated in Figure 5.33. A gap forms on the inside of the bend, which eliminates contact friction with the die and results in the large hoop strains at the 90º region of the section, shown in Figure 5.30 for experiment. This effect is much more pronounced in the experimental data than in the FE data, which suggests that the model does not capture the end seal boundary condition (causing lift-off) particularly well. The loss of support of the die causes the tube to expand circumferentially with an increase in hoop strain. This increase can be seen in Figure 5.34, which plots the measured strains after bending and after hydroforming. The increase in hoop strain for $60º < \alpha^* < 120º$ is evident, however there is no evidence of localization at the outside of the tube

($240º < \alpha^* < 300º$). This differs from the change in predicted strains in Figure 5.35, which shows sharp peaks on the outside of the tube.

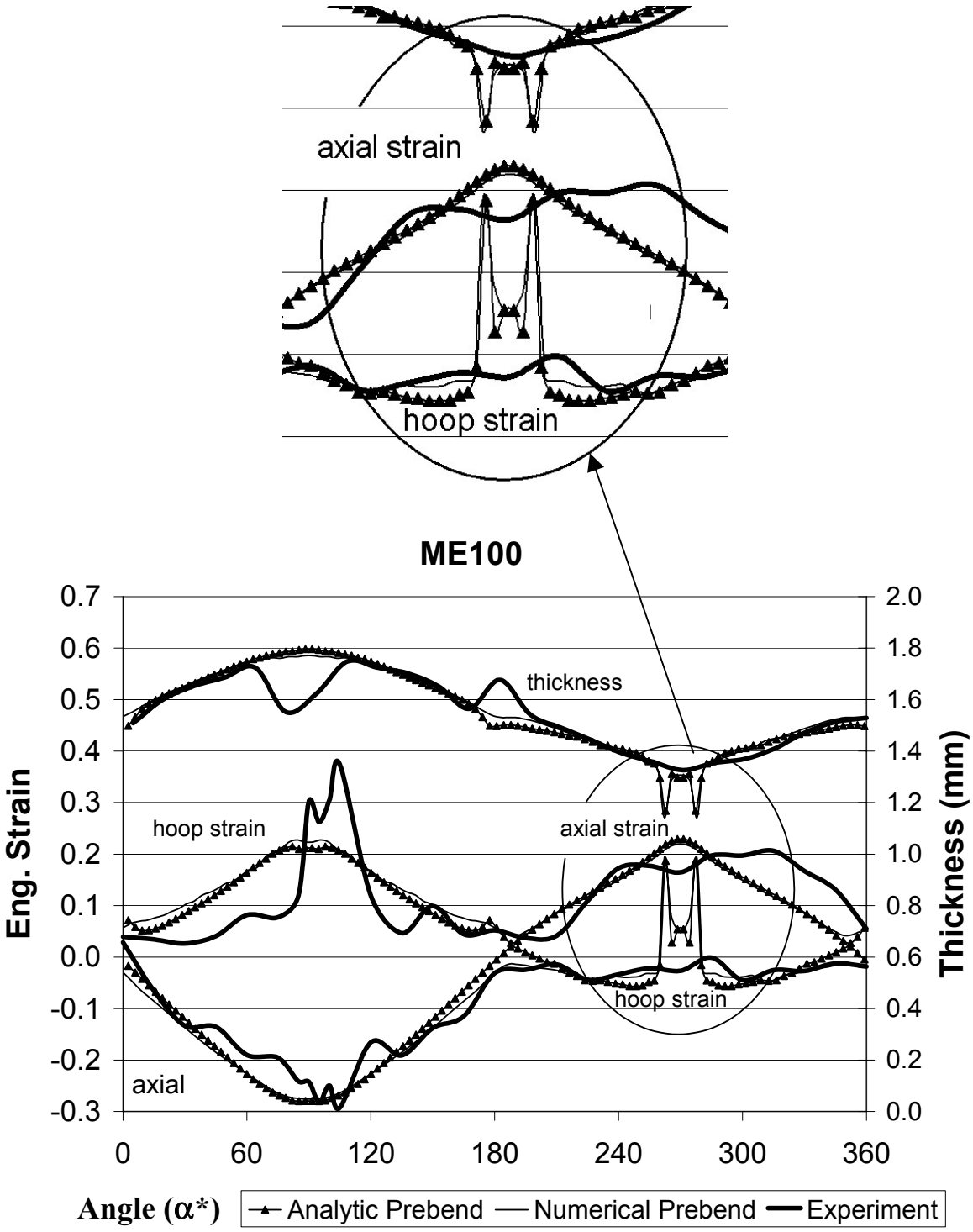

Figure 5.30: Strain and thickness comparison for analytic and numerical pre-bend, with experiment, at 45º location

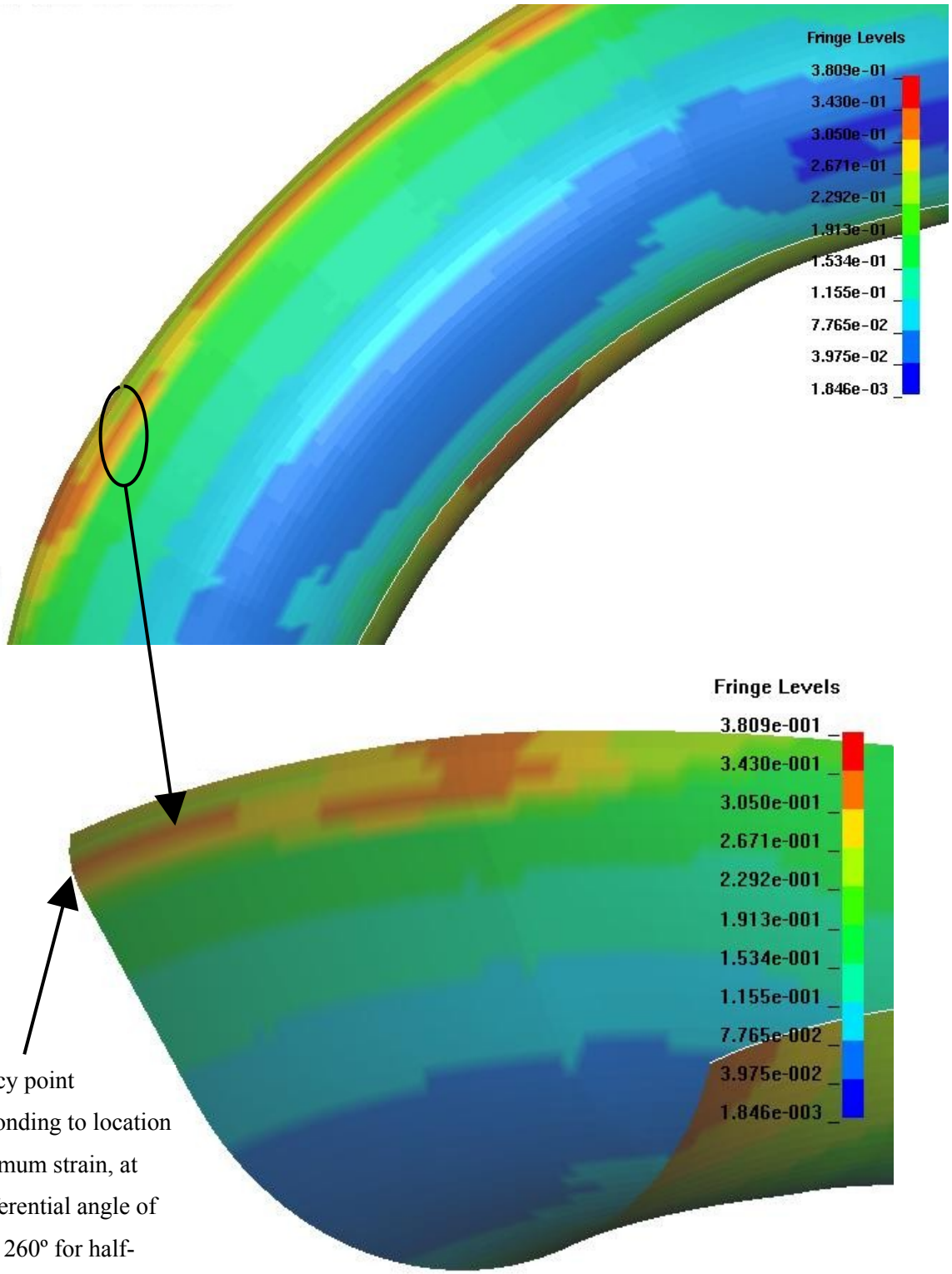

Figure 5.31: Location of maximum effective plastic strain at tangency point

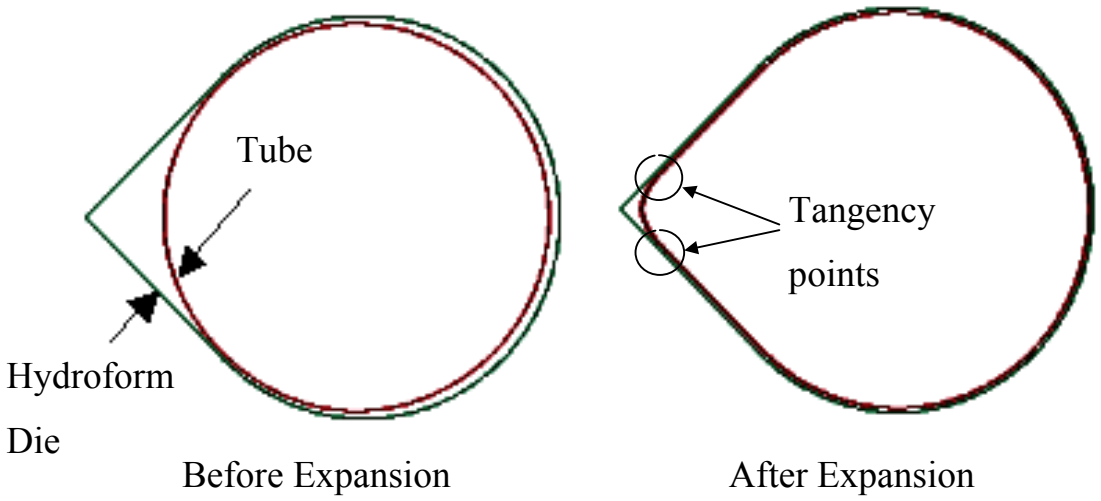

Figure 5.32: Tangency point on hydroformed tube

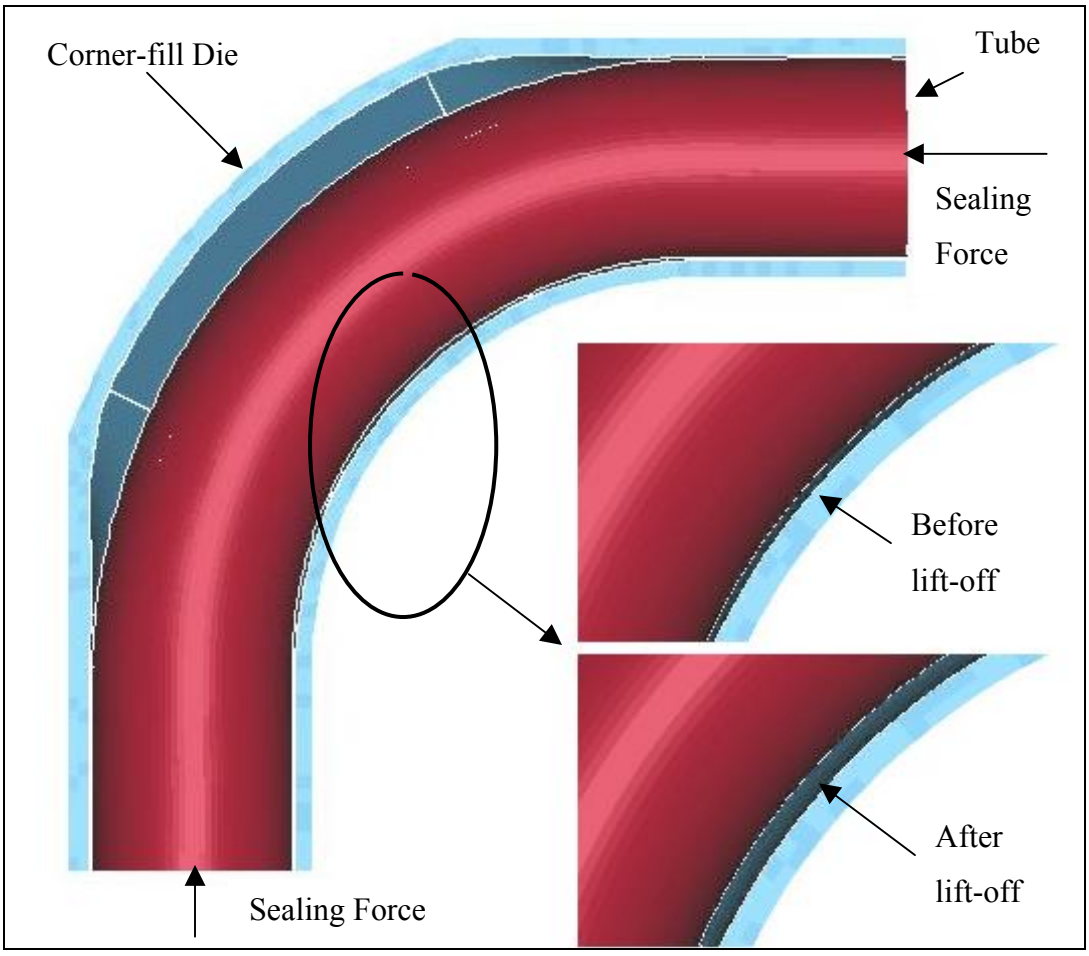

Figure 5.33: Tube lift-off in hydroforming die

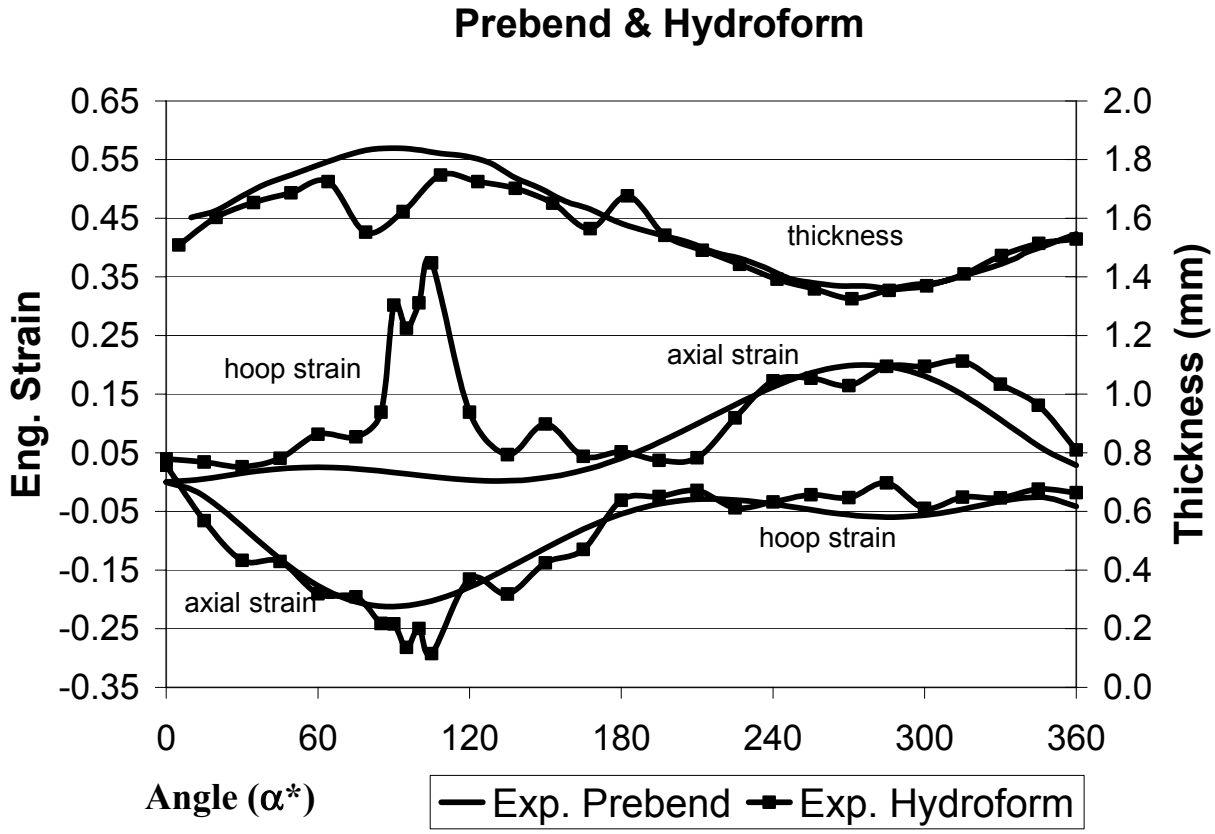

Figure 5.34: Experimental pre-bend and hydroforming

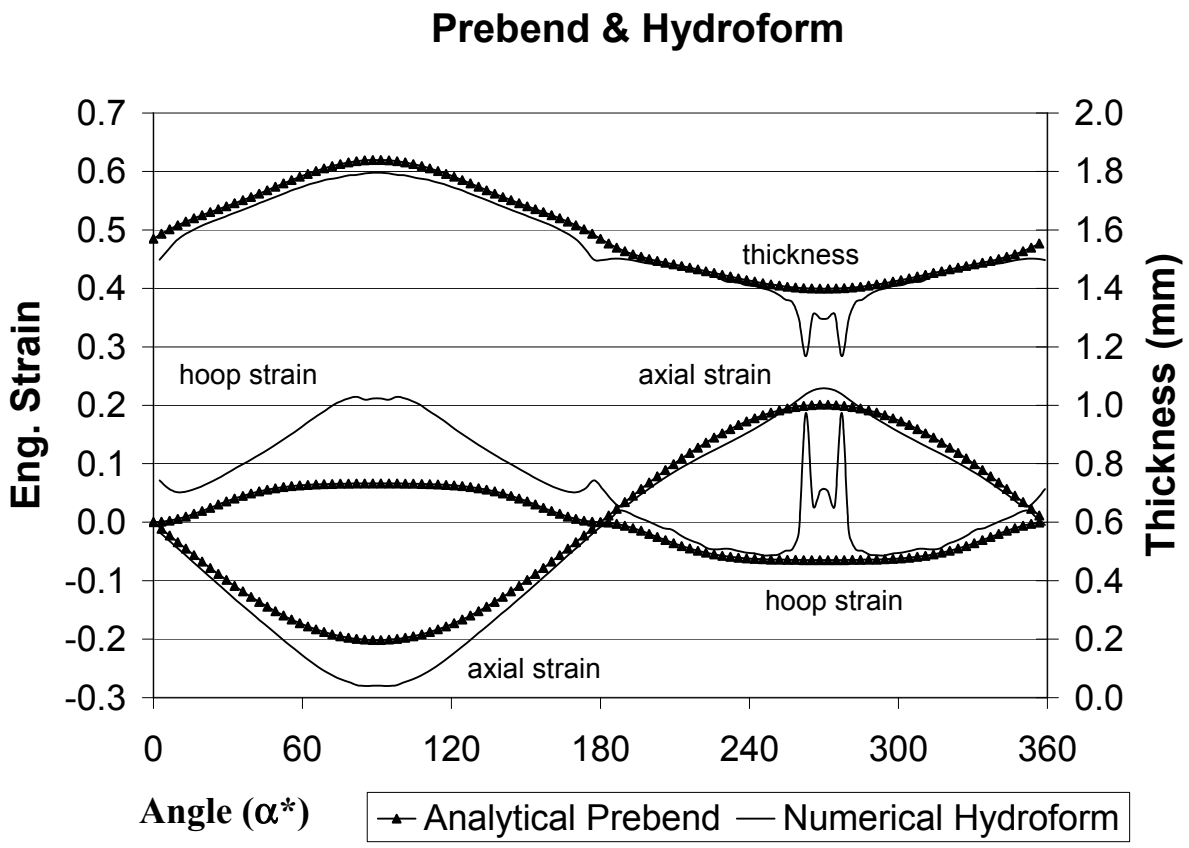

Figure 5.35: Numerical pre-bend and hydroforming

The lack of an evident localization peak in the experimental data is attributed to the actual failure in the experiment *not* occurring at the center of the bend. Instead the tubes failed prematurely at the clamp region, the region of local thinning during bending (Figure 5.37). Figure 5.36 is a photograph of a failed hydroform sample, which shows failure in the $\theta^* = 92^o$ region.

Figure 5.38 shows the strain and thickness distribution along the outside of the bend after hydroforming. The FE hydroforming predictions based on the two bend models, analytic and numerical, agree very well. The predictions show transient regions at the start and stop of

the bend and a "near steady-state" between roughly 20 – 70º. The experimental strain and thickness levels are close to the model predictions in the middle of the bend (θ* = 45º). There is a dramatic peak in the axial strain and thickness on the outside of the bend region (90 – 100º), corresponding to the same peak in the post-bending strains and thickness. As mentioned, this peak was unexpected and led to the bursting failure at the clamp end of the tube.

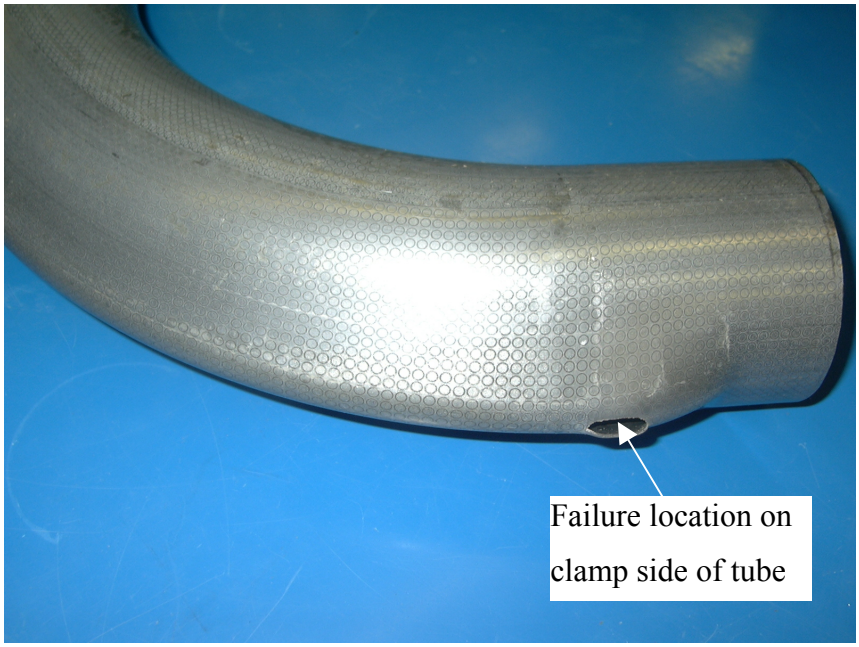

Figure 5.36: Failed tube sample

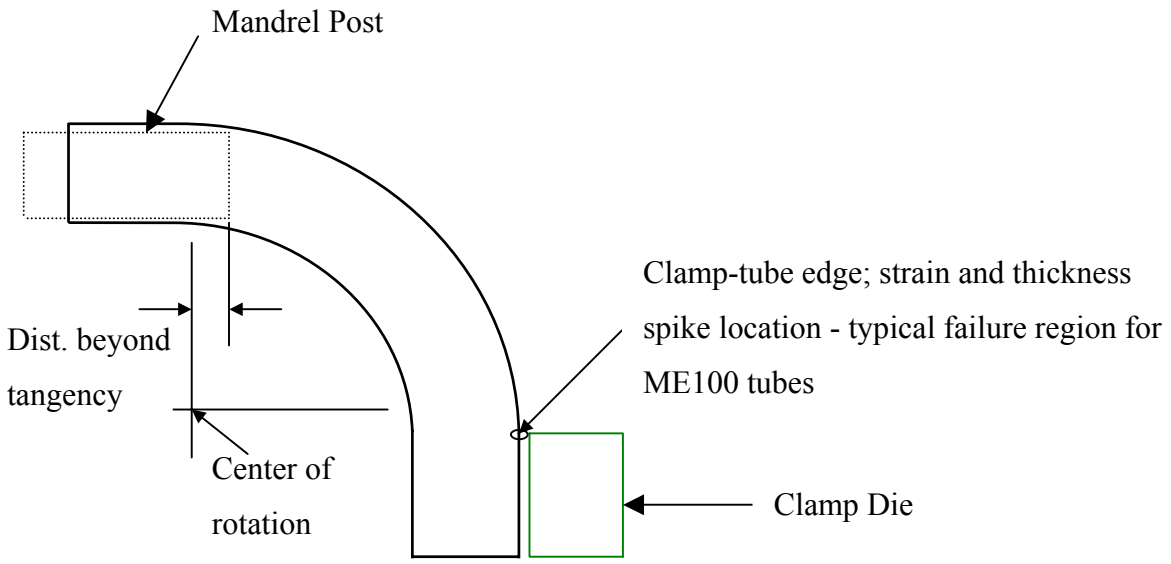

Figure 5.37: Failure region in tube after hydroforming

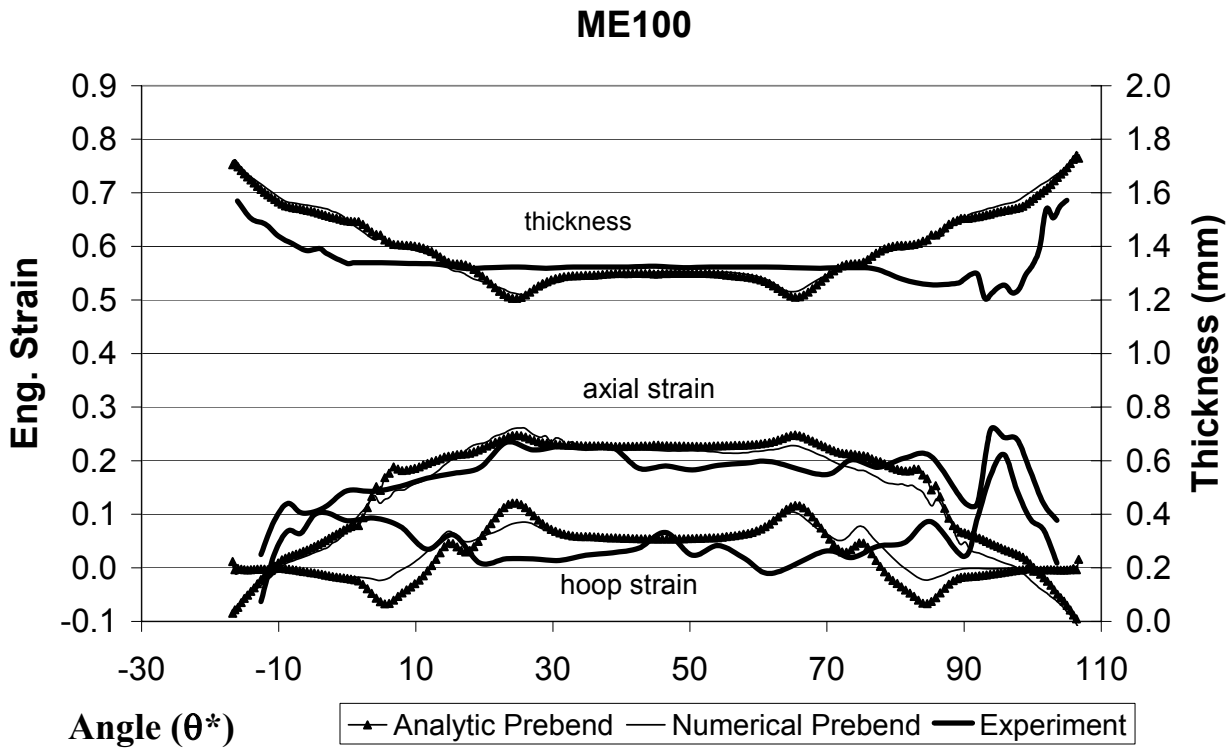

Figure 5.38: Strain and thickness comparison for analytic and numerical pre-bend, on outside

5.6.2 Pressure vs. Corner-fill Expansion

Figure 5.39 shows the corner-expansion versus pressure data for the models and experiment, for the ME100 case. The expansion is measured at $\theta^* = 45^\circ$ and $\alpha^* = 270^\circ$. The experimental data is for a single representative tube sample, hydroformed to burst.

The measured data lies between the predictions based on the two bend models. The analytical pre-bend leads to an over-prediction of the expansion, while the numerical pre-bend gives an under-prediction, as compared to experiment. The general shape of the curves are in reasonable agreement, however further effort is required to refine the current hydroforming predictions.

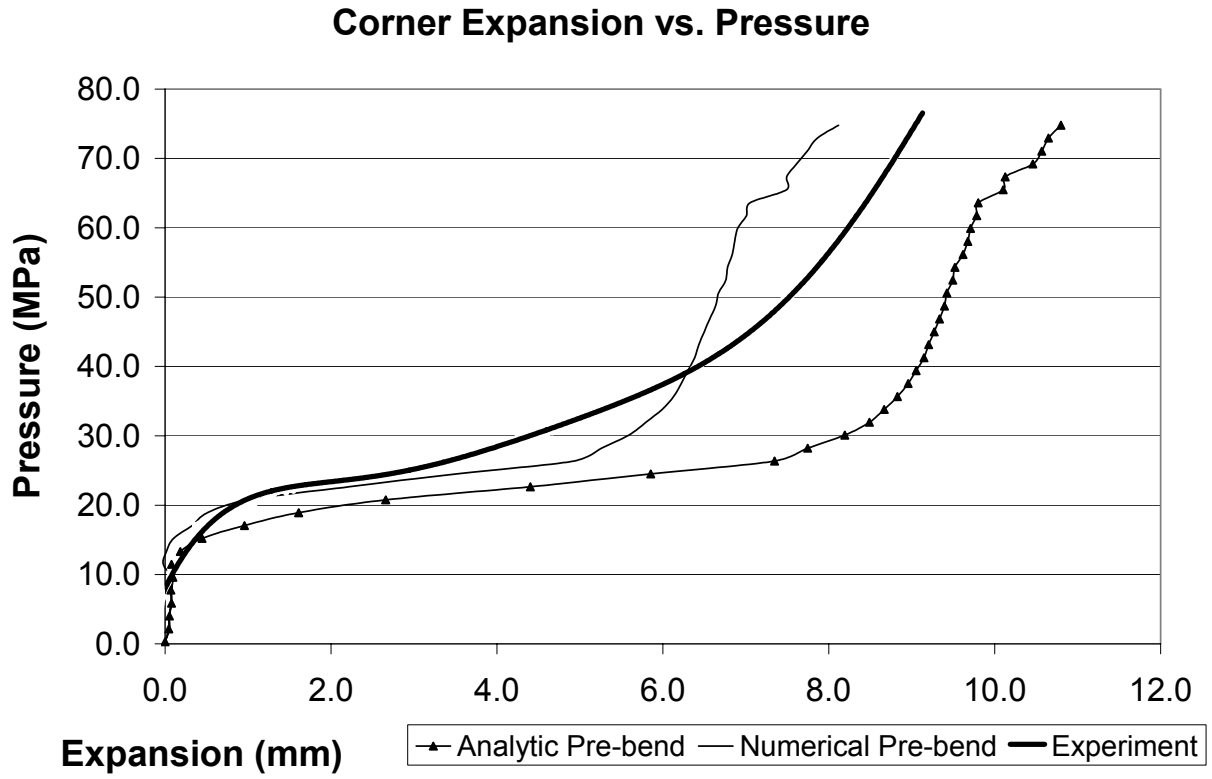

Figure 5.39: Corner expansion for ME100

Chapter 6- Discussion

The analytical bend model proves to be a very useful tool for approximating the tube bending process, as well as for predicting approximate bend parameters such as pressure die boost force, pre-springback bend angle, and minimum tube stock length for bending. This information can be quite useful for initial design studies, that can be further refined in accuracy through subsequent experimental or detailed FEA studies.

Another useful feature of the bend model, not studied in detail here, is its accommodation of bends in three-dimensions. This feature is attractive when one attempts to model multiple bends in complex parts; such models can take a great deal of time to set up in an FEA model, as well as requiring a much longer run time.

The analytical model compares well with experiment and FE predictions, and captures trends well, such as the decrease in axial strain due to increased boost levels. The analytical and FE pre-bend models also prove to result in similar hydroforming predictions of strains and thickness. When comparing the hydroforming simulations, using the analytical and numerical

pre-bend predictions, the analytical pre-bend model is of equal value to the numerical pre-bend model.

A clear shortcoming in the analytical and numerical modeling is the isotropic material assumption. There is a need to account for anisotropy such as the r-value effects present in steel and aluminum tubes that control rate of thinning. As shown in the tensile measurements in the 3, 6, and 9 o'clock positions, there is a difference in the stress-strain curves. Although small, these differences are indicative of variation in the as-received tube; however it is likely that the effect of these differences is small. Also, the influence of the weld seam on the material properties was not taken into account. Since the weld seam was oriented to lie close to the neutral axis, its effect is also thought to be small.

It is also the case that friction conditions weren't well represented in the models, especially in the analytical bend model. Estimated friction coefficients were used in the numerical FE model input, but the effect of friction on strain distribution and on tooling loads is neglected in the analytical models. Ongoing work by Bardelcik [39] seeks to determine improved friction coefficients.

As it turns out, friction mostly affects the external moments and forces required to bend a tube. For example, prescribed percent boost, bend angle, and net boost force are boundary conditions directly affecting the deformation of the tube, and thus affect the strains and thickness almost entirely independent of frictional affects. Therefore, neglecting friction in the analytical model is quite reasonable.

The premature failures that occur during hydroforming were caused by problems in the bend process settings. This problem was resolved by reducing the clamp die force. The

analytical model neglects this level of detail and is likely only useful in well-controlled processes.

Chapter 7- Conclusions and Future Work

7.1 Conclusions

The following conclusions are drawn for the experimental and modeling investigations.

Experiments:

1. Boost conditions, such as low, medium and high, are primary factors affecting the final tube strains and thickness after bending, for a given tube size diameter and R_c/d ratio.

2. Excessive clamp die pressure risks inducing a material weak point and premature failure in the hydroforming operation.

Analytical and numerical bend models:

1. The analytical bend model provided strain and thickness predictions in good accord with the experimental and numerical results, at a computation time that is three orders of magnitude less than the numerical FE model.

2. The analytical model can be used in engineering design studies as an alternative to a more detailed, much more time consuming FE model.

3. Friction conditions in the experiments are poorly modeled in the numerical simulations and neglected entirely in the analytical model.

7.2 Future Work

The following recommendations for future work stem from the results of this thesis:

1. Further improvements should be made to the existing analytical bend model, such as:
- accounting for material anisotropy
- accounting for non-uniform percent boost and boost force
- accommodating initial small variations in original tube wall thickness, as a function of circumferential angle
- improve residual stress calculations to better approximate static equilibrium after springback.

2. Improve friction modeling in the numerical models. To facilitate this, work is underway to gather more accurate friction data from twist compression tests.

3. Increase the available boost force in the tube bender to accommodate higher boost levels in future experimental bending trials.

4. Set up an apparatus to measure relative slip between the pressure die and tube as a function of time during bending, as a means to better understand transient slip behavior and to provide better validation data.

References

1. Tube sample hydroformed at the University of Waterloo, as part of the Auto21 project on tube and sheet forming, 2004.
2. L.G. Afendik, "Bending Thin-Walled Tubes with Considerable Curvature Beyond the Elastic Limit", *Prikladnaya Mekhanika*, Vol.4, No.6, pp. 45-51, 1968.
3. L.C. Zhang, T.X. Yu, "An Investigation of the Brazier Effect of a Cylindrical Tube under Pure Elastic-Plastic Bending", *International Journal of Pressure Vessels and Piping*, vol. 30, pp. 77-86, 1987.
4. K.Pan, K.A. Stelson, "On the Plastic Deformation of a Tube During Bending", *Transactions of the ASME*, vol. 117, pp. 494-500, November 1995.
5. Z.T. Zhang and J.L. Duncan, "Strain Modeling and Measurement in Tube Bending", *ASME*, pp. 151-157, February 1996.
6. N.C. Tang, "Plastic-deformation analysis in tube bending", *International Journal of Pressure Vessels and Piping*, vol. 77, pp. 751-759, 2000.
7. H.A. Al-Qureshi, "Elastic-plastic analysis of tube bending", *International Journal of Machine Tools and Manufacture*, vol. 39, pp. 87-104, 1999.
8. H.A. Al-Qureshi, A.Russo, "Spring-back and residual stresses in bending of thin-walled aluminum tubes", *Materials and Design*, vol. 23, pp. 217-222, 2002.
9. K. Trana, "Finite element simulation of the tube hydroforming process-bending, preforming and hydroforming", *Journal of Materials Processing Technology*, vol. 127, pp. 401-408, 2002.
10. N. Dwyer, M. Worswick, J. Gholipour, C. Xia, G. Khodayari, "Pre-bending and subsequent hydroforming of tube: simulation and experiment", *Proceedings of Numisheet 2002,* pp. 447-452, 2002.
11. J. Yang, B. Jeon, S. Oh, "The tube bending technology of a hydroforming process for an automotive part", *Journal of Materials Processing*, vol. 111, pp. 175-181, 2001.

12. J. N. Dyment, M. J. Worswick, F. Normani, D. Oliveira, G. Khodayari "Effect of endfeed on the strains and thickness during bending and on the subsequent hydroformability of Steel Tubes", *IBEC 2003 Conference Proceedings*, pp. 717-722, 2003.
13. J. Gholipour, M. J. Worswick, D. Oliveira, "Application of damage models in bending and hydroforming of aluminum alloy tube", *SAE congress proceedings*, 2004.
14. E. E. Pavlovskaia, Z. C. Xia, "Analytical modeling of hydroforming pre-bend process: Without Inner Mandrel", *SAE International*, pp. 25-33, 2004.
15. M. Koc, T. Altan, "An overall review of the tube hydroforming (THF) technology", *Journal of Materials Processing Technology*, vol. 108, pp. 384-393, 2001.
16. F. Dohmann, C. Hartl, "Tube hydroforming – research and practical application", *Journal of Materials Processing Technology*, vol. 71, pp. 174-186, 1997.
17. M. Ahmetoglu, T. Altan, "Tube hydroforming: state-of-the-art and future trends", *Journal of Materials Processing Technology*, vol. 98, pp. 25-33, 2000.
18. B. Carleer, G. van der Kevie, L. de Winter, B. van Velhuizen, "Analysis of the effect of material properties on the hydroforming process of tubes", *Journal of Materials Processing Technology*, pp. 158-166, 2000.
19. M. Koc, Y. Aue-u-lan, T. Altan, "On the characteristics of tubular materials for hydroforming – experimentation and analysis", *International Journal of Machine Tools & Manufacture*, vol. 41, pp. 761-772, 2001.
20. N. Asnafi, "Analytical modelling of tube hydroforming", *Thin-walled Structures*, pp. 295-330, 1999.
21. C. L. Chow, X. J. Yang, "Bursting for fixed tubular and restrained hydroforming", *Journal of Materials Processing Technology*, vol. 130-131, pp. 107-114, 2002.
22. G. Nefussi, A. Combescure, "Coupled buckling and plastic instability for tube hydroforming", *International Journal of Mechanical Sciences*, vol. 44, pp. 899-914, 2002.
23. H. L. Xing, A. Makinouchi, "Numerical analysis and design for tubular hydroforming", *International Journal of Mechanical Sciences*, vol. 43, pp. 1009-1026, 2001.

24. W. Rimkus, H. Bauer, M. J. A Mihsein, “Design of load-curved for hydroforming applications”, *Journal of Materials Processing Technology*, vol. 108, pp. 97-105, 2000.
25. Z. C. Xia, “Failure analysis of tubular hydroforming”, *Journal of Engineering Materials and Technology*, vol. 123, pp. 423-429, 2001.
26. J. Tirosh, A. Neuberger, A. Shirizly, “On tube expansion by internal fluid pressure with additional compressive stress”, *International Journal of Mechanical Sciences*, No. 8-9, pp. 839-851, 1996.
27. M. Koc, T. Altan, “Prediction of forming limits and parameters in the tube hydroforming process”, *International Journal of Machine Tools & Manufacture*, vol. 42, pp. 123-138, 2002.
28. M. Koc, “Investigation of the effect of loading path and variation in material properties on robustness of the tube hydroforming process”, *Journal of Materials Processing Technology*, vol. 133, pp. 276-281, 2003.
29. N. Asnafi, A. Skogsgardh, “Theoretical and experimental analysis of stroke-controlled tube hydroforming”, *Materials Science and Engineering*, A279, pp. 95-110, 2000.
30. J. Kim, S. J. Kang, B. S. Kang, “A comparative study of implicit and explicit FEM for the wrinkling prediction in the hydroforming process”, *International Journal of Advanced Manufacturing Technology*, pp. 547-552, 2003.
31. M. Koc, T. Allen, S. Jiratheranat, T. Altan, “The use of FEA and design of experiments to establish design guidelines for simple hydroformed parts”, *International Journal of Machine Tools & Manufacture*, vol. 40, pp. 2249-2266, 2000.
32. J. C. Gelin, C. Labergere, “Application of optimal design and control strategies to the forming of thin walled metallic components”, *Journal of Materials Processing Technology*, vol. 125-126, pp. 565-572, 2002.
33. B. J. MacDonald, M. S. J. Hashmi, “Near-net-shape manufacture of engineering components using bulge-forming processes: a review”, *Journal of Materials Processing Technology*, vol. 120, pp. 341-347, 2002.

34. B. J. MacDonald, M. S. J. Hashmi, "Three-dimensional finite element simulation of bulge forming using a solid bulging medium", *Finite Elements in Analysis and Design*, vol. 37, pp. 107-116, 2001.
35. Y. M. Hwang, T. Altan, "Finite element analysis of tube hydroforming processes in a rectangular die", *Finite Elements in Analysis and Design*, vol. 39, pp. 1071-1082, 2002.
36. G. T. Kridli, L. Bao, P.K. Mallick, Y. Tian, "Investigation of thickness variation and corner filling in tube hydroforming", *Journal of Materials Processing Technology*, vol. 133, pp. 287-296, 2003.
37. K. Manabe, M. Amino, "Effects of process parameters and material properties on deformation process in tube hydroforming", *Journal of Materials Processing Technology*, vol. 123, pp. 285-291, 2002.
38. G. Khodayari, H. Reid, J. V. Reid, "The influence of the lubricant during tube hydroforming", *Industrial Research and Development Institute*, Midland, Ontario, Canada, 2003.
39. A. Bardelcik, ongoing study in TCT, private communication, MASc candidate, University of Waterloo, 2004.
40. F. Vollertsen, M. Plancak, "On possibilities for the determination of the coefficient of friction in hydroforming of tubes", *Journal of Materials Processing Technology*, vol. 125-126, pp. 412-420, 2002.
41. D. A. Oliveira, M. J. Worswick, R. Grantab, J. Dyment, "Effect of lubricant in mandrel-rotary draw tube bending of steel and aluminum", submitted to *Canadian Metallurgical Quarterly*, under review, 2004.
42. K. Gong, US/CAR hydroforming study, Alcan, 2001.
43. J. Dyment, private communication, MASc candidate, University of Waterloo, 2004.
44. D. A. Oliveira, M. J. Worswick, G. Khodayari, J. Gholipour, M. Wenner, "Effect of bending parameters on subsequent hydroformability of AlMg3.5Mn tubes (Part II)". Soon to be published, April, 2004.
45. Y. Lee, "Formability of aluminum alloy tailor welded blanks", Masters Thesis, Dept. of Mechanical Engineering, University of Waterloo, 2002.

46. N. Cinotti, “Stretch flange formability of aluminum alloy sheet”, Masters Thesis, Dept. of Mechanical Engineering, University of Waterloo, 2002.
47. A. C. Ugural, S. K. Fenster, “Advanced Strength and Applied Elasticity”, 3rd ed., *Prentice Hall*, pp. 473-474, 1995.
48. R. C. Hibbeler, “Mechanics of Materials”, 2nd ed., *Prentice Hall*, pp. 330-334, 1994.
49. W. H. Press, B. P. Flannery, S. A. Teukolsky, W. T. Vetterling, “Numerical Recipes in C: The Art of Scientific Computing”, 2nd ed., *Cambridge University Press*, pp. 353-354, 1992.
50. A. C. Ugural, S. K. Fenster, “Advanced Strength and Applied Elasticity”, 3rd ed., *Prentice Hall*, pp. 28-31, 1995.
51. A. C. Ugural, S. K. Fenster, “Advanced Strength and Applied Elasticity”, 3rd ed., *Prentice Hall*, pp. 117, 1995.

Appendix A – Details of the Analytical Bend Model

This appendix outlines the more detailed mathematical formulations of the analytical bend model, which are not covered in Chapter 3.

A.1 - Numerical Procedure for Solving Hoop Strain

From Chapter 3, equations (3.9) – (3.12) were introduced as a mathematical means to approximate hoop strain:

$$\varepsilon_1^a = \frac{1}{E_s^a} \cdot (\sigma_1^a - \frac{1}{2}\sigma_2)$$

$$\varepsilon_2^a = \ln(1+\frac{m}{L_a}) = \frac{1}{E_s^a} \cdot (\sigma_2 - \frac{1}{2}\sigma_1^a)$$

$$\varepsilon_1^b = \frac{1}{E_s^b} \cdot (\sigma_1^b - \frac{1}{2}\sigma_2)$$

$$\varepsilon_2^b = \ln(1-\frac{m}{L_b}) = \frac{1}{E_s^b} \cdot (\sigma_2 - \frac{1}{2}\sigma_1^b)$$

Substituting the expressions, discussed earlier, for ε_1^a, ε_1^b, E_s^a, E_s^b, L_a, L_b, one can solve for m in (3.9) – (3.12). The numerical technique used to solve these is the Bisection Method and is applied as follows.

First bound σ_2, σ_1^a and σ_1^b, knowing that the solution must lie within certain bounds. Since the tube material is treated as isotropic, the effective von-Mises stress formulation is used, for plane stress,

$$\sigma_{eff} = \sqrt{\sigma_1^2 - \sigma_1 \cdot \sigma_2 + \sigma_2^2} \tag{A.1}$$

Now, let us look at a "worst case" where the stresses are quite high for a plane strain condition where $\varepsilon_{hoop} = 0$. This means that $\sigma_2 = \frac{1}{2}\sigma_1$. Substituting this into the expression for σ_{eff} one can solve for σ_1. Therefore, solving one obtains $\sigma_1 = \pm\frac{2}{\sqrt{3}}\sigma_{eff}$. Now, this is not an expression for σ_2, but since $|\sigma_1| > |\sigma_2|$ then let us use $|\sigma_2| = \frac{2}{\sqrt{3}}\sigma_{eff}$ as an upper and lower bound for σ_2, without being so large that σ_{eff} is exceeded. Treating σ_{eff} as a constant, and setting $\overline{\sigma}_{\max} \equiv \sigma_{eff}$, its value is chosen to be large and a suitable upper bound.

In the case of a given power law expression, $\sigma_{eff} = K \cdot (\varepsilon_{eff}^{pl} + \varepsilon_{yp})^n$, one sets $\overline{\sigma}_{\max} = K \cdot (1.0)^n$ which is for a strain of 1.0, clearly an upper bound. Given a flow curve, $\overline{\sigma}_{\max}$ is the value corresponding to the largest strain.

As a result, one can now write the upper and lower bound for σ_2.

$$\begin{aligned} \sigma_2^{lower} &= -\frac{2}{\sqrt{3}}\overline{\sigma}_{\max} \\ \sigma_2^{upper} &= \frac{2}{\sqrt{3}}\overline{\sigma}_{\max} \end{aligned} \tag{A.2}$$

Let's consider now the upper and lower bounds for σ_1^a and σ_1^b. For σ_1^a look first at the lower bound. This can be deduced by using a lower bound value for E_s^a in (3.9). One can

choose this lower bound to be $E_s^a = \dfrac{\sigma_{yield}}{\varepsilon_{\max}}$, where ε_{max} is ε_{max} = 1.0, or ε_{max} is the largest strain value in the flow curve. Therefore, solving for σ_1 in (3.9), one obtains

$$\sigma_1^a = \frac{\sigma_{yield}}{\varepsilon_{\max}} \cdot \varepsilon_1^a + \frac{1}{2}\sigma_2 \tag{A.3}$$

Since ε_1^a < 0, this value for σ_1^a becomes a *lower* bound when σ_2^{upper} and σ_2^{lower} is substituted for σ_2.

For an *upper* bound for σ_1^a substitute σ_2^{upper} and σ_2^{lower}, for σ_2, into $\overline{\sigma}_{\max} = \sqrt{\sigma_1^2 - \sigma_1 \cdot \sigma_2 + \sigma_2^2}$ and solve for σ_1, calling it σ_1^a. One obtains (rejecting the positive root)

$$\sigma_1^a = -\sqrt{\overline{\sigma}_{\max}^2 - \frac{3}{4}\sigma_2^2} + \frac{1}{2}\sigma_2 \tag{A.4}$$

Using the same methodology for σ_1^b, one obtains

$$\sigma_1^b = \frac{\sigma_{yield}}{\varepsilon_{\max}} \cdot \varepsilon_1^b + \frac{1}{2}\sigma_2 \tag{A.5}$$

which becomes an *upper* bound when σ_2^{upper} and σ_2^{lower} is substituted for σ_2 (since ε_1^b > 0). As before, but rejecting the negative root,

$$\sigma_1^b = \sqrt{\overline{\sigma}_{\max}^2 - \frac{3}{4}\sigma_2^2} + \frac{1}{2}\sigma_2 \tag{A.6}$$

and this becomes a *lower* bound when σ_2^{upper} and σ_2^{lower} is substituted for σ_2.

A.2 - Application of Bisection Method for Hoop Strain Calculation

The Bisection method is an iterative technique to solve a function based on a lower bound, upper bound and a midpoint value [49]. To illustrate consider Figure A.1:

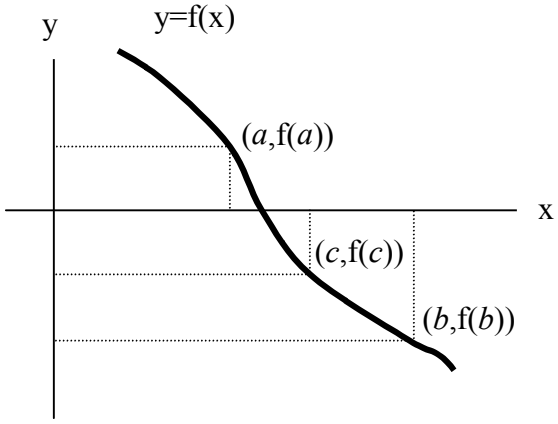

Figure A.1: Illustration of bisection method for a function y = f(x)

Here, a represents an upper bound guess, and b a lower bound guess. c is the midpoint of a and b, $c = \frac{a+b}{2}$. Also, a and b must be such that y(a) > 0 and y(b) < 0 or vice versa.

There is a point p such that y(p) = 0. By progressively marching through an iteration scheme the point c gets closer and closer to the exact value p, so that after a sufficient number of iterations one achieves a very good approximation for p.

Given two initial guesses for upper and lower bound, call them a_1 and b_1, one calculates $c_1 = \frac{a_1 + b_1}{2}$. With these starting values calculated, one can now write the remainder of the method in a mathematical way.

For $1 \leq i \leq N$, N sufficiently large for convergence, apply the following:

If f(c_i) < 0 and f(a_i) > 0, set $a_{i+1} = a_i$ and $b_{i+1} = c_i$

If f(c_i) < 0 and f(b_i) > 0, set $a_{i+1} = c_i$ and $b_{i+1} = b_i$

If f(c_i) > 0 and f(b_i) < 0, set $a_{i+1} = c_i$ and $b_{i+1} = b_i$

If f(c_i) > 0 and f(a_i) < 0, set $a_{i+1} = a_i$ and $b_{i+1} = c_i$

and repeat N times, with the result f(c_N) ≅ 0, where c_N is approximately the solution.

To solve for m in (3.9) – (3.12), one first divides up the problem so that one solves (3.9), (3.10) for $m \equiv m_1$, and solves (3.11), (3.12) for $m \equiv m_2$; then various values of σ_2 are "marched" through until $m_1 \cong m_2$ (compatibility), which allows us to find the engineering hoop strain easily.

With the known quantities: ε_1^a, ε_1^b, E_s^a, E_s^b, L_a, L_b; one can then proceed to solve for m. Key mathematical terms can be written as follows:

Set

$$y_1 = f_1(\sigma_1^a) = \frac{1}{E_s^a} \cdot (\sigma_1^a - \frac{1}{2}\sigma_2) - \varepsilon_1^a$$

$$y_2 = f_2(\sigma_1^b) = \frac{1}{E_s^b} \cdot (\sigma_1^b - \frac{1}{2}\sigma_2) - \varepsilon_1^b \qquad \text{(A.7)}$$

$$y_3 = f_3(\sigma_2) = m_1 - m_2$$

To start the iteration, to solve for m_1, set $a_{11} = \sigma_1^a$ from (A.3) and set $b_{11} = \sigma_1^a$ from (A.4) (to set an upper and lower bound), and calculate midpoint c_{11}. To start the iteration, to solve for m_2, set $a_{12} = \sigma_1^b$ from (A.5) and set $b_{12} = \sigma_1^b$ from (A.6) (to set an upper and lower bound), and calculate midpoint c_{12}.

Using slightly different notation from before, define the algorithm to solve for m_1:

$\{$ If $f_1(c_{i1}) < 0$ and $f_1(a_{i1}) > 0$, set $a_{(i+1)1} = a_{i1}$ and $b_{(i+1)1} = c_{i1}$

If $f_1(c_{i1}) < 0$ and $f_1(b_{i1}) > 0$, set $a_{(i+1)1} = c_{i1}$ and $b_{(i+1)1} = b_{i1}$

If $f_1(c_{i1}) > 0$ and $f_1(b_{i1}) < 0$, set $a_{(i+1)1} = c_{i1}$ and $b_{(i+1)1} = b_{i1}$

If $f_1(c_{i1}) > 0$ and $f_1(a_{i1}) < 0$, set $a_{(i+1)1} = a_{i1}$ and $b_{(i+1)1} = c_{i1}$ $\}$ (A)

repeat this N_1 times until convergence, for $1 \le i \le N_1$ to solve for $m \equiv m_1$

Similarly for m_2:

$\{$ If $f_2(c_{i2}) < 0$ and $f_2(a_{i2}) > 0$, set $a_{(i+1)2} = a_{i2}$ and $b_{(i+1)2} = c_{i2}$

If $f_2(c_{i2}) < 0$ and $f_2(b_{i2}) > 0$, set $a_{(i+1)2} = c_{i2}$ and $b_{(i+1)2} = b_{i2}$

If $f_2(c_{i2}) > 0$ and $f_2(b_{i2}) < 0$, set $a_{(i+1)2} = c_{i2}$ and $b_{(i+1)2} = b_{i2}$

If $f_2(c_{i2}) > 0$ and $f_2(a_{i2}) < 0$, set $a_{(i+1)2} = a_{i2}$ and $b_{(i+1)2} = c_{i2}$ $\}$ (B)

repeat this N_1 times until convergence, for $1 \le i \le N_1$ to solve for $m \equiv m_2$.

Note that (A) and (B) are for a given value of σ_2. The value of σ_2 must be such that $m_1 = m_2$ (compatibility). So, to solve for σ_2 one uses the bisection algorithm again. Basically two bisection algorithms, (A) and (B), are nested inside a main bisection algorithm, call it (C). (A) and (B) are executed inside (C) each N_1 times (for each single value of σ_2) and then $y_3 = f_3(\sigma_2) = m_1 - m_2$ is calculated.

For (C), the iteration must be started off by setting $a_{13} = \sigma_2^{lower}$, setting $b_{13} = \sigma_2^{upper}$, and calculating the midpoint c_{13}. As before, let's now define (C):

$\{$If $f_3(c_{i3}) < 0$ and $f_3(a_{i3}) > 0$, set $a_{(i+1)3} = a_{i3}$ and $b_{(i+1)3} = c_{i3}$

If $f_3(c_{i3}) < 0$ and $f_3(b_{i3}) > 0$, set $a_{(i+1)3} = c_{i3}$ and $b_{(i+1)3} = b_{i3}$

If $f_3(c_{i3}) > 0$ and $f_3(b_{i3}) < 0$, set $a_{(i+1)3} = c_{i3}$ and $b_{(i+1)3} = b_{i3}$

If $f_3(c_{i3}) > 0$ and $f_3(a_{i3}) < 0$, set $a_{(i+1)3} = a_{i3}$ and $b_{(i+1)3} = c_{i3}$ $\}$ (C)

and this is repeated N_2 times until convergence, for $1 \le i \le N_2$, to solve for σ_2 such that $m \cong m_1 \cong m_2$.

Therefore, one can now calculate ε_{hoop} directly with the expressions from before

$$\varepsilon_2^{a,eng} = \frac{m}{L_a}$$

and

$$\varepsilon_2^{b,eng} = -\frac{m}{L_b}$$

Then the final result is,

$$\varepsilon_{hoop} = \begin{Bmatrix} f \cdot \varepsilon_2^{b,eng}, \, for \, 0 \le \alpha \le \alpha_{NA} \\ f \cdot \varepsilon_2^{a,eng}, \, for \, \alpha_{NA} \le \alpha \le \pi \end{Bmatrix}$$

A.3 - Calculation of upper and lower bound value for l^b

The initial bounds of l^b (to calculate F_{boost}), as mentioned earlier, are not trivial to calculate. The bounds are such that the axial strains (over $-d/2 \le y \le d/2$) are entirely compressive or entirely tensile, in a borderline sense. This means that the upper bound for l^b, a positive value (corresponding to $F_{boost} < 0$), must be such that $\varepsilon_1 \le 0$ everywhere, and $\varepsilon_{max} \approx 0$ at $y = d/2$. In other words, the compressive "push" force F_{boost} is high enough so that the induced positive membrane strain $e(\alpha=0)$ cancels out the maximum tensile strain created by pure

bending, at y = d/2. The lower bound for l^b, a negative value (corresponding to $F_{boost} > 0$), must be such that $\varepsilon_1 \geq 0$ everywhere in the local coordinate system, and $\varepsilon_{min} \approx 0$ at y = -d/2. In other words, the tensile "pull" force F_{boost} is high enough so that the induced negative membrane strain $e(\alpha=\pi)$ cancels out the maximum compressive strain created by pure bending, at y = -d/2.

These limits for l^b bound the problem nicely, and are quite reasonable since at the upper bound of l^b one is, in reality, risking serious wrinkling on the inside of the tube. In contrast, at the lower bound of l^b one is risking tensile fracture on the outside of the tube due to excessive stretching of material. Thus it is impractical and unrealistic to accommodate the model to account for a boost force F_{boost}, which would push the axial strain outside the allowed bounds.

Therefore, one can solve for the *upper* bound of l^b, from (3.19), by setting $y = r_o$, and setting

$$e(\alpha = 0) = -\ln\left(1 + \frac{y + A}{R_c - A}\right) \tag{A.8}$$

One can then solve for l^b from the volume conservation equation (3.27) shown earlier (at α=0).

To solve for the *lower* bound of l^b one sets $y = -r_o$, and set

$$e(\alpha = \pi) = -\ln\left(1 + \frac{y + A}{R_c - A}\right) \tag{A.9}$$

and again using the volume conservation equation one can solve for l^b (at $\alpha=\pi$).

As a side-note, it is interesting to mention that, as the axial strain approaches a fully tensile or compressive value over the tube cross-section, the hoop strain calculated, by the model, approaches zero. Physically this makes sense since every element in the cross-section is either "pushing" or "pulling" against each other in the hoop direction. This results in much less

hoop straining than if some elements were “pulling” and others “pushing”, in the hoop direction, as is the case in a regime with axial compression and tension regions. So based on this observation one can speculate that there is *no* (or very little) hoop straining when the axial strain regime is fully tensile or fully compressive.

A.4 - Mesh Generation

The program user enters geometric data for the tube such as the length of the straight regions, the centerline bend radii, bend angle, and tube rotation. The shell mesh is generated so as to keep the aspect ratio as close to one as possible.

To clearly illustrate this consider the following step-by-step illustration for a tube with four distinct, non-coplanar bends, in Figure A.2.

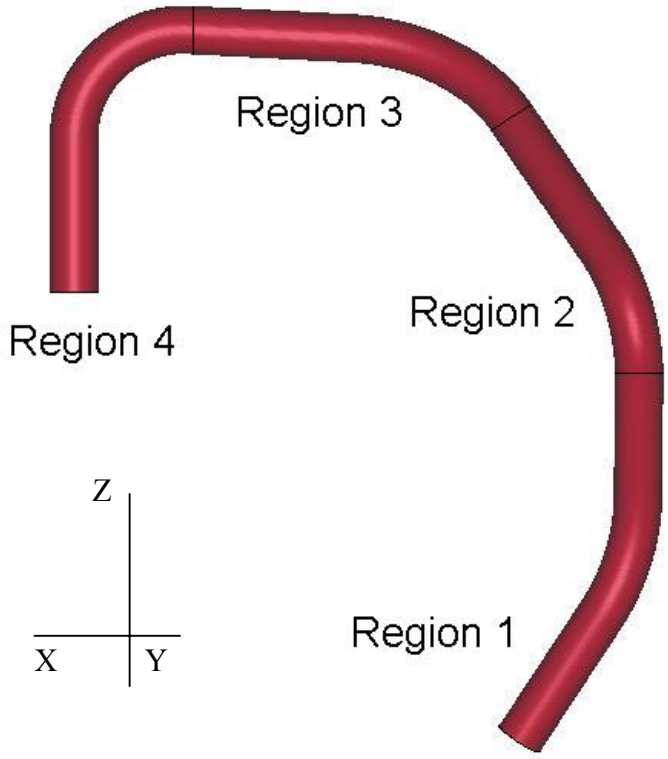

Figure A.2: Final configuration of bent tube with four bend regions

In the final finite element mesh the nodal coordinates, of each distinct region, is calculated from a set of transformations performed on the finite element mesh of each distinct region, in its original orientation (Figure A.3). To illustrate, let's consider an arbitrary region k in its original orientation, relative to the global Cartesian axes.

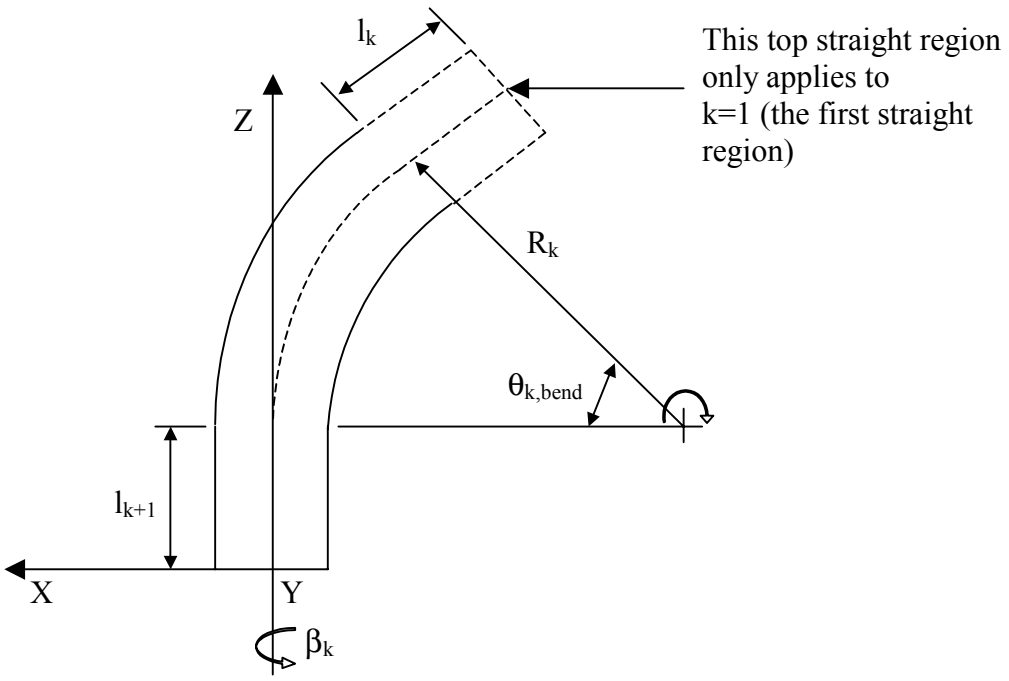

Figure A.3: Region k shown, in original configuration

R_k and θ_k (> 0) correspond to the centerline radius and the bend angle (about Y axis, normal to page) after springback, that is, the desired final geometry. l_k, l_{k+1} is the straight region length and β_k is the tube rotation about the Z axis following the (positive or negative) sign convention according to the right hand rule. Note that for bends all in one plane $\beta_k = \pm 180°$.

Also, the coordinates of the nodes in the original configuration are denoted as (X_o, Y_o, Z_o). From a physical perspective, β_k is a Z-rotation performed on the tube *after* a single bend of centerline radius R_k, at an angle $\theta_{k,bend}$ and translation in the positive Z-direction a distance l_{k+1} .

For example, let's look at the transformations T_k needed for each region k in a bent tube with 4 bend regions ($1 \leq k \leq N$) such that the final nodal coordinates (for those regions)

correspond to the final configuration shown in Figure A.2. Note that for N bend regions there are N+1 straight regions.

Region 1: The original configuration corresponds to k = 1. This region has the most transformations. Each transformation group consists of (in order) a Z-rotation β, a Y-rotation θ_{bend} and a Z-translation by a positive distance l. The final configuration (orientation) for region 1 is a result of 3 consecutive transformations of this sort.

For convenience, call each transformation group G_i where $1 \le i \le N-1$.

Now,

$$
\begin{aligned}
G_i : X_1 &= Ro_1 \cos(\theta o_1 + \beta_i) \\
Y_1 &= Ro_1 \sin(\theta o_1 + \beta_i) \\
Z_1 &= Z_o \\
\theta o_1 &= a\tan\left(\frac{Y_o}{X_o}\right),\ Ro_1 = \sqrt{X_o^2 + Y_o^2} \\
X_2 &= Ro_2 \cos(\theta o_2 - \theta_{i+1,bend}) - R_{i+1} \\
Y_2 &= Y_1 \\
Z_2 &= Ro_2 \sin(\theta o_2 - \theta_{i+1,bend}) + l_{i+2} \\
\theta o_2 &= a\tan\left(\frac{Z_1}{X_1 + R_{i+1}}\right),\ Ro_2 = \sqrt{(X_1 + R_{i+1})^2 + Z_1^2}
\end{aligned}
\qquad \text{(A.10)}
$$

Now,

$T_1 = \{G_1, G_2, G_3\}$, and for G_2 and G_3 the (X_o,Y_o,Z_o) values are set to the (X_2,Y_2,Z_2) values from the previous G operation. For G_1 the (X_o,Y_o,Z_o) values are from the original configuration as shown in Figure A.3. Note that for region 1, and *only* for region 1, the original (X_o,Y_o,Z_o) values correspond to the bend region R_1 and the *two* straight regions l_1 and l_2 .

Similarly, $T_2 = \{G_2, G_3\}$, the original (X_o,Y_o,Z_o) values correspond to the bend region R_2 and the *one* straight region l_3. The (X_o,Y_o,Z_o) values for G_3 correspond to the (X_2,Y_2,Z_2) values from the previous G_2.

$T_3 = \{G_3\}$, and the original (X_o,Y_o,Z_o) values correspond to the bend region R_3 and the straight region l_4.

The last region, defined by R_4 and l_5, requires no transformation and stays in the original orientation.

So, to generalize for a tube with N bend regions, for each region k, with $1 \le k \le N-1$:

$T_k = \{G_k, G_{k+1}, ..., G_{N-1}\}$, where the G operations are performed in order from G_k to G_{N-1}, and the transformation (T_K) is performed on the nodal coordinates on the finite element tube mesh in the original configuration (orientation) as shown in Figure A.3, to give the final configuration, as shown in Figure A.2. For each of $G_{k+1},\ldots,G_{N-1}$ the (X_o,Y_o,Z_o) values are taken from the (X_2,Y_2,Z_2) values from the previous G operation. For G_k the (X_o,Y_o,Z_o) values are from the original tube configuration.

A.5 - Stress and Strain Transformation

To transform the stresses and strains, in the local coordinate frame, to the corresponding stresses and strains in the global reference frame (as required for LS-DYNA input) one needs direction cosines. From the 4 nodal coordinates (in the final configuration) for each shell element it is simple to calculate the three normals in the 1, 2, and 3 directions (aligned with the local $x_1 x_2 x_3$ reference frame). These nodal coordinates are relative to the global reference frame,

therefore the direction cosines will be *relative* to the global reference frame. Let's call these direction normals $\mathbf{n_1} = (l_1, m_1, n_1)$, $\mathbf{n_2} = (l_2, m_2, n_2)$, $\mathbf{n_3} = (l_3, m_3, n_3)$.

To calculate the residual stresses and strains in the global reference frame one needs the direction cosines of the global reference frame *relative* to the local reference frame. These direction cosines are then $\mathbf{N_1} = (L_1, M_1, N_1)$, $\mathbf{N_2} = (L_2, M_2, N_2)$, $\mathbf{N_3} = (L_3, M_3, N_3)$, where $L_1 = l_1$, $M_1 = l_2$, $N_1 = l_3$, $L_2 = m_1$, $M_2 = m_2$, $N_2 = m_3$, $L_3 = n_1$, $M_3 = n_2$, $N_3 = n_3$. See Figure A.4.

Therefore, the residual stresses in the global frame are [50]:

$$\begin{aligned}
\sigma_{XX} &= \sigma_1^{res} \cdot L_1^2 + \sigma_2^{res} \cdot M_1^2 \\
\sigma_{YY} &= \sigma_1^{res} \cdot L_2^2 + \sigma_2^{res} \cdot M_2^2 \\
\sigma_{ZZ} &= \sigma_1^{res} \cdot L_3^2 + \sigma_2^{res} \cdot M_3^2 \\
\sigma_{XY}^{g} &= \sigma_1^{res} \cdot L_1 \cdot L_2 + \sigma_2^{res} \cdot M_1 \cdot M_2 \\
\sigma_{XZ}^{g} &= \sigma_1^{res} \cdot L_1 \cdot L_3 + \sigma_2^{res} \cdot M_1 \cdot M_3 \\
\sigma_{YZ}^{g} &= \sigma_1^{res} \cdot L_2 \cdot L_3 + \sigma_2^{res} \cdot M_2 \cdot M_3
\end{aligned} \tag{A.11}$$

The strains in the global frame are [50]:

$$\begin{aligned}
\varepsilon_{XX} &= \varepsilon_1 \cdot L_1^2 + \varepsilon_2 \cdot M_1^2 + \varepsilon_3 \cdot N_1^2 \\
\varepsilon_{YY} &= \varepsilon_1 \cdot L_2^2 + \varepsilon_2 \cdot M_2^2 + \varepsilon_3 \cdot N_2^2 \\
\varepsilon_{ZZ} &= \varepsilon_1 \cdot L_3^2 + \varepsilon_2 \cdot M_3^2 + \varepsilon_3 \cdot N_3^2 \\
\varepsilon_{XY}^{g} &= \varepsilon_1 \cdot L_1 \cdot L_2 + \varepsilon_2 \cdot M_1 \cdot M_2 + \varepsilon_3 \cdot N_1 \cdot N_2 \\
\varepsilon_{XZ}^{g} &= \varepsilon_1 \cdot L_1 \cdot L_3 + \varepsilon_2 \cdot M_1 \cdot M_3 + \varepsilon_3 \cdot N_1 \cdot N_3 \\
\varepsilon_{YZ}^{g} &= \varepsilon_1 \cdot L_2 \cdot L_3 + \varepsilon_2 \cdot M_2 \cdot M_3 + \varepsilon_3 \cdot N_2 \cdot N_3
\end{aligned} \tag{A.12}$$

The residual stresses and strains are calculated for each integration point. For stresses, the program user has the option of selecting calculations to be performed on 7 or 28 integration

points, for each shell element. For each shell element the strains are calculated at 2 points - the inner integration point and the outer integration point (ip1 = -0.9491, ip7 = 0.9491), at the element center, as used by LS-DYNA. The $\mathbf{N_1}$, $\mathbf{N_2}$, $\mathbf{N_3}$ surface normals are constant over the shell element and for each integration point in the shell, with no accounting for the slight variation due to curvature, which is very small anyway over the tiny shell element.

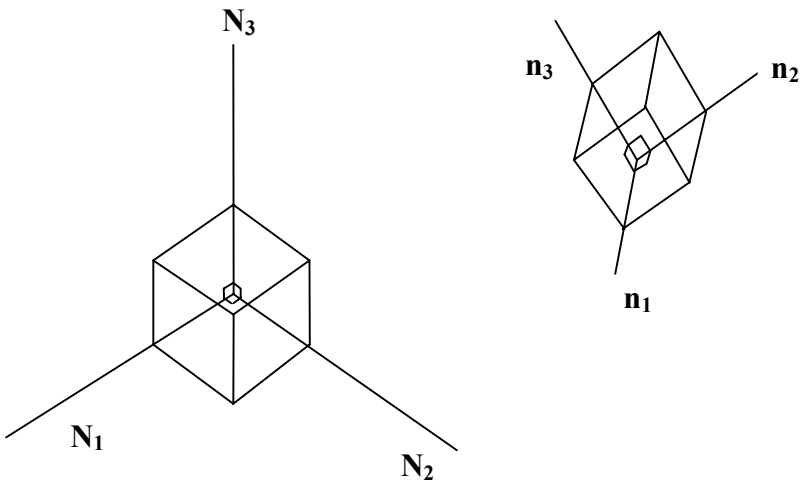

Figure A.4: Direction cosines for global and local coordinate systems

Figure A.5 shows the general stress state on an infinitesimal cube of material in a Cartesian system $X_1X_2X_3$. Note that the strains ε_{ij}, act in the same direction as the stresses σ_{ij}.

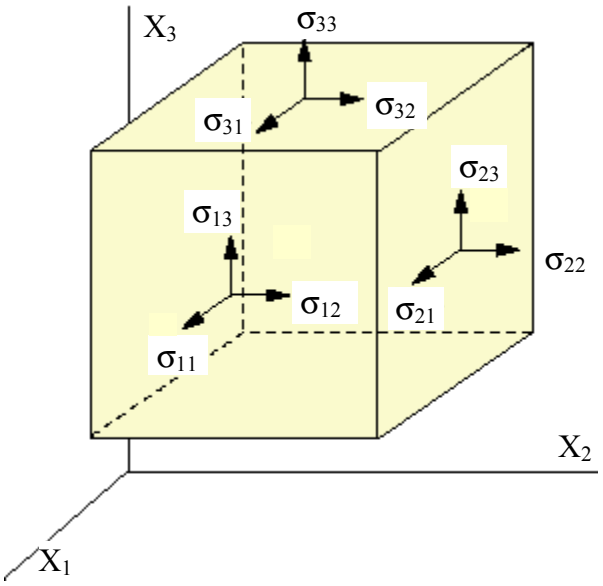

Figure A.5: General stress state for an element cube

A.6 – Location of Integration Points

The seven through-thickness integration points (ip) are defined to lie on a normal to the plane of the shell element (at the center). Their location can be calculated by simply choosing the correct radial distance r; since r by its definition coincides with the shell normal at the center of the shell plane (x_o, y_o, z_o). Therefore,

$$r_{\text{int } pt} = r_o + \frac{tnew}{2} \cdot ip \qquad \text{(A.13)}$$

where $r_o = \frac{d}{2} - \frac{t}{2}$ and is the midsurface radius,

and $ip \in \{-.9491, -.7415, -.4058, 0, .4058, .7415, .9491\}$

For 28 integration points, *each* of the seven through-thickness planes (at the location of the seven ip), contains 4 in-plane integration points. For 7 integration points, each plane contains one point at the center of the plane (Figure A.6).

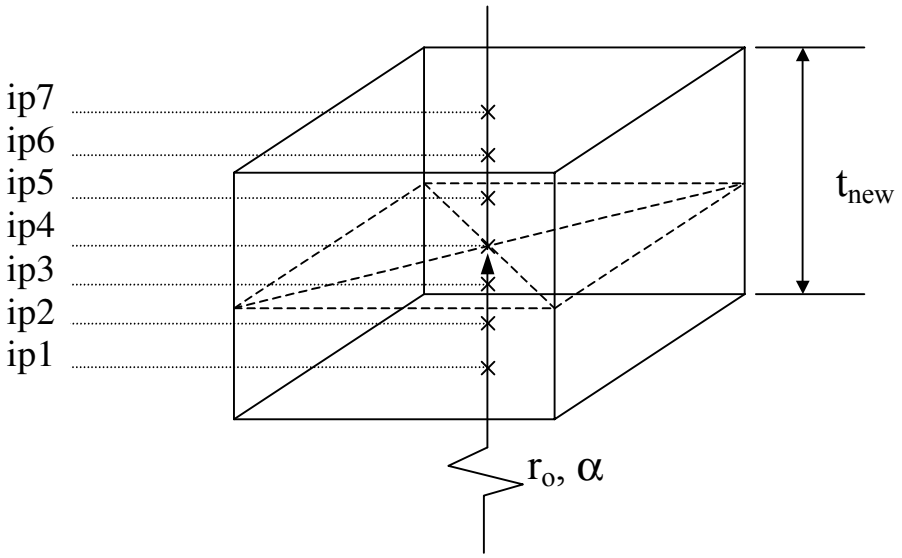

Figure A.6: Tube shell element shown, with 7 through-thickness integration points [*]

A.7 – Decay Formulation

Stresses, strains and change in wall thickness, decay from fully developed values to the "zero" condition corresponding to the un-deformed state. This decay starts in the bend region near the ends of the bend (Figure A.7), and continues into the straight section until the zero condition is reached. The nature of the decay is a function of the bending conditions and tooling contact, similar to the end effects on piping networks discussed in the literature review. Based on experimental and numerical results, for $R_c/d = 2.5$, decay angles are approximated as 7.5° from each end, and independent of bend angle θ.

[*] For 28 integration points there are 4 points in the same plane as *each* of the 7 points, at the parametric coordinates $(\pm\frac{1}{\sqrt{3}},\pm\frac{1}{\sqrt{3}})$ following the order defined by the right hand rule, with the shell normal.

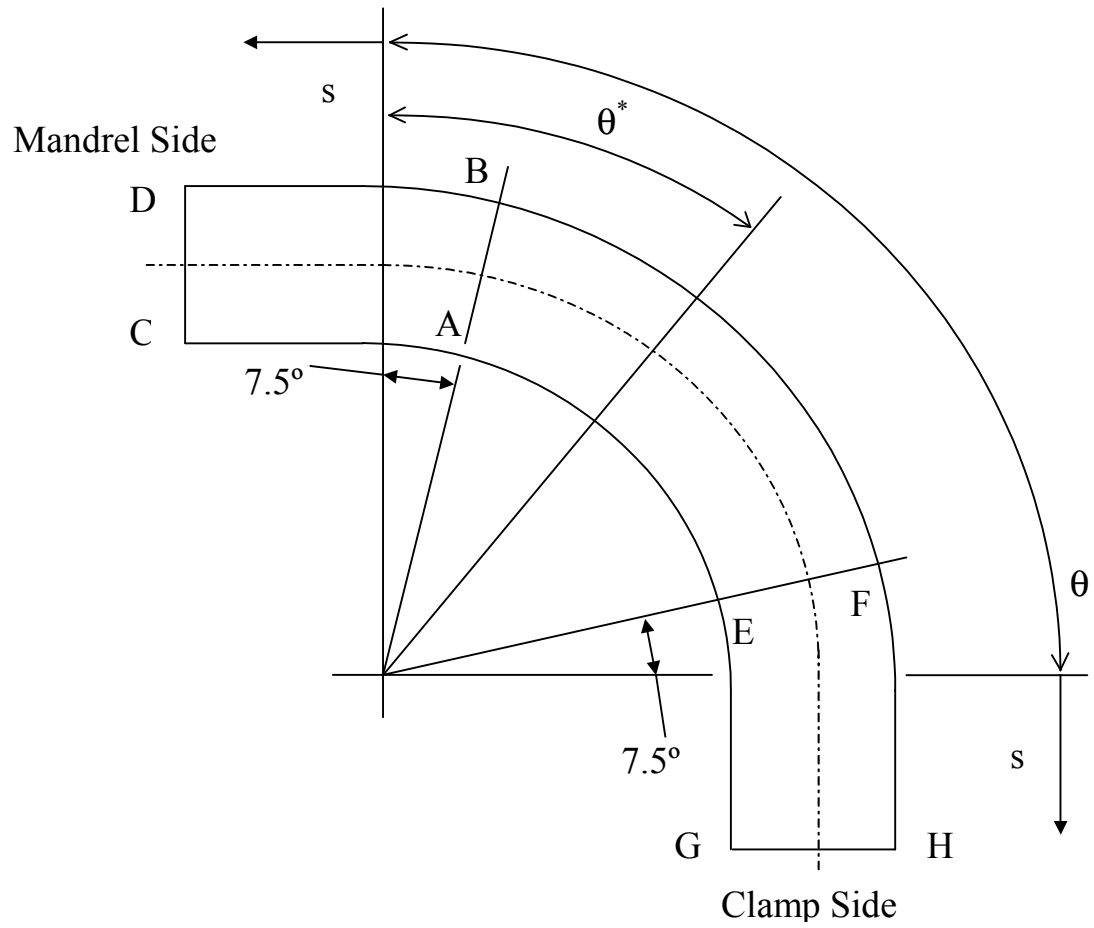

Figure A.7: Regions of stress, strain, and wall thickness decay for a 90º bend angle

Exponential functions are used to treat the decay in stresses, strains and change in wall thickness, inside the regions ABCD & EFGH, starting from the bands AB & EF, respectively. In the region ABEF, the stresses, strains (in local $x_1x_2x_3$) and wall thickness are uniform along θ. In other words, there is no gradient in the θ direction ($\partial/\partial\theta = 0$) in this region, where the bend is fully developed.

Now consider the following general form for the decay function, chosen to be exponential in nature:

$$fn = 1 - \exp\left(\frac{a}{[188.6 \cdot (\phi_d - \theta^* \pm \frac{s}{R})]^2} \right) \tag{A.14}$$

where ϕ_{d2} = 7.5º on the mandrel side and ϕ_{d1} = θ-7.5º on the clamp side. a = -350 is a constant for all R_c/d, and ± s/R is the angle in the straight region at bend radius R and *only* applies to the straight part of the tube. In other words, the s/R term is not in the expression (A.14) inside the curved region. On the mandrel side +s/R applies, and on the clamp side –s/R applies. This is described in detail below.

$s > 0$ is a linear length measured from the start of the straight region, and *only* applies to the straight region of tube (on clamp and mandrel side), which means that the term ± s/R is made to vanish for calculations *inside* the bend region, $0 \le \theta^* \le \theta$. For calculations *outside* the bend (in the straight regions), the numerical value of θ^* in *fn* is set to be 0 or θ depending on whether the straight region is on the clamp side or the mandrel side, and the term ± s/R continues the numerical decay. A more generic functional form for *fn* is shown below, in the form of a multiplier, as used in the bend program.

A more generic function in the form of a multiplier for residual stress, strain, and change in wall thickness, as used in the program, is:

$$mult = \left\{ 1 - op1 \cdot \exp\left(\frac{a}{[188.6 \cdot (\phi_{d1} - \theta^* - op3 \cdot \frac{s}{R})]^2} \right) \right\} \times \left\{ 1 - op2 \cdot \exp\left(\frac{a}{[188.6 \cdot (\phi_{d2} - \theta^* + op3 \cdot \frac{s}{R})]^2} \right) \right\} \tag{A.15}$$

where $\phi_{d1} = \theta - 7.5^{o}$, and $\phi_{d2} = 7.5^{o}$; and *op*1, *op*2, and *op*3 are logical operators in (A.15) . Refer to Figure A.7.

In region ABCD: *op*1=0, *op*2=1. For $\theta^{*} \geq 0$, *op*3 = 0. In the straight region on mandrel side, *op*3=1 and set $\theta^{*} = 0$. In region EFGH: *op*1=1, *op*2=0. For $\theta^{*} \leq \theta$, *op*3=0. In the straight region on clamp side, *op*3=1 and set $\theta^{*} = \theta$. In ABEF, the fully developed region, *op*1=*op*2=0.

In the program, this multiplier (eq. (A.15))is used to "decay" the fully developed values of strain, residual stress, and change in wall thickness, in the transition regions ABCD and EFGH. In the fully developed region ABEF, *mult* = 1, meaning that no decay takes place there.

Mathematically, one can write:

$$\begin{aligned} \varepsilon_{ij} &= \varepsilon_{ij}(\textit{fully developed}) \cdot \textit{mult} \\ t_{new} &= t + [t_{new}(\textit{fully developed}) - t] \cdot \textit{mult} \\ \sigma_{ij} &= \sigma_{ij}(\textit{fully developed}) \cdot \textit{mult} \end{aligned} \qquad \text{(A.16)}$$

The fully developed strains, stresses, and wall thickness are simply the values calculated using the analytical formulas developed. These fully developed values apply to the region inside ABEF.

Now there are cases where the bend angle θ is small, such as 7º. In such a case the decay regions must merge, inside the curved bend region, and consequently a fully developed region does *not* develop. Mathematically it is difficult to describe how this is dealt with in the bend program, so instead, a graphical explanation will be given in Figure A.8, and illustrated with an example.

In Figure A.8 (i), the flat region is the fully developed region for the stresses, strains and thickness, for θ = 45º. The point A_d is the limiting decay point which corresponds to the center of the bend in an undeveloped bend (ii), which in the example shown is for θ = 10º. In (ii) the bend angle θ is too small so the fully developed condition is never reached.

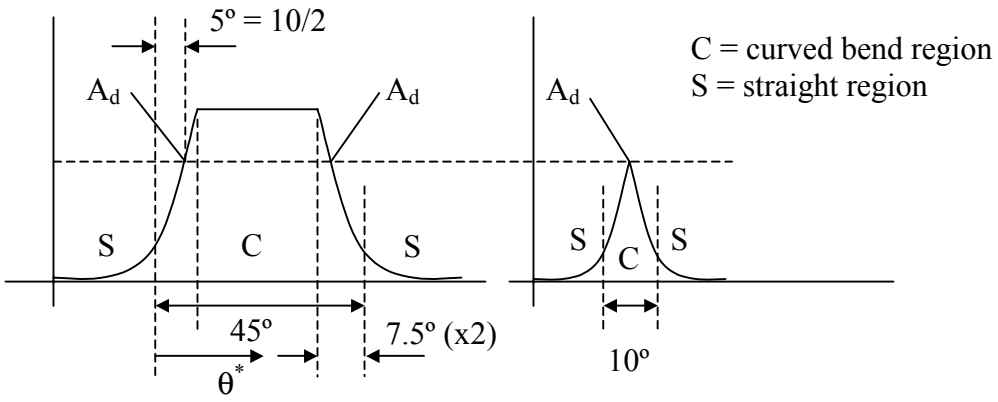

Figure A.8: Decay for (i) Fully developed – 45º bend angle and (ii) Undeveloped – 10º bend angle

A.8- Variation of Hoop Strain Through Thickness

Previously the average through-thickness hoop strain, ε_{hoop}, was calculated. Using this average hoop strain one can now proceed to approximately calculate its variation through the wall thickness.

For cylindrical coordinates, the expression for engineering hoop strain is [51]

$$\varepsilon_2 = \frac{1}{r}\left(w_r + \frac{dv}{d\alpha} \right) \tag{A.17}$$

where α is in the circumferential direction, w_r is the radial displacement, v is the circumferential displacement, and r is the radial distance, at a point. At $\alpha = \alpha_{NA}$, $v = m$ (Figure

3.2). The mid-surface radius is denoted as r_o. At $r = r_o$, $w_r \cong 0$ approximately. Then at $r = r_o + t/2$, $w_r \cong (t_{new} - t)/2$, and at $r = r_o - t/2$, $w_r \cong -(t_{new} - t)/2$. Assuming a linear distribution for w_r for a thin wall, one can write (in terms of the integration points – Appendix A.6):

$$w_r = ip \cdot \frac{(t_{new} - t)}{2} \tag{A.18}$$

This makes sense since (for the convention used) $ip < 0$ for $r < r_o$, and $ip > 0$ for $r > r_o$. One can also write $r = r_o + ip \cdot t_{new}/2$.

Now v can be assumed constant through the (thin wall) thickness. One has a calculation for the average through-thickness hoop strain (ε_{hoop}) which can be thought of as the hoop strain at the midsurface $r = r_o$, which is roughly constant in the tensile and compressive regions. Therefore, one can write

$$v \cong r \cdot \alpha \cdot \varepsilon_{hoop} \tag{A.19}$$

Substituting (A.19) and (A.18) into (A.17) one can formulate an approximate expression for the hoop strain as a function of the through-thickness ip,

$$\varepsilon_2(ip) = ip \cdot \frac{(t_{new} - t)}{(2 \cdot r_o + ip \cdot t_{new})} + \varepsilon_{hoop} \tag{A.20}$$

This can be used to calculate the hoop strain at each of the seven integration points (Appendix A.6). Note that at ip = 0, $\varepsilon_2(ip) = \varepsilon_{hoop}$.

A.9 - Original Tube Stock Length

It is very useful to know the minimum original straight tube length of a tube necessary to give all the required bends, and straight region lengths. This is especially important to know

for a tube bent numerous times and with varying degrees of boost, where it is not obvious what the original length would be.

Mathematically, one can write the original length as

$$L_{stock} = \sum_{i=1}^{N} (R_{ci} - A_i) \cdot \theta_i + \sum_{i=1}^{N+1} l_i + \sum_{i=1}^{N} l_i^b \qquad \text{(A.21)}$$

- N is the number of bend regions
- R_{ci} is the desired centerline radius, after springback, for each bend region i
- A_i is the neutral axis distance below the centerline for the pure bending condition, for each bend region i (Figure 3.1).
- θ_i is the bend angle (in radians) for each bend region i
- l_i is the desired straight region length, after bending, as shown in the Appendix A.4 section on mesh generation
- l_i^b is the boost length, as given by eq. 3.21, for each bend region i

A.10 - End Feed Corresponding to Pure Bending

In tube bending practice, it can be useful to know the percentage boost corresponding to pure bending (zero boost force) on a rotary draw bender, for a particular size tube and a particular R_c/d ratio. This unique percent boost is simply the displacement the back of the tube (feeding into the bend) experiences under *no* influence of any boost force. In other words, a pressure die moving at this specific percent boost value actually does nothing in terms of introducing axial membrane strains into the tube bend, since it is *neither* pushing material into the bend or pulling material out of the bend. See Appendix A.13 for a physical proof of pure bending.

The analytical model calculates, approximately, the unique percent boost value corresponding to pure bending. Looking at eq. (3.21):

$$l^b = R_c \cdot \theta \cdot \frac{percent\ boost}{100} - (R_c - A) \cdot \theta$$

For pure bending, *l* must equal 0. Therefore one can solve for *percent boost*:

$$percent\ boost = (R_c - A) \cdot \frac{100}{R_c} = 97.6\%$$

This is for $R_c/d = 2.5$, d = 76.2 mm, R_c = 190.5 mm, 1.57 mm original wall thickness, and A = 4.53 mm (calculated). This is an important result because it says that for *percent boost* > **97.6%** material is "pushed" into the bend to introduce compressive membrane strains ($e(\alpha) < 0$). For *percent boost* < **97.6%** material is "pulled" out of the bend to introduce tensile membrane strains ($e(\alpha) > 0$). In the latter case, frictional force between the pressure die and the tube is the means to control the movement of the tube. In the former case, the reaction of the boost block on the back of the tube is the means to control the movement.

A.11 - Accounting for Slip between Tube and Pressure Die

For the case where friction is the mode of boost (for *percent boost* < 97.6%) there is the chance for slippage, resulting from inadequate friction between tube and pressure die. Note that for the case where the boost block is utilized (for *percent boost* > 97.6%) then slip is impossible, since the forward displacement of the pressure die exceeds that of the tube.

Let's say that for a particular friction boost there is a slip of, say, 16.5 mm between the pressure die and the tube during the course of the bend (as in the NB100 experimental case), which was bent to 91° (over-bent to allow springback to 90°). The prescribed boost was 100%, which is different from the "effective" boost the tube experienced because of slip. The pressure

die moved 16.5 mm ahead of the back of the tube. In other words the pressure die was moving faster than the straight part of the tube feeding into the bend (the part in contact with the pressure die).

During the course of the bend, the centerline of the tube moves an arc length distance

$$d_1 = R_c \cdot \frac{91}{90} \cdot \frac{\pi}{2} \tag{A.22}$$

Now, at 100% boost the pressure die moves

$$d_2 = 1.0 \cdot d_1 \tag{A.23}$$

Because of slip the back of the tube, in reality, moves

$$d_3 = d_2 - 16.5 \tag{A.24}$$

Thus, d_3 corresponds to an effective percent boost. One can solve for this mathematically,

$$d_3 = \frac{percent\ boost}{100} \cdot d_1 \tag{A.25}$$

For R_c = 188.595 mm (bend die radius in the experimental study), one calculates effective *percent boost* = 94.5%. This is a rough estimate because during the course of the bend the degree of slip is not necessarily uniform. So the effective percent boost calculated is essentially an average value, and is coincidently very close to the LE95 boost case.

A.12 - Bend Die Torque

Consider the tube, shown in Figure A.9, sectioned at the tangent line. This choice of sectioning conveniently allows one to calculate tool contact forces and moments, given the known force F_{boost} (eq. 3.36), and moment M (eq. 3.45).

As shown in Figure A.9, the forces F_x, F_z are the resultant forces acting on the tube, at point P, due to contact with the bend die and clamp die. The moment M_{bd} is the resultant moment acting on the tube due to contact with the bend die and clamp die. The bending moment M is due to the axial stresses acting on the tube cross-section. This moment M is about the centroid of area of the cross-section, c. T_o is the necessary net torque applied to the bend die about the center of rotation o. T_o does not take into account friction between mandrel and tube, therefore T_o is the net torque needed by the bend die. The sign convention is as shown in Figure A.9.

First, perform a force balance on the tube:

$$\begin{aligned} \sum F_{x-dir} &= 0 \rightarrow F_x = 0 \\ \sum F_{z-dir} &= 0 \rightarrow F_z = F_{boost} \end{aligned} \tag{A.26}$$

Now, perform a moment balance on the tube, about centroid c:

$$\sum M_c = 0 \tag{A.27}$$

Therefore,

$$M - M_{bd} - F_z \cdot r_x = 0 \tag{A.28}$$

Now, perform a moment balance on the bend die, about o, keeping in mind that the force F_z and moment M_{bd} act in the opposite sense, due to Newton's 3rd law.

Summing moments about o,

$$\sum M_o = 0 \tag{A.29}$$

Therefore,

$$-T_o + M_{bd} - F_z \cdot (R - r_x) = 0 \tag{A.30}$$

As a result, with $R = R_c - E_{ct}$,

$$T_o = M - F_{boost} \cdot (R_c - E_{ct}) \tag{A.31}$$

This result is interesting because it says that the net torque is independent of bend rotation angle θ, and is constant. It should be noted that the net torque is an underestimate of the actual torque needed by the bend die, due to friction. There are two sources of frictional losses to consider. The first source of friction is due to the internal resistance in the bend die, which must be overcome for the bend die to rotate. The second source is from the friction with the mandrel balls. The mandrel balls lie inside the tube in the section as shown in Figure A.10, and therefore their contribution to the force and moment balance must be taken into account for accurate accounting of friction. The friction force F_f is the friction force acting on the tube due to contact between the mandrel balls and tube inside-wall. The difficulty is in determining F_f to obtain a reasonable friction estimate.

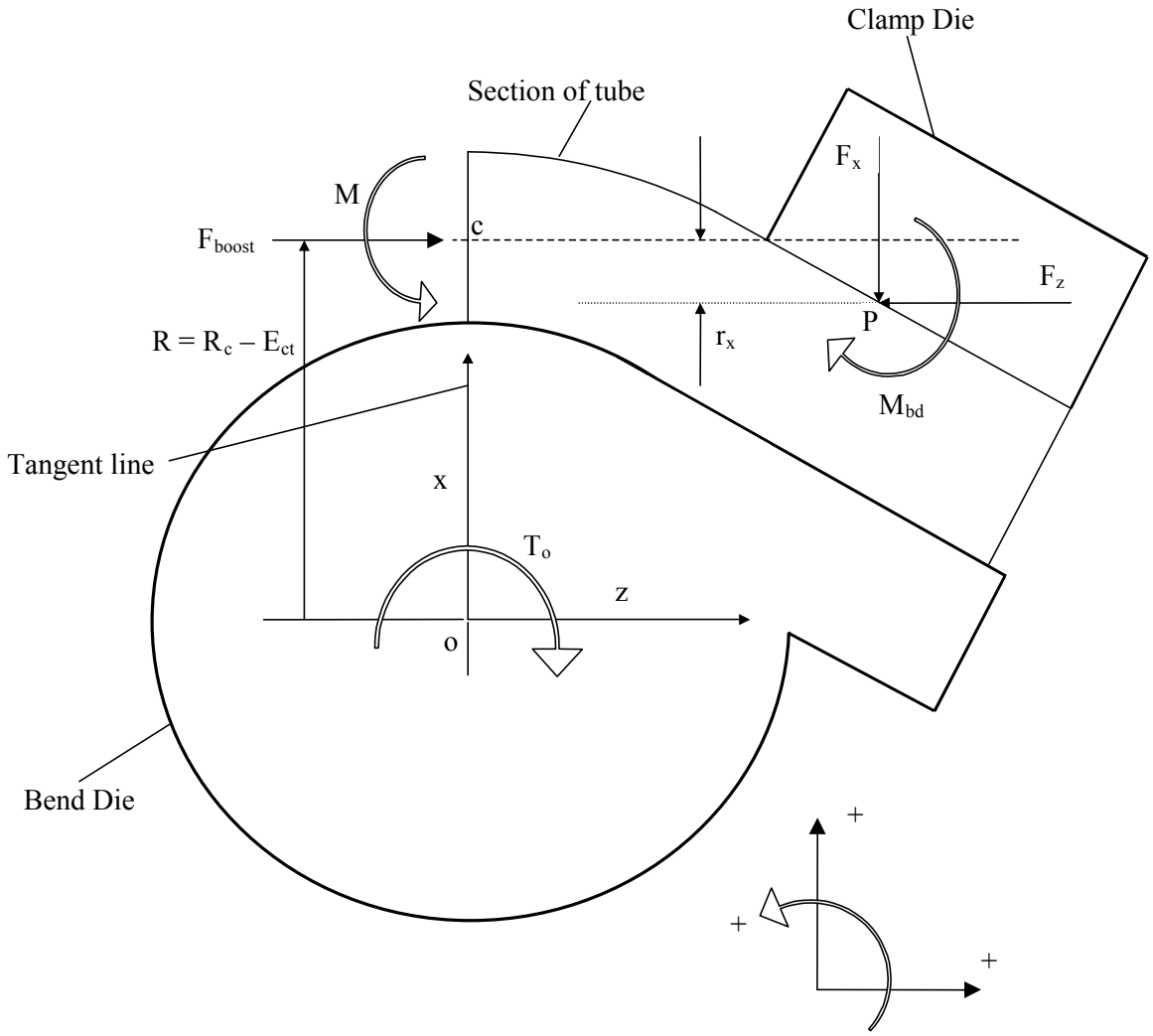

Figure A.9: Section of tube showing the resultant forces and moment acting on it due to contact with bend die and clamp die

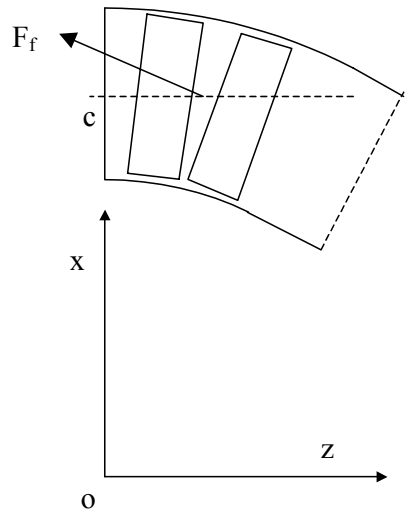

Figure A.10: Tube section showing friction force acting on tube due to contact with mandrel balls

A.13 – Pure Bending Case

Consider the straight tube section A in Figure A.11. M_s is the resultant moment acting on the straight section due to contact with the pressure die and the wiper. F_{boost} is the net boost force acting on the section due to the pressure die.

Perform a force balance on section A:

$$\sum F_{z-dir} = 0 \rightarrow F_c = F_{boost} \tag{A.32}$$

Now, perform a moment balance on section A:

$$\sum M = 0 \rightarrow M_s = M_c \tag{A.33}$$

Consider the curved section B. σ_1 is the axial stress distribution acting on the cross-section. F_c is the resultant axial force acting on the cross-section due to σ_1, with line of action passing through the centroid of area c. M_c is the resultant moment due to σ_1, calculated about the centroid c.

For pure bending $F_c = 0$, and there is only a resultant moment M_c acting on the tube cross-section. Furthermore, for pure bending, $F_c = F_{boost} = 0$. This means that to obtain a pure bending condition, the net boost force acting on the tube must be zero.

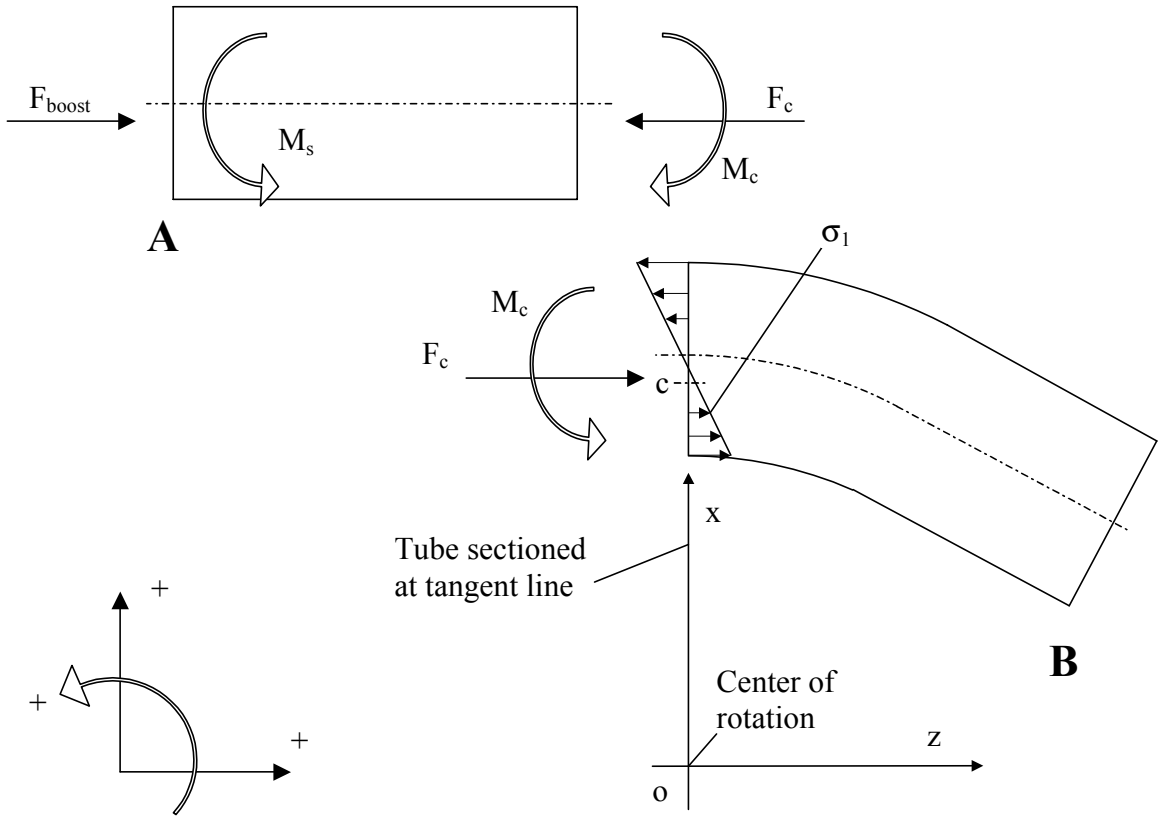

Figure A.11: Free-body diagram illustrating pure bending case

Appendix B – Outline of Analytical Model

The purpose of the discussion in this appendix is to summarize the more practical aspects of the bend model to provide a simple understanding of the main aspects of input and output requirements, limitations and assumptions, and built-in efficiencies.

B.1 - Input Considerations

The main advantage over the FEA model is the much simpler setup and consequently the much reduced run time. The user can input all parameters from a GUI (Graphical User Interface), which visually shows the different stages of, say, a multiple bend operation in progress (see Figure B. 1). The geometric parameters of each stage of the bend (such as centerline bend radius, bend angle, straight region length) are input into the GUI. The corresponding bend is visually shown to the user, as each bend specification is input.

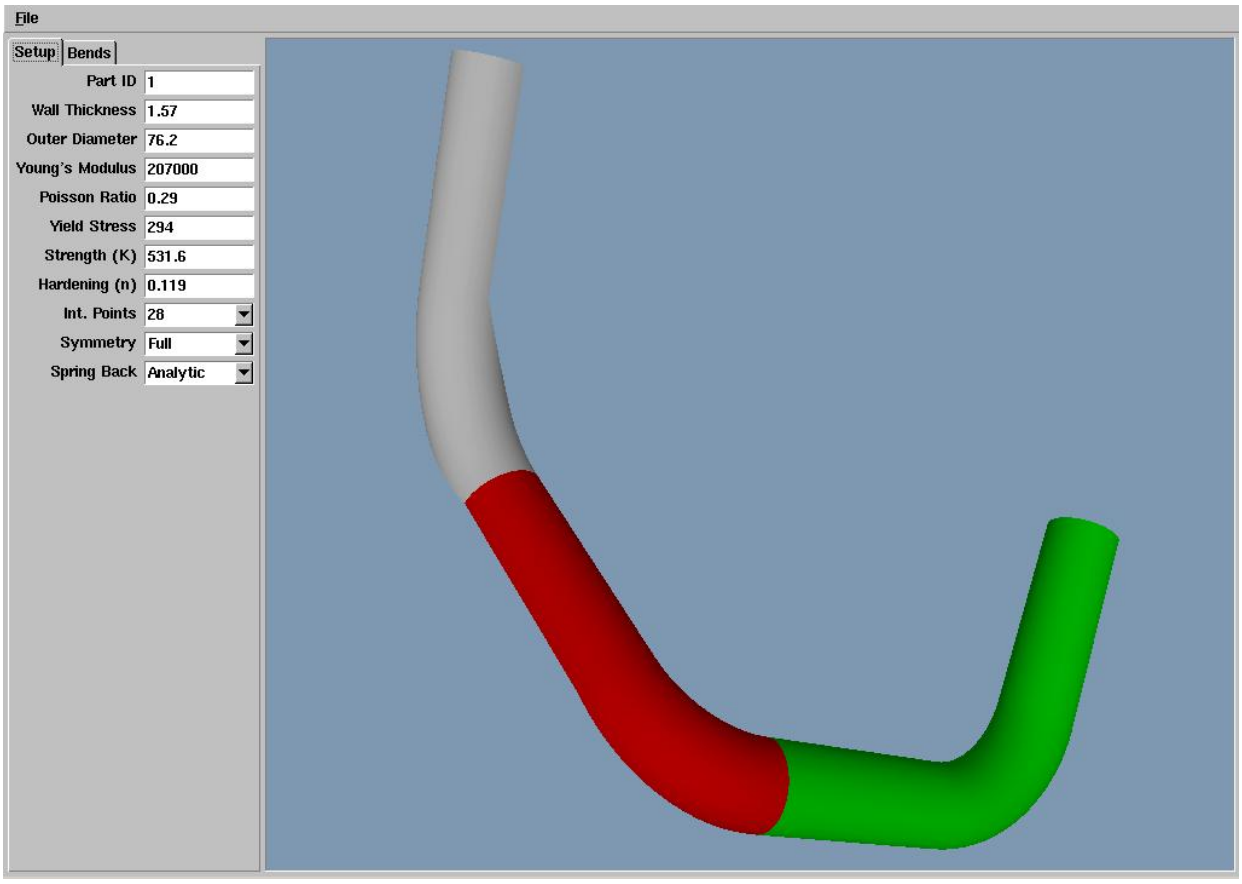

Figure B. 1: GUI setup menu showing tube bent in three-dimensions

All geometric parameters required as input are:

- Tube outside diameter
- Original tube wall thickness
- For each bend region: desired centerline radius (after springback), desired bend angle (after springback), straight region length, z-axis rotation after each bend – for creating tubes with multiple bends in three dimensions

Non-geometric parameters required as input are:

- Desired part ID
- Elastic modulus of tube material
- Poisson's ratio
- Yield Stress
- Half-symmetry option or full-symmetry option (see below)
- For each shell element in the tube mesh, 7 integration points or 28 integration points can be chosen.
- A flow curve input file can be input for calculations in plasticity equations, or a simpler hardening rule can be input, by the user, in the form of a K and n value, corresponding to a power law model for the tube material, as given by $\sigma_{eff} = K \cdot (\varepsilon_{yp} + \varepsilon_{eff})^n$, discussed in Section 3.1.1.
- Percent boost or boost force can be specified as input
- Option to allow LS-DYNA to numerically calculate residual stresses for an analytically bent tube

Note that the half symmetry option *only* applies to tubes bent in a single plane (z-axis rotation is $\beta = \pm 180^o$, see Appendix A.4), meaning that all the bends of the tube lie in a single plane. Full-symmetry *always* applies to tubes bent in three dimensions (where one or more z-rotations are *not* equal to $\pm 180^o$), meaning that not all bends lie in the same plane. The full-symmetry option is available, if desired, for tubes where all the bends lie in a single plane.

By default, the bend model analytically calculates the residual stresses, by subtracting elastic stresses from total elastic-plastic stresses, to account for springback. Alternatively, one can set the option of *not* having the analytical model subtract the elastic stresses, therefore retaining the total elastic-plastic stresses before unloading of the tube (springback). The motivation for having this option is that the analytically calculated residual stresses don't fully satisfy static equilibrium in the tube. LS-DYNA can then be used to perform springback (unloading) calculations (based on the analytical elastic-plastic stresses after bending). In this approach, the

resulting residual stresses better satisfy the static equilibrium requirement. The LS-DYNA-calculated residual stresses are then to be used in place of the analytically calculated residual stresses. The analytically calculated strains, thickness, and nodal coordinates can be kept as in the original analytical output. It is especially important to keep the original analytically determined nodal coordinates since those correspond to the desired final dimensions of the tube which can be quite important for fit in a die during a secondary forming operation. Also, if one wishes, the LS-DYNA-calculated strains and thickness can be used in place of the analytical ones. Running a FE springback calculation is not very time consuming, so there is no real disadvantage in incorporating it.

B.2 - Output

The bend program generates residual stress after springback, or elastic-plastic stress, before springback, in output files; as well as strain, shell thickness, and nodal coordinate output files. These output files can be used as input for a subsequent springback simulation (if residual stresses *not* calculated analytically). Then the data, after springback, can be used as input to a secondary forming simulation. Alternatively, if residual stresses are calculated analytically, then the analytical output files can be used directly as input data for a secondary forming simulation, with *no* intermediate FE springback simulation.

Furthermore, for information purposes, a results output file is created showing stress, strain, and thickness distribution around the tube circumference in the fully developed bend region.

In this results output file, the program also outputs, for each bend region, the boost force corresponding to the prescribed percent boost, or the percent boost corresponding to the prescribed boost force, as well as the net bend die torque. The program also outputs the

centerline bend radius to bend the tube at, such that the *desired* centerline radius is achieved after springback, for each bend region. This can be used to estimate the required bend die size to allow for residual springback. Furthermore, the program outputs the necessary bend angle such that, after springback, the tube springs back to the desired bend angle, for each bend region.

For each bend region, the program additionally outputs the percent boost corresponding to *pure bending*, which is for zero boost force. This can be useful information since below this value the boost "pulls" material out of the bend, and above it the boost "pushes" material into the bend.

Finally, the program outputs the minimum original straight stock length of the tube such that it will be long enough to accommodate all the bends and all the straight region lengths'.

Figure B.2 schematically shows the basic sequence and structure of the input and output.

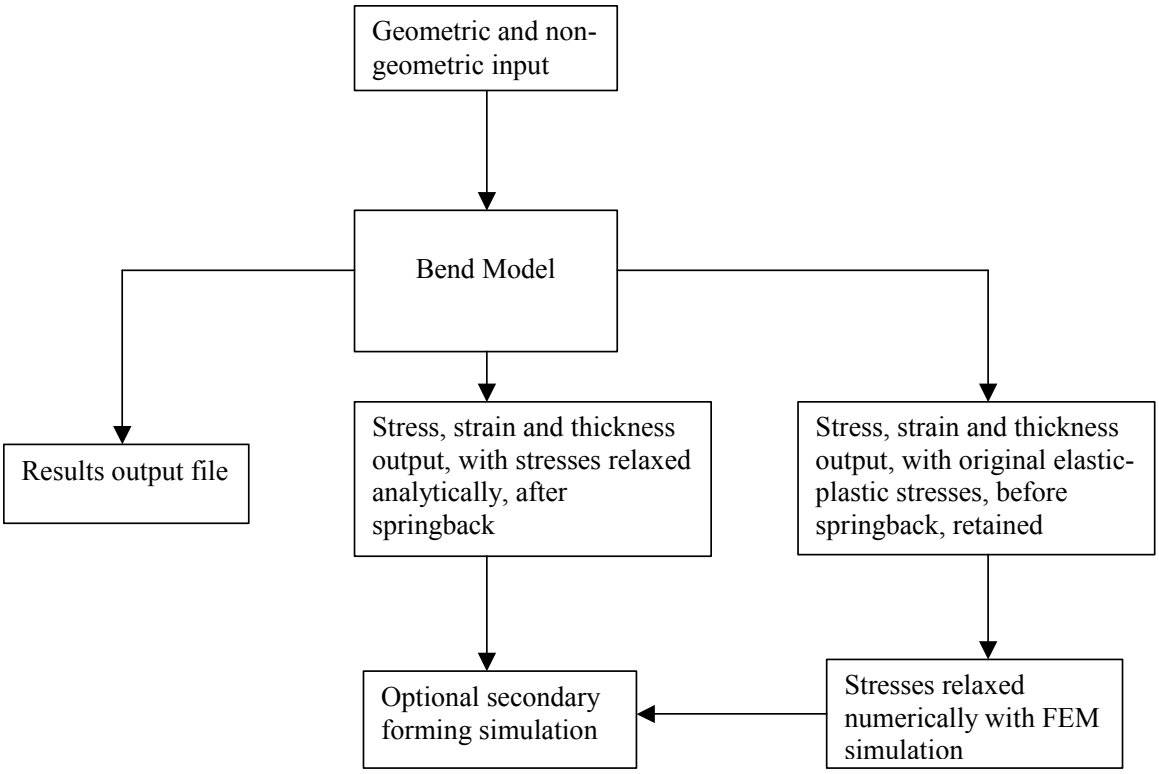

Figure B.2: Flow chart showing basic structure of input and output

B.3 - Limitations and Assumptions

Among the main assumptions of the model are the following:

- Isotropic material
- Constant percent boost or constant boost force throughout duration of bend
- The strain distribution in the tube cross-section is such that the tube is either borderline fully-tensile or borderline fully-compressive, at the extremes.

In other words, for borderline fully-tensile the minimum axial strain is 0, located at the innermost compressive region of the tube (inside bend radius), owing to a very low boost tensile membrane strain component. For borderline fully-compressive, the maximum axial strain is 0 at the outermost tensile region of the tube (outside bend radius), owing to a very high boost

compressive tensile membrane strain component. As it turns out these ranges of strain and boost are very comfortably in the practical range of tube bending practice anyway. This is discussed in more detail in Appendix A.3.

- No normal stress in the thickness direction of the shell, consistent with thin shell theory assumptions
- No shear strain or shear stress in the local $x_1 x_2 x_3$ directions of the tube, consistent with typical bending theory, as found in the literature

B.4 - Efficiency

The program has several built-in means with which to significantly reduce run time and increase computational efficiency. Among these are:

- The finite element mesh of the tube is generated automatically by the bend program. The mesh density is arbitrary, and defined by the user.

- If there are multiple bend regions of identical boost and bend radius, the program then performs array calculations only once for those regions, so as to avoid having to repeat calculations, and waste computation time.

- For *each* distinct bend region, array calculations containing stress, strain and thickness are only performed *N*xP times, where *N* is the number of elements around the circumference, and P is the number of integration points per element. In other words, the model calculations are performed for each shell element, and for each integration point in the element. This allows greater efficiency in computation since the stress, strain and thickness data in each element, in each bend, can only correspond to one of the *N*xP array calculations, identified by circumferential (α) position. The fact that the prescribed boost

is constant allows this to be the case. Near the ends, of course, decay functions reduce the numerical values of the stress, strain and thickness, but only as a calculation external to the original array calculations.

- The constant boost means that only *N*xP individual array calculations are needed for each bend region. If the boost were allowed to vary during the duration of the bend then the array calculations would have to account for the longitudinal (θ) position of each shell element in the bend, as well as the circumferential (α) position of the shell element. This would greatly reduce run-time, as the number of longitudinal positions to take into account would be equal to the number of elements in the longitudinal direction for each bend. And if this number is *M*, then the calculations would take *M* times as long for *each* bend.

- The program runs much faster if percent boost is prescribed instead of boost force. The reason is that prescribed boost force requires expensive iteration to find the corresponding membrane strain component, using the bisection method, whereas with given percent boost one can easily and directly find the corresponding membrane strain component. This is explained in more detail in Section 3.1.2.